Author:
Dibble, Robert P

Title:
Resonance avoidance in variable speed rotorcraft using an applied compressive load

Resonance avoidance in variable speed rotorcraft using an applied compressive load

A Thesis in Aerospace Engineering

By

ROBERT P DIBBLE

Department of Aerospace Engineering
UNIVERSITY OF BRISTOL

A dissertation submitted to the University of Bristol in accordance with the requirements of the degree of DOCTOR OF PHILOSOPHY in the Faculty of Engineering.

DECEMBER 2019

Word count: 55,000 words

Abstract

One of the concepts considered by the rotorcraft industry to improve aircraft performance whilst reducing emissions is the use of a variable speed rotor. This concept varies the rotor speed, in addition to collective pitch, to achieve trim and minimise fuel burn. However, a rotor blade's natural frequencies and rotor harmonics (both functions of rotor speed) may intersect due to the change in speed which will induce unsatisfactory vibrations in the aircraft. The present research considers the use of an applied compressive load to the blade to alter its natural frequencies and avoid resonance.

Initially, an in-vacuo model of an untwisted blade subject to an applied compressive load is developed and validated using a Finite Element model and an experiment. Subsequently, it is shown that compressive loading is able to sufficiently alter the in-plane and out-of-plane natural frequencies of the blade such that a desired separation between the natural frequencies and rotor harmonics would likely be achievable. The load required did not exceed the buckling load of the blade, nor would it have required large powerful actuation.

The model fidelity was increased to capture torsional deformation, pretwist and noncoincident mass and elastic axes. It was then shown that, for a set of three test aircraft, the range of rotor speeds that would be operable increased significantly through the use of an applied compressive load.

Finally, the fidelity was again increased to include geometric nonlinearities and unsteady aerodynamic loads in hover. The investigation that followed showed that rotor speed and the applied compressive load had a marked impact on the damping ratios of the natural frequencies of the blade. It is possible to exploit these impacts to change damping ratios, as well as natural frequencies, to expand the operable range of rotor speeds of an aircraft.

Dedication and acknowledgements

I would like to express my gratitude towards a number of people and organisations for their support over the last eight years as I completed my Masters and Doctorate degrees in Aerospace Engineering.

To my supervisor, Dr Branislav Titurus, whose engaging lectures first got my interested in dynamics, I would like to thank for being my supervisor during my undergraduate research project and Doctorate degree. I would like to thank my second supervisor, Dr Ben K S Woods, for his guidance which provided a viewing useful perspective for the research presented herein. Although not formally a supervisor, I am very grateful to Dr Vaclav Ondra for his advice and experimental help during our co-authored publications.

To my family, housemates, coursemates, triathlon teammates and girlfriend, thank you all for your unwaivering support and understanding throughout this long process, restoring a sensible work-life balance when things got too busy and being around to celebrate the milestones achieved.

A final thankyou goes to the EPSRC who provided the funding, under Grant Number EP/M507994/1, that made this research possible.

AUTHOR'S DECLARATION

I declare that the work in this dissertation was carried out in accordance with the requirements of the University's Regulations and Code of Practice for Research Degree Programmes and that it has not been submitted for any other academic award. Except where indicated by specific reference in the text, the work is the candidate's own work. Work done in collaboration with, or with the assistance of, others, is indicated as such. Any views expressed in the dissertation are those of the author.

SIGNED: ..... DATE: .....

Table of Contents

List of Tables

NOMENCLATURE

Symbol	Description	Unit
A	Cross-sectional area	m^2
B_1	Section constant	m^5
B_2	Section constant	m^6
C	Wagner function	
C_d	2D drag coefficient	
C_{d0}	2D parasitic drag coefficient	
C_l	2D lift coefficient	
$C_{l,\alpha}$	2D lift coefficient slope	rad^{-1}
D	Drag	$\mathrm{N\,m}^{-1}$
E	Youngs modulus	Pa
F_x	Internal shear force in the x direction	N
F_y	Internal shear force in the y direction	N
F_z	Internal shear force in the z direction	N
G	Shear modulus	Pa
H	Frequency Response Function, $\frac{input}{output}$	$\mathrm{m\,N}^{-1}$ or $\mathrm{rad\,N}^{-1}\,\mathrm{m}^{-1}$
I_y	Bending moment of inertia about major neutral axis	m^4
I_z	Bending moment of inertia about minor neutral axis	m^4
J	Torsional stiffness constant	m^4
K_C	Modal stiffness due to compression	$\mathrm{N\,m}^{-1}$
K_G	Modal stiffness due to geometry	$\mathrm{N\,m}^{-1}$
K_R	Modal stiffness due to rotation	$\mathrm{N\,m}^{-1}$
L_C	Circulatory lift	$\mathrm{N\,m}^{-1}$
L_{NC}	Non-circulatory lift	$\mathrm{N\,m}^{-1}$
L_x	Aerodynamic force distribution on the blade in the x direction	$\mathrm{N\,m}^{-1}$
L_y	Aerodynamic force distribution on the blade in the y direction	$\mathrm{N\,m}^{-1}$
L_{y0}	Aerodynamic excitation force distribution on the blade in the y direction	$\mathrm{N\,m}^{-1}$
L_z	Aerodynamic force distribution on the blade in the z direction	$\mathrm{N\,m}^{-1}$

Symbol	Description	Unit
L_{z0}	Aerodynamic excitation force distribution on the blade in the z direction	$\mathrm{N\,m^{-1}}$
M	Modal mass	kg
M_0	Magnitude of oscillatory excitation moment	N m
M_C	Non-circulatory torque	$\mathrm{N\,m\,m^{-1}}$
M_{NC}	Circulatory torque	$\mathrm{N\,m\,m^{-1}}$
M_g	Gross mass of aircraft	kg
M_ϕ	Aerodynamic torque on the blade about the x axis	$\mathrm{N\,m\,m^{-1}}$
$M_{\phi 0}$	Aerodynamic excitation torque on the blade about the x axis	$\mathrm{N\,m\,m^{-1}}$
M_t	Tip mass	kg
M_v	Mach value of vehicle at cruise	
M_x	Internal moments about the x axes	N m
$M_{x'}$	Internal moments about the deformed x axes	N m
M_y	Internal moments about the y axes	N m
$M_{y'}$	Internal moments about the deformed y axes	N m
M_z	Internal moments about the z axes	N m
$M_{z'}$	Internal moments about the deformed z axes	N m
N_b	Number of blades	
P	Compressive force	N
P_c	Critical compressive force that leads to buckling	N
P_i	Installed power	W
P_m	Maximum allowable compressive force	N
P_o	Optimum compressive force	N
P_x	Component of compressive force in x direction	N
P_y	Component of compressive force in y direction	N
P_z	Component of compressive force in z direction	N
R	Radius	m
R_0	Radial location of blade root/hinge	m
R_C	Radial location of aerodynamic root of blade	m
T	Internal tension in the blade	N
T_t	Internal tension in the tendon	N
U	Lateral deformation of the blade for the modeshape in the x direction	m
V	Lateral deformation of the blade for the modeshape in the y direction	m

Symbol	Description	Unit
V_t	Lateral deformation of the tendon for the modeshape in the y direction	m
W	Lateral deformation of the blade for the modeshape in the z direction	m
W_t	Lateral deformation of the tendon for the modeshape in the z direction	m
a_c	Longitudinal cyclic trim	rad
a_s	Lateral cyclic trim	rad
c	Blade chord	m
e	Euler's number; or Distance between mass and elastic axis - positive when mass axis lies ahead	m
e_0	Distance at root between the elastic axis of the blade and the axis of rotation, positive when elastic axis lies ahead	m
e_A	Distance between area centroid and elastic axis - positive when area centroid axis lies ahead	m
i	imaginary number, $\sqrt{-1}$, or mode number	
k	Reduced frequency	
k_A	Polar radius of gyration of the cross-sectional area about the elastic axis	m
k_m	Polar radius of gyration of the cross-sectional mass about the elastic axis	m
k_{m1}	Mass radii of gyration about the major axis	m
k_{m2}	Mass radii of gyration about an axis perpendicular to the major axis that intersects the elastic axis	m
m	Mass distribution of the blade	$\mathrm{kg\,m^{-1}}$
m_t	Mass distribution of the tendon	$\mathrm{kg\,m^{-1}}$
q_v	Modal participation factor in the y direction	
q_w	Modal participation factor in the z direction	
s	complex form of harmonic frequency	$\mathrm{rad\,s^{-1}}$
t	Time	s
u	Lateral oscillatory deformation of the blade in the x direction	m
u_0	Lateral static deformation of the blade in the x direction	m
u_*	Lateral deformation of the blade in the x direction	m
v	Lateral oscillatory deformation of the blade in the y direction	m
v_0	Lateral static deformation of the blade in the y direction	m
$\bar{v}$	v normalised against radius	

Symbol	Description	Unit
v_f	Forward flight velocity	$\mathrm{m\,s^{-1}}$
v_{in}	Inflow velocity	$\mathrm{m\,s^{-1}}$
v_*	Lateral deformation of the blade in the y direction	m
v_t	Lateral deformation of the tendon in the y direction	m
v_{t*}	Lateral oscillatory deformation of the tendon in the y direction	m
w	Lateral oscillatory deformation of the blade in the z direction	m
w_0	Lateral static deformation of the blade in the z direction	m
$\bar{w}$	w normalised against radius	
w_*	Lateral deformation of the blade in the z direction	m
w_t	Lateral deformation of the tendon in the z direction	m
w_{t*}	Lateral oscillatory deformation of the tendon in the z direction	m
x	Undeformed elastic axis	m
$\bar{x}$	x normalised against radius	
x'	Deformed x axis	m
y	Axis orthogonal to x and z axes	m
y'	Deformed y axis	m
z	Axis of rotation	m
z'	Deformed z axis	m
Γ	Orthogonality value	
Φ	Angle of torsional deformation of the blade for the modeshape about the elastic axis	rad
Ψ	Angular displacement of beam, used in Timoshenko beam theory	rad
Ω	Rotor speed	$\mathrm{rad\,s^{-1}}$
Ω_0	Nominal rotor speed	$\mathrm{rad\,s^{-1}}$
α	Elastic contribution to natural frequency	$\mathrm{rad^2/s^2}$
α_{in}	Inflow angle	rad
β	Rotation contribution to natural frequency	
γ	Compressive load contribution to natural frequency	$\mathrm{rad^2/s^2/N}$
δ	Linear twist, $\theta(R)-\theta(R_0)$	rad
ϵ	Modal Separation	
ϵ_m	Minimal Modal Separation	
ζ	Damping ratio, -Re(λ)/λ_0	
η	Aeroelastic resonance metric	
θ	Blade pitch angle prior to deformation	rad
κ	Timoshenko shear coefficient	

Symbol	Description	Unit
λ	Natural frequency	$\mathrm{rad\,s^{-1}}$
λ_0	Undamped natural frequency, $\lvert\lambda\rvert$	$\mathrm{rad\,s^{-1}}$
λ_D	Damped natural frequency, $\mathrm{Im}(\lambda)$	$\mathrm{rad\,s^{-1}}$
μ	Torsional-translational factor	m
ρ	Material density	$\mathrm{kg/m^3}$
ρ_∞	Air density	$\mathrm{kg/m^3}$
$\rho_{\infty,d}$	Air density in dynamic analyses	$\mathrm{kg/m^3}$
$\rho_{\infty,s}$	Air density in static analyses	$\mathrm{kg/m^3}$
ϕ	Angle of torsional oscillatory deformation of the blade about the elastic axis	rad
ϕ_0	Angle of torsional static deformation of the blade about the elastic axis	rad
$\bar{\phi}$	ϕ normalised against radius	$\mathrm{rad\,m^{-1}}$
ϕ_*	Angle of torsional deformation of the blade about the elastic axis	rad
ψ	Azimuth position	rad
ω	Harmonic frequency	$\mathrm{rad\,s^{-1}}$
$\mathbf{C}$	Azimuth coefficients matrix	
$\mathbf{D}$	Modal drag matrix	
$\mathbf{D}_1$	Modal drag matrix, constant term	
$\mathbf{D}_2$	Modal drag matrix, linear term	
$\mathbf{D}_3$	Modal drag matrix, nonlinear term	
$\mathbf{K}$	Modal stiffness matrix	
$\mathbf{L}$	Modal lift matrix	
$\mathbf{L}_1$	Modal lift matrix, constant term	
$\mathbf{L}_2$	Modal lift matrix, linear term	
$\mathbf{M}$	Modal mass matrix	
$\mathbf{Q}$	Modal participation factor matrix	
$[\ ]_{i,j,k}$	$[\ ]$ pertaining to the i^{th} mode or the i^{th}, j^{th}, k^{th} iteration	
$[\ ]_{\phi,u,v,w}$	$[\ ]$ pertaining to motion in the ϕ,u,v,w directions, respectively	
$[\ ]'$	Spatial derivative of $[\ ]$, $\frac{\partial[\ ]}{\partial x}$	
$\dot{[\ ]}$	Temporal derivative of $[\ ]$, $\frac{\partial[\ ]}{\partial t}$	
BVI	Blade Vortex Interaction	
BVP	Boundary Value Problem	
CAR	Cumulative Aeroelastic Response	
CFD	Computational Fluid Dynamics	

Symbol	Description	Unit
CSD	Computational Structural Dynamics	
FE	Finite Element	
FRF	Frequency Response Function	
HHC	Higher Harmonic Control	
IBC	Individual Blade Control	
I,O,T	In-plane, Out-of-plane and Torsion mode	
MAC	Modal Assurance Criterion	
MMS	Minimum Modal Separation	
MS	Modal Separation	
ODE	Ordinary Differential Equation	
PDE	Partial Differential Equation	
PSD	Power Spectral Density	

LIST OF FIGURES

CHAPTER 1

INTRODUCTION

Within this chapter, the motivation for the current research is provided and the concept that is to be investigated is be introduced. Firstly, the requirements of the industry, and how variable speed rotors may be employed to meet them, are discussed along with the associated problems with variable speed rotors that currently prohibit their widespread use. Secondly, the suite of existing vibration suppression techniques that are currently available, or in development, are discussed and their applicability to overcome the problems associated with variable speed rotors is evaluated. The limitations of the current methods shall, in turn, be used to derive the requirements of the proposed compressive loading based resonance avoidance concept. Subsequently, the concept will be introduced and the research objectives of the current work concerning this concept are defined.

1.1 Motivation

Since the invention of rotary-winged aircraft, engineers have been attempting to improve their performance; a trend that holds to this day. The performance improvements currently desired consist primarily of increases in cruise speed, range, service ceiling and payload among other characteristics while reducing economic cost, fuselage vibrations, noise and greenhouse gas emissions. These changes are motivated partly by the desire of customers and consumers to operate more difficult missions in increasingly harsh environments, but also increasing regulation of greenhouse gas emissions and improved operating conditions for equipment, pilots, passengers and crew members. For example, the Advisory Council for Aeronautics Research in Europe has set several environmental goals to reduce CO_2 and NO_x emissions in the order of 50 % and 80 %, respectively, for new aircraft entering service in 2020 [4].

In rotor blade design, the need to improve comfort, stability, and fatigue life leads to stringent vibration limits [5]. *Moffatt and Griffiths* [6] stated that low vibration levels promise reduced cost of ownership through reduced maintenance of structures and sensitive equipment, improved ride quality for passengers, and improved safety through reduced aircrew fatigue and improved sensor accuracy. A survey by *Friedmann* [7] highlighted that some rotorcraft contracts have been awarded based on vibration criteria and that the requirements for vibration in the pilot's seat are ever reducing.

As our understanding of rotary-winged aircraft has improved and the tools used to design them became more accurate, the opportunities for further improvements have become increasingly limited. To achieve the desired performance improvements, increasingly unusual methods, such as alternative aircraft configurations, morphing geometries and variable operating conditions, are now being considered.

1.2 Variable rotor speed

Conventional rotorcraft operate with a single rotor speed, varying the cyclic and collective pitch of a blade to achieve trim. Conversely, remote-control model rotorcraft and drones tend to employ a fixed-pitch rotor and vary rotor speed to control thrust. One of the techniques being considered to achieve the desired performance improvements is to employ a variable rotor speed [8], whereby collective pitch and rotor speed are varied to achieve trim. This may be used in a conventionally configured helicopter or in an alternatively configured rotorcraft to supplement the improvements of the chosen configuration. The use of two operational parameters, blade pitch and rotor speed, allows the simultaneous achievement of trim and improved performance.

1.2.1 Operational benefits of a variable rotor speed

Variable speed rotors are able to influence many of the performance metrics which are to be improved. The means with which these improvements are achieved is discussed below.

The most sought after benefit is a reduction in power requirements of the rotor. These reductions in power can be realised as a combination of increased range, endurance, service ceiling, speed, payload or manoeuvrability and a reduction in greenhouse gas emissions and economical costs. For an aircraft operating with a fixed forward speed and thrust, a slowed rotor speed can yield a reduction in the power required. The total power required by a helicopter is comprised mainly of main and tail rotor power along with fuselage parasite power [9]. The main rotor power can be split into induced power and profile power with profile power being the larger of the two. A slower rotor speed reduces dynamic pressure, lowering the profile drag, and therefore power, of the main rotor. As thrust remains unchanged, induced drag, and therefore induced power, also remain unchanged. To maintain thrust at reduced rotor speeds requires an increase in collective pitch. The limit of the reduction in rotor speed is governed by retreating blade stall which

occurs at high pitch angles and increases the drag coefficient resulting in diminished power reductions. This phenomenon has been extensively researched to improve our understanding of it and assess its performance in a variety of scenarios.

Aside from the reduction in power requirements, one of the more highly desired performance improvements is a reduction in noise. Reducing the tip speed of a rotor is one of the most effective ways to lessen the noise emitted by a rotor [10, 11]. Therefore, a variable speed rotor could be used to reduce the rotor speed, and thereby noise, when taxiing, flying over densely populated areas or in other areas with particularly stringent noise regulations are enforced.

A change in rotor speed can also improve rotor control limits. An increase in rotor speed increases the proportion of the local air velocity on the blade that is due to blade rotation, as opposed to the forward speed of the aircraft. However, this variation is limited by drag divergence. This reduces the asymmetry in the flow velocity, and therefore aerodynamic forces, across the disc resulting in a reduced influence of forward speed on roll control limits and trim [12, 13]. If operating near the torque limit of the rotor, the power margin can be increased by increasing the rotor speed [10]. Yaw manoeuvrability can also be improved by altering rotor speed if the tail rotor is approaching its maximum pitch [10].

A selection of studies on conventional rotorcraft are summarised below:

Gustafson and Gessow [14] assessed the effect of tip speed on hover performance and maximum forward speed over 70 years ago. They advised that tip speeds should be lowered (below 500 ft/s) for hover and increased in forward flight to avoid retreating blade stall. They recommended that a two-speed transmission be used to achieve this.

Allongue et al [10] summarised, with the support of empirical evidence, some of the effects of rotor speed: A 10 % reduction in rotor speed can lead to an increase in mission gross mass of 3 % and reduces noise by 3dB during take-off and low altitude fly-overs and improves hover efficiency. Power and fuel flow can be reduced if the rotor speed is set such that trim is achieved at the maximal lift-to-drag ratio. An expansion of the flight envelope, in terms of speed and load factor, can be sought if the rotor speed is increased as the stall boundary is approached [10, 15].

Karem used the effect of variable rotor speeds in his patented Optimum Speed Rotor [12], which has since been leased to Boeing. Some of the benefits of variable rotor speed are outlined qualitatively and a quantitative example claims a potential power reduction of up to 70 % as well as increases in speed, endurance and range.

Steiner [16] investigated the performance benefits and trim requirements of a variable speed helicopter rotor. The analyses were performed for a range of forward speeds, weights and altitudes using a trim simulation program with a momentum theory based inflow model and Prandtl tip loss correction. To maintain weight and power estimates, a variable speed transmission was not used, restricting the rotor speed reduction to 15 % (to be controlled by engine speed). Variable rotor speed was shown to be a good way to reduce power and expand flight envelope with

power reductions of up to 17 % observed in sea level cruise. At low forward speeds, increasing rotor speed resulted in a shaft torque reduction with minimal power penalty. The limit of rotor speed reduction is governed by retreating blade stall which itself is significantly affected by the required thrust. Similarly, power was shown to be reduced during high-speed forward flight in high and heavy conditions with a higher rotor speed to avoid stall.

Datta et al [13] investigated the fundamentals of slowed rotors at high advance ratios experimentally. A full-scale UH-60A rotor was tested at the NASA Ames Research Centre at 65 % and 40 % of its nominal rotor speed. The performance measurements were consistent with previous test data. They also observed that at higher advance ratios, dynamic loads are comparable or significantly higher than the nominal rotor due to asymmetry in local airspeeds. The asymmetry of the aerodynamic loads also have a significant effect on the ability of the aircraft to achieve trim.

Han et al [17] used a computationally inexpensive rigid blade model with a Pitt-Peters inflow model to demonstrate the power reduction and identify that the reduction occurs primarily through reducing the rotor's profile power.

A selection of studies on variable rotor speeds in non-conventional rotorcraft configurations or in conjunction with other performance improvement techniques are summarised below:

Johnson et al [18] investigated a variety of different heavy-lift rotorcraft configurations as Runway Independent Aircraft. Delays for airline passengers are ever more frequent due to increasing runway congestion. The utilisation of vertical take-off aircraft for short-haul journeys may be considered as a method to reduce runway congestion with minimal additional infrastructure required [19]. The configurations considered were: tiltrotor, compound tandem and compound coaxial. All three configurations utilised a variable speed rotor with a cruise condition operating at 54 %, 32 % and 39 % of nominal, respectively. Noise limitations can be prominent in heavy-lift rotorcraft [20], therefore the ability to reduce rotor speed to control noise would be additionally beneficial for the heavy-lift rotorcraft. The tiltrotor exhibited the best cruise efficiency and therefore the lowest weight and cost and was therefore identified as the configuration most likely to meet the desired goals.

Russell and Johnson [21] investigated the use of a different configuration; a large compound helicopter with a single main rotor, but still with a variable rotor speed as another Runway Independent Aircraft. Conventional rotorcraft and tilt-rotors are suited to journeys of 100nm and 1000nm, respectively [18]. The suitability of a compound rotorcraft was considered for a journey of 500nm and compared to a conventional configuration and a tilt-rotor. It was concluded that the conceptual aircraft examined would not be competitive to the other configurations but possibilities for improving performance were identified.

Floros and Johnson [22] stated that the expanded flight envelope of rotorcraft is of increasing interest for non-civilian purposes in attack, scout and rescue rotorcraft to improve their mission effectiveness. The performance of the slowed-rotor compound helicopter configuration was anal-

ysed as a means to achieve the desired flight envelope expansion. The comprehensive rotor code, CAMRAD II [23], was used for the analysis after first validating it against measured data for the desired flight conditions. They concluded that: profile drag is the main source of the power requirements of both the rotor and the wing; at high forward speeds, the rotor speed must be reduced to avoid compressibility and drag divergence effects on the advancing blade; and that a rotor, regardless of the presence of a wing, in an autorotative state at a high forward speed requires less power at lower rotor speeds.

Kang et al [24] investigated rotor speed reduction and a selection of rotor morphing concepts to improve cruise performance and increase maximum forward speed and payload capabilities. It was shown that a variable rotor speed in conjunction with a variable chord showed considerable improvement in cruise performance. These benefits could be increased if the variable chord component was able to operate at a 1/rev frequency.

Bowen-Davies [25] investigated the performance and loads of variable tip speed rotorcraft at high advance ratios by considering both variable rotor speed and variable radius concepts. For a UH-60A rotor, trimmed for 80 000 N of thrust, a mean reduction of 100 hp was achieved across the flight envelope by reducing the rotor speed by between 10 % to 20 %. It was also showed that induced power is not influenced by reducing the rotor speed until stall is reached, at which point the induced power increases. All power savings are due to a reduction in dynamic pressure reducing profile drag and a reduction in compressibility induced drag. For large rotor speed reduction, large pitch angles increase drag coefficients and preclude further reductions in profile power. In general, it was concluded that at hover and low forward speeds, the low and high rotor speeds were limited by thrust or autorotative capability and noise emissions respectively; while at cruise and high rotor speeds, the low and high rotor speeds were limited by compressibility and retreating blade stall, respectively. Concerning trim, it was shown that both the collective and cyclic pitches increased to maintain trim but did not exceed the capabilities of the aircraft.

Han et al [9] considered the performance benefits available from variable rotor speed and twist. It was shown that in hover and at low forward speeds, rotor power is dominated by induced drag which cannot be reduced resulting in limited power reductions being available due to variable rotor speeds. In high-speed forward flight, a reduction in rotor speed requires an increase in blade pitch which may exacerbate stall in the retreating blade limiting the ability to reduce required power. The available power reduction was shown to initially increase with rotor speed and then decrease. At a forward speed of 250 km/h, when considering variable rotor speed in isolation a reduction in rotor power of 17.8 % was obtained. Comparatively, when considering variable blade twist in isolation a reduction of 10.4 % was obtained. When the two techniques were combined, a reduction of 20.9 % was achieved.

Ward et al [26] investigated the combination of rotor speed reduction with self-twisting blades which yielded many benefits. It was shown that at 85 % of the nominal rotor speed, a 20 % increase in lift-to-drag ratio was possible and that as rotor speed reduces, so does twist which

reduces tensile strain and improves rotor efficiency.

It can be concluded from these previous research efforts that the performance implications of variable speed rotors have been extensively researched, using a combination of computational and experimental investigations. The effect of lowering rotor speed is primarily a reduction in main rotor power requirements but additional effects, such as reduced noise emissions because of the lower tip speed, are also beneficial. The induced power of the rotor (for a constant thrust) is unaffected by a change in rotor speed; the reductions occur primarily through a reduction in profile power. The limiting factor of reducing rotor speed, particularly at high forward speeds, is retreating blade stall. Either due to an increase in blade pitch to maintain lift at lower rotor speeds or an increase in forward flight speed, aerodynamic stall of the blade on the retreating side may be induced which will detrimentally affect power and trim requirements of the rotor. The capability to reduce power requirements of the main rotor allows the flight envelope of an aircraft to be expanded. Improvements such as increased range, lower fuel costs and increased payload capability make this concept very appealing to industry. The concept has been considered beneficial to military aircraft and may be utilised in the development of large civilian aircraft to alleviate runway congestion at airports.

1.2.2 Problems with a variable rotor speed

Despite all the benefits associated with the variable rotor speed concept, there are two main problems that prohibit its widespread use; namely, the means with which the rotor speed changes are achieved and the risk of blade resonance [27, 28, 25]. The difficulties in changing rotor speed are not the focus of this research but shall be discussed briefly before the blade resonance problem is discussed.

1.2.2.1 Engine and transmission

The two main ways with which the rotor speed can be reduced, which can be used either in isolation or in conjunction with each other, are to reduce the engine shaft speed or to vary the reduction ratio of the transmission. Each of these methods has their drawbacks which must be understood to ensure that they do not impede the sought after benefits of variable speed rotors.

Modern turboshaft engines used in rotorcraft are designed to operate very efficiently across a narrow range of shaft speeds [15]. It is possible to reduce the power output of a gas turbine with only a small detrimental change in specific fuel consumption, if shaft speed is maintained, but maintaining power while reducing rotor speed significantly increases specific fuel consumption [29]. For these reasons, shafts speeds are usually constrained to not vary by more than 15 % [30] which may result in as little as a 5 % penalty in specific fuel consumption [26].

Miste and Benini [31] used an off-design steady-state model of a generic turboshaft engine and a simple rotor analysis coupled to investigate the effects of engine shaft speed and rotor

speed on rotor power and fuel consumption. They concluded that the objectives of reduced rotor power and reduced fuel consumption generally aligned well with each other, i.e. a change in engine shaft speed would have a similar impact on both objectives, but that the exact optimum of each objective was not identical. This shows that whilst, in general, reducing rotor power will reduce fuel consumption, this is not always the case. Therefore, when designing a variable speed rotor for minimum fuel consumption, the performance of the engine must be included. An optimisation routine was used to demonstrate that, for the test case studied, a 16 % reduction in fuel flow could be obtained.

In NASA's tiltrotor concept study, *D'Angelo* [32] concluded that an efficient propulsion system with a high range of output speeds was integral to improve tiltrotor efficiency. Due to off-design engine efficiencies, rotor speed reduction was limited to 18 %, much lower than the stated optimum of 50 %, costing 15 %-22 % in efficiency. To overcome this, *D'Angelo* theorised and modelled a turbine designed for variable speeds and achieved a 14 % increase in overall efficiency. The performance of this model was confirmed using 2D and 3D CFD [33, 34].

Due to the off-design efficiency losses of turbines when varying their shaft speed, the use of the transmission to vary rotor speed is of great interest. Transmissions with multiple speeds or a variable speed are relatively efficient at changing rotor speed but do incur a weight and complexity penalty [25]. One challenge that is faced by transmissions with multiple speeds or a variable speed is that power must be smoothly and continuously available [25]. Therefore, the design and comparison of fixed-ratio, discrete multi-ratio and continuously variable transmissions are a popular topic of research. A few of these studies are summarised below:

Palcic et al [35] developed and patented a transmission for the main rotor of a rotary-winged aircraft that permitted the use of two-speeds without altering its output speed or disengaging the engine. The gearbox consisted of a freewheel and a clutch (ideally multi-plate) for each engine. When the clutch is engaged, the gearbox operates in a 'high rotor speed' mode but when the clutch is disengaged, the power is transferred through the freewheel and a different gear path powers the rotor in a 'low rotor speed' mode. Additionally, the system could be configured to operate with a tail rotor that operated either at a fixed rotor speed or that changed with the speed or the main rotor.

Stevens et al [36] evaluated two-speed and continuously variable speed transmissions for use in NASA's Large Civil Tilt Rotor; a two-input differential planetary gear was identified as a viable solution. A dynamic model of this transmission was developed by *Lewicki et al* [37] and then *DeSmidt et al* [38] which correlated well with experiment; however the mass of the system was not discussed.

A pericyclic variable speed transmission, investigated by *Saribay* [39], was shown to be a viable replacement for traditional transmissions with comparable weight and volume.

Miste and Benini [15] compared fixed-ratio and continuously variable transmissions. Some rotorcraft, such as those designed for surveillance, sightseeing, and pilot training etc, will spend

considerable amounts of time in multiple areas of their flight envelope, such as hover, loiter and cruise. Therefore, there will be many optimal rotor speeds, each of which will have their own corresponding optimum engine shaft speed, which is not realisable using a fixed-ratio gearbox. Using a gas turbine performance model coupled with a trim simulator for steady-state forward flight, it was shown that across a wide range of forward speeds, the continuously variable transmission did not yield a significant fuel usage benefit over the fixed-ratio transmission. However, in hover and cruise conditions, two conditions which will dominate a rotorcraft's mission profile, there are significant differences. It was shown that engine performance is inhibited by the fixed-ratio transmission, ensuring that a continuously variable transmission is required to realise the fuel reductions.

It can be concluded from these research efforts that whilst discrete multi-speed gearboxes with a few rotor speeds are viable replacements for traditional transmission systems, a wide range of rotor speeds will likely be required if the benefits of variable rotor speeds are to be fully utilised. Therefore, efforts should continue to be made to develop gearboxes that are either continuously variable or offer a wide range of discrete speeds. Additionally, it should be noted that as the aviation industry moves towards the increasing electrification of aircraft, the use of electric motors, instead of gas turbines, may reduce the off-design efficiency losses.

1.2.2.2 Dynamic excitation

The other problem associated with variable speed rotors is that operating over a range of rotor speeds results in a high likelihood of resonance being encountered [25]. In rotor blades, resonance occurs when the blade is subject to an oscillatory excitation load that occurs at a frequency that is similar to one of the natural frequencies of the blade. In this case, an oscillatory motion of the blade at the frequency of the excitation shall begin and the amplitude of this motion shall continue to increase until a limit value is reached.

The desire to maintain a low weight leads to flexible blades with a high density of natural frequencies in the range of interest. The frequencies of most interest are those with transversal deformations occurring in- or out-of- the plane of rotation (herein referred to as in-plane and out-of-plane, respectively) as well as torsional deformations about the longitudinal axis of the blade. Frequencies associated with deformations in other directions, such as transversal axial deformation, are generally sufficiently high that they can be considered insignificant. When the rotor is not rotating, the natural frequencies are dependent on the geometry of the blade (cross-sectional shape and length etc) and its material properties. However, when the blade is rotating, effects such as Coriolis forces and centrifugal loads due to the blade's rotation about the rotor shaft significantly alter the static and dynamic behaviour of the blade.

These centrifugal loads act parallel to the plane of rotation and radially outward from the centre of rotation and therefore have a differing effect on each of the different motions considered. These effects shall be described qualitatively in the context of a point mass at the end of a light,

rigid bar with a hinge offset from the centre of rotation and aerodynamic and centrifugal forces in static equilibrium.

For the out-of-plane transversal deflections of a blade, this is shown in Fig. 1.1a. If the blade is perturbed from its equilibrium with an increased inclination to the rotation plane, the centrifugal force will remain parallel to the plane of rotation. This increases the angle between the centrifugal force and the blade which will increase the component of the centrifugal force that is perpendicular to the blade and therefore acts as a moment about the hinge to restore the original equilibrium. For a perturbation in the opposite direction, a reduction in this moment due to the centrifugal force is observed, which also acts to restore the original equilibrium. This effect is similarly observed for the in-plane transversal deflections of a blade, as shown in Fig. 1.1b. However, in this orientation, the direction of the centrifugal force follows the perturbation and the angle of the centrifugal force with the blade is due to the offset of the hinge from the centre of rotation. Due to this, the effect of this restoring force is much weaker for the in-plane motion.

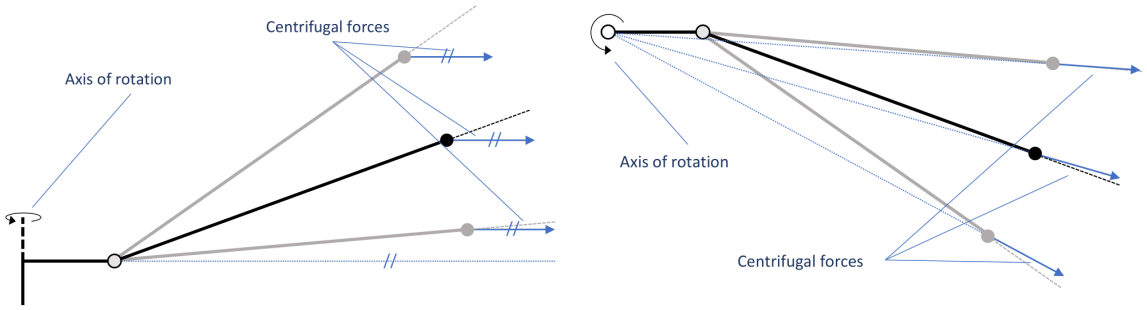

(a) Out-of-plane (side view)

(b) In-plane (top view)

Figure 1.1: Diagram of mechanism for centrifugal stiffening in the transversal motion of a blade.

This effect can also be observed in the torsion of a blade if a chordwise distribution of mass is considered. Mass at the front of the profile observes a component of the centrifugal force acting in the forward direction, while mass at the rear observes a force in the opposite direction. This effect is visualised in Figs. 1.2a and 1.2b using two point masses, one at each end of the chord. When viewed from an end-on perspective, it can be seen that a torsional perturbation would exhibit an increased torsional restoring moment, similar to that observed in the out-of-plane transversal deformation. However, the moment arm for these forces is the same order as the chord, whereas the moment arm for the transversal motion is the same order as the radius of the blade. This smaller moment arm results in the effect of these restoring moments for torsional deformations being much smaller than its effect on the in-plane and out-of-plane transversal motions.

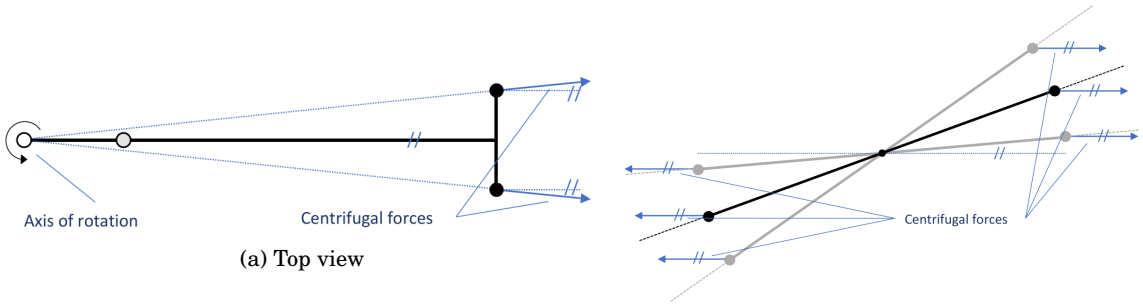

(a) Top view

(b) End view

Figure 1.2: Diagram of mechanism for centrifugal stiffening in the torsional motion of a blade.

The restoring moments in the in-plane, out-of-plane and torsional directions due to centrifugal loads are akin to an increase in stiffness, due to their dependence on displacement. As these effects are similar to an increase in stiffness, the phenomenon is therefore known as *centrifugal stiffening* [40].

In addition to centrifugal stiffening, there are a few additional effects observed in rotor blades due to centrifugal loads that can influence their statically deformed shape as well as their dynamic behaviour; namely the *trapeze effect* and *veering*.

The trapeze effect, named after its analogous comparison to a twisted trapeze, untwists twisted beams under axial tension [41, 42] due to the component of this force that acts perpendicular to the elastic axis. This effect may create a restoring moment in perturbed twisted blades, which would compound the previously described effect of centrifugal stiffening.

Additionally, there is the effect of veering. This phenomenon is not directly caused by the centrifugal load but is most often observed in rotorcraft as the natural frequencies of the rotor change with rotor speed due to the aforementioned centrifugal stiffening. For a beam with no coupling between its motions, natural frequencies of different motions can intersect as rotational speed is increased. However, *Yoo et al* [43] and *du Bois et al* [44] suggest that if there is coupling between these modes, they may diverge as they approach the point at which they would be expected to cross; this effect is known as *veering*. Both modes then follow the trajectory expected of the other, as if they had crossed, with the associated mode shapes and properties of that mode. *Balmes* [45] represented the mode shapes during the interaction as a fractional combination of each of the two original mode shapes. The contribution of each original mode shape varies sinusoidally throughout the interaction.

As well as a rotor blade having many natural frequencies, they are also subjected to excitation at a range of frequencies. The excitation originates from the main rotor primarily which occur due to a multitude of effects such as, but not limited to:

- As the rotor blade passes over the tail (and other parts of the fuselage) there is a change

in the local air pressure which changes the aerodynamic loads on the blade.

- During forward flight, the blade on the advancing side experiences an increase in local air velocity and the blade on the retreating side experiences a decrease in local air velocity. These differences in local air velocity cause an increase and decrease in lift on the advancing and retreating side of the rotor, respectively. For rotorcraft with very high forward flight speeds, this effect can be more severe as shocks and dynamic stall may be experienced on the advancing and retreating sides, respectively. Dynamic stall is one of the dominant sources of high vibration levels for high advance ratios [46].

- Due to the difference in the lift on the advancing and retreating side of the rotor it is necessary to alter the distribution of lift around the rotor disc to avoid a rolling moment being produced. The lift is altered by using cyclic control to vary the pitch of each blade in the rotor as they rotate about the shaft. This changes the lift of the blades and can be tuned to achieve rolling trim but it will also change other aerodynamic loads, such as drag.

- When in forward flight, the induced airflow velocity into the rotor varies fore and aft as well as port and starboard which significantly affects the variation in aerodynamic loads observed by the blades at each azimuth angle.

- As each blade rotates, it passes through the wake of the preceding blade which alters the aerodynamic loading. The effect is known as the Blade Vortex Interaction (BVI) and is most prominent at low speeds where the wake of the blades is not washed downstream sufficiently quickly.

Some of these excitations, such as those due to the variation in local air velocity and cyclic trim, occur sinusoidally. However, some of the excitations, such as those due to tail shadow and induced velocity, are periodic but not sinusoidal. These periodic excitations can be broken down into a set of sinusoidal excitation acting across a discrete range of frequencies using a Fourier series. Additionally, the combination of sinusoidal excitations at the 1/rev frequency, such as those due to forward speed and cyclic trim, results in excitation at integer multiples of the rotor speed higher than 1/rev. Therefore, the rotor will experience excitation at integer multiples of the rotor speed frequency, commonly referred to as the *rotor harmonics*. However, it should be noted that due to the combination of these frequencies, the lowest frequency excitation will have the most energy and the amount of energy shall decrease with increasing frequency excitations as demonstrated in flight tests of a CH-53A [47]. An example fan diagram demonstrating how the natural frequencies and harmonics of a typical rotor blade vary with rotor speed and the subsequent resonances (shown for the upper half of rotor speeds only) is shown in Fig. 1.3.

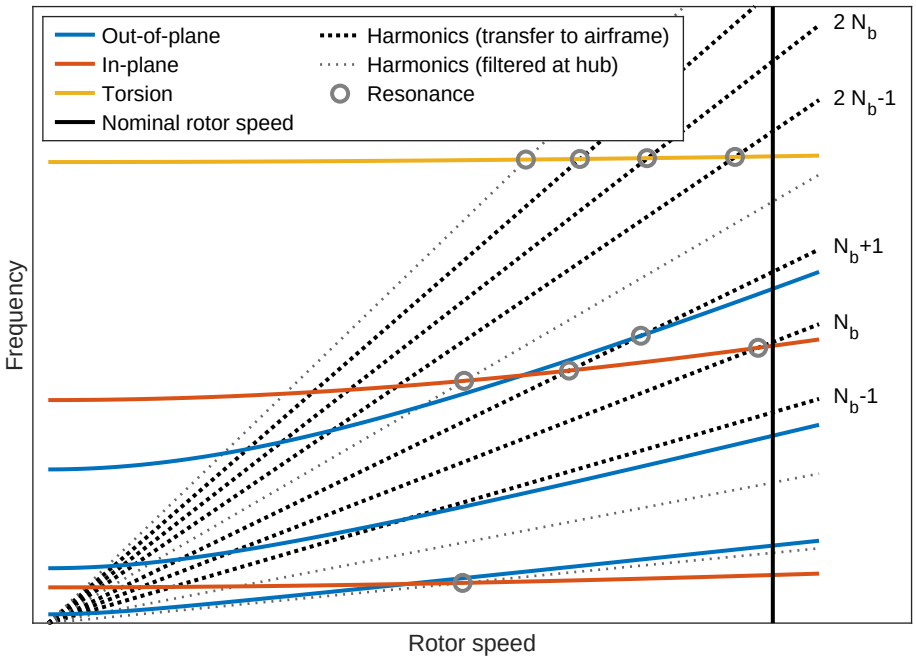

Figure 1.3: Sketch of typical fan diagram for a four-bladed rotor

If a rotor is designed such that any of its natural frequencies are similar to any of its excitation frequencies, as observed in Fig. 1.3, a phenomenon known as *resonance* will occur. In this situation, the excitation will drive the mode of the corresponding natural frequency to increase in amplitude which will, in turn, increase the vibratory loads observed at the root of the blade and may limit the flight envelope of the aircraft or damage the structure of the blade [48, 49]. This phenomenon has been observed experimentally by *Berry and Chopra* [50] who researched the vibration of variable speed rotors in a scaled wind tunnel test and observed an increase in root bending moments and high harmonic pitch link loads with a reduction in rotor speed. Furthermore, *Bowen-Davies* [25] investigated the loads involved with variable rotor speeds at high advance ratios and concluded that these loads are uniformly and significantly increased at high airspeeds when the rotor speed is reduced due to excitation of the blade's natural frequencies. Due to the summation of the loads at the hub, many of the vibrations cancel each other out. The only vibrations that transfer from the blade, through the hub, to the airframe are those at a frequency of $nN_b, nN_b \pm 1$ [51], as shown in Fig. 1.3. Once transferred to the airframe these vibrations may: be unpleasant for passengers; increase crew fatigue; degrade the performance and reliability of avionics used for primary control, navigation, weapons and surveillance.

To avoid this, rotorcraft are typically designed to operate with sufficient separation between the natural and excitation frequencies. Conventionally, this is achieved by designing the mass and stiffness distributions of the blades at a single, fixed, rotor speed. Due to the abundance of natural and excitation frequencies and their dependency on rotor speed it is not possible to vary the rotor speed otherwise the natural and excitation frequencies would change and resonance

would likely be encountered. An example rotor speed for which there is sufficient separation between all of the blade modes and all of the rotor harmonics is shown in Fig. 1.3.

It should be noted that not all resonances are of equal importance. Due to the higher energy levels in the lower rotor harmonics [8], resonances involving these harmonics (as seen in the interaction between the first in-plane mode and the first harmonic in Fig. 1.3) may be more severe. Whilst all resonances will affect the rotor blade, due to the filtering effect at the hub, only vibrations at a frequency of $nN_b, nN_b \pm 1$ will transfer to the hub and be experienced by the onboard equipment and crew. Therefore only resonances at these frequencies (as seen in the interaction between the second out-of-plane and in-plane modes with the third and fifth harmonic, respectively, in Fig. 1.3) are of importance when considering vibrations in the fuselage.

1.2.3 Experimental and demonstrator aircraft

Despite the considerable complications associated with a variable rotor speed, as described in Section 1.2.2, the benefits detailed in Section 1.2.1 are sufficiently appealing to industry for them to make significant amounts of resources available. Due to this, multiple experimental and demonstrator aircraft have been developed and tested; some of which are detailed herein.

A Eurocopter AS365 aircraft, without significant alterations, was used as a demonstrator aircraft to achieve a $-10.5\,\%$ to $4\,\%$ rotor speed alteration [10]. The demonstrator was so successful that Eurocopter used the results of the study to improve the EC 155 [52] and intended to incorporate the technology into future aircraft.

Variable speed rotors have also been successfully employed on unmanned military rotorcraft such as the 11 m wide Boeing A160T Hummingbird [53]. This aircraft, which can reduce its rotor speed by up to $40\,\%$ [28] using a small number of well-defined rotor speeds [25, 15], demonstrated great performance improvement [54] including an endurance flight record [55] in 2008. This aircraft was powered by a piston engine as this allowed a variable speed transmission to be used with less difficulty than would be observed using a turbine engine. In an attempt to avoid the dynamics issues previously discussed, composite rotor blades were designed with very high stiffness-to-weight ratios to avoid resonances at the operational rotor speeds, as specified in [12]. However, excessive vibrations led to a crash which caused significant scheduling delays that ultimately resulted in the programme being cancelled. Variable speed rotors have also been utilised for non-traditional rotorcraft configurations. Sikorsky created an experimental coaxial thrust compounded rotorcraft, the X2 Technology Demonstrator, in 2008 to demonstrate solutions to problems uncovered during flight testing of the XH-59A. The aircraft was capable of reducing its rotor speed to $80\,\%$ of nominal [56] and has had its dynamics [57] and high-speed flight capabilities [58] studied. It should be noted that active vibration control was used [59, 57] which may have been required due to resonance caused by the variable rotor speed. Eurocopter also developed an experimental compound helicopter, the X3, which first flew in 2010. This aircraft also utilised a variable speed rotor and was able to usurp the unofficial speed record set by

the Sikorsky X2 [60].

Two-speed rotors are often employed on tiltrotors (aka convertiplanes) such as the XV-15 [61], V22 Osprey [28] and the Bell Eagle Eye [15] for the helicopter and plane configuration. The V22 Osprey employs an 18 % reduction in rotor speed for forward flight [62].

The number of existing experimental and demonstrator aircraft exemplifies the amount of resources that industry is willing to expend on this concept. Across a range of these aircraft, the performance benefits discussed in Section 1.2.1, were obtained which will serve only to increase the motivation of industry to pursue the concept of variable speed rotor. One common negative observed across some of these aircraft was that of vibration. For one aircraft this was the underlying problem which eventually resulted in the cancellation of the program and serves to motivate further research into the reduction of vibration levels in variable speed rotorcraft.

1.3 Existing vibration suppression techniques

Despite rotorcraft being designed to operate at a single rotor speed with sufficient separation between natural and excitation frequencies to avoid catastrophic resonance, high levels of vibration have been an undesirable feature of helicopters since their inception [63]. The industry has made significant efforts to lower helicopter vibration levels to those observed in other forms of air travel [63, 48], with particular focus being paid to the vibrations experienced at the pilot's seat [64]. However, this *Jet Smooth Ride*, with vibration levels below 0.05 g, is still not achieved for production type helicopters [8]. Despite the improvements made in rotorcraft vibration levels, they remain a prominent problem due to increasing forward speeds, which increase vibration levels, and a reduction in the tolerance of passengers, crew and equipment to vibrations [63, 48].

Historically, vibration problems in rotorcraft have been treated with a variety of passive and active means [65, 66, 67]. These methods are still being actively pursued by industry [8]; however, recently, adaptive-passive systems have come to the fore as an alternative to these strategies [49].

These three types of vibration suppression system shall be explained herein, along with specific examples for each type of system. Subsequently, a set of characteristics that would be required of a system to be deployed in a variable speed rotor shall be defined. The set of existing vibration suppression techniques that will have been described will then be discussed in the context of their ability to meet the required characteristics.

1.3.1 Passive methods

Passive methods of vibration suppression are those that involve no modification or actuation during their use. In general, these systems are not very adaptable, due to their lack of modification, and therefore are not very effective across a broad range of operating conditions. However, their lack of actuation ensures that the system requires no additional power to be provided.

These methods have been extensively researched and deployed where applicable but it is believed that some production aircraft are already very close to the limit of what is realistically achievable with passive methods of vibration control [63]. The two most common passive methods for vibration attenuation, which may be used in conjunction with each other, are to design the rotor to avoid excessive resonance being encountered and to use vibration absorbers to absorb the vibrations once they have been created. These two methods shall be discussed in more detail in the following sections.

1.3.1.1 Rotor design

Rotor design for vibration reduction is a technique adopted during the design of most rotorcraft; however, the level to which it is exploited varies. This technique involves designing the rotor such that the natural frequencies of the rotor are sufficiently separated from the rotor harmonics to avoid resonance. Examples are the parameters typically used include: taper, twist, tip shape, mass and stiffness distributions, hub configuration and composite layup. This technique has very few negatives as there is no requirement for additional actuators or devices but it does limit the rotor to a very small set of operating conditions if not used in conjunction with other techniques. A summary of a few documented cases of this technique is included below:

Blackwell suggested that blade design is an underutilised method for reducing vibrations in rotorcraft [68]. Due to the expense of designing and constructing new rotor configurations, more so than retrofitting a secondary device to an existing rotor, very little experimental or flight test data is available. Therefore, using the Normal Modes Blade Aeroelastic Response Analysis (Y2OO Program), a set of studies were performed to analyse the capability of different blade properties, such as mass and stiffness distributions, to alter the mode shapes of a blade and increase damping ratios and the separation between natural and excitation frequencies. A reduction of 10 %-20 % in root shear forces at 3/rev and 4/rev were predicted using a mid-span located lumped mass. Assessments of the effectiveness of varying stiffness distributions yielded much less substantial results. This is likely due to rotor blade's stiffness being largely influenced by centrifugal forces resulting in a limited impact of varying their elastic stiffness.

Pritchard and Adelman investigated the use of tuning masses for vibration reduction in rotor blades [69]. Multiple optimisation strategies were devised and compared to reduce shear forces at the blade root with the best performing strategy demonstrating the ability to reduce the shear load due to the response of multiple blade modes to multiple rotor harmonics. This method was able to reduce the peak shear force in one revolution by over 99 %, subject to an increase in blade mass of 12.7 %.

During experimental flight tests conducted by Eurocopter [8], the inclusion of an additional blade (increasing the rotor from four-bladed to five-bladed) yielded a 70 % reduction in vibratory hub loads. This was because, for a four-bladed rotor, only the 3/rev, 4/rev and 5/rev blade loads contribute to hub loads, whereas for the five-bladed rotor this is due to the 4/rev, 5/rev and

6/rev. There is much less energy in the 6/rev excitation than the 3/rev which was the cause of the reduction in vibratory loads. The limiting factor for including extra blades is usually cost, the mechanical complexity of housing additional rotor blades in the hub and the manufacturability of increasingly high aspect ratio blades associated with increasing blade number while maintaining solidity.

The use of frequency placement and structural and aeroelastic coupling was exploited extensively during the development of the BERP IV demonstrator blade [6]. The aim of the new blade design was to maintain the forward flight capabilities of BERP III and to improve the payload/range performance and combat survivability. An optimisation procedure, based around the in-house aeroelastic code R150, was used to develop the design of the new BERP IV blade. The objective function used for this optimisation was the vibration in the fuselage. This required characterising the fuselage, in the form of a transfer function, to assess the impact of different components of hub vibration on the fuselage vibration. It was identified that excitation of the second and third flap mode were primary causes of vibration in a four-bladed rotor, therefore the placement of these modes was of particular interest. Structural coupling was the main mechanism to reduce vibration of the second flap mode at 3/rev, therefore this mode remained relatively unchanged. However, the third flap mode was increased from 5.65/rev to 5.8/rev. This may seem counterintuitive as this moves the mode closer to its nearest excitation harmonic, 6/rev, but it was in fact correct. This placement did increase the 6/rev flapping moment but it also reduced the 5/rev vertical shear load which was more impactful on the fuselage vibration, resulting in a net reduction of fuselage vibration. The manner in which these changes were implemented is also noteworthy as a universal increase in flapwise stiffness would increase both modes. The change in the third flap mode was achieved by increasing stiffness on the outboard 60 % of the blade. The second flap mode was maintained by avoiding placing the additional stiffness in areas of peak curvature of this mode and by adding masses at its antinode. The results of this optimisation yielded part of the desired improvement but it did not capture the expected change in lagwise vibrations. It was anticipated that the 4/rev lagwise shear could have been reduced by increasing the second lag mode from the existing BERP III frequency of 5.0/rev to a value above 6/rev. However, the use of a gradient-based optimiser meant that this design space was never explored. Therefore, the optimisation was restarted with an artificial increase in lagwise bending stiffness, giving a starting point with the L2 frequency above 6/rev. The resulting optimisation positioned the L2 mode at around 7/rev, which drastically reduced the 4/rev in-plane shear. This highlights the high level of multi-modality of the design space and implies that the use of a global optimiser may be required to precede local gradient-based optimisation if the best performance is to be realised. The results of these optimisations lead to a blade design with unconventional frequency placements. However, the design was vindicated during the subsequent testing which exhibited the expected reduction in vibration levels.

Rotor design was also utilised by *Karem* [12] in his patented Optimum Speed Rotor. Unlike

the rotor design in BERP IV, which carefully placed frequencies between excitation frequencies and utilised coupling to reduce vibration, these blades were designed to be substantially stiffer and lighter than conventional blades. The purpose of this was to drastically increase the frequency of the blade's mode such that they would only interact with very high harmonics of the rotor which have far less energy available to excite the blade. The blades are designed to be 85x stiffer than conventional articulated rotor blades at about a 10 % radius. This requires a 3.5x increase in maximum blade thickness and a large root chord. However, no discussion of the effectiveness of this technique or the accompanying impact upon performance or manufacturability was provided.

1.3.1.2 Vibration absorbers

Vibration absorbers and dampers are the most common type of passive vibration suppression device deployed. Despite their many names they almost always consist of a secondary mass-spring-damper system attached to the primary structure. The frequency of the absorber is tuned to correlate with the frequency of the vibration in the primary structure. The absorber will then absorb the vibration from the main structure at this specific frequency. These systems are usually much simpler, lighter (typically less than 1 % of vehicle weight [70]) than active techniques and require no power. However, their effective bandwidth is dictated by the mass used; a small mass will keep the system light but result in a narrow effective bandwidth and poor off-design performance. However, in some cases, the use of existing masses within the aircraft, such as a battery [71], may be used to incorporate a large mass without increasing the weight of an aircraft. These systems have been extensively reviewed [72, 73] and patented [74]. A summary of a few additional research efforts is made below:

Han and Smith [75] investigated the use of a chordwise mass-spring-damper absorber, embedded within the blade, to attenuate lagwise root vibration. Aeroelastic simulations of forward flight were provided using a moderate deflection finite element model with the absorber modelled as a one degree of freedom system. From these analyses, it was shown that a chordwise absorber, embedded within the blade, can decrease the 1/rev and 2/rev (i.e. once and twice per revolution) lagwise root bending moments by about 50 % and 90 %, respectively. It was also shown that the tip of the blade is the ideal location for the absorber to maximise vibration reduction.

Hebert and Lesieutre [76] investigated the use of using multiple vibration absorbers that were highly distributed, both spatially along the blade span and in frequency, for lag damping. It was demonstrated that substantial damping over a wide range of frequencies may be achieved through the careful selection of design parameters such as: the number of discrete tuning frequencies, the mass per unit length of the absorber system and the frequency range of the absorbers. Simulation results showed that using no more than 3 % of the total blade mass, damping comparable to or better than that provided by existing methods could be provided. To

reduce the need to increase the mass of the blade, it was suggested that leading-edge weights that are already incorporated into the blade could be used for the damper. These weights exceed the mass requirements of the system resulting in potentially very little additional mass being required for the system.

Additionally, there are a few examples of hybrid isolator-absorbers. These systems use a large moment arm to increase the inertial effect of mass for a traditional style absorber. These systems can be attached between the gearbox and fuselage and used to absorb and isolate vibration that would otherwise transmit to the fuselage. Eurocopter has developed and certified 2 forms of this: ARIS, a hydraulic-based system which is equipped on EC135 and SARIB, which is a mechanical based system equipped on NH90 and Tiger. Despite the increased inertial effect of the mass due to the moment arm used, these systems are still subject to the same limitations of other vibration absorbers. They must also be designed such that the displacements they undergo to absorb vibration does not cause misalignment between driveshafts in the gearbox and fuselage.

Hamouda and Alvin [77] used a linearised set of nonlinear structural equations coupled with a quasi-steady aerodynamic model to investigate the capability of simple pendulum absorbers to suppress the vibration of a helicopter rotor blade. Pendulum absorbers are an alternative form of vibration absorbers whereby the secondary system the form of a pendulum aligned with the centrifugal loads. In this form, the restoring force is provided, not by a physical spring, but by the centrifugal force, similarly to centrifugal stiffening as detailed in Section 1.2.2.2. These absorbers have been used to control in-plane out-of-plane and torsional vibrations of rotors [77]. A pendulum mass of 10 % of the blade mass was used and tuning was achieved by varying the spanwise location of the pendulum. For 4/rev excitation, it was shown that an out-of-plane pendulum tuned to 3.87/rev could reduce the out-of-plane shear force and moment at the root by 98.7 % and 85.8 %, respectively. Additionally, via structural coupling, a reduction of the in-plane shear force and moment of 95.8 % and 77.2 %, respectively, despite the lack of an absorber in this orientation. However, it was also observed that an incorrectly tuned vibration absorber may result in large increases in vibration. Despite the dependency of the pendulum frequency on the speed of the rotor, it has been stated that torsional vibration absorbers remain effective across a range of rotor speeds if they are correctly configured [78].

1.3.2 Active methods

Conversely to passive methods, active methods of vibration suppression involve imparting loading on the structure by direct actuation at the frequency of interest. The majority of active methods that have been developed aim to reduce the formation of vibrations in the rotor as this is the main source of vibration [8] and is suspected to be the most cost-effective form of vibration reduction [7]. However, some methods are designed specifically to attenuate the vibrations once they have been created [49]. Most active systems comprise of four main components: sensors, a controller, a power supply and actuators. The sensors are used to monitor the vibration levels

in the regions of interest. The controller uses this data to calculate the requisite output from the actuator which is itself requires a power supply. These systems are usually more effective than passive systems and are significantly more adaptable to changing operating conditions. However, the requirement of these systems to have these components results in a system that, compared to passive systems, is complex, heavy and with significant power requirements - typically weighing 1 % of vehicle's weight and requiring 3 % of installed power [70]. Despite their impressive performance capabilities, there is limited use of active vibration suppression methods in production aircraft, primarily due to safety concerns [49]. Active methods are often integrated into the primary flight control system or the airframe itself. Therefore, any structural failure in the system would likely result in a catastrophic failure of the aircraft. Additionally, these systems may induce stability issues in the aircraft [49].

1.3.2.1 Higher Harmonic Control

Higher Harmonic Control (HHC) provides inputs to the collective pitch of the blades, in addition to those of the pilot, at higher harmonic frequencies (2/rev, 3/rev etc). These inputs are provided using the primary flight control system, by actuating the swashplate in the fixed frame. The oscillation caused in the rotor blades due to these inputs induce higher harmonic unsteady aerodynamic loads that cancel the original loads that cause the vibration.

As it targets vibrations in the rotor, HHC has the benefit of reducing vibrations in the rotor blades as well as the resultant vibrations in the fuselage. However, the actuators used must be able to accurately and reliably deliver large forces over a wide range of frequencies without failing, being excessively heavy or requiring large amounts of power. Additionally, the integration into the primary flight control system will increase the oscillatory loads the pitch link undergoes and require a suitable mechanism to ensure control of the aircraft can be maintained in the event of a failure. The key to a successful implementation of HHC is the development of appropriate actuators, an accurate and successful control algorithm [63] and suitable safety contingencies.

The use of HHC to expand flight envelopes, reduce power requirements and improve vibration characteristics has been extensively researched; some of the key research efforts and findings are be summarised below:

Payne [79] and *Arcidiacono* [80] showed, using 2/rev and 3/rev inputs, that the stall boundary of the flight envelope can be expanded. However, *Cheng et al* [81, 82] demonstrated only small power reductions of a four-bladed articulated rotor, like that of a UH-60A Black Hawk. *Wachspress et al* [83] used HHC to reduce induced power as this is a large component of total power in both hover and forward flight. The result showed that using 2/rev or 3/rev HHC reduced the induced power of a 4-bladed rotor by 3 %-4 % in forward flight.

Nguyen [84] showed that HHC was effective in reducing hub vibration in a four-bladed rotor using 3/rev, 4/rev and 5/rev inputs. However, it was also observed that the power requirements

and actuator amplitudes increased significantly at forward speeds exceeding 100 knots.

Shaw et al [85] demonstrated the concept experimentally in the Boeing Helicopter Wind Tunnel using a scaled model of a CH-47D rotor. A 90 % reduction of 3/rev out-of-plane shear forces, and 2/rev and 4/rev in-plane shear forces was achieved using 2/rev, 3/rev, and 4/rev inputs up to a forward speed of 188 knots. Similar to that observed by *Nguyen* [84], an increase in blade and control system loads was observed due to the large pitch inputs of up to 3 degrees that were required.

Walsh and Eng [86] deployed the system on Sikorsky S-76A for flight tests. The aircraft was modified by removing existing passive devices and implementing the HHC with 3/rev, 4/rev and 5/rev inputs targeting a reduction in 4/rev fuselage vibration. A significant reduction in level of these vibrations was shown alongside the expected increase in blade and control system loads.

1.3.2.2 Individual Blade Control

Individual Blade Control (IBC) is very similar to HHC in that higher harmonic unsteady aerodynamic loads are created to cancel those that cause vibration. The most notable difference is that instead of each blade being actuated identically in the fixed-frame, each blade is actuated individually in the rotating frame. The ability to control each blade individually may improve the performance of the system and allow multiple objectives to be obtained simultaneously. This actuation is most commonly achieved using either active pitch links or active flaps.

Actuation using active pitch links is similar to the actuation of HHC in that it will likely consist of a hydraulic or electric linear actuator. However, for IBC it is located between the pitch horn and swashplate, replacing the traditional pitch link. It has been suggested that IBC using active pitch links would be well suited to controlling flutter, gust response [87] and noise [88] as well as vibration. A summary of the research performed on IBC using active pitch links is compiled below:

Research conducted by Leonardo Helicopters, known as Westlands at the time, achieved a 95 % reduction in vibration using IBC. This exceeds the 90 % reduction they observed using HHC, reducing the remaining vibration by a further 50 % [63].

Kube and Van Der Wall [89] reported results from a full-scale flight test that were performed using a modified MBB Bo105. Tests were performed at a range of forward speeds, using inputs of 0.5 degrees at 2/rev or 1 degree at 3/rev. These tests yielded a 50 % and 40 % reduction in vibration for the 2/rev and 3/rev cases, respectively.

One of the main drawbacks of active pitch link actuation is the active pitch links themselves as they suffer from many of the same restraints as those required for HHC. One option is to entirely redesign the primary control system and remove the swashplate altogether [90]. Actuation of each blade would be performed individually using a combination of actuators, pumps and power supplies integrated into the rotor hub. The removal of the swashplate and its accompanying

appendages is estimated to reduce rotor profile drag and the weight of the primary control by 40 % each. The actuation of such a concept would be integral to its success and is therefore an actively researched area. The use of hybrid piezohydraulic actuators [91] for such a concept would be preferable due to their low weight and complexity.

IBC can also be actuated using active flaps. This involves the placement of a deformable flap within the blade which is actuated to create the unsteady aerodynamic loads. The system has the benefits of requiring less actuation power than active pitch links and is not part of the primary flight control system. However, it does incur aerodynamic penalties due to discontinuities in the blade causing additional vortices and turbulence as well as requiring the flap actuators to be embedded within the blade. A summary of the research performed on IBC using active flaps is compiled below:

Millott [92] analytically investigated the use of active flap based IBC on a trimmed four-bladed rotor. A substantial reduction in vibration was achieved and the power required to actuate the flaps was approximately 90 % lower than using active pitch links. However, it should be noted that this analysis was performed using a quasi-steady aerodynamic model that would not be capable of capturing the additional penalties observed due to unsteady effects. It was also observed that the flap location may influence the effectiveness of vibration reduction and that its geometry had a minor impact on vibration effectiveness but a significant impact on power and actuator demands.

Another analytical study on a trimmed four-bladed was performed by *Milgram* [93], however, this study used an unsteady incompressible aerodynamic model. Active flap inputs at 3/rev, 4/rev and 5/rev were again shown to reduce hub vibration. However, the effectiveness was shown to be dependent on the flap's geometry and location but effectiveness could be retained if sufficient flap deflection was available.

Dawson et al [94] used a McDonnell Douglas rotor to test the ability of active flaps to reduce BVI noise and vibrations. 5/rev flap inputs were shown to yield a significant improvement in the vibratory pitching moment.

Flight tests of active flap actuated IBC were performed by Eurocopter and reported by *Konstanzer et al* [8]. For these flight tests actuators that could withstand high mechanical loads, operate at the 8th rotor harmonic and fit within the blade were developed. They demonstrated a 90 % reduction in 4/rev hub loads but also showed that the best location of active flaps for manufacturability, vibration response and BVI interactions were not coincident.

Glaz et al [46] used a comprehensive aeroelastic rotor code to assess the optimal performance of active flaps in conjunction with optimised blade structures to achieve simultaneous improvement in vibration and power. Firstly, the rotor blade, without active flaps was optimised for maximum vibration and power improvement in isolation. The maximum vibration reduction achieved was 34.2 % subject to a 13.9 % increase in required power. The maximum power reduction achieved was 5.93 % subject to an 81.4 % increase in vibration. These analyses were then

repeated with the inclusion of active flaps. The maximum vibration reduction case showed a further 7 %-22.9 % reduction in vibration with a negligible additional change in required power. The maximum power reduction case showed an increase in power savings of up to 0.16 % for a similar vibration penalty. Due to the conflicting nature of these objectives, a multi-objective optimisation was performed. Firstly, the optimisation was performed sequentially such that the blade design was optimised and fixed before the active flaps were included. Secondly, a combined approach was used to optimise the blade-flap combination simultaneously. The sequential approach achieved a 30.5 %-36.5 % and 1.2 %-1.3 % reduction in vibration and power, respectively. The combined approach yielded a 27.4 %-27.6 % and 3.06 %-3.13 % reduction in vibration and power, respectively.

The use of active flaps has also been considered in conjunction with other active control methods. The use of multiple methods simultaneously may allow the benefits of each system to be achieved while sharing penalties associated with additional power requirements and transfer. The SHARCS project [88] uses three active control subsystems: active impedance device, active trailing edge flap, active tip to simultaneously reduce noise and vibration.

1.3.2.3 Active Control of Structural Response

Active Control of Structural Response is another form of active vibration suppression. However, unlike HHC and IBC, it is designed to attenuate vibration directly in the fuselage. The system generally consists of: sensors located at points of particular interest, such as near the crew seats and electronic equipment; a controller to calculate the requisite frequency, magnitude and phase of the load; and actuators (often located between the rotor and the fuselage) to apply the loads to the fuselage. This technique has the benefits of not being part of the primary control system which reduces the concerns of safety during a system failure. However, finding the ideal actuator locations may be difficult and an improved vibratory response at the sensors may not be indicative of an improved vibratory response of the entire airframe. A summary of the research on this technique is made below:

An analytical study conducted by *Chui and Friedmann* [95] demonstrated sufficient vibration reduction in the fuselage to achieve a *Jet Smooth* ride. However, large amounts of power were required to achieve this level of vibration.

Welsh et al [96] performed an experimental study on a modified Sikorsky S-76B. The study showed that the system was able to reduce vibration in the fuselage across a range of rotor speeds and required less power than HHC systems.

The system has been flight-tested on a Westland 30 [97] and a UH-60 Black Hawk [98] and subsequently deployed on production helicopters such as the Westland EH101 [99] and the Sikorsky S-92 [100].

A variation of this has been designed and developed by Eurocopter using actuators located

within the fuselage as opposed to between the rotor and the fuselage [8]. The system has been deployed in the EC225, weighs less than 0.8 % of the vehicles total weight and reduces accelerations by 50 % ensuring vibration levels are below 0.1g across all flight speeds.

1.3.3 Adaptive-passive methods

In the fast few decades, efforts have been made to combine active and passive techniques to create adaptive-passive techniques (sometimes referred to as semi-active) [49]. These techniques work by modifying structural properties, such as stiffness and damping, as opposed to directly actuating the primary system.

These techniques require significantly less power than active systems but maintain their adaptability to changing operating conditions. They would also exhibit the reliability and fail-safe nature of passive systems as they are much less complex than active systems, and their failure would stop the modification of the structure's parameters but not damage the structure or control system itself. The composition of such systems would likely be very similar to an active system, comprising of sensors, a controller and actuators. Control system stability is almost guaranteed for the adaptive-passive techniques since very little power is introduced into the semi-active control system [49].

These techniques have been successfully used in automotive suspension systems [101] and variable stiffness members [102] have been used in the civil engineering industry for earthquake prevention. In recent decades, they have started to be considered for use in rotorcraft vibration control [49]. The most prominent is the use of a cyclic variation of the root stiffness of a blade which shall be discussed below:

Nitzsche [103] analytically modelled a rotor blade with variable blade root stiffness. The blade was assumed to exhibit only uncoupled flap-torsion motion and the aerodynamic loads omitted compressibility and BVI. Blade properties for the analysis were obtained experimentally from a dynamically scaled model of an MBB Bo105 blade. Using 1/rev, 3/rev and 5/rev variation in blade root torsional stiffness, a reduction in the 4/rev blade torsional response was observed.

Nitzsche [104] assessed the performance of the concept on a four-bladed rotor during a low-speed descent condition with the inclusion BVI, compressibility and dynamic stall effects. It was shown that 3/rev variation of blade root torsional stiffness was able to considerably reduce the 4/rev out-of-plane and torsional responses.

Phuriwat [49] researched the use of controllable in-plane, out-of-plane and torsional root stiffnesses as a means to reduce helicopter vibration in moderate to high speed forward flight using the University of Maryland Advanced Rotorcraft Code [105]. Initial assessment of the effectiveness of varying flap, lag and torsional stiffnesses showed very different responses: varying flap stiffness may result in meaningful reductions in vibratory hub moments (roll and pitch) and forces; varying lag stiffness may considerably lower hub yawing moments and all vibratory hub

forces; while varying torsional stiffness could only produce modest reductions in vibratory hub vertical force. Additionally, for amplitudes larger than an optimal value, varying stiffness may increase vibration. For stiffness variation at 1/rev, some hub vibrations could be lowered to the detriment of other hub vibration components. Due to the limited capabilities of variation at 1/rev, higher harmonic variations were considered. Using 2/rev and 3/rev variations in flap and lag stiffnesses, hub vibration was lowered, which reduced the hub vibration index by 90 %. This analysis was then repeated using a discretised system as this is the only feasible way to realise higher harmonic stiffness variation. The results showed that reductions of all hub components of 55 %-75 % could still be achieved.

du Bois et al [106] employed a cable with variable tension as an adaptive-passive vibration absorber to reduce vibration in a helicopter tail boom. A finite element model of a Lynx tail boom was created and validated against experimental data obtained for the first six modes. A cable running axially along the length of the boom was then incorporated into the model. Tensioning the cable up to the first buckling mode showed negligible variation in the lower bending modes. However, the modes of the cable exhibited significant variation and were able to interact with the structure akin to a vibration absorber and reduce the vibration of all six modes.

Acar and Yilmaz [107] designed a vibration absorber consisting of a string-mass system which was adaptable using a variable string tension, similar to that seen in [108]. However, the tension adjusting system utilised a negative stiffness to reduce the required tuning force to create a compact vibration absorber with low power requirements that were effective across a range of frequencies. An algorithm was designed to tune the absorber based on the magnitude and frequency of the most dominant component of vibration. The system was modelled analytically and validated experimentally and using a finite element model. The results of forced vibration tests showed that the system could significantly reduce the vibration level of the structure over the range of operating frequencies. These results were achieved with only small displacement inputs and a tuning force that was near zero throughout the operational frequency range.

Abouobaia et al [78] considered combining a passive pendulum absorber, similar to that detailed in Section 1.3.1.2, with a magnetorheological damper to attenuate torsional vibration across a range of excitation frequencies. A magnetorheological damper contains a smart fluid which is able to reversibly change from free-flowing viscous liquids to semisolids in milliseconds when exposed to a magnetic field. The controllable viscosity in the liquid provides the magnetorheological damper, and therefore the overall system, with the adaptability required to operate effectively across a range of excitation frequencies. The subsequent investigation demonstrated that the proposed hybrid absorber was effective in reducing the amplitude of torsional vibration; moreso than either of its components in isolation.

1.3.4 Applicability to variable speed rotors

It can be seen that there is a wide range of existing vibration suppression techniques, either in development or in production. To establish how applicable each of these techniques is to avoiding resonance in variable speed rotors, a set of characteristics that will be required are defined below:

- The system must be effective at avoiding resonances in the rotor blades across a wide range of rotor speeds. Owing to the nature of rotors to have multiple resonances across the range of rotors speed desired, it will be likely that the system will have to be effective in avoiding resonances of all the modes across a range of frequencies. The resonances must be avoided in the rotor blade, not just the fuselage, as the stresses these resonances induce may lead to a loss of the structural integrity of the blade and subsequently the loss of the aircraft.
- The system must have a high likelihood of being certified for deployment on rotorcraft. Certification is a large cost in the development of aircraft and their subsystems, therefore improving the ease with which a system could be certified will improve the chances of it being used in production aircraft with variable speed rotors. To achieve this it would be preferable for the system to be fail-safe and not dependent on unproven and immature technologies.
- The impact of the system on the performance of the aircraft, either directly through its requirements in terms of mass and power etc or indirectly through its influence on the rotor itself, should be minimal. The purpose of avoiding resonance is to permit the use of variable speed rotors to improve the performance of rotorcraft. The more imposing the requirements of the resonance avoidance system, the lower the net gain in performance will be.

The ability to effectively avoid resonance of a wide range of modes across a wide range of rotor speeds precludes the majority of passive techniques from being used as they do not have the adaptability required to influence multiple modes across a range of excitation frequencies. Additionally, the hybrid absorber-isolators are deployed between the fuselage and the rotor and would therefore not be capable of avoiding any resonances in the rotor blade itself. The one system which may remain effective across a range of rotor speeds is the torsional pendulum absorber. This is due to the lack of influence of centrifugal loading on torsional modes ensuring almost constant natural frequencies for the torsional modes.

Similarly to hybrid absorber-isolators, active methods that are effective in the fuselage, such as Active Control of Structural Response are not suitable as they would not avoid resonance of the rotor blades. Active systems such as HHC and IBC target the vibrations in the rotor,

and would potentially be suitably adaptable, but have significant limitations of their own. HHC and IBC actuated by active pitch links, both require actuators with high levels of repeatability, controllability and that are capable of generating large loads across a wide range of frequencies. This is likely to lead to complex heavy actuation systems with large power requirements which would significantly detract from the net performance improvements available through the use of a variable rotor speed. In conjunction with this, their complexity and integration into the primary flight control system will increase their susceptibility to failure and the worsen the repercussions experienced in the event of a failure which will, in turn, impede their certification. IBC actuated by active flaps overcomes some of these problems by avoiding direct integration with the primary control system and requiring less power than their active pitch link counterparts. However, the actuators themselves must be sized such that they can be embedded within the blade and also require the transfer of power from the hub to their location on the blade. Additionally, the effectiveness of active flaps has been shown to be dependant on their spanwise location which may result in reduced effectiveness at different rotor speeds. Additionally, these active techniques are designed to reduce what may already be small vibrations to even lower levels, not avoid catastrophic resonance in a rotor which may result in the structural failure in the blade. It is not known whether these techniques would remain effective under the much larger oscillations associated with resonance.

Adaptive passive techniques do exhibit a promising compromise but there are few techniques available, let alone that are sufficiently mature to be deployed and certified. While the power requirements of a variable root stiffness device may be lower than comparable active systems, they may still be undesirably high due to the frequency of their actuation at higher harmonics. Additionally, their effectiveness in a rotor with variable rotor speeds has not been considered and therefore cannot be guaranteed. The adaptive-passive vibration absorber showed promising results with low power requirements and a simplicity that would aid certification but this was employed in the context of a helicopter tail boom. It is not known whether this technique would be effective for rotor blades or how effective it would be across a range of operating conditions. Despite the plethora of existing vibration techniques, each with their own advantages and disadvantages, there appears to be no single technique that exhibits all of the required characteristics. The adaptive-passive techniques show the most potential to meet these characteristics, particularly if one could be developed that requires low frequency actuation to keep the actuation requirements and complexity low.

1.4 Effect of applied loading on structural dynamics

The use of applying loading to structures to alter their dynamic properties has been extensively investigated, both analytically and experimentally, under many different guises for various purposes, including adaptive passive resonance avoidance. A summary of a range of research efforts

has been made below:

Turkstra and Semercigil [109] theorised that spinning shafts with supercritical operating speeds could avoid resonant conditions when passing through critical speeds using a switching tensile member. As a critical rotational speed is approached, a binary tensile member's state is switched. The change in axial load alters the shaft's natural frequency, allowing the previously critical rotor speed to be passed through. This switching of states would continue until the operational rotor speed had been reached. An analytical study of an axially tensioned shaft quickly and simply demonstrated that the theory should work but careful designing of the tensile member would be required to ensure sufficient separation between the natural frequencies of the shaft in its two different states.

Virgin and Plaut [110, 111] explored the effects of axial loads on the forced vibrations of non-rotating beams. Analytical solutions of Euler-Bernoulli beam equations provided insight into the static and dynamic behaviour under these axial loads. The relationship between load and the square of frequency was almost linear, even if the mode of vibration and the buckling mode were not identical; however, the linearity may deteriorate as near buckling. The fraction of the critical buckling load that was applied was also shown to have an approximately squared relationship with the amplitude of resonance but a linear relationship with the static amplitude of the unforced beam.

du Bois et al [112] used the introduction of known loads to adaptively retune the dynamics of structures. A structurally redundant, cross-braced rectangular frame was tested experimentally and modelled using finite element, with excellent correlation, to demonstrate the ability of structural loading to tune the dynamics of the structure. It was suggested that the tuning capability could be used to shift the natural frequencies outside the range of the excitation frequencies or align antiresonances with the excitation frequencies. A feasibility study for automated load control was then performed which demonstrated an improved vibratory response with a low power requirement. However, warnings were made about the need for a suitable controller to avoid rapid change in actuation demands and account for delays and lags in the actuation system.

Zhang et al [113] discovered that a beam's dynamics become more sensitive to loading as the critical buckling load is approached. Therefore, accurate modelling of the effects of structural loading becomes paramount to ensure the correct trade-off between desired sensitivity and structural stability.

Nudehi et al [114] used a buckling type end force to actively control the transverse vibration of a flexible cantilevered beam. The system used measurements and estimations of modal amplitudes to appropriately apply a load such that it will remove vibration energy from the structure. The end load is binary, switching between two sub-buckling values, at a predetermined frequency. The efficacy was demonstrated using both simulations and physical experiments. It was observed that using a single sensor and actuator all modes within the bandwidth of the actuator could be controlled but the chosen loads influenced the effectiveness.

Tian et al [115] experimented with active tendons, controlled with Integral Force Feedback, to increase the damping in targeted modes of a suspension bridge. The additional damping was successfully demonstrated, as was the ability to alter the mode shapes and frequencies.

Preumont et al [116] used active tendons to control a large truss structure. A tendon was chosen as it is a lightweight method to alter stiffness and shape and actively damp vibrations. The tendon's dynamics are excluded from the model which is subsequently experimentally validated. The model is then used to show that the effects on damping and stiffening are not independent. Additionally, it was shown that the mass of the tendon and the value of tension must result in a first mode of the tendon that is above the frequency range to be damped to minimise the detrimental effect of the tendon vibration on the structure.

Issa et al [117] used cable actuators for structural vibration suppression. They considered the interaction between the cable and the structure and showed that there are two main effects on the structure: the parametric effect where the load changes the structures stiffness; and the direct effect that provides an external force on the structure.

Suzuki and Kagawa [118] investigated the use of Shape Memory Alloy tendons as actuators in active vibration control. A set of Shape Memory Alloy tendons were attached to the tip of a cantilevered beam with bending-torsion coupling and a control system was designed using H-infinity theory. The system was evaluated experimentally and using a mathematical model, with good correlation shown between the two. The system was able to simultaneously damp the four vibrational modes considered - one torsional and three bending.

Svendsen et al [119] computationally investigated the use of oscillatory compressive loading to actively control the dynamic response of a single mode of a wind turbine rotor blade. The time-varying compressive load was to be generated using an active strut and a resonant controller based on a sensor collocated with the actuator. It was demonstrated that this collocated sensor-actuator system was able to reduce modal vibrations at the targeted mode in the specified operating conditions.

Krishnan et al [120] used the application of an applied compressive load in an aeroelastic context. Unlike variable speed rotors, where resonance is to be avoided, the purpose of this research was to use compressive loading to reduce flutter speed as this is a desirable trait for systems such as energy harvesters that require large amplitude oscillations. An experiment was devised using an aerodynamic plate attached to the main structure via a cantilevered beam. The structure was placed in a wind tunnel to determine the flutter speed. A compressive load was applied axially along the beam to reduce its natural frequency which successfully reduced the flutter speed by 12 %.

The use of applied loading to alter the vibratory characteristics of a wide array of structures has been investigated both theoretically and experimentally. There are two clear ways in which applied loading has been utilised. One of which uses oscillatory loads which operate at frequencies similar to that of the vibration they are intended to alter. The second is to use a constant

applied load to alter the dynamic properties of the structure such that resonant interactions are avoided. Both of these techniques have been shown to be effective, however, their application to rotorcraft blades has not been considered. One additional phenomenon that would be encountered should these methods be employed in a rotor blade would be that of aerodynamics. Unlike the majority of the aforementioned structures researched, rotor blades undergo significant aerodynamic loading which may couple with the altered dynamics resulting in unusual aeroelastic behaviours, as hinted in [120].

1.5 Compressive loading based resonance avoidance concept

The concept being explored in this research is the use of applied compressive loading to a rotor blade, as shown in Fig. 1.4, to tune the frequencies of the rotor blade so as to avoid resonance.

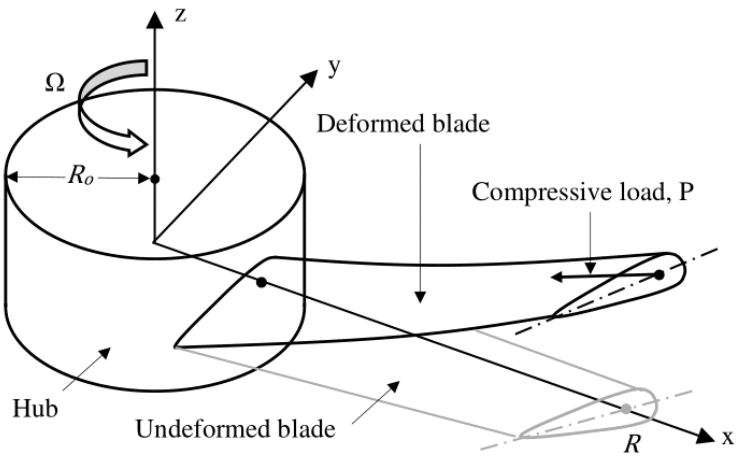

Figure 1.4: Schematic of compressively loaded blade concept.

It is well understood that centrifugal loads provide a significant contribution to the effective stiffness of a rotor blade which in turn determines its dynamic properties. It is hypothesised that an applied compressive force would partially oppose the centrifugal force, reduce the centrifugal stiffening effect and therefore lower the natural frequencies of the blade.

To demonstrate the core principle behind this concept, an analytical solution for the natural frequencies of a simplified blade are derived in Appendix A. The equations can be seen to take the form shown in Eq. (1.1) whereby each coefficient, α, β, γ, is real and positive and represent the contributing effects of rigidity, rotation and applied compressive loading, respectively.

$$-\lambda^2 = \alpha + \beta\Omega^2 - \gamma P \tag{1.1}$$

The format of these equations is similar to the equations developed by Southwell [121] and clearly show the separate contributing effects. It can be seen that the terms pertaining to rigidity

and rotation are positive, demonstrating the known behaviour of rigidity and rotation to increase effective stiffness and therefore frequency. However, the compressive loading term is negative which implies that all of the frequencies will reduce with the application of a compressive load.

If the natural frequencies of a rotor blade can be manipulated then it would be possible to avoid resonance by reducing the natural frequency of a blade if it coincides with an excitation frequency. Therefore, a rotor would be able to operate across a range of rotor speeds without experiencing resonance. An example fan diagram for a loaded and unloaded rotor blade are shown in Fig. 1.5 to demonstrate how a change in natural frequency would avoid resonance.

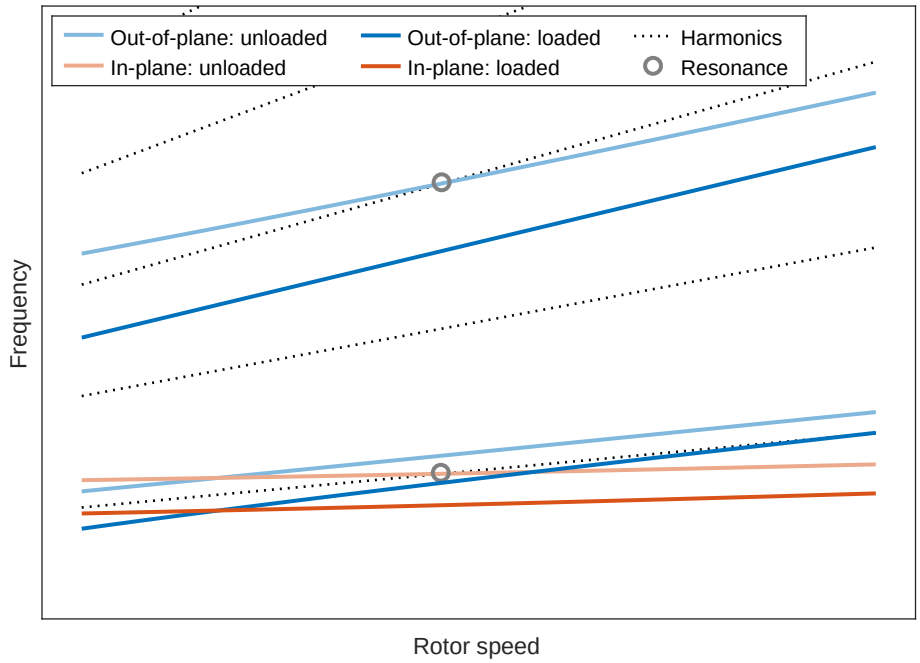

Figure 1.5: Fan diagram of a typical rotor blade showing the resonance avoidance capability of compressive loading.

It can be seen that when the blade is unloaded, there are multiple instances where, at the correct rotor speed, the natural frequency of the blade and the rotor harmonics coincide which would likely cause resonance. With the application of a compressive load, the natural frequencies reduce and no longer coincide with a rotor harmonic.

This concept offers many benefits over the aforementioned vibration suppression techniques in terms of its ability to exhibit the characteristics required of a resonance avoidance system for variable speed rotors that were stated in Section 1.3.4. Regardless of rotor speed, the compressive load would still influence the dynamics of all desired modes. Therefore, it will remain able to reduce the resonance of any mode at any rotor speed which is not true of the passive techniques discussed in Section 1.3.1. Unlike the active, and some of the adaptive-passive techniques, discussed in Sections 1.3.2 and 1.3.3 which are inhibited by actuation demands and safety concerns,

this concept should not encounter such issues. As actuation would only be required when operating conditions change, the actuator would be operating at a frequency many orders of magnitude lower than that of the aforementioned active and adaptive-passive techniques which would save considerable amounts of power. The current concept also has the benefit of not being integrated with the primary flight control system. Therefore, any failure would result in a loss off the ability to manipulate frequencies, which would limit the range of operational rotor speeds available, but it would not prohibit the aircraft from flying.

1.6 Aims and objectives

Rotorcraft with a variable rotor speed are one means that are being considered by the industry to improve their performance, particularly with respect to fuel usage and the emission of greenhouse gases. Whilst the performance benefits are well established, there is an accompanying resonance problem which is one of the key factors preventing the widespread use of variable speed rotors. The variation of rotor speed alters the natural and excitation frequencies of a rotor, often resulting in resonant interactions between the two. These interactions may cause increased vibratory loads which deteriorate passenger comfort and equipment functionality, or potentially the loss of the structural integrity of the rotor blade and subsequently the loss of the aircraft.

The aim of this research is to investigate the use of compressive loading as an effective means to avoid resonance in variable speed rotorcraft.

The proposed concept employs an applied compressive load to alter the dynamic properties of the rotor so as to avoid resonant interactions and their associated effects which would allow the safe operation of the rotorcraft across a wide range of rotor speeds.

This aim can be broken down into a few key objectives:

1. Establish the capability of compressive loading to alter modal properties of a rotor blade and reduce vibratory loads.

2. Assess the magnitude of loads that would be required and feasibility of the requisite actuators.

3. In the context of a variety of realistic rotor blades, evaluate the capability of compressive loading to avoid resonance of all significant modes across a wide range of operational rotor speeds.

4. Evaluate the impact of the aerodynamic loads in hover on the ability of compressive loading to intentionally alter the aeroelastic properties of a rotor blade, such as natural frequencies and aerodynamic damping ratios, and avoid resonances across a wide range of operational rotor speeds.

1.7 Overview of dissertation

Chapter 1 has introduced the motivation for this research; detailing the performance benefits of variable speed rotors along with the actuation and vibratory problems associated with them. A review of existing vibration techniques was performed to evaluate the capabilities of existing and emerging methods to solve the resonance avoidance problem that is the focus of this research. Finally, a summary of existing research efforts in to the influence of applied loading on structural dynamics precedes the explanatory introduction of the proposed concept.

Chapter 2 details the modelling methodology, mathematical problem definition, numerical solver and algorithmic solution procedure that is common to each of the sub-models that form the foundation of the subsequent work.

Chapter 3 evaluates the initial feasibility of the proposed concept. An experimental study is performed on the impact of compressive axial loading on the structural dynamics of a non-rotating beam. The results of this study are used to inform and validate the modelling methodology for the applied compressive load that is used throughout the rest of the presented research. A case study is performed to assess the magnitude of compressive loading that would be needed to achieve the maximum expected change in natural frequency that may be required for a range of different full-scale aircraft. A subsequent sizing of a theoretical actuator is performed to assess the spatial and power requirements that may be incurred if the proposed system were to be employed. Finally, a brief investigation of the vibratory loads experienced in forward flight, and the reduction available using compressive loading, is performed to establish the relationship between compressive loading based modal tuning and a reduction in vibratory loads.

Chapter 4 incorporates the additional physical features of initial twist, torsional deformation and non-coincident mass and elastic axes to improve the ability of the model to realistically represent a rotor blade. Once validated, the model is used to evaluate the implications of the additional physical features on rotor blades across a range of rotor speeds and compressive loads. A case study is then performed on a range of aircraft to optimise the modal tuning at each rotor speed. The loading values used were within a prescribed range to avoid the loss of structural stability of the blade. A subsequent assessment of the proportion of the desired rotor speed range that is safely operable is then made and compared with the case with no compressive loading.

Chapter 5 incorporates geometric nonlinearities and unsteady aerodynamics to further increase the fidelity of the model. Once validated, the model is used to evaluate the implications of the additional physical features on rotor blades across a range of rotor speeds and compressive loads. Subsequently, a case study is then performed on a set of aircraft to optimise the aeroelastic response using compressive loading and evaluate the range of rotor speeds that could be safely operated in.

Chapter 6 summarises the conclusions drawn from the research effort and recommends some

potential future research efforts that would further progress the development of compressive loading based resonance avoidance for use in variable speed rotorcraft.

CHAPTER 2

MODELLING APPROACH

The concept being investigated, as introduced in Section 1.5, uses the controlled application of an applied compressive load to the blade to alter the natural frequencies of the blade. The ability to alter the natural frequencies of the blade will allow them to be shifted away from potentially resonant excitation frequencies and ensure the safe operation of the aircraft across a range of rotor speeds.

To assess the capability of compressive loading to avoid resonances, it is necessary to be able to calculate the dynamic properties of rotor blades. Therefore, a model that is capable of capturing the physical behaviour of rotor blades, including the effects of an externally applied compressive force, is developed.

Within this chapter, a brief review of existing rotor blade models is provided before the modelling methodology for the present model is chosen. Subsequently, the numerical solver and algorithmic procedure that form the model is described.

2.1 Existing models of rotor blade dynamics

Due to the importance of the aeroelastic behaviour of rotor blades, extensive efforts, both in research and industrial environments, have been expended to be able to model the behaviour of helicopter rotors. A wide variety of different methodologies have been developed and used to target specific modelling capabilities.

It is commonplace for rotor blades to be modelled as one-dimensional entities as the span of the rotor blade is the dominant geometric dimension of a blade; most rotor blades have an aspect ratio (radius:chord) between 10 and 20 [122]. Therefore, the analysis of the inherently three-dimensional structure can be split into a two-dimensional analysis of the blade cross-

section and a one-dimensional analysis along the span of the blade. It can be assumed that the shape of the cross-section is unaffected by variation in the other dimension such that it can be parameterised independently of the one-dimensional analysis. *Truong et al* [123] showed that one-dimensional analysis can compare well to three-dimensional analysis for the lowest eight modes of rotor blades if the cross-section is small compared to the wavelength of the vibrations of interest, i.e. the aspect ratio is greater than ten.

Models that capture the coupling between structural and aerodynamic aspects of a rotor blade are the most all-encompassing type of rotor model. Broadly, these models can be separated into two types: CFD-CSD and comprehensive rotor codes. CFD-CSD models consist of high fidelity three dimensional Computational Fluid Dynamics (CFD), to calculate the aerodynamic loads, coupled with high fidelity three dimensional Computational Structural Dynamics (CSD), to calculate the subsequent structural deformations. Comprehensive rotor codes consist of mid-fidelity aerodynamic models (e.g. 2D aerofoil table lookups and prescribed wake models) coupled with multi-body structural models (e.g. one-dimensional beam models) to analyse rotor blades in a range of scenarios. The complicated nature of the constituent components and their coupling means these types of model are often very complex and require extensive validation to ensure all physical phenomena are correctly captured. Due to the large expenditure required to formulate and validate such codes, they are usually developed by large organisations such as universities, governmental entities or commercial companies.

A brief history of comprehensive rotor codes and their development over time has been compiled by *Kunz* [124] and *Johnson* [125]. They commented that Finite Element (FE) techniques using beam elements and continuous one-dimensional beam theory were both used for the structural models in a variety of codes. It was also noted that second-generation comprehensive codes use a lifting line aerodynamics model. These models used a two-dimensional lookup table for aerofoil properties and calculated the rotor inflow using a free wake model that evolves over time and captures the interaction between different vortices. These types of inflow model are computationally expensive and often require initialisation from uniform or linear inflow models and prescribed wake models. Despite this initialisation, the computational expense remains too high for some simulations, such as aeroelastic stability analysis, where lower fidelity inflow models are required.

A direct code to code comparison of the ability of *DYMORE II* and *CAMRAD II* (a well-established commercial comprehensive rotor code) to model a rotor in descending flight was performed by *Park and Kee* [126]. Despite *CAMRAD II*'s more elaborate structural and aerodynamic models it was only able to offer occasional and marginal performance improvements; most of these were due to *DYMORE II* being unable to model the effects of Blade Vortex Interaction (BVI). As BVI frequencies are often too high for elastic vibrations to be sensitive to them [127], it was expected that the ability of *CAMRAD II* to capture this phenomenon would only result in minor changes to the results.

Despite the attempts of comprehensive rotor codes to capture all of the physical phenomena experienced by a rotor, they are not always suited to research environments. Due to the inherent novelty associated with many aspects of research, comprehensive rotor codes are often unable to capture the effects of the concept being researched. For example, the present concept utilises the effects of an applied compressive load; a feature which may not be captured using existing comprehensive rotor codes. This may be overcome with the use of a surrogate model to fit the research concept into the framework of an existing comprehensive rotor code but due to the complexity of creating a surrogate model and validating its use in a comprehensive rotor code, this is not always possible. More commonly, an independent model is developed that is specifically targeted at capturing the key physical behaviour of the rotor and the concept being investigated. For this approach to rotor blade aeroelastic analyses, it is commonplace to use a structural beam model based on a set of one-dimensional Partial Differential Equations (PDEs) coupled to a blade element aerodynamic model and solved as a Boundary Value Problem (BVP) [128]. A few examples of these models are summarised below:

Hodges and Ormiston [3] used nonlinear beam equations coupled with a 2D unsteady blade element model and a uniform steady inflow to investigate the aeroelastic stability of hingeless rotor blades in hover. A linearisation procedure was performed and the subsequent perturbations were solved using a two-stage Galerkin method. A similar model was used by *Gennaretti* [129] to investigate vibration reduction using a combination of active flaps and variable stiffness. The main addition to the model was the incorporation of a free wake inflow model to include higher frequency effects.

Ryu et al [130] used intrinsic beam theory in conjunction with blade element theory and a finite-state dynamic inflow model to model the HART II rotor in descending flight. The aerodynamic and structural model were loosely coupled, whereby each model runs in series and aerodynamic loads and structural responses are transferred between the models. This process repeats until the desired convergence criterion has been met. A model based on the same intrinsic beam theory was used by *Amoozgar et al* [131] to replicate the aforementioned work of *Hodges and Ormiston* [3]. The model was solved using a Differential Quadrature Method to demonstrate the capability of the solution method.

It can be concluded from these modelling efforts that the choice of modelling methodology is determined by its intended use. For commercial companies which require high levels of accuracy during their design process, have large budgets, and are not aiming to incorporate technologies outside of the scope of CFD-CSD or comprehensive rotor codes, these more complex and computationally expensive models are the most suitable. However, for research of new and novel concepts, lower-fidelity models which are specifically formulated to capture the key physical behaviours of a rotor blade and the concept being investigated, are the preferred choice.

2.2 Methodology of chosen modelling approach

Due to the different features and characteristics of various modelling methodologies, careful consideration must be used when deciding what type of model to develop. Herein, a methodology shall be chosen that is capable of capturing the key physical behaviours of a rotor blade and the influence of an applied compressive load. This shall be used to create three sub-models to capture different physical phenomena.

Whilst the accuracy of comprehensive rotor codes across a range of flight conditions and their level of validation is appealing, they are not suitable for the present research as they do not have the capability to capture the effects of applied compressive loads. Unfortunately, modification of these codes to include this capability may not be possible and would require rigorous validation of the new capability. Additionally, the complexity of these models, particularly their coupled aeroelastic modelling, may result in computationally expensive simulations which offer improvements that are either small or only pertinent in specific flight conditions. Therefore, an independently developed model shall be formulated that captures the desired phenomena and is computationally efficient to improve its performance during computationally expensive procedures such as optimisations or large parametric sweeps.

Similarly to those discussed previously, the model used for this research will take the form of a two-point BVP. This consists of a set of equations governing the behaviour within the solution domain and constraints at the two limits of the domain to define its end conditions.

One option to solve BVPs is the FE method. This consists of discretising the solution space into *elements*, applying the desired constraints to the boundaries and formulating mass and stiffness matrices which can, in turn, be used to create a weak form characteristic equation to calculate natural frequencies. The main benefit of FE methods in this instance is that they are available via existing commercial packages which contain a large library of elements to choose from and are extensively validated and are therefore reliably accurate if the user configures the problem correctly.

The alternative option is to solve the differential equations directly in the strong form. These problems are formulated using a set of smooth continuous first-order Ordinary Differential Equations (ODEs), h, over a finite domain, x, and a set of constraints at the boundary of the domain, g, as shown below.

$$\begin{aligned} &\frac{dh}{dx}(x,h,s), \quad R_0 \leq x \leq R \\ &g(h(R_0),h(R),s) = 0 \end{aligned} \tag{2.1}$$

The use of a one-dimensional modelling approach imposes additional limitations. For instance,

three-dimensional modelling approaches would capture localised deformations of the cross section which may influence the response of the blade at high deformations or compressive loadings.

To ensure that the problem is sufficiently well posed to allow a solution to be found, it is necessary to ensure that the number of constraints at the domain boundary is equal to the number of the first-order ODEs. If an additional parameter is to be solved for then an accompanying boundary condition is required.

This form does not inherently require the discretisation involved in FE methods which usually permits a more general variation of blade properties. However, most solution methods will involve some form of spatial discretisation of the PDE over the solution domain. Similarly to the choice of element in FE, the choice of differential equation will dictate the assumptions, limitations and computational cost of the model.

Despite the number of well established FE beam models, for the current work, the continuous differential equations shall be solved directly. The main benefit of this approach is in the control and flexibility over the capturing of physical phenomena that it provides. For instance, the adoption of a strong form approach makes it possible to examine the differential equations governing the solution domain and the boundary conditions and identify the physical phenomena that individual terms pertain to at all points along the domain. These terms can subsequently be subdued or amplified to evaluate their impacts and provide insight into which physical phenomena are influencing the results. Additionally, the ability to choose differential equations will allow structural and aerodynamic models developed specifically for rotorcraft to be used.

For this research, three different sets of PDEs are used to form three separate sub-models. Although high fidelity beam theories, such as VABS [132] and geometrically exact intrinsic beam theory [133], have been developed and used to model rotor blades [131, 134], the additional capabilities that they offer are beyond the scope of this research. Therefore, to avoid any unnecessary modelling complications, each of the three sub-models shall use a set of PDEs based upon Euler-Bernoulli beam theory (also referred to as Classical beam theory). Euler-Bernoulli beam theory is a special case of Timoshenko beam theory. For an unforced linearly elastic, isotropic, homogeneous beam of constant cross-section, Timoshenko beam theory states [135],

$$\begin{aligned} m\frac{\partial^2 w}{\partial t^2} &= \frac{\partial}{\partial x}\left[\kappa GA\left(\frac{\partial w}{\partial x}-\Psi\right)\right] \\ \underline{mk_{m1}^2\frac{\partial^2 \Psi}{\partial t^2}} &= \frac{\partial}{\partial x}\left(EI_y\frac{\partial \Psi}{\partial x}\right)+\kappa GA\left(\frac{\partial w}{\partial x}-\Psi\right) \end{aligned} \tag{2.2}$$

However, it is often assumed that rotational inertia and shear deformation are negligible. This removes the rotational inertia term (underlined in Eq. (2.2)) and implies that $\Psi = \frac{\partial w}{\partial x}$ which reduces Eq. (2.2) to Euler-Bernoulli beam which forms the basis of the models presented

herein. This simplification typically results in a slight underestimation of deflections and overestimation of natural frequencies, particularly at higher frequencies [136]. The use of the full Timoshenko beam theory may offer improvement for non-slender beams or for high-frequency responses. However, Euler-Bernoulli beam theory is reasonably justified for isotropic homogeneous slender beams featuring simple cross-sections.

Initially, a relatively low fidelity set of PDEs is used to capture the principle behaviours of the dynamics of a rotor blade and provide an understanding of the principle effects of compressive loading. The PDEs are subsequently replaced to capture additional behaviour and increase the fidelity and realism of the model.

The first set of PDEs [51] represent the motion of an untwisted in-vacuo rotor blade in the plane of rotation (herein referred to as in-plane motion) and out of the plane of motion (herein referred to as out-of-plane motion), as seen in Fig. 2.1 and Eq. (2.3).

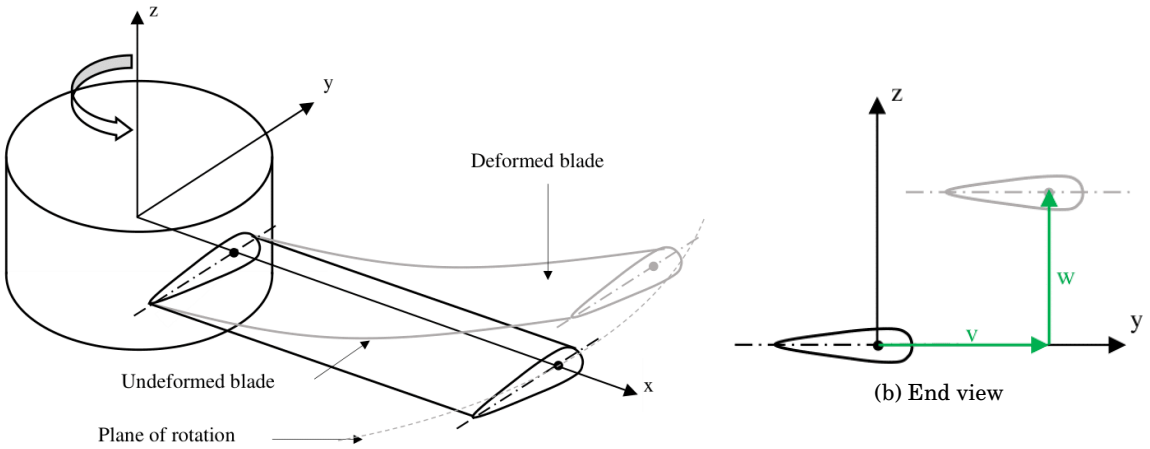

(a) Isotropic view

(b) End view

Figure 2.1: Schematic of the blade and motion that can be captured by the first set of PDEs.

$$\begin{aligned} -\left(Tw'_*\right)' + EI_y w^{iv}_* + m\ddot{w}_* &= 0 \\ -\left(Tv'_*\right)' + EI_z v^{iv}_* + m\ddot{v}_* - m\Omega^2 v_* &= 0 \end{aligned} \tag{2.3}$$

These equations capture effects of rigidity (EI_y,EI_z), blade inertia ($m\ddot{v}_*$,$m\ddot{w}_*$) and internal axial loads (T,$m\Omega^2 v_*$) such as that induced by centrifugal forces and applied compressive loads for an untwisted blade. The lack of interaction between the in-plane and out-of-plane motions is due to the omission of phenomena such as twist which would induce coupling.

The second set of PDEs used are those derived by *Houbolt and Brooks* in [137]. These equations represent the torsional motion of the rotor blade in addition to the in-plane and out-of-

plane of the previous set of equations. The equations also account for blade pitch, twist and a non-coincident mass and elastic axis, as shown in Fig. 2.2 and Eq. (2.4).

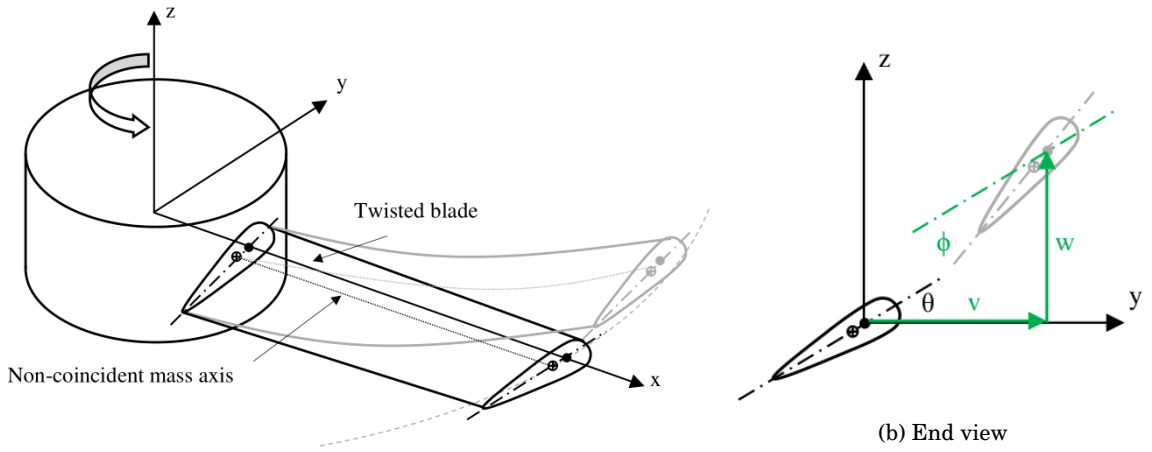

(a) Isotropic view

(b) End view

Figure 2.2: Schematic of the blade and motion that can be captured by the second set of PDEs.

$$
\begin{aligned}
&-(Tw_*')' + \left[-Te_A\phi_* \cos(\theta) + (EI_z - EI_y)\cos(\theta)\sin(\theta)v_*'' + [EI_z \sin^2(\theta) + EI_y \cos^2(\theta)]w_*'' \right]'' \\
&\quad + m\ddot{w}_* + me\ddot{\phi}_* \cos\theta - (me\Omega^2 x\phi_* \cos(\theta))' \\
&\quad = \left(Te_A \sin(\theta)\right)'' + \left(\Omega^2 mxe \sin(\theta)\right)'
\end{aligned}
$$

$$
\begin{aligned}
&-\left(Tv_*'\right)' + \left[Te_A\phi_* \sin(\theta) + \left[EI_z \cos^2(\theta) + EI_y \sin^2(\theta)\right]v_*'' + (EI_z - EI_y)\cos(\theta)\sin(\theta)w_*'' \right]'' \\
&\quad + m\ddot{v}_* - me\ddot{\phi}_* \sin\theta - m\Omega^2[v_* - e\phi_* \sin(\theta)] + (me\Omega^2 x\phi_* \sin(\theta))' \\
&\quad = \left(Te_A \cos(\theta)\right)'' + \left(\Omega^2 mxe \cos(\theta)\right)' + \Omega^2 me \cos(\theta)
\end{aligned}
\tag{2.4}
$$

$$
\begin{aligned}
&-\left[Tk_A^2\phi_*'\right]' - Te_A(w_*'' \cos\theta - v_*'' \sin\theta) - (GJ\phi_*')' + mk_m^2\ddot{\phi}_* + m\Omega^2\phi_*(k_{m2}^2 - k_{m1}^2)\cos 2\theta \\
&\quad + me\Omega^2 x(w_*' \cos\theta - v_*' \sin\theta) - (\ddot{v}_* - \Omega^2 v_*)\sin\theta + \ddot{w}_* \cos\theta \\
&\quad = \left(Tk_A^2\theta'\right)' - m\Omega^2(k_{m2}^2 - k_{m1}^2)\sin(\theta)\cos(\theta)
\end{aligned}
$$

The twist and non-coincident axes result in significant amounts of coupling between the aforementioned motions which will improve the accuracy with which the model represents a realistic

rotor blade.

The final set of PDEs used are those derived by *Hodges and Dowell* in [138]. These equations represent the axial motion of the rotor blade in addition to the torsional, in-plane and out-of-plane of the previous set of equations, as seen in Eq. (2.5).

$$
\begin{aligned}
&-(T)w_*')' + \Big[-EAe_A\Big(u_*' + \frac{v_*'^2}{2} + \frac{w_*'^2}{2}\Big)\sin(\theta+\phi_*) + (EI_z - EI_y)\cos(\theta+\phi_*)\sin(\theta+\phi_*)v_*'' \\
&\quad + [EI_z\sin^2(\theta+\phi_*) + EI_y\cos^2(\theta+\phi_*)]w_*''\Big]'' + m\ddot{w}_* + me\ddot{\phi}_*\cos\theta \\
&\quad - (me\Omega^2 x\sin(\theta+\phi_*) + 2\Omega\dot{v}_*\sin\theta)' = L_z \\
\\
&-(T)v_*')' + \Big[-EAe_A\Big(u_*' + \frac{v_*'^2}{2} + \frac{w_*'^2}{2}\Big)\cos(\theta+\phi_*) + [EI_z\cos^2(\theta+\phi_*) + EI_y\sin^2(\theta+\phi_*)]v_*'' \\
&\quad + (EI_z - EI_y)\cos(\theta+\phi_*)\sin(\theta+\phi_*)w_*''\Big]'' + 2m\Omega\dot{u}_* + m\ddot{v}_* - me\ddot{\phi}_*\sin\theta \\
&\quad - 2me\Omega(\dot{v}_*'\cos\theta + \dot{w}_*'\sin\theta) - m\Omega^2[v_* + e\cos(\theta+\phi_*)] \\
&\quad - (me\Omega^2 x\cos(\theta+\phi_*) + 2\Omega\dot{v}_*\cos\theta)' = L_y \qquad (2.5) \\
\\
&-T' - m(\Omega^2 x + 2\Omega\dot{v}_*) = L_x \\
\\
&-\Big[EAk_A{}^2(\theta+\phi_*)'\Big(u_*' + \frac{v_*'^2}{2} + \frac{w_*'^2}{2}\Big)\Big]' - EAe_A\Big(u_*' + \frac{v_*'^2}{2} + \frac{w_*'^2}{2}\Big)(w_*''\cos\theta - v_*''\sin\theta) - (GJ\phi_*')' \\
&\quad + (EI_z - EI_y)\Big[(w_*''^2 - v_*''^2)\cos\theta\sin\theta + v_*''w_*''\cos 2\theta\Big] + mk_m^2\ddot{\phi}_* \\
&\quad + m\Omega^2\phi_*(k_{m2}{}^2 - k_{m1}{}^2)\cos 2\theta + me\Omega^2 x(w_*'\cos\theta - v_*'\sin\theta) - (\ddot{v}_* - \Omega^2 v_*)\sin\theta \\
&\quad + \ddot{w}_*\cos\theta = M_\phi - m\Omega^2(k_{m2}{}^2 - k_{m1}{}^2)\cos\theta\sin\theta
\end{aligned}
$$

In addition to the behaviour captured by the previous set of equations, these equations also account for geometric nonlinearities and allow for the inclusion of aerodynamic loading. Although there is no explicit inclusion of aerodynamic loading in these equations, the inclusion of generalised forces allows for an external aerodynamic model to be incorporated. The aerodynamic model used is that derived by *Greenberg* in [139]. This model calculates the unsteady aerodynamic loads generated by a harmonically oscillating rotor blade in an inviscid flow.

The focus of this research is to assess the ability of compressive loading to alter the natural frequencies of a rotor blade as a means to avoid resonance in variable speed rotors. Therefore, the method with which that load is applied, and any associated implications, is beyond the scope of this work and can be considered a separate topic of research in its own right. It is expected that if the effects of compressive loading can be shown to yield the desired benefits of variable

speed rotors, this would motivate further research in answering the necessary questions about load application system such as:

- Could the load be applied using technology embedded within the blades such as Shape Memory Alloys?
- Could the load be applied using a physical entity located within the blade such as a flexible tendon, a pin-jointed lattice structure, a solid bar, or a flexible beam with a tailored cross-section?
- If using a physical entity within the blade, would its dynamics be suppressed, e.g. using viscoelastic coatings or embedding within the internal foam often used to layup composite blades, or potentially exploited, as demonstrated in [106]?

Some efforts are already being made to investigate load application systems and their implications on blade dynamics. The SABRE project [140] is investigating this in the context of flexible tendons [141, 142, 143, 144].

As the focus of this research is the compressive load, the dynamics of a load application system shall not be considered. Instead, a point force applied at the tip of the blade shall be used to apply the compressive load. This is common practice and has been utilised in many previous research efforts such as: avoiding critical rotor speeds in spinning shafts [109]; investigating the effects of compressive loads on the vibration of beams [110, 114, 113]; the use of shape memory wires to augment structural damping [145]; active control of large trusses using tendons [116]; the use of a tendon to control the vibration of a cantilever beam [118]; and resonant vibration control of rotating beams [119]. There are instances where the load application system has been modelled, using FE or analytical models, such as when researching: suppression of structural vibrations using cable actuators [117]; the use of tensioned cables as an adaptive tuned vibration absorber for response suppression in rotorcraft [106]; dynamic vibration absorbers composed of a string-mass system [107]; active tendon control of a suspension bridge [115]. Often, the reason the application system is modelled because it is being used as a vibration absorber [106, 107], for which the inclusion of the system's dynamics are integral. The effects of this modelling methodology are discussed in detail in Section 3.2.

The formulation and handling of the aforementioned equations of motion and their associated boundary conditions is inextricably linked to the modelling methodology of the applied compressive load. Therefore, the implementation details of the previously described equations and the associated boundary conditions are described in situ for each sub-model.

2.3 Model formulation

The mathematical model used to solve the aforementioned BVP and assess the capability of compressive loading to tune the modal properties of a rotor blade such that resonance can be avoided in rotors with a large range of operational rotor speeds is described herein. The model can be split into two components which shall be discussed separately. Firstly, the numerical solver used to solve the BVP, along with the requirements associated with it, shall be discussed. Secondly, the algorithmic procedure for using the numerical solver to calculate the desired modal properties across a range of operating conditions is described.

2.3.1 Numerical boundary value problem solver

The numerical solver used was chosen to ensure it was capable of handling the complexities involved in solving the aforementioned PDEs. Due to the coupling between the equations for each different motion observed in Eqs. (2.4) and (2.5), it is necessary that the model can simultaneously solve multiple coupled equations. There is also a high likelihood that in an analysis of any given rotor configuration, there will be multiple modes with similar natural frequencies. Therefore, the solver must be capable of calculating both natural frequencies, despite their similar values and proximity to one another. In Eq. (2.5) there are nonlinear terms present as well as aerodynamic loading which will induce complex eigenvalues with both a real and imaginary component. Therefore, the solver must additionally be capable of solving nonlinear problems and handling complex eigenvalues. Finally, it would be beneficial for the implementation of the model and the run time of simulations if the model was: computationally efficient; able to generate and update its discretisation mesh automatically; and did not require analytical derivatives to be provided a priori.

Subsequently, the numerical method employed to solve the BVP is Collocation. Collocation methods use a set of candidate solution which are evaluated at prescribed points within the problem domain and refined to reduce residual errors. These methods are widely used for solving differential equations and are well known for their ease of implementation, good convergence characteristics and computational efficiency when compared to Galerkin and FE methods [146, 147, 148]. Due to the popularity of this solution method, there are existing solvers, such as bvp4c, which are readily available for solving differential equations in MatLab [149, 150].

bvp4c was developed with the intention of making it easy to solve large classes of BVPs for ODEs in MatLab. The numerical method of bvp4c can be viewed as Collocation method with a C_1 continuous piecewise cubic polynomial used to define a candidate solution. The polynomials evolve iteratively to minimise residuals across the domain and at the boundaries. This is performed by linearisation of the equations and utilises the linear equation solvers of Matlab. Error estimation, the addition and removal of Collocation points to the mesh, and convergence criteria are all based on the residuals of the candidate solution.

Due to the broad range of problems with which it is designed to solve, it exhibits many attributes not always common in alternative BVP solvers: it can solve for a vector of unknown parameters which will allow for the calculation of natural frequencies; it does not require analytical derivatives, and there is no explicit requirement of linearity or wholly real solutions which will be necessary for the final set of PDEs, Eq. (2.5). Although the speed of calculation was not a requirement of its development, bvp4c is able to reduce run time by allowing the user to vectorise the problem and provide analytical Jacobians. There are a few stipulations in how the BVP to be solved by bvp4c is formed:

- As it is possible for BVPs to have more than one solution, bvp4c requires an initial estimate for the desired solution and an initial mesh that reveals its behaviour. Attaining a suitable initial estimate is often a problematic aspect of solving BVPs. However, bvp4c is very robust and able to handle poor initial estimates and meshes and still converge on a solution. It should be noted that the solution converged upon may not be the one desired if the initial estimate is very poor and multiple solutions exist in close proximity to each other.
- The equations that represent the blade's behaviour within the domain, herein referred to as the field equations, must be one-dimensional ODEs. This requires that the PDEs described previously are reduced to ODEs.
- The number of boundary conditions must be equal to that of the order of the field equations to ensure that the problem is well posed. For example, a set of ten first-order equations would require ten boundary conditions.

Each set of PDEs must be processed into a set of first-order equations that conform with the aforementioned stipulations. An example of this process of shown below using the following set of arbitrary differential equations.

$$\begin{aligned} iw_*'' + j\ddot{w}_* + kv_* = 0 \\ iv_*'' + j\ddot{v}_* + kw_* = 0 \end{aligned} \tag{2.6}$$

Firstly, the principle of separation of variables and a harmonic motion is assumed.

$$\begin{aligned} w_*(x,t) = w(x)e^{st} \\ v_*(x,t) = v(x)e^{st} \end{aligned} \tag{2.7}$$

This form of harmonic motion, e^{st}, is chosen over the oft used form, $e^{i\omega t}$, to retain the conventional form of damped frequencies, i.e. the real component pertains to damping/stability.

When substituted into Eq. (2.6), the factor of e^{st} can be dropped to remove the temporal domain from the PDEs resulting in the ODEs below.

$$\begin{aligned} iw'' + js^2 w + kv = 0 \\ iv'' + js^2 v + kw = 0 \end{aligned} \tag{2.8}$$

For the final sub-model, a linearisation process will be performed to form two separate BVPs: a *static* BVP which is used to calculate the statically deformed shape of the blade subject to any applied loading and a *dynamics* BVP which is used to calculate the natural frequencies as described above.

Then the set of remaining higher-order ODEs are reduced into a set of first-order ODEs. The reduction from a set of two second order equations to a set of four first order equations allows them to be represented in a matrix form that can be solved using the aforementioned bvp4c solver.

$$\begin{bmatrix} 0 & i & 0 & 0 \\ -1 & 0 & 0 & 0 \\ 0 & 0 & 0 & i \\ 0 & 0 & -1 & 0 \end{bmatrix} \begin{bmatrix} v \\ v' \\ w \\ w' \end{bmatrix}' = \begin{bmatrix} -js^2 v - kw \\ -v' \\ -js^2 w - kv \\ -w' \end{bmatrix} \rightsquigarrow \begin{bmatrix} v \\ v' \\ w \\ w' \end{bmatrix}' = \begin{bmatrix} 0 & i & 0 & 0 \\ -1 & 0 & 0 & 0 \\ 0 & 0 & 0 & i \\ 0 & 0 & -1 & 0 \end{bmatrix}^{-1} \begin{bmatrix} -js^2 v - kw \\ -v' \\ -js^2 w - kv \\ -w' \end{bmatrix} \tag{2.9}$$

Within the research presented herein, two solutions types are used: a *harmonic* and an *eigenvalue* solution.

The *harmonic* solution calculates the shape and magnitude of the response of the blade to excitation at a prescribed frequency. This is performed by prescribing a value for the frequency and calculating the response shape. As the frequency is prescribed, not a solution parameter, it is the simpler of the two solution types and only has one unique solution which the robustness of the solver will converge to, regardless of the quality of the initial estimate. The response shapes calculated are used to identify the potential presence of natural frequency at the prescribed frequency being analysed as well as provide initial estimates for any *eigenvalue* solutions.

The *eigenvalue* solution is used to calculate the natural frequencies and corresponding mode shapes of the blade in the form of an eigenvalue problem. This solution utilises the ability of bvp4c to solve for unknown parameters and uses it to calculate a natural frequency of the blade in question. This solution type introduces an additional unknown to the solver and must, therefore, be accompanied by an additional boundary condition. This additional boundary condition

will consist of a normalisation condition for the mode shapes calculated. As a blade will have many natural frequencies, it is imperative that the initial estimate be very good, otherwise, the solver may converge on a different natural frequency to the one targeted. This initial estimate used is that from the *harmonic* solution. The presence of aerodynamic loading in the final sub-model will likely induce aerodynamic damping. This will be represented in the eigenvalue problem as a complex eigenvalue where the composition of real and imaginary components will provide the undamped natural frequency and damping ratio.

Additionally, for the calculation of the static deformed shape of the blade, a special case of the *harmonic* analysis is used. As there is no natural frequency to be solved for, an *eigenvalue* solution is not possible; therefore, a *harmonic* is used. The static response is independent of time; therefore, will be no frequency terms present in this analysis, i.e. no frequency to be prescribed as with the previously described *harmonic* solution.

2.3.2 Algorithmic procedure for parametric sweeps

The concept being investigated is to use applied compressive loading to alter the natural frequencies of a variable speed rotor blade. Therefore, a procedure to calculate the natural frequencies of a rotor blade across a range of operating conditions (rotor speeds and compressive loads) is required.

The procedure to calculate these natural frequencies over a range of operating conditions (rotor speed and compressive load), as shown in Fig. 2.3, uses two parts.

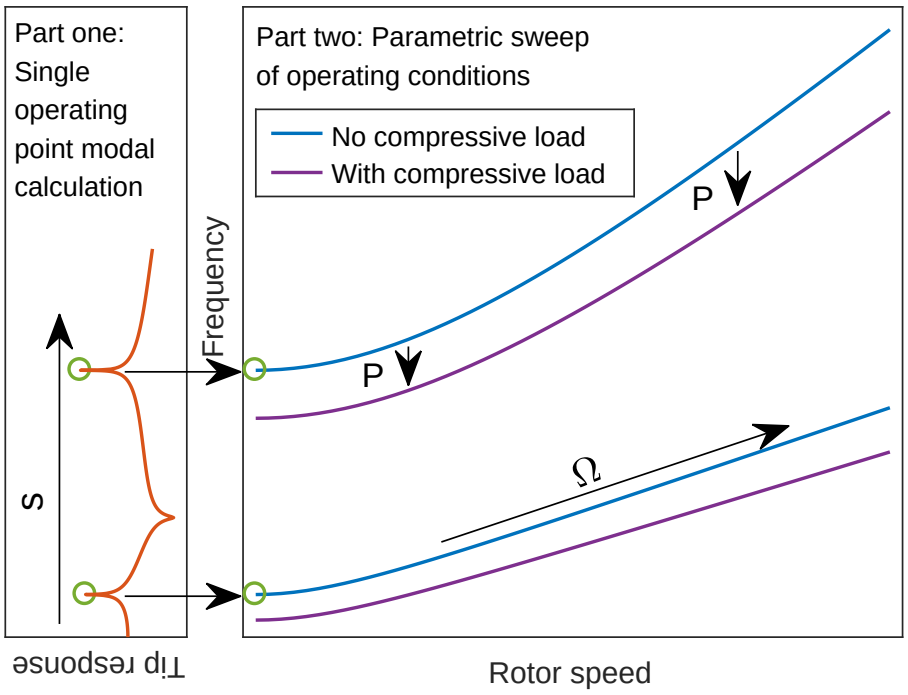

Figure 2.3: Schematic of model calculation process and results

In the first part, the natural frequencies of the desired modes are obtained for a single set of operating conditions. Once the natural frequencies of the desired modes have been obtained, the second part incrementally sweeps through the range of rotor speeds and compressive loads to calculate the natural frequencies.

2.3.2.1 Single operating point modal calculation

To calculate the natural frequencies at a single operating point, a combination of harmonic and eigenvalue analyses are used to identify potential modes across a range of prescribed frequencies and calculate the natural frequencies of the desired modes, as observed in Fig. 2.3. The process for this identification and calculation is shown below.

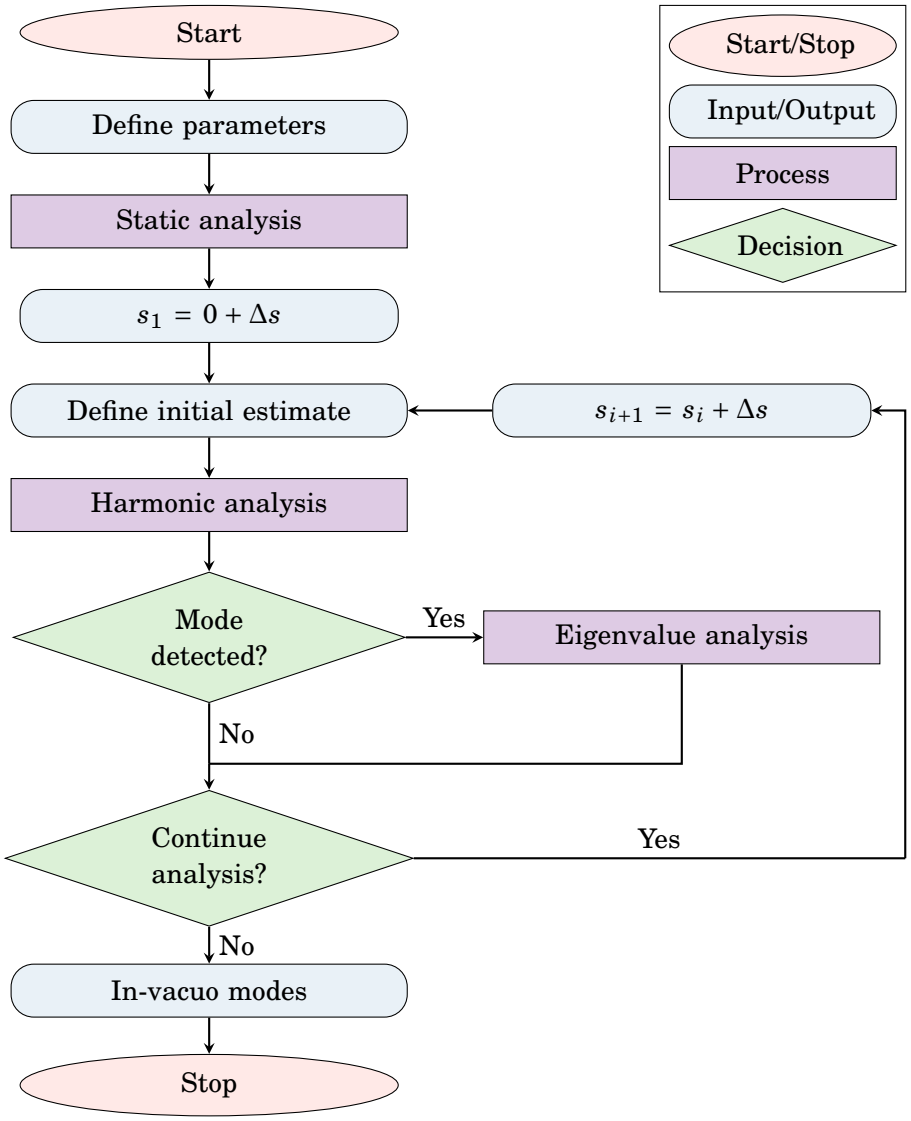

Figure 2.4: Process to calculate eigenvalues of rotor blade at a single value of rotor speed and compressive load.

Firstly, the blade parameters and operating conditions, such as EI_y,R,Ω,P, are defined. For this component of the algorithmic procedure, if aerodynamic loading is present, air density, ρ_∞ is set to zero. When using the sub-model that incorporates geometric nonlinearities, a static analysis is performed to calculate the static deformation at the defined operating conditions. For the other two sub-models, this is omitted.

A prescribed frequency, s, close to zero is used to initialise the frequency sweep and a harmonic analysis is then performed to calculate the response of the blade at this frequency. For the first analysis, the initial estimate for the response shape is zero. Due to the robustness of bvp4c to poor initial estimate and the simplicity of the response shape solution at very low frequencies, the correct solution is acquired.

The response shape is then assessed to identify whether the current prescribed frequency is close to a natural frequency. If a potential mode has been identified then an eigenvalue analysis is performed to calculate the exact natural frequency. For this eigenvalue analysis, the prescribed frequency and corresponding response shape that identified the proximity of a mode are used as the initial estimate.

If the desired number of modes have been obtained or the specified range of frequencies has been evaluated the process will stop. However, if this is not the case, then the prescribed frequency is incrementally increased and the harmonic analysis is repeated. However, for the second harmonic analysis onwards, the solution of the previous iteration is used as the initial estimate to ensure quick and correct conversion despite the increasing complexity of the response shape at higher frequencies.

The proximity of the prescribed frequency to a mode is identified by the presence of either one of two different conditions: a *resonance* condition and an *orthogonality* condition.

The resonance condition identifies resonance by examining the response shape for the previous iterations and assessing whether the response, in any of the directions of motion considered, is maximal. This condition is evaluated at the tip of the blade as this location will never be a node, for any mode, ensuring that all modes may be detected. This technique is similar to that used to identify resonance experimentally and is therefore very robust.

The orthogonality condition used to identify the proximity of the prescribed frequency to a natural frequency assesses the orthogonality of the response shape with respect to a known mode shape. Theoretically, the mode shapes of two modes will be orthogonal which can be expressed mathematically as having a dot product of zero [1]. However, the response shapes will never be exact mode shapes unless the prescribed frequency exactly coincides with a natural frequency. Therefore, the orthogonality condition identifies a minimum in the magnitude of the value of the orthogonality condition from the previous iterations. This will identify when the prescribed frequency is closest to that of a natural frequency.

The equation used to evaluate the orthogonality, Eq. (2.10), was derived by *Murthy* [1] based

on the equations of *Houbolt and Brooks* [137].

$$\Gamma = \int_0^R m\Big[k_m^2\Phi_1\phi_i + W_1 w_i + V_1 v_i - \underline{e\sin\theta\big(\Phi_1 v_i + \phi_i V_1\big)} + \underline{e\cos\theta\big(\Phi_1 w_i + \phi_i W_1\big)}\Big]dx \tag{2.10}$$

This equation includes the most significant effects included in [137] such as twist and mass-elastic axes offset but does omit the offset between the centre of area and the elastic axes. This simplification is likely to exhibit only minor changes in the result. As the purpose of this condition is only to identify the proximity of a natural frequency, these discrepancies are considered acceptable.

This condition is not as robust as the first condition as it can only be employed once the first mode has been calculated to be used as a reference. However, its ability to capture the effects of coupling will help ensure all mode shapes are identified even when significant inter motion coupling is observed.

The reason that air density is set to zero in this initial analysis is two-fold. Firstly, it ensures that there is no aerodynamic damping of the natural frequencies. This ensures sharp resonant peaks which will improve the effectiveness of the first mode identification condition as well as ensure the validity of the orthogonality equation used in the second mode identification condition. Additionally, it ensures that the eigenvalue analysis solutions calculated correlate better with the initial estimate used for their calculation. This ensures better and quicker convergence with less chance of incorrectly omitting a mode from the analysis. Secondly, it removes aerodynamic loads which ensures that the static deformation, and subsequently geometric nonlinearity effects, are small. This aids the validity of the aforementioned orthogonality condition.

An example of how these two separate conditions work and complement each other is shown in Fig. 2.5.

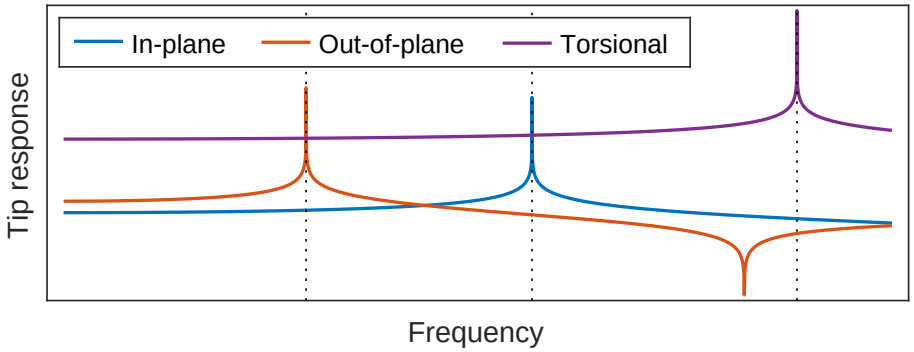

(a) Resonance condition

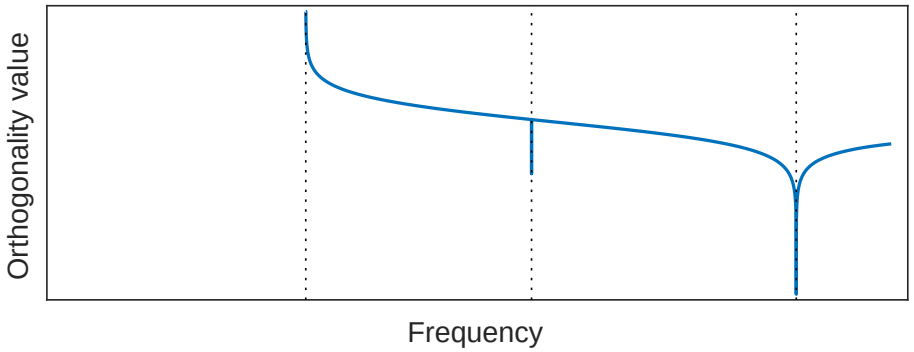

(b) Orthogonality condition

Figure 2.5: Diagram of modal presence condition operation.

It can be seen in Fig. 2.5a that it is necessary to monitor the in-plane, out-of-plane and torsional response. If any of these motions were overlooked then the mode associated with that motion would not be detected or captured in the model. Unfortunately, the orthogonality condition is not present until the first mode has been identified using the resonance condition. Hereafter, the orthogonality indicates a minimum that identifies all subsequent modes with the use of a single metric, regardless of the orientation of the mode.

There is one additional step that is required for the calculation of the modal properties at a single operating point which is the inclusion of the aerodynamic loads. This step is only required for the final sub-model which includes aerodynamic loading. This step starts from the in-vacuo set of modal properties previously described. The air density value is incrementally increased from zero to the final prescribed values. For each iteration, the static deformation is calculated to account for the change in static deformation due to the changing aerodynamic loads and subsequently, the natural frequency for each mode is calculated accounting for the updated static deformation and aerodynamic loads. For each of the static analysis and eigenvalue analyses, the solution from the previous iteration is used as the initial estimate.

2.3.2.2 Parametric sweep of operating conditions

Once the natural frequencies of the desired modes have been calculated for a single set of operating conditions, they are used to initiate the parametric sweep procedure, as seen in Fig. 2.3. The resulting comprehensive set of natural frequencies for each combination of rotor speed and compressive load in the prescribed range can then be used to evaluate the ability of compressive loading to avoid resonance across a range of rotor speeds. This process consists of a parametric sweep of the prescribed range of rotor speeds nested within a sweep of compressive loads as shown below.

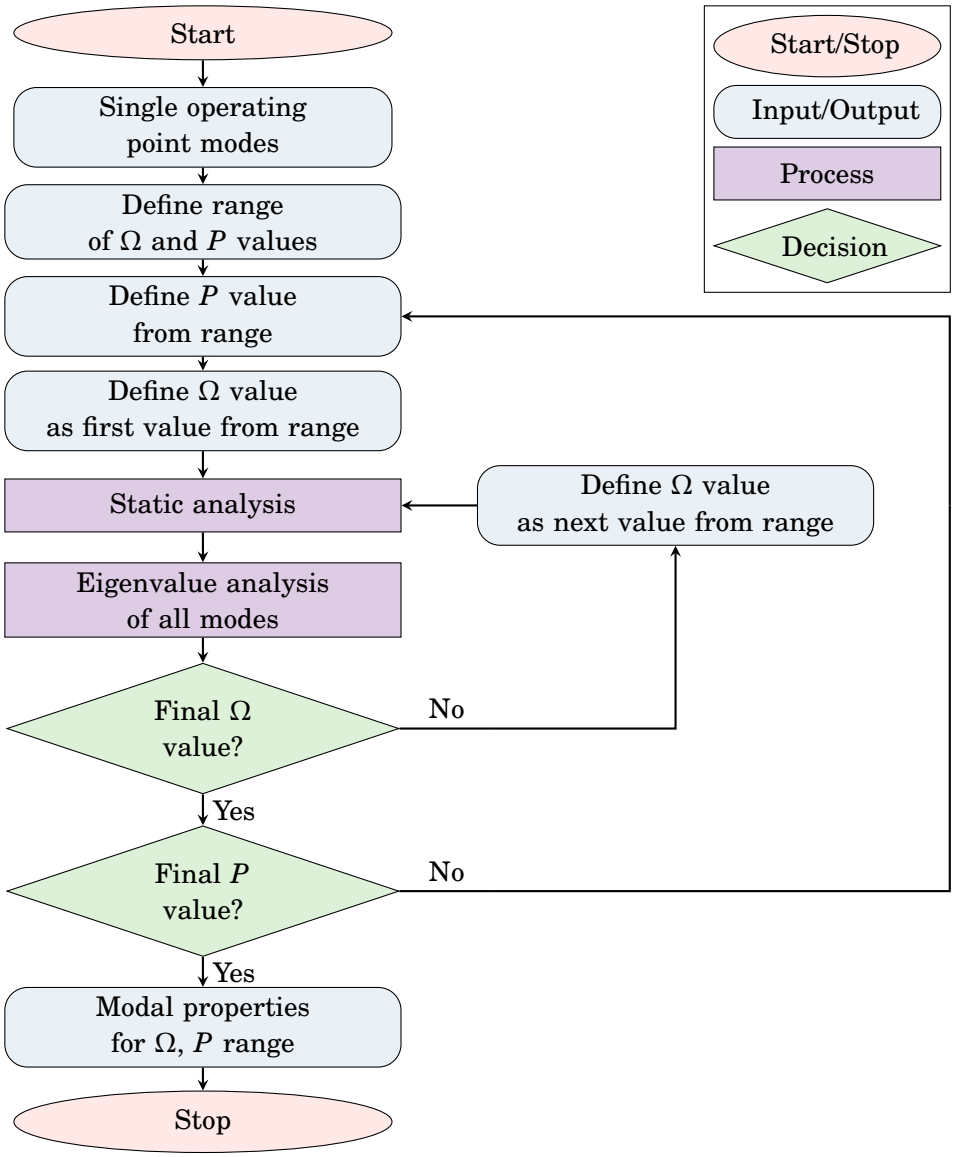

Figure 2.6: Process to calculate the eigenvalues of the rotor blade for each value of rotor speed and compressive load.

As previously mentioned, this process is initialised by the modal properties for a single operating point as calculated in Section 2.3.2.1. The desired range of rotor speeds and compressive loads are defined and the present value for rotor speed and compressive load are defined as the lowest value from their respective ranges.

A static analysis is then performed, if the final sub-model is being used, to calculate the static deformation of the blade in the current operating conditions. Subsequently, an eigenvalue analysis is performed to calculate the natural frequencies of each of the desired modes. For each mode, the solution from the single operating point analysis is used as the initial estimate.

The rotor speed is then incrementally increased and the static analysis and subsequent eigenvalue analyses are repeated. In this case, the solution from the previous rotor speed is used as the initial estimate.

Once the full range of rotor speeds have been evaluated for the initial value of the compressive load, the compressive load itself is incrementally increased and the previous sweep of rotor speeds is repeated. For this sweep of compressive loads, the initial estimate for each mode at each rotor speed is provided by the solution from the previous compressive load iteration.

Once each of the modes has been calculated for the full range of rotor speeds at each compressive load the procedure is finished and the set of natural frequencies can be analysed.

Whilst researching mode shape tracking criterion, *Mogenier et al* [151] highlighted that the complexity of gyroscopic systems emanates from veering or crossing phenomena. Therefore, unlike the aforementioned sweep of air density, it is expected that a sweep of rotor speed or compressive loading values will incur significant interactions between the different modes. Therefore, relatively fine increments of rotor speeds may be required. Consequently, after each iteration of rotor speed or compressive load has completed, the results are checked to ensure that the full complement of unique solutions remain present. If this is not the case, it will likely be due to the convergence of some of the solutions due to their similarity. To rectify this, iterations which have converged will be removed and an intermediate value of rotor speed or compressive will be added. This will reduce the increment of rotor speed or compressive load in the region with significant coupling.

The algorithmic procedure detailed in the previous two sections allows the PDEs and numerical solver detailed in Sections 2.2 and 2.3.1 to be used to identify a specific set of natural frequencies at any single combination of rotor speed and compressive load. The natural frequencies identified and calculated at this operating point are then used to initialise a parametric sweep to track the evolution of these modes with changing rotor speed and compressive loads. The result of this procedure is a comprehensive set of natural frequencies for each possible combination of rotor speed and compressive load with the prescribed range which can subsequently be used to evaluate the capability of compressive loading to avoid resonance in variable speed rotors.

CHAPTER 3

INITIAL FEASIBILITY ANALYSIS

To demonstrate the capability of the proposed concept, a beam model capable of capturing the in-plane and out-of-plane dynamic behaviour of a compressed rotor blade is developed. The model is compared with an experimental study and a subsequent assessment of the modelling methodology of the compressive load is made. A case study is then used to assess the change in frequency that is achievable, without encountering buckling instabilities, on an full-scale example. A further study is performed to demonstrate the correlation between modal tuning achieved via compressive loading with a reduction in vibratory loads at resonant conditions during forward flight.

3.1 In-vacuo bending-bending model

To investigate the effects of compressive loading on the in-plane and out-of-plane dynamic properties of a rotor blade, the first sub-model outlined in the previous chapter is developed. The model captures the effects of: bending stiffness due to the shape of the blade and its material properties; inertial forces due to the in-plane and out-of-plane motion of the blade; and internal tension in the blade due to centrifugal loading and applied compressive loads.

3.1.1 Compressive load

The compressive load is applied on the elastic axis at the tip of the blade directed towards the root as this is a likely attachment point for any actuation system that would be used to create the compressive loads. To incorporate this load into the model, it is separated into a spanwise component in the x direction and an in-plane and out-of-plane component in the y and z directions, respectively. This approach was successfully used by *Nudehi et al* [114] when implementing a

similar model. The force is decomposed into components in the x, y and z directions, as shown in Fig. 3.1.

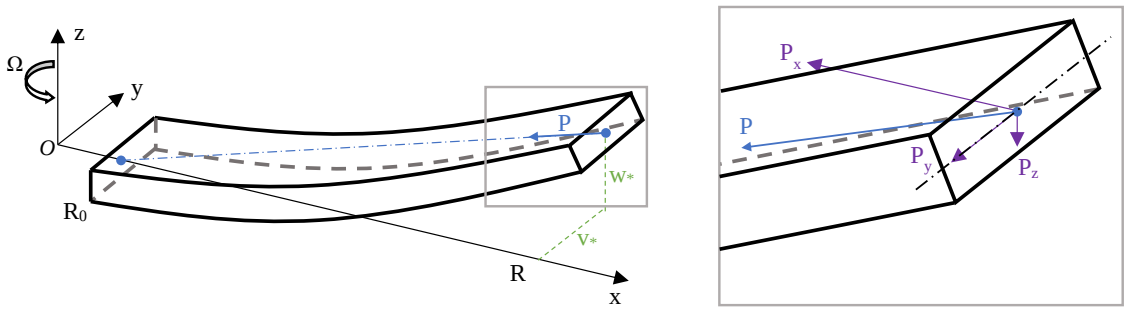

Figure 3.1: Schematic of compressive force decomposition

The geometry of the beam and its deformations can then be used to calculate the orientation of the load and the subsequent component of the applied force in each direction as shown below in Eq. (3.1).

$$\begin{aligned} P_x &= P\frac{R-R_0}{\sqrt{(R-R_0)^2+v_*(R)^2+w_*(R)^2}} \\ P_y &= P\frac{v_*(R)}{\sqrt{(R-R_0)^2+v_*(R)^2+w_*(R)^2}} \\ P_z &= P\frac{w_*(R)}{\sqrt{(R-R_0)^2+v_*(R)^2+w_*(R)^2}} \end{aligned} \tag{3.1}$$

To allow these loads to be incorporated into the linear field equations and boundary conditions, it is necessary to linearise these loads. This is performed using a Taylor expansion about v_* and w_* up to the second term, the results of which are shown in Eq. (3.2).

$$P_x = P \tag{3.2a}$$

$$P_y = P\frac{v_*(R)}{(R-R_0)} \tag{3.2b}$$

$$P_z = P\frac{w_*(R)}{(R-R_0)} \tag{3.2c}$$

As $(R-R_0) \gg v_*(R)$ and $(R-R_0) \gg w_*(R)$ the change in orientation of the load is minor, hence Eq. (3.2a) is expected. Furthermore, it can also be seen that Eqs. (3.2b) and (3.2c) take the form of linear springs of stiffness $\frac{P}{(R-R_0)}$ as was observed in [114].

3.1.2 Field equation

The equations of motion that represent the motion of the blade within the domain are a pair of linear non-homogenous coupled Partial Differential Equations (PDEs); one for each of the motions to be captured. Each of the PDEs contains just one state (translational or rotational deformation in the x,y,z axes), v_* and w_* respectively, and is a function of one spatial domain, x and one temporal domain, t. These equations are shown below in Eq. (3.3).

$$-\left(Tw_*'\right)' + \left[EI_y w_*''\right]'' + m\ddot{w}_* = 0 \tag{3.3a}$$

$$-\left(Tv_*'\right)' + \left[EI_z v_*''\right]'' + m\ddot{v}_* - m\Omega^2 v_* = 0 \tag{3.3b}$$

Where internal tension is defined as a combination of centrifugal loading and applied compressive force in the x direction, shown below in Eq. (3.4).

$$T = \int_x^R \Omega^2 m\hat{x}d\hat{x} - P_x = \frac{1}{2}\Omega^2 m\left(R^2 - x^2\right) - P \tag{3.4}$$

As outlined in Chapter 2, the principle of separation of variables and an assumed harmonic response is employed with the assumed solution taking the form shown in Eq. (3.5).

$$\begin{aligned} v_*(x,t) &= v(x)e^{st} \\ w_*(x,t) &= w(x)e^{st} \end{aligned} \tag{3.5}$$

Once the assumed solution was substituted into Eq. (3.3), the terms that are linearly proportional to e^{st} are gathered to form a set of Ordinary Differential Equations (ODEs) that represent the oscillatory shape of the beam. This process removes the temporal domain ensuring that the equations are suitably formatted for the numerical solver.

$$
\begin{aligned}
-\left(Tw'\right)' + \left[EI_y w''\right]'' + m\ddot{w} = 0 \\
-\left(Tv'\right)' + \left[EI_z v''\right]'' + m\ddot{v} - m\Omega^2 v = 0
\end{aligned}
\tag{3.6}
$$

Finally, these equations were converted from their current form, two fourth-order equations, to a set of eight first-order equations as exemplified in Section 2.3.1. This ensures that the format requirements of the numerical solver described in Section 2.3.1 are met.

3.1.3 Boundary conditions

Cantilevered boundary conditions are enforced to imitate the hub configuration of a bearingless rotor. The field equations for the beam consist of two fourth-order equations which necessitate eight boundary conditions to ensure the problem is properly posed. Half of these conditions will enforce a fixed root and the other half shall enforce a free tip, subject to the augmentation due to the applied compressive load.

The fixed boundary condition at the root consists of constraining the displacements and angles of the beam to zero, as seen in Eq. (3.7).

$$
\begin{aligned}
v_* &= 0 \\
w_* &= 0 \\
v'_* &= 0 \\
w'_* &= 0
\end{aligned}
\tag{3.7}
$$

The free boundary conditions at the tip for a traditional cantilevered beam consists of constraining forces and moment to zero. However, due to the application of the applied compressive load, the force and moment equilibria are enforced as a balance of internal loads within the beam and the externally applied compressive load as seen in Fig. 3.2 and Eq. (3.8).

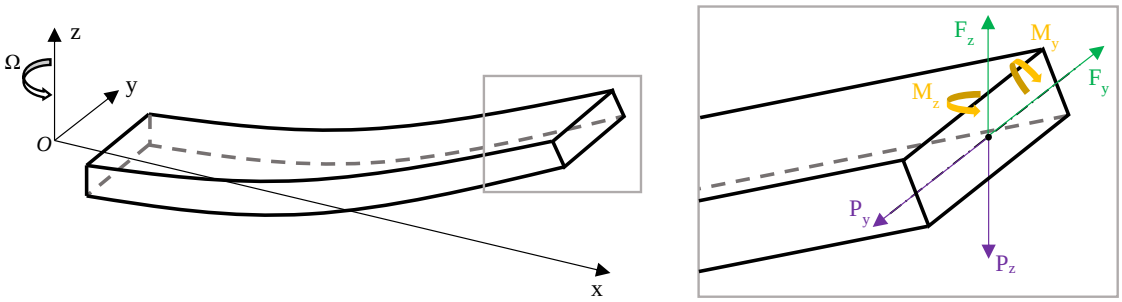

Figure 3.2: Schematic of boundary conditions at the blade tip.

$$\begin{aligned} M_y &= \underline{M_0 e^{st}} \\ M_z &= \underline{M_0 e^{st}} \\ F_y &= \underline{\underline{-P_y}} \\ F_z &= \underline{\underline{-P_z}} \end{aligned} \tag{3.8}$$

The singly underlined terms in Eq. (3.8) represent the harmonically applied moments that provide the excitation for the *harmonic* analyses. The doubly underlined terms are the additional terms present due to the applied compressive load that would not be present in a traditional cantilevered boundary condition. The internal loads within the beam are defined as follows.

$$\begin{aligned} M_y &= EI_y w_*'' \\ M_z &= EI_z v_*'' \\ F_y &= \underline{Tv_*'} - M_z' \\ F_z &= \underline{Tw_*'} - M_y' \end{aligned} \tag{3.9}$$

The underlined terms in Eq. (3.9) denote terms in the internal loads which would not be present in a rotor blade without compressive loading. Without compressive loading, the internal tension in the blade would be solely due to centrifugal loading which is 0 at the tip.

Once the assumed motion of the blade, as stated in Eq. (3.5), and Eqs. (3.2) and (3.9) are substituted into Eqs. (3.7) and (3.8) the final boundary conditions are formed, as shown in Eq. (3.10).

$$
\begin{aligned}
v(R_0) &= 0 \\
w(R_0) &= 0 \\
v'(R_0) &= 0 \\
w'(R_0) &= 0 \\
EI_y w''(R) &= M_0 \\
EI_z v''(R) &= M_0 \\
Tv'(R) - M_z' + P\frac{v(R)}{(R-R_0)} &= 0 \\
Tw'(R) - M_y' + P\frac{w(R)}{(R-R_0)} &= 0
\end{aligned}
\tag{3.10}
$$

3.2 Non-rotating study

The core principle of the concept is the ability to use an applied compressive load to alter the dynamic properties of a rotor blade. Therefore, the first component of this feasibility analysis is to experimentally demonstrate the ability of compressive loading to alter a blade's dynamics. A supporting study is subsequently performed to verify and validate the modelling methodology and implementation of the compressive load.

3.2.1 Experimental configuration

An experimental test rig to assess the impact of compressive loading on a rotor blade for resonance avoidance in variable speed rotors was first presented in [152]. In collaboration with the SABRE project, a test rig was developed that was able to more repeatably and accurately capture the natural frequencies of the test piece than the configuration used in [152] as well as having the additional capability to capture the accompanying mode shapes. This rig was used by the SABRE project to evaluate the impact of compressive loading on the dynamic properties of a beam with a closed cross-section [143] and by the present author, in collaboration with the SABRE project, to evaluate an open cross-section [153].

The experimental test rig devised for these bench-top experiments, seen in Fig. 3.4, consists of a number of components. A prismatic beam, clamped at one end, is used to represent a rotor blade. A tendon is used to apply the compressive force to the tip of the blade. A shaker, located toward the root, is used to provide the excitation and an accelerometer located near the tip is used to record the response of the blade.

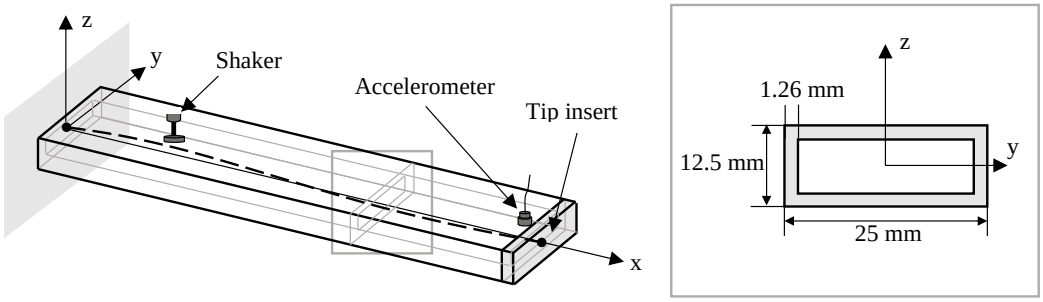

Figure 3.3: Experimental configuration diagram used for non-rotating demonstration of the influence of compressive loading on the dynamic properties of a beam.

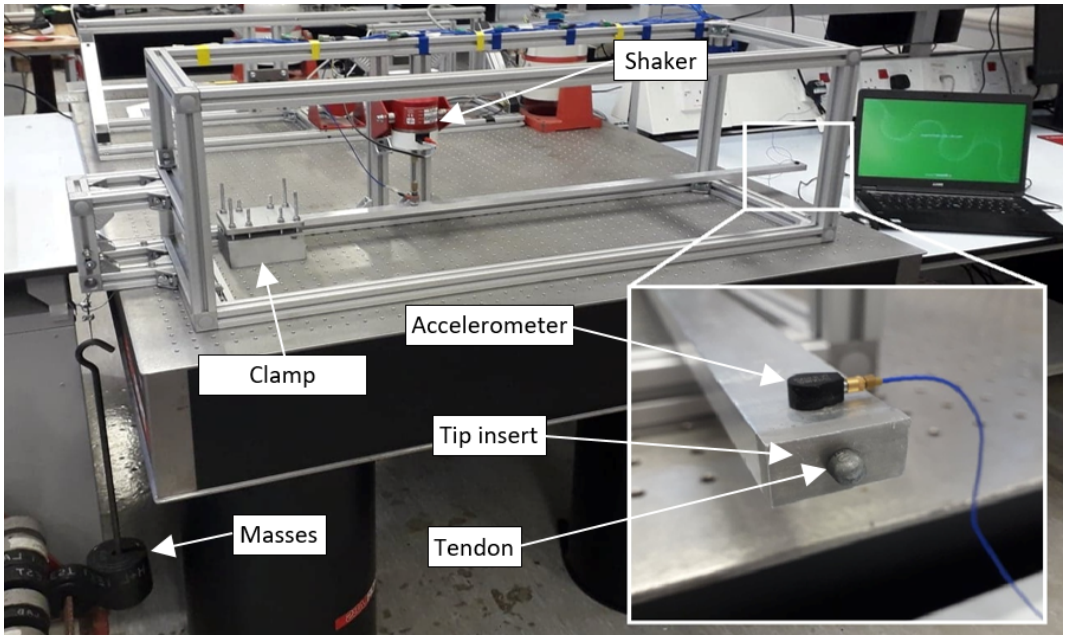

Figure 3.4: Experimental configuration used for non-rotating demonstration of the influence of compressive loading on the dynamic properties of a beam.

As the focus of this research is compressive loading, ideally, a purely compressive load would be applied. However, this idealisation is not possible to achieve experimentally due to the inevitable presence of a system to apply the compressive load. In this case, a tensioned tendon was chosen due to its similarities to a potential actuation system for this concept.

A prismatic beam with low bending rigidity is chosen to ensure an observable change in frequency within the achievable loading range. The beam is rigidly clamped at the root and free at the tip to replicate a bearingless hub configuration. The tendon is attached to a plug-type insert secured at the tip of the beam and passes freely inside the beam towards the clamp at the root. The tendon continues through the clamp, over a pulley and is attached to a mass hanger. The tension in the tendon, and hence the compressive load applied to the beam, is controlled by

varying the amount of mass on the platform.

The beam is subsequently excited by providing filtered, pseudo-random, excitation via an electromagnetic modal shaker located approximately one quarter of the way along the beam at the middle of the cross section. The response data was collected from a single-axis piezoelectric accelerometers located at the tip of the beam. The input force and response data were used to estimate frequency response functions using the H_v-estimator [154]. Subsequently, natural frequencies were estimated using the Least-Square Complex Frequency estimator [155]. For the calculation of mode shapes, excitation was provided using an impact hammer at a series of locations along the span of the beam.

The properties of the beam-tendon system were obtained either by direct measurement or, in the case of the stiffness values, calculated from the geometry using typical material values. These values were subsequently updated to improve the correlation with the baseline beam model without compressive loading or tip insert. These parameter values, as provided in [143], are summarised in Table 3.1.

Table 3.1: Beam properties for doubly-symmetric experiment

Property	Value
Radius, R [m]	1
Mass distribution of the blade, m [kg m^{-1}]	0.2929
Mass distribution of the tendon, m_t [kg m^{-1}]	0.0125
Tip mass, M_t [kg]	0.0062
Out-of-plane bending rigidity, EI_y [Nm^2]	157.79
In-plane bending rigidity, EI_z [Nm^2]	517.33

The results presented herein are for the closed cross-section beam presented in [143]. They consist of: the natural frequencies and mode shapes of the beam without the presence of the tip insert or applied compressive loading; the natural frequencies of the beam with the presence of the tip insert but without any applied compressive loading; and the natural frequencies of the coupled beam-tendon system subject to loading from 2 kg to 50 kg in 2 kg increments. These results will demonstrate the ability of compressive loading to alter the dynamic properties of a rotor blade and be used to validate a model of a coupled beam-tendon system which shall be used to evaluate the compressive loading methodology detailed in Section 3.1.1

3.2.2 Model alteration to include tendon

To capture the behaviours in the experimental configuration correctly, a few modifications to the model described in Section 3.1 are required which replicates the model created in [152]. This comprises of setting the rotor speed to zero, as rotation is not present in the experiment, as well as including the dynamics of the tendon and the inertial effects of the tip insert. Additionally, the presence of the tendon invalidates the orthogonality condition equation used in Section 2.3.2.1,

which was developed without the presence of a tendon, so a new one is required.

3.2.2.1 Field equations

In addition to the beam, the tendon is represented using a PDE, known as the wave equation [156], that is used to model the vibration of strings. This equation captures the effects of the inertia of the tendon and its internal tension. However, it does not capture the effect of bending stiffness but due to the small cross-section of the tendon, the effect of this omission is negligible. The equations are formulated as linear, homogenous, PDEs that each have one state, w_{t*} and v_{t*}, and is a function of one spatial domain, x and one temporal domain, t, as seen in Eq. (3.11).

$$-\left(T_t w'_{t*}\right)' + m_t \ddot{w}_{t*} = 0 \tag{3.11a}$$

$$-\left(T_t v'_{t*}\right)' + m_t \ddot{v}_{t*} = 0 \tag{3.11b}$$

As this version of the model is intended to represent the experimental configuration so that it can be used to validate the compressive loading methodology, the tension in the beam and tendon are solely due to the applied compressive load and there are no centrifugal loads considered. Therefore, the tension terms are defined as shown in Eq. (3.12).

$$\begin{aligned} T &= -P_x \\ T_t &= P_x \end{aligned} \tag{3.12}$$

The tendon is also subject to the same assumed harmonic motion of the blade as shown below.

$$\begin{aligned} w_{t*}(x,t) &= w_t(x)e^{st} \\ v_{t*}(x,t) &= v_t(x)e^{st} \end{aligned} \tag{3.13}$$

Once these equations are defined, they are processed identically to that of the model described in Section 3.1. The result of which is four uncoupled ODE as shown in Eq. (3.14).

$$
\begin{aligned}
-\left(-Pw'\right)' + EI_y w^{iv} + ms^2 w = 0 \\
\left(-Pw_t'\right)' + m_t s^2 w_t = 0 \\
-\left(-Pv'\right)' + EI_z v^{iv} + ms^2 v = 0 \\
\left(-Pv_t'\right)' + m_t s^2 v_t = 0
\end{aligned}
\tag{3.14}
$$

3.2.2.2 Boundary conditions

The additional presence of the tendon has a significant impact on the boundary conditions originally defined in Eq. (3.10). As the tendon itself is being modelled, there is no requirement to include an externally applied point force as defined in Section 3.1.1. However, it is necessary to include the influence of the tension in the tendon, which performs a very similar role to that of the aforementioned point force. Additionally, there is the requirement to model the inertial effects of the tip insert used to attach the tendon to the tip of the beam. The updated set of boundary conditions are shown below.

$$
\begin{aligned}
v(R_0) = 0 \\
w(R_0) = 0 \\
v'(R_0) = 0 \\
w'(R_0) = 0 \\
EI_y w''(R) = M_0 \\
EI_z v''(R) = M_0 \\
-Pv'(R) - M_z' + \underline{Pv_t'(R)} + \underline{\underline{M_t s^2 v(R)}} = 0 \\
-Pw'(R) - M_y' + \underline{Pw_t'(R)} + \underline{\underline{M_t s^2 w(R)}} = 0
\end{aligned}
\tag{3.15}
$$

It can be seen that the required alteration only impacts the force equilibria. The singly underlined terms pertain to the tension present in the tendon. This is analogous to the point force used previously and can be seen to take a similar form; the difference being that the force is orientated with the tangent of the tendon at the tip as opposed to directed towards the root of the blade. Additionally, the doubly underlined terms represent the inertial forces of the tip insert.

The addition of the two second-order equations also necessitates an additional four boundary conditions. These conditions ensure that the tendon and beam remain coincident at the root and the tip by enforcing that their displacements at these locations be equal to one another, as defined below.

$$\begin{aligned} w_t(R_0) &= w(R_0) \\ w_t(R) &= w(R) \\ v_t(R_0) &= v(R_0) \\ v_t(R) &= v(R) \end{aligned} \tag{3.16}$$

3.2.2.3 Orthogonality

Due to the presence of the tendon, Eq. (2.10) is no longer an applicable orthogonality condition for this model. Therefore, following the same calculation procedure as [1], a new orthogonality condition is derived for the coupled beam-tendon configuration. The governing ODEs are written in terms of the first and i^{th} mode and multiplied by the i^{th} and first mode respectively. The difference between these two sets of equations is integrated along the length of the beam and the non-trivial solution becomes the new orthogonality condition. The full derivation of this condition is detailed in Appendix B and the resulting condition is shown below.

$$\Gamma = m\int_{R_0}^{R}\Big[W_1W_i + V_1V_i\Big]dx + m_t\int_{R_0}^{R}\Big[W_{t1}W_{ti} + V_{t1}V_{ti}\Big]dx \tag{3.17}$$

This equation can now be used to identify the presence of modes for the current beam-tendon model.

3.2.3 Model-experiment comparison

Having developed the model detailed in Sections 3.1 and 3.2.2, its results can then be compared with the experimental data to give confidence in its validity. Subsequently, this model is used to assess the chosen point load modelling methodology detailed in Section 3.1.1.

The experimental results discussed herein were obtained by the SABRE project [143] using the aforementioned experimental test rig that was developed by the present author in collaboration with the SABRE project.

The experimentally identified natural frequencies for the system with no tendon but with and without a tip insert are shown in Fig. 3.7 alongside the equivalent natural frequencies calculated using the model.

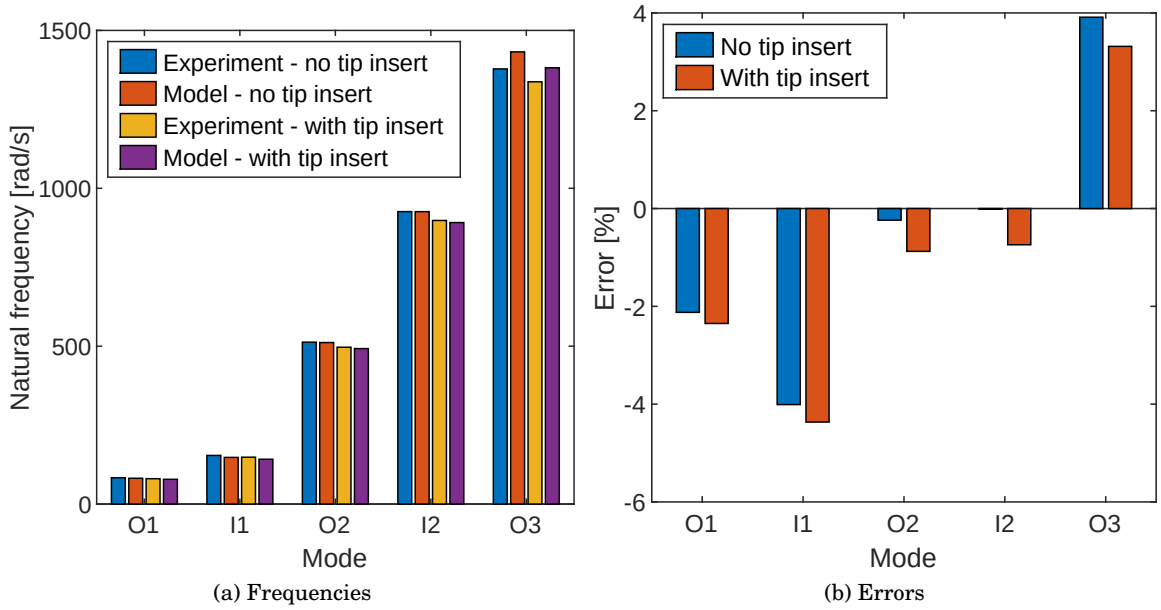

(a) Frequencies (b) Errors

Figure 3.5: Comparison of natural frequencies from the experiment and the model without the presence of the tendon to verify the underlying beam model.

It can be seen in Fig. 3.5a that the experimental beam has five vibration modes within the frequency range examined: two in-plane modes (I1-I2) and three out-of-plane modes (O1-O3).

The errors values for these frequencies, shown in Fig. 3.5b, are small, <5 %, which gives confidence that the model has been correctly developed and implemented. It can be seen that there is a trend for the model to underpredict natural frequencies of the first mode and overpredict those of the third mode which may be due to the inability of the experimental to provide perfectly rigid root attachment which will be discussed in more detail.

In addition to the natural frequencies, the experimentally calculated mode shapes are quantitatively compared to those calculated from the model to ensure the model is correctly calculating the mode shapes as well as the natural frequencies. This quantification of this comparison is performed using the Modal Assurance Criterion (MAC), a metric that quantitatively compares the similarity of mode shapes. The definition of the MAC used for this research is shown below [157].

$$\frac{\left|W_i W_j^* + V_i V_j^* + \Phi_i \Phi_j^*\right|^2}{\left(W_i W_i^* + V_i V_i^* + \Phi_i \Phi_i^*\right)\left(W_j W_j^* + V_j V_j^* + \Phi_j \Phi_j^*\right)} \tag{3.18}$$

These mode shapes, and their associated MAC values are shown in Fig. 3.6.

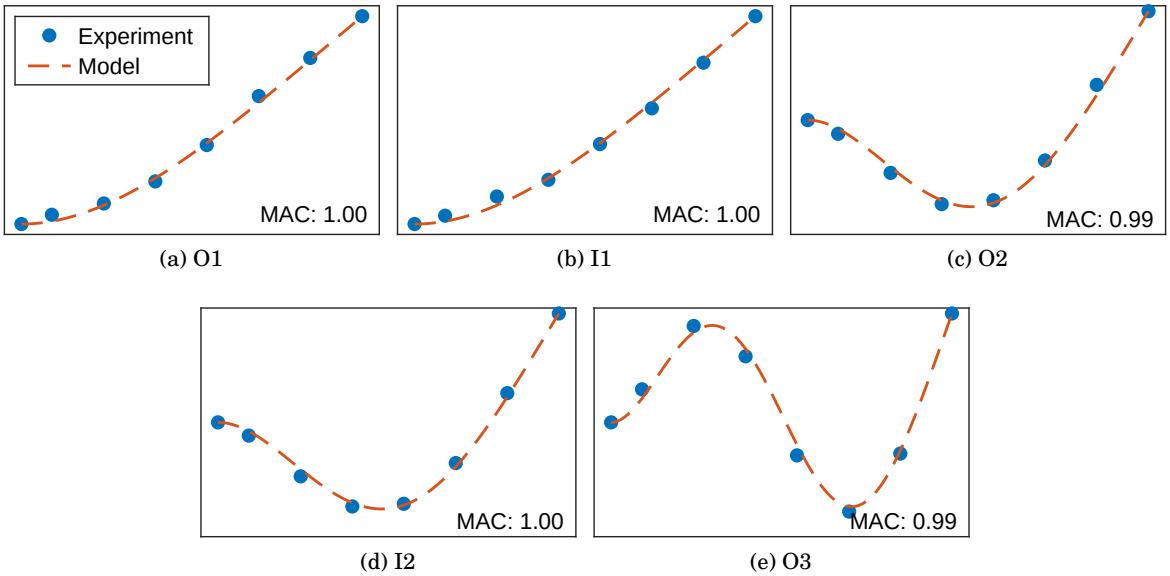

(a) O1 (b) I1 (c) O2

(d) I2 (e) O3

Figure 3.6: Comparison of mode shapes from the experiment and the model without the presence of a tendon to verify the underlying beam model.

As can be seen from the visual correlation between the shapes, and the corresponding MAC values, the agreement is excellent. This serves to further validate the underlying beam model, demonstrating its ability to correctly calculate mode shapes, as well as natural frequencies.

One likely cause of the discrepancies observed is the boundary conditions in the experiment. Whilst a fully fixed condition was desired at the root of the beam it is unlikely that this was perfectly achieved; resulting in a boundary condition that was not infinitely stiff. This effective softening would reduce the frequencies of all modes in the experiment. Due to the comparatively larger second and third derivatives of mode shapes at the root in the higher-order modes, their frequencies would have reduced more. Due to the updating of the beam parameters to improve the experimental correlation in [143], the stiffness values would have been increased to compensate for this. This effect can be observed in Eq. (3.18) as a larger deformation near the root observed in the experiment than the model.

Once the underlying beam model had been validated the tendon and compressive load could then be included. The experimentally calculated natural frequencies for the system with a compressive load applied using the tendon are shown in Fig. 3.7. The experimental frequencies for the case with tip mass but no tendon, as introduced in Fig. 3.5a, are also shown for context.

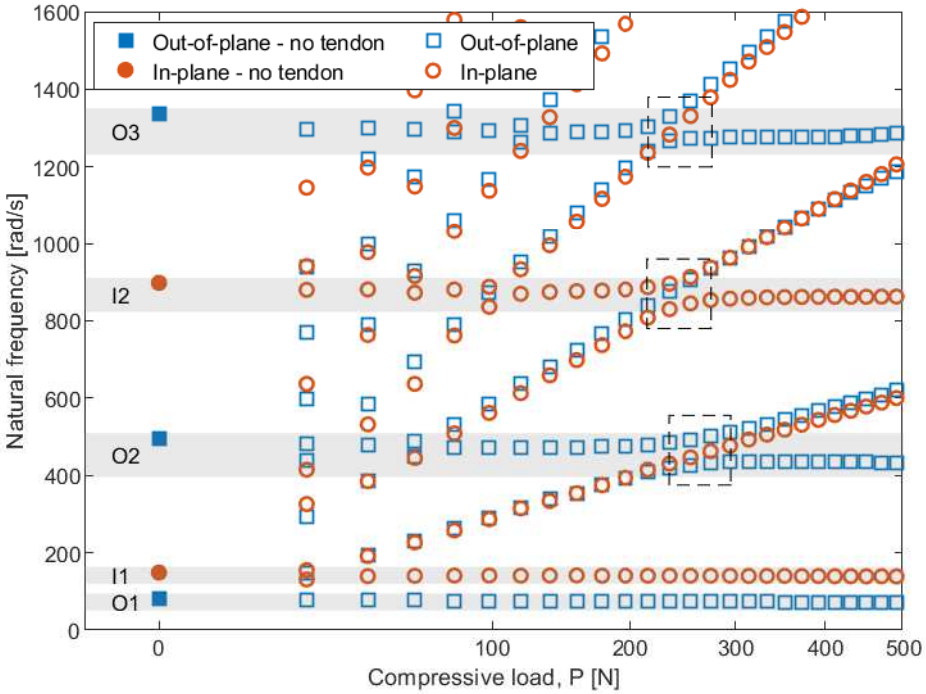

Figure 3.7: Variation of natural frequencies of the beam-tendon system with applied compressive load. Grey shaded regions denote high influence of beam behaviour. Dashed boxes denote veering interactions.

It can be seen that there are two types of mode present in the system: beam dominated modes and tendon dominated modes. There are also regions where these modes overlap and there is significant interaction between the beam and the tendon.

The beam dominated modes can be identified from the case where frequencies were calculated without the presence of the tendon. The frequency ranges containing these modes have been highlighted for ease of identification. It can be seen that there is a small reduction in frequency from the case with no tendon to the case with the tendon with low levels of loading which is likely to be due to the presence of the tendon increasing the inertia of the system, not the compressive loading effect. As compressive loading is increased, these modes can be seen to exhibit small reductions in frequency with applied compressive load, similar to a reduction in effective stiffness, which demonstrates the ability of compressive loading to alter a blade's dynamics properties.

The tendon dominated modes exhibit a linear relationship with the square root compressive load. This trend is expected as the analytical equation for frequencies a pinned-pinned tendon is proportional to the square root of the compressive load. For low values of compressive load, there are a large number of tendon-dominated modes present in the range of frequencies investigated, particularly for compressive loads of less than 100 N. For compressive loads greater than 100 N

it is easy to identify the first four tendon dominated modes that have been captured.

In addition to the beam- or tendon- dominated modes, there are regions where the two mode types appear to interact, resulting in considerable amounts of coupling between their dynamics. These regions that are present above 100 N have also been indicated in Fig. 3.7 for ease of identification. This interaction is similar to the veering discussed Section 1.2.2.2 and [43, 44] which is normally observed between the modes of different motions of a blade as they change with rotor speed. As the modes approach the indicated region in which they would be expected to cross, their trajectories change and they veer away from each other. Beyond this region, the modes continue along the trajectories of the mode they are expected to have crossed with all of the associated properties of that mode. This effect shows that, for this experiment, there is a significant amount of coupling between the tendon and the beam. It would also suggest that if the concept of compressive loading based resonance avoidance were employed on a production aircraft using a tendon that was able to vibrate freely, significant efforts would need to be made to analyse, understand and potentially suppress the effects of the tendon's vibration.

The model described in Chapter 2 and Sections 3.1 and 3.2.2 is used to calculate the natural frequencies between $30\,\mathrm{rad\,s^{-1}}$ and $1600\,\mathrm{rad\,s^{-1}}$ for compressive loads between 100 N and 500 N to be compared with the experimentally calculated frequencies. The comparison of these results can be seen in Fig. 3.8.

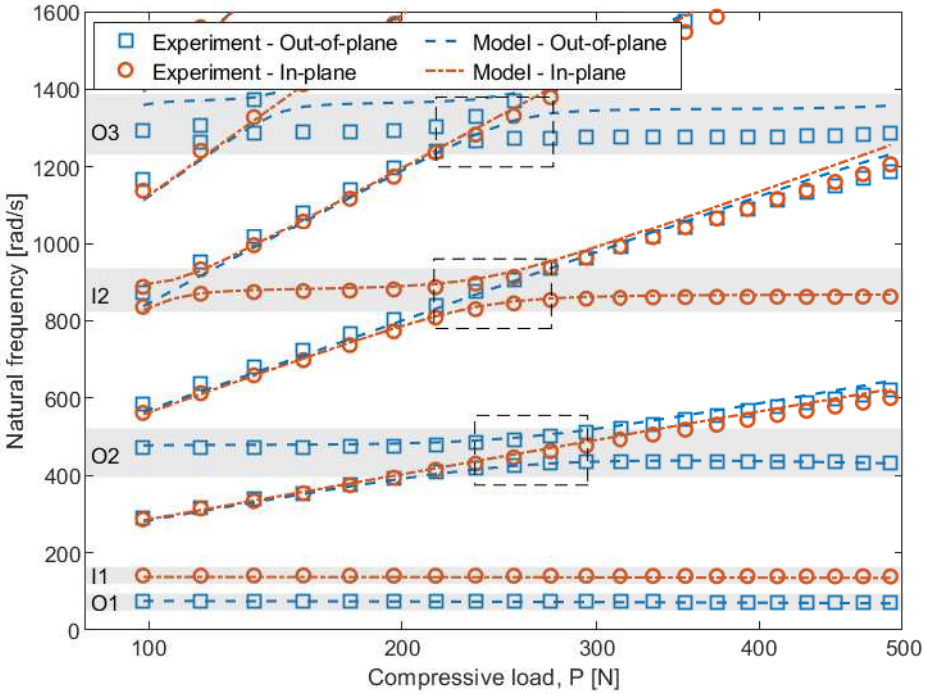

Figure 3.8: Comparison of experimental and computationally calculated natural frequencies of the beam-tendon system for a range of compressive loads to validate the model. Grey shaded regions denote high influence of beam behaviour. Dashed boxes denote veering interactions.

It can be seen in Fig. 3.8 that the correlation between experimental and modelled results is very strong for beam-dominated and tendon-dominated modes even in the regions where veering is observed. The exception to this is the third out-of-plane beam-dominated mode. For this mode the experimentally observed frequency is lower than that of the model, exhibiting an almost constant offset. Whilst it is difficult to quantify, due to the presence of veering in both sets of data, the offset error is in the region of 4 % to 5 %, which is consistent with that observed in the underlying beam model as shown in Fig. 3.5b. As the discrepancy occurs in the experimental boundary conditions, whether or not the tendon is present, it is likely that the error is not related to the tendon. The overall correlation is good and verifies that the model has been correctly developed and implemented and that is it capable of modelling a coupled beam-tendon system, even when significant amounts of coupling are present.

3.2.4 Compressive load modelling methodology

It is clear from the results presented in Section 3.2 and [152] that there are two main effects present when a beam is compressively loaded using a tendon: The effect of the compressive load reducing the effective stiffness of the beam; and the dynamics of the tendon itself. As the focus of this research is to evaluate the first effect, the reduction in effective stiffness due to

the compressive load, the model was developed using a point force located at the elastic axis of the tip of the blade directed towards the root. Herein, a study shall be performed, using the model described in Chapter 2 and Sections 3.1 and 3.2.2 to assess the chosen methodology, as obtained in [158]. This will consist of using the model of the coupled beam-tendon system, which represents one potential option for applying compressive loading to a rotor blade, and removing the effects of the dynamics of the tendon. The results of the coupled beam-tendon model shall be compared with the point force modelling options considered in [158] to evaluate which, if any, correlate suitably well to be considered for the following research.

The three modelling options considered are:

- The *hub* option, as seen in Section 3.1.1, is orientated towards the hub as this is a likely attachment point of any compressive load application system.
- The *inward* option which applies the force parallel to the plane of rotation which would act similarly to a reduction in centrifugal load.
- The *tangent* option will act tangentially to the deformed blade at its tip.

These three options are displayed in Fig. 3.9. Each of these options shall be implemented in the point force model and the corresponding results compared with that of the coupled beam-tendon model and used to determine which point force methodology best replicates the changes in frequency observed in the beam-tendon model.

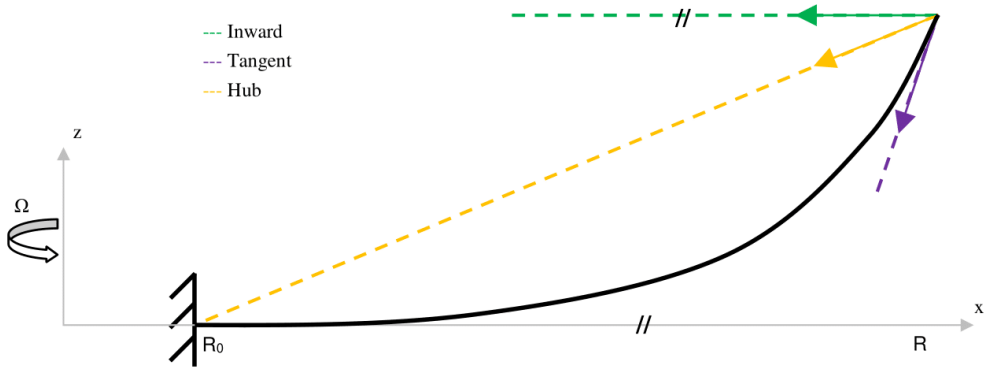

Figure 3.9: Schematic of point force modelling options considered to approximate tendon-induced compressive load.

The implementation of these point force models consists of redefining P_x, P_y and P_z to correspond to the orientation of the force in each option. The *hub* model is detailed in Section 3.1.1 and the equations for the remaining remaining two options are detailed below.

The *inward* option contains no in-plane or out-of-plane components and therefore is defined as follows.

$$\begin{aligned} P_x &= P \\ P_y &= 0 \\ P_z &= 0 \end{aligned} \tag{3.19}$$

The remaining option, *tangent*, is defined as follows.

$$\begin{aligned} P_x &= P\frac{dx(R)}{\sqrt{dx^2(R)+dv^2(R)+dw^2(R)}} \\ P_y &= P\frac{dv(R)}{\sqrt{dx^2(R)+dv^2(R)+dw^2(R)}} \\ P_z &= P\frac{dw(R)}{\sqrt{dx^2(R)+dv^2(R)+dw^2(R)}} \end{aligned} \tag{3.20}$$

Following the same Taylor expansion as used in Section 3.1.1, Eq. (3.20) is linearised to produce the follow set of equations.

$$\begin{aligned} P_x &= P \\ P_y &= Pv'(R) \\ P_z &= Pw'(R) \end{aligned} \tag{3.21}$$

3.2.5 Point force model comparison

Using the three options for the point force model described in Section 3.2.4, a comparison is performed against the coupled beam-tendon model. The model of the coupled beam-tendon system shall be used to asymptotically remove the impacts of the dynamics of the tendon. The results of this shall be compared to those using the point models to identify which correlates best.

The mass of the tendon is reduced to lessen the impact of the tendon's dynamics on the results. The properties used for this analysis are identical to the ones shown in Table 3.1. The results of these analyses are shown in Fig. 3.10.

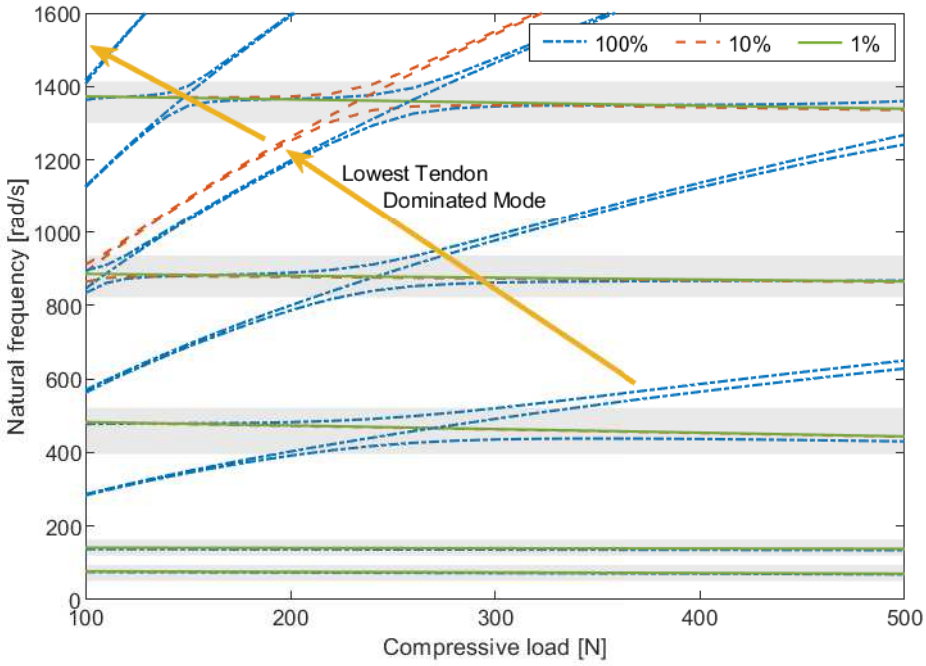

Figure 3.10: Natural frequencies of the coupled beam-tendon system with tendon mass values of 100 %, 10 % and 1 % of the nominal. Arrow shows the change in the frequency of the lowest tendon dominated mode for each tendon mass value.

It can be seen that reducing the mass of the tendon to 10 % of the nominal value drastically reduces the number of tendon dominated modes observed in the frequency range that has been explored from four to one. However, the presence of this tendon dominated mode still introduces veering between itself and two of the beam-dominated modes. Therefore, a case with an even lighter tendon, 1 % of the nominal was also assessed. It can be seen that the tendon dominated modes for this case are sufficiently high that they exceed the observed range and therefore, there are are no veering interactions. Due to the lack of veering interactions, this data set will be used as the datum to compare the point load models to. The natural frequencies of the beam calculated using the coupled model with a light tendon and the aforementioned point force models are shown below in Fig. 3.11.

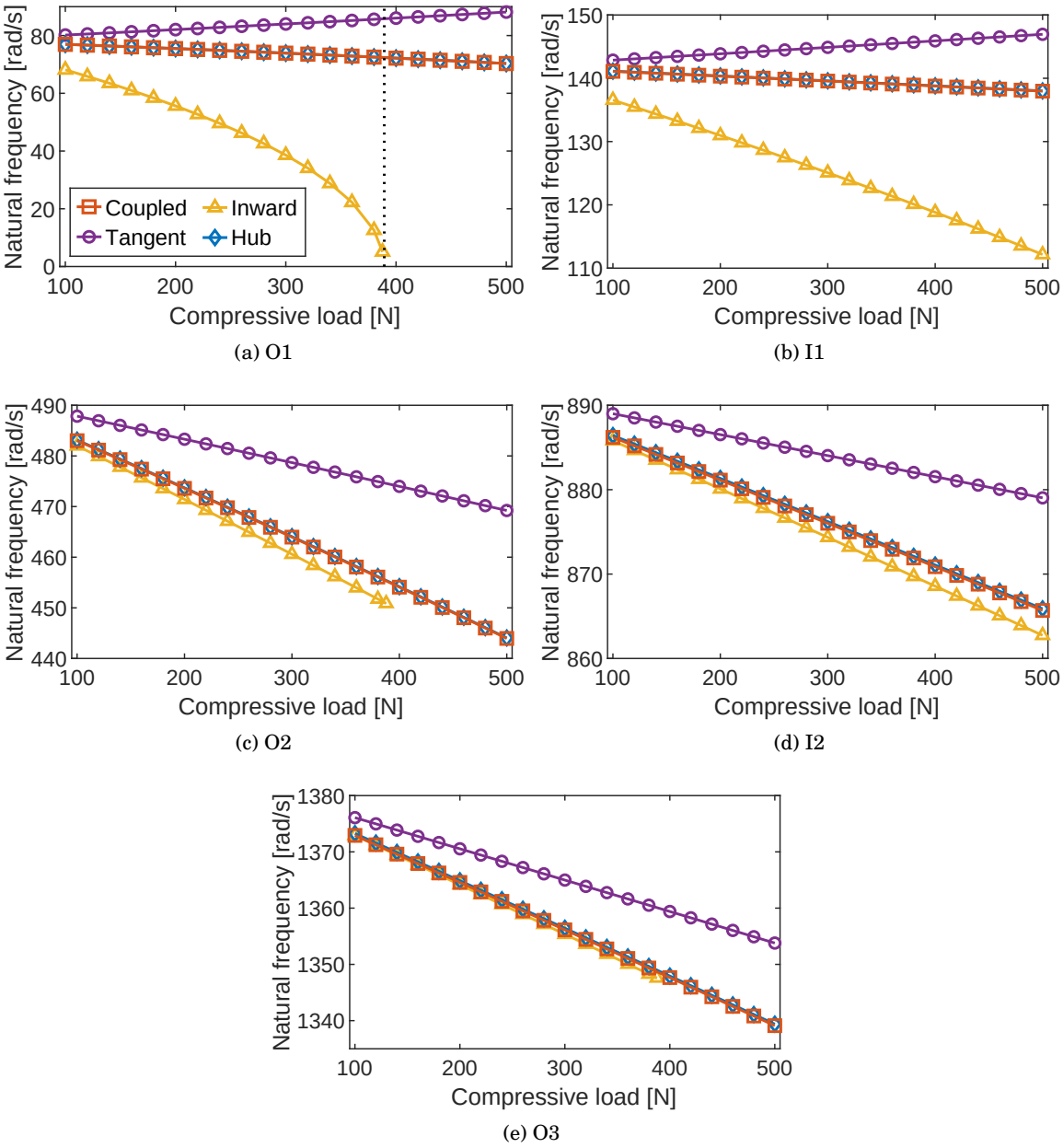

(a) O1

(b) I1

(c) O2

(d) I2

(e) O3

Figure 3.11: Natural frequencies for the first five modes and their variation with compressive loading to compare the different point force modelling options with coupled beam-tendon model.

When considering the *tangent* model, it can be seen that across all modes, this model exhibits a response to increased loading that is similarly linear to the datum coupled model in the observed range. However, the rate with which the frequencies change is significantly different. For the higher order modes, shown in Figs. 3.11c to 3.11e, a reduction in frequency is observed but the *tangent* model significantly underpredicts the amount of frequency reduction compared to that observed in the coupled model. For the lowest mode in each orientation, shown in Figs. 3.11a

and 3.11b, the *tangent* model predicts an increase in frequency with compressive loading. This response may appear erroneous but is actually in agreement with the behaviour of cantilevered beams subject to this loading orientation as stated in [111]. Due to these observed discrepancies with the coupled model, the *tangent* model is not used in future work.

When considering the *inward* model, all modes apart from the first mode in the out-of-plane direction, Figs. 3.11b to 3.11e, exhibit a linear reduction in frequency in the range investigated. The magnitude of these reductions is an overprediction of those calculated using the coupled model. For the fundamental mode, shown in Fig. 3.11a, the reduction in frequency starts with a gradual reduction, as observed in the other modes, but the rate of decrease gets larger; eventually reducing such that the solver is unable to find a converged solution, likely due to the presence of buckling. The buckling load can be defined as the load at which the lowest natural frequency reaches zero [114, 111] which is clearly observable in Fig. 3.11a. This hypothesis is confirmed using the buckling load calculated using Euler's critical buckling theorem as defined below.

$$P_c = \frac{\pi^2 E I_y}{(2R)^2} \tag{3.22}$$

For this case, the value is 389 N which is shown in figure Fig. 3.11a for reference. It can be seen that this agrees that buckling is being approached which demonstrates that the model is capable of predicting the critical buckling load. The increasing rate of change of the change in frequency with applied compressive load suggests that the sensitivity to compressive loading increases as buckling is approached which agrees with conclusions from other research investigating the effects of compressive loading on the buckling of beams [113]. Furthermore, as the *inward* model suggests that buckling would have been observed during the experiment, which was not the case, it is clear that this model is also not a suitable point force model. If it were used, it would overpredict frequency changes and result in underpredictions of the loads required to achieve sufficient avoidance of resonance.

Finally, the *hub* model is considered. Unlike the other two models, this one correlates exceptionally well with the coupled model. The shape and magnitude of the trends of frequency with increasing compressive load are very similar to the coupled model. Therefore, this point force model shall be used for the rest of this research.

For each of the point force models considered, $P_x = P$, and the differences are purely in P_z. Despite the magnitude of P_z being much smaller than that of P_x, it is clear from the comparisons shown Fig. 3.11 that even small changes in the direction of the applied load have a significant impact on the resulting changes in natural frequency.

3.3 Rotating study

Once the effect of compressive loads on the dynamics of beams had been demonstrated experimentally and a suitable model had been created and validated, the effectiveness of altering the dynamics of full-scale rotorcraft blades using compressive loading is investigated. This will provide insight into the sensitivity of full-scale rotor blades to the loading and therefore the amount of load that may be required to avoid resonance. The magnitude of this load will likely be one of the key factors determining the success of such a system. If the load is too large, the cost of actuation, in terms of power, space and mass, would likely prohibit the deployment of a compressive loading based resonance avoidance system.

3.3.1 Aircraft case study

Using the model described in Chapter 2 and Section 3.1, which uses the *hub* point force model and includes the effects of the centrifugal loads, a case study is performed to investigate the influence of compressive loading on full-scale rotor blades. This will assess the scalability of the concept from the small scale experiment and provide insight into how the stiffening and softening effects of rotation and compressive loading combine.

To improve our understanding of the effect of compressive loading on different types of aircraft and therefore how broad the application of a resonance avoidance system based on compressive loading may be, a range of different aircraft are assessed. For this case study, the three aircraft described and defined in Appendix C are used: the MBB Bo 105, the Westland Lynx, and Westland AW101. These aircraft exhibit a varying set of uses, sizes and performance characteristics which is reflected in their blade properties, as shown in Appendix C.

Firstly, the parameters of the case study shall be defined. The blade properties shall be defined using the required parameters from Appendix C and the range of rotor speeds considered will be 60 % to 100 % of the nominal value to replicate the large 40 % reduction of the Boeing A160T Hummingbird [28], the largest reduction observed in existing aircraft. The critical buckling loads shall then be calculated and used to determine the maximum compressive loading applied to each blade. As demonstrated in Section 3.2.5, the model can be used to calculate the critical buckling load as the load at which the lowest frequency equals zero. Therefore, the natural frequency of the buckling mode for each aircraft is calculated up to the critical buckling load. This calculation is performed at the lowest rotor speed considered to ensure that a conservative value is obtained for the range of rotor speeds considered. The evolution of the natural frequency of the buckling mode for each aircraft with increasing compressive loading is shown below in Fig. 3.12.

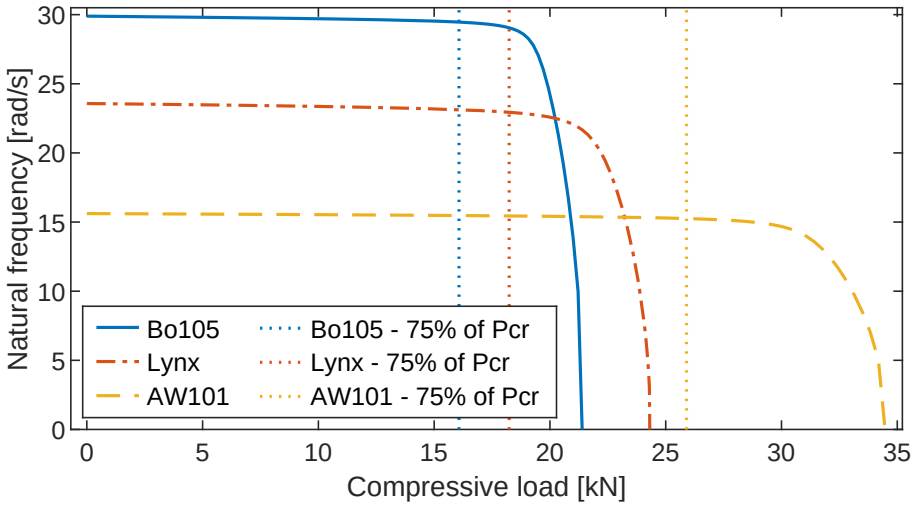

Figure 3.12: Variation of the fundamental mode's natural frequency under compressive loading up to the buckling load at 60 % of the nominal rotor speed.

It can be seen that the natural frequency of the fundamental mode of each aircraft exhibits a somewhat similar response to the loading; initially, the negative gradient is small and negative but as buckling is approached the magnitude of the gradient increases until the blade loses stability. To ensure that buckling is avoided, the maximum load considered in the subsequent analyses is 75 % of the buckling load. This value allows the maximum load possible while remaining within the region with a shallow gradient to avoid the sudden onset of buckling. The value of 75 % of the buckling load is chosen to be conservative in the knowledge that localised buckling of the surface of the blade may reduce the limit buckling load and cannot be modelled using the current method. A summary of the critical and maximum allowable loads are provided in Table 3.2.

Table 3.2: Buckling and maximum allowable loads for each aircraft

Aircraft	MBB Bo105	Westland Lynx	Westland AW101
Critical compressive force, P_c [N]	21.43×10^3	24.32×10^3	34.53×10^3
Maximum compressive force, P_m [N]	16.07×10^3	18.24×10^3	25.90×10^3

Due to the different values of the natural frequency under no compressive loading and the different magnitudes of buckling load, it is difficult to compare the responses of the natural frequency to compressive loading for each aircraft. Therefore, Fig. 3.12 is also modified and shown using natural frequencies and compressive loads that are normalised against the unloaded natural frequency and buckling load, respectively. This can be seen in Fig. 3.13.

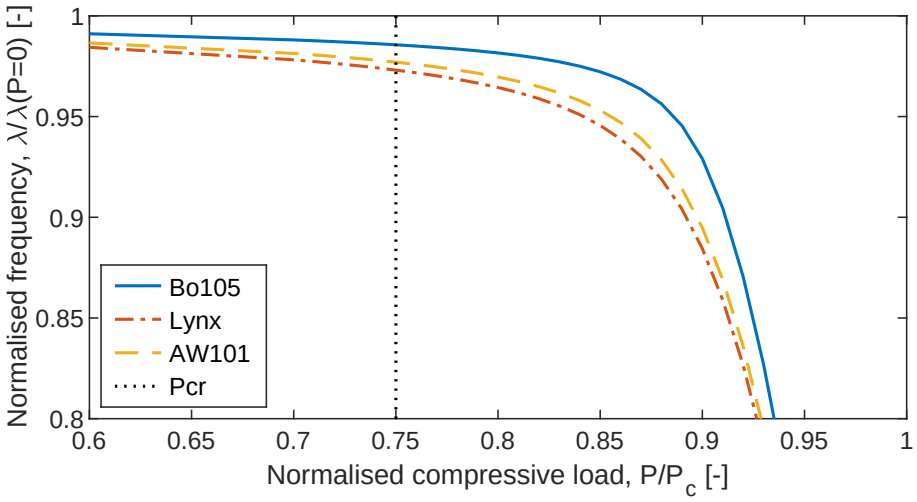

Figure 3.13: Comparison of the buckling behaviour of each aircraft at 60 % of the nominal rotor speed.

It is clear that each aircraft has a different response to the compressive loading, with the Bo105 exhibiting the most sudden onset of buckling when compared with the Lynx and the AW101. This is likely to be due to the Bo105 having the softest blades and highest rotor speed. This indicates that the abruptness with which buckling is reached is influenced by the ratio of bending and centrifugal stiffness. This may be indicative that larger aircraft would be more suitable to a compressive loading based resonance technique as their frequencies are more sensitive to loading below P_m. However, this study only investigates the fundamental mode which may not be indicative of behaviour across all modes.

Once the maximum compressive load to be applied had been calculated, it was possible to calculate the natural frequencies for the first three out-of-plane modes (O1-O3) and the first two in-plane modes (I1-I2) across a range rotor speeds and compressive loads up to P_m, as seen in Fig. 3.14. For ease of comparison between modes, each mode for each test aircraft is plotted individually and the scale is consistent for each mode of an aircraft.

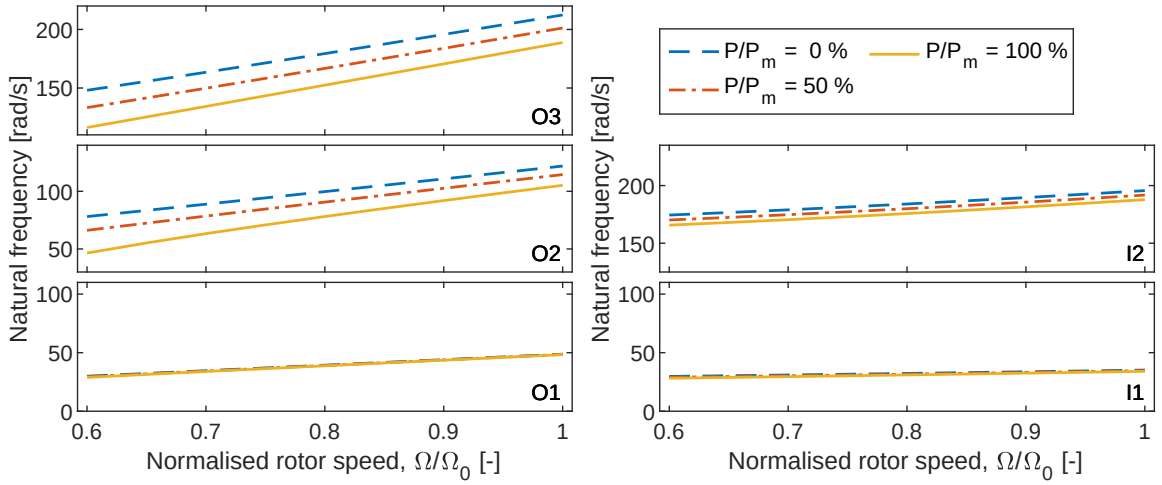

(a) Bo105: out-of-plane

(b) Bo105: in-plane

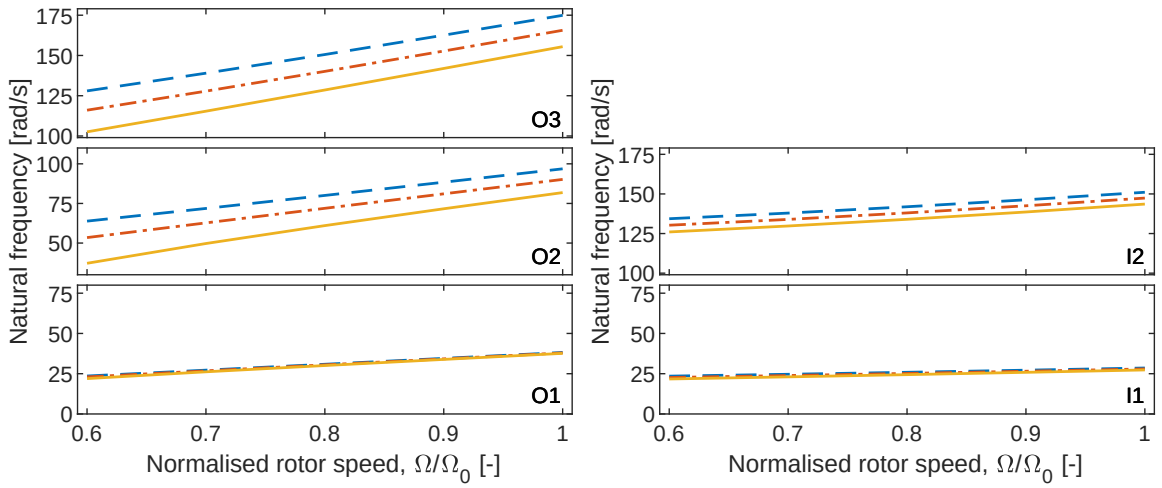

(c) Lynx: out-of-plane

(d) Lynx: in-plane

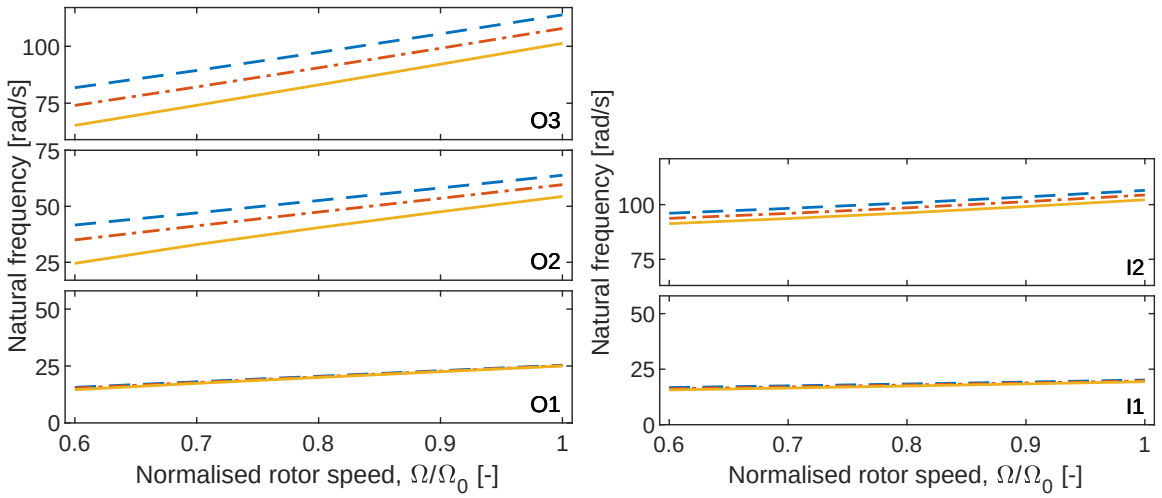

(e) AW101: out-of-plane

(f) AW101: in-plane

Figure 3.14: Variation of the natural frequencies of the rotor blades between 60 % and 100 % of the nominal rotor speed under compressive loading up to P_m.

There are multiple factors that can be seen to influence the response of the blade to the applied compressive loading. Firstly, it can be seen in Fig. 3.14 that the change in frequency is greater at lower rotor speeds. This is because at higher rotor speeds the centrifugal forces are larger, reducing the impact of the compressive loading. Secondly, it can be seen that the out-of-plane natural frequencies are more sensitive to the compressive loading than the corresponding in-plane natural frequencies. This is likely due to the lower bending stiffness observed in this direction. These differences in sensitivity are consistent across all three test aircraft and implies that there are multiple factors influencing the sensitivity of a blade's natural frequencies to compressive loading.

These factors should be considered when designing a resonance avoidance system based on compressive loading. For example, if a system were to be retrofitted to a blade, it would perform better if the blade exhibited its resonances at lower rotor speeds or in the out-of-plane modes where the compressive loading would yield a greater change in frequency.

The model can additionally be used to evaluate the magnitude of the compressive load that may be required to avoid resonance. As the model does not have the capability to capture the effects of torsion or twist, it will not capture the torsional natural frequencies or the coupling between the in-plane and out-of-plane modes. This limitation is expected to have a small effect on the in-plane and out-of-plane modes away from regions where coupling would be present. Due to this limitation, the model is not able to accurately capture all of the modes present in a rotor blade across the range of rotor speeds. Therefore, it would be inappropriate to attempt to evaluate the proximity of natural frequencies to rotor harmonics that would excite the modes in question. However, the model can be used to evaluate the magnitude of the change in frequency that can be achieved.

The use of separation between natural and excitation frequencies has traditionally been used as a design technique in rotor blades to ensure that resonance is avoided [68, 6]. While the exact value of separation that is required is likely to differ between each potential case of resonance depending on factors such as the amount of damping in the mode and the magnitude of excitation loads, a value of 10 % of the main rotor frequency is generally considered sufficient [6]. In the most conservative case, with a natural frequency 10 % higher than the excitation frequency, a change of 20 % of the rotor frequency would be required.

For this study, the modes of the three test aircraft shall be calculated at the highest and lowest rotor speed considered to ensure the results capture both extremes and are conservative. The change in the natural frequencies as a percentage of the rotor speed, alongside the 20 % target are shown below in Fig. 3.15.

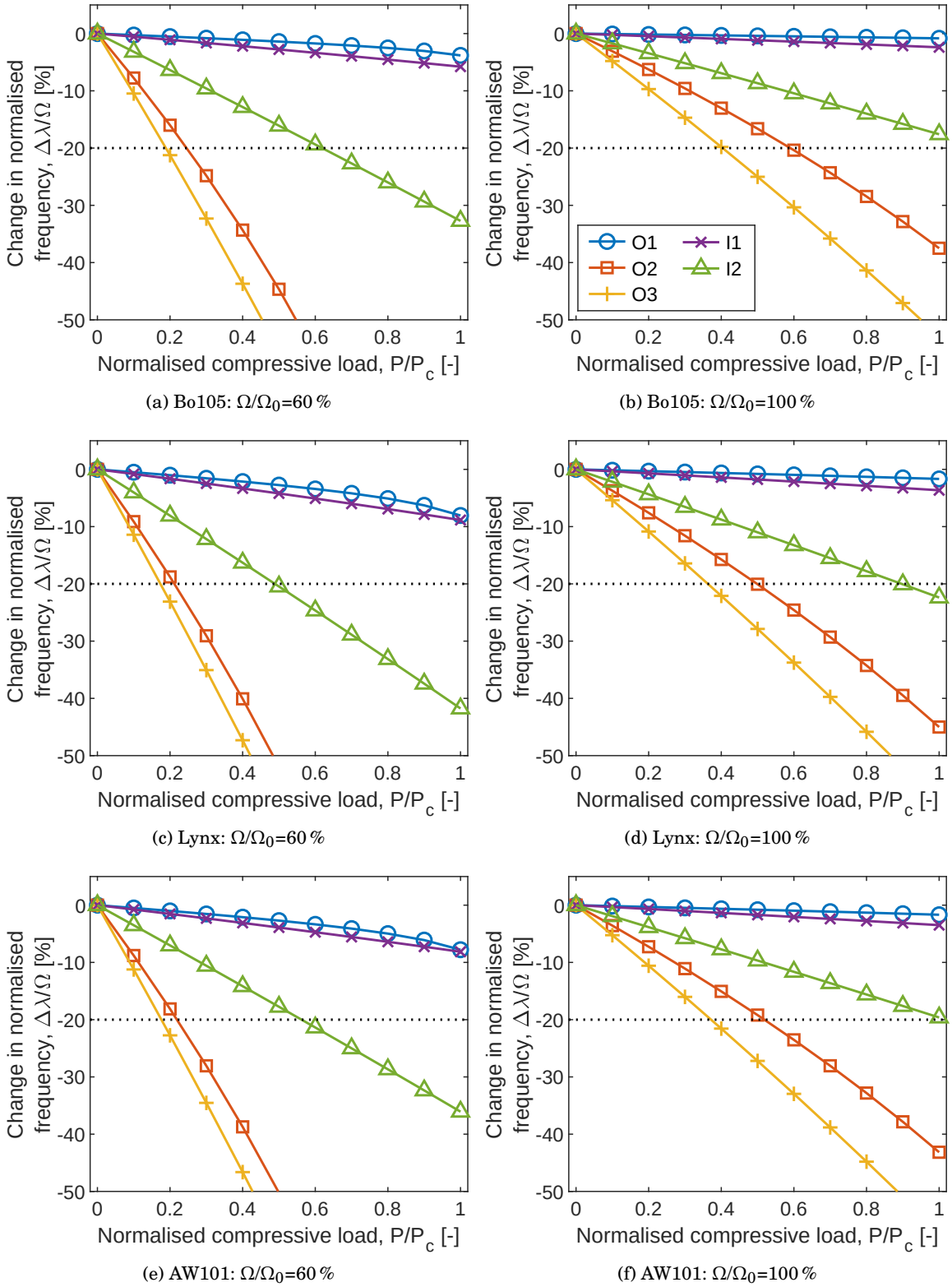

(a) Bo105: Ω/Ω_0=60 %

(b) Bo105: Ω/Ω_0=100 %

(c) Lynx: Ω/Ω_0=60 %

(d) Lynx: Ω/Ω_0=100 %

(e) AW101: Ω/Ω_0=60 %

(f) AW101: Ω/Ω_0=100 %

Figure 3.15: Reduction of the natural frequencies of the rotor blade with compressive loading up to P_m at 60 % and 100 % of the nominal rotor speed.

It can be seen in Fig. 3.15 that the fundamental in-plane and out-of-plane modes' insensitivity to loading prohibit a change of 20 % of the rotor frequency for almost every combination of aircraft and rotor speed. However, this insensitive behaviour may be beneficial for several reasons. Firstly, the fundamental out-of-plane frequency is often involved in the analysis of a rotor's control power. For example, hingeless rotors, which are often employed in agile combat aircraft such as the Westland Lynx, typically have values of between 1.05-1.15/rev [159]. Conversely, articulated rotors, which are often used in transport aircraft as they require less agility, typically have values between 1-1.04/rev [159]. As this frequency may be impactful on other aspects of the rotor performance, it may be beneficial for it to remain relatively unchanged. Secondly, as stated, the fundamental out-of-plane frequency typically resides just above the 1/rev harmonic. Therefore, lowering the frequency would subsequently reduce the separation between this mode and the 1/rev harmonic which would make it beneficial to lessen the amount of reduction achieved through compressive loading. Additionally, due to the effect of the out-of-plane motion on the aerodynamic loads, there is a significant amount of aerodynamic damping present in this mode; values of damping ratio oscillating around 45 % have been calculated for forward flight conditions [63]. For the fundamental in-plane mode, the natural frequency values are typically sufficiently below the 1/rev harmonic and are also possible to remove from consideration. Any reduction in this frequency would serve only to increase the separation. Each of the other modes considered is able to achieve this target within the allowable compressive load range with the exception of the second in-plane mode of the Bo105 at the higher rotor speed which only achieves a reduction of 17.58 %. Furthermore, many of these modes achieve this separation with much less than the maximum allowable load. It may, therefore, be possible to reduce the required loading by designing the rotor's mass and stiffness distributions such that the separation of the least sensitive modes is sufficient across the range of rotor speed desires. This would likely result in other modes encountering more resonant interactions but as these modes are more sensitive to the compressive loading, the resonances the encounter can be avoided.

3.3.2 Actuation sizing

Whilst the focus of this research is not to design the system to be used to implement a compressive load, some consideration of the scale of this system will briefly be given here.

The implementation of different mechanisms within a blade has previously been considered: *Falls* [160] researched the embedding of trailing edge flap within rotor blade and a patent by *Gandhi* [161] embeds a complex mechanism of brakes, jackscrews and gears into a rotor blade to actuate a variable span rotor blade. *Dawson et al* [94] used a pretensioned cable to actuate an active flap mechanism during wind tunnel tests. Therefore it can be assumed that it may be possible to embed an actuator and associated attachments within a blade.

It also remains useful to establish the magnitude of the loads presented in Table 3.2 in the context of current aerospace actuation capability. Aerospace hydraulic systems typically oper-

ate at a high pressure to reduce the amount of fluid required and keep actuator size small to lower the overall mass of the actuation system. Hydraulic systems have become standardised using pressures up to 20.7 MPa (3000PSI) with efforts being made to increase this to 34.5 MPa (5000PSI) to further reduce size and mass [162]. Using the current standardised pressure of 20.7 MPa, an estimate of the actuator diameter is shown in Table 3.3. The actuator diameter is also shown as a fraction of the blade chord for context. One of the benefits of a compressive loading based resonance avoidance system, as stated in Section 1.5, is that the applied force is intended to be changed due to a change in rotor speed. As the changes in rotor speed will be slow and infrequent, the actuation required will be relatively slow compared to many actuators, such as those employed in active vibration suppression techniques as described in Section 1.3.2. The low speed with which the actuation may be applied would permit the use of a very slow stroke rate which would, in turn, reduce the power required. The power required for an actuator in each blade to be actuated at $10\,\mathrm{mm\,s^{-1}}$ is also shown in Table 3.3 alongside the time taken to achieve the full range of excitation loads (based on a steel cable not exceeding its critical stress) and the total actuation power as a fraction of the installed power in the aircraft.

Table 3.3: Theoretical actuator specifications

Aircraft	MBB Bo105	Westland Lynx	Westland AW101
Maximum compressive force, P_m [N]	15833	17715	25073
Bore [mm]	31	33	39
Bore / c [%]	11	10	9
Power per blade [W]	158	177	251
Max actuation time [s]	3.8	4.7	6.7
Total power / P_i [%]	0.101	0.042	0.027

It can be seen that the size of the actuators are unlikely to be so large that they prohibit their use to apply the required compressive force. The power required for the actuation is a very low fraction of the available power, significantly lower than the 3 % typically observed in active systems [70]. Additionally, unlike active systems which require constant operation, the actuator may only be required when changing rotor speeds and can be locked otherwise which will significantly reduce the amount of energy consumed by the system. Finally, the short time to cover the full range of compressive loading will ensure the appropriate load is achieved before large resonant vibrations accumulate.

Unfortunately, it has not been possible to provide an estimate for the mass of an actuation system. However, it should be noted that traditional tuning masses, which can be up to 5 kg [11] would cease to be necessary. The removal of these tuning masses would significantly offset the mass penalties associated with implementing an actuation system.

Additionally, alternative forms of actuation which are becoming increasingly prominent may be more suitable. For example, electric motors, potentially coupled with epicyclic gearboxes may

be very suitable due to their high torque capabilities and increasing amounts of electrification in aircraft. It may also be possible to incorporate the actuation into the attachments. For instance, shape memory alloys are well suited to low-frequency actuation and, when compared to other electric actuators, are lightweight with no moving parts and a simple structure [118].

3.4 Reduction in vibratory loads during forward flight

While the use of separation between natural and excitation frequencies as a metric for dynamic blade design is well established [68, 6], it remains pertinent to illustrate that an increase in separation between natural and excitation frequencies will result in a reduction of vibratory loads. This shall be performed by using a model of a flexible rotor blade with quasi-static aerodynamic loads to assess the vibratory loads in the blade across a range of rotor speeds while at cruise.

3.4.1 Model description

A model of the motion of a rotor blade undergoing pure out-of-plane motion or pure in-plane motion during forward flight, with the associated aerodynamic loads, has been developed, as detailed in Appendix D. This condition was chosen as the asymmetric flowfield experienced during forward flight, as well as the accompanying cyclic trim, generate the rotor harmonics that provide the excitation for the vibratory loads.

The structural aspect of the model is based on the same equations of motion as those used in Section 4.1.2. The aerodynamic forces are provided in the in-plane and out-of-plane directions by a two-dimensional quasi-steady blade element model that incorporates lift-induced drag and induced velocity. The motion of the blade is assumed to take the following form.

$$\begin{aligned} w_*(x,t) &= \sum_{\forall i} q_{w\,i}(t) W_i(x) \\ v_*(x,t) &= \sum_{\forall i} q_{v\,i}(t) V_i(x) \end{aligned} \tag{3.23}$$

These equations of motion and assumed motion are multiplied by W_j and V_j and integrated along the length of the blade to form a set of equations in terms of modal mass, stiffness and forcing matrices as seen below.

$$\begin{aligned} \mathbf{M}_v \ddot{\mathbf{Q}} + \mathbf{K}_v \mathbf{Q} &= \mathbf{D}(\psi) \\ \mathbf{M}_w \ddot{\mathbf{Q}} + \mathbf{K}_w \mathbf{Q} &= \mathbf{L}(\psi) \end{aligned} \tag{3.24}$$

The forcing matrices are defined as follows.

$$\begin{aligned} \mathbf{D}(\psi) &= \left(\mathbf{D}_1 + \mathbf{D}_2\dot{\mathbf{Q}} + \mathbf{D}_3\dot{\mathbf{Q}}^2\right)\mathbf{C}_v(\psi) \\ \mathbf{L}(\psi) &= \left(\mathbf{L}_1 + \mathbf{L}_2\dot{\mathbf{Q}}\right)\mathbf{C}_w(\psi) \end{aligned} \tag{3.25}$$

where

$$\begin{aligned} \mathbf{C}_v &= \begin{bmatrix} 1 & \sin\psi & \cos\psi & \sin 2\psi & \cos 2\psi & \sin 3\psi & \cos 3\psi & \sin 4\psi & \cos 4\psi \end{bmatrix}^T \\ \mathbf{C}_w &= \begin{bmatrix} 1 & \sin\psi & \cos\psi & \sin 2\psi & \cos 2\psi & \sin 3\psi & \cos 3\psi \end{bmatrix}^T \end{aligned} \tag{3.26}$$

This model is designed to represent a blade that will undergo out-of-plane excitation up to 3/rev and in-plane excitation up to 4/rev. For this study, only one aircraft, the Bo105, is analysed. This aircraft was chosen as it has the highest rotor speed and therefore the highest excitation frequencies captured by the model.

The forward speed chosen for this analysis is the cruise speed of the aircraft. This is because, in low speed forward flight, the vibratory loads are caused by Blade Vortex Interaction (BVI)s which are not captured by the model. However, in moderate-to-high speed cruise, the large periodic vibratory loads on the blades are created by variations in blade velocity and angle of attack [49] therefore it is in these operating conditions that the model is most appropriate. The cyclic pitch values used are those calculated to achieve trim for an example aircraft at a similar forward speed [122]; these values are summarised in Table 3.4.

The mode shapes used for this analysis are the ones calculated alongside the frequencies shown in Fig. 3.14. The use of the exact mode shape for each rotor speed and compressive loading condition will ensure the fixed-free boundary conditions remain enforced.

Table 3.4: Additional forward flight parameters

Property	Value
Forward speed, v_f [$\mathrm{m\,s^{-1}}$]	56.67
Air density, ρ_∞ [$\mathrm{kg/m^3}$]	1.225
Parasitic drag coefficient, C_{d0} []	0.01
Lateral cyclic trim, a_s [rad]	0.0855
Longitudinal cyclic trim, a_c [rad]	-0.0401

To evaluate the variation in aerodynamic loads that drive the oscillatory motion of the blade, the total aerodynamic load in the in-plane and out-of-plane directions at each azimuthal location is calculated. The variation in the deviation of the total load from the mean value is shown below.

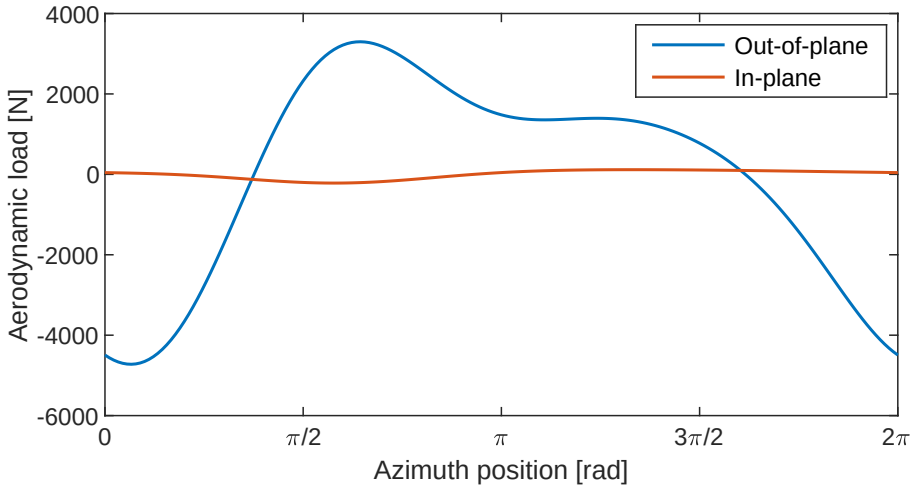

Figure 3.16: Periodic variation of aerodynamic loads from the mean.

It can be seen that the variation in out-of-plane loads is significantly larger than that of the in-plane loads which will result in a larger excitation load for motion in this direction. Additionally, while the variation of the out-of-plane load is periodic, it is not sinusoidal due to the combination of longitudinal and lateral cyclic and asymmetry in the local airflow due to forward motion of the aircraft. The non-sinusoidal nature of this loading will ensure that the motion of the blade is non-sinusoidal; hence it is not appropriate to use a harmonic assumed motion.

3.4.2 Aircraft case study

Firstly, the model was used to simulate the steady-state out-of-plane and in-plane response of the blade across the desired range of rotor speeds. The amplitude of the steady-state oscillations of the blade's tip are shown below in Fig. 3.17.

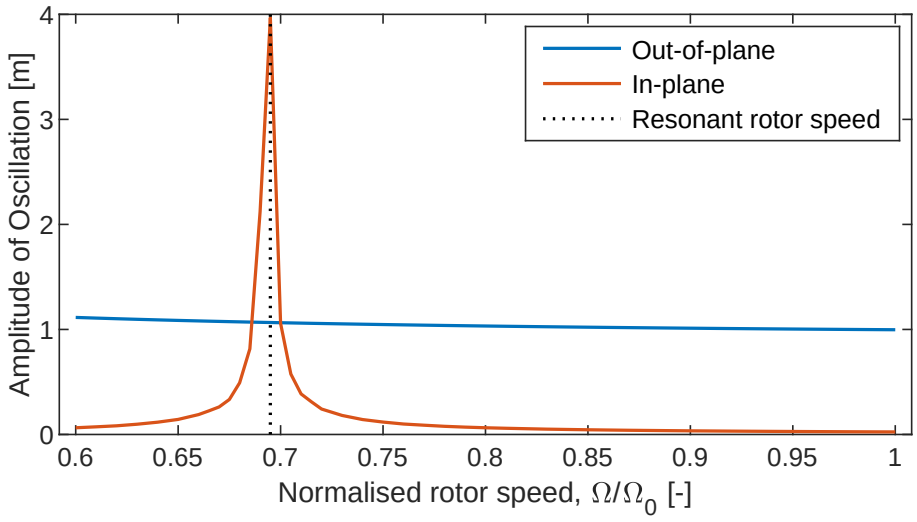

Figure 3.17: Oscillation amplitudes of the steady state response of the blade tip across a range of rotor speeds.

The out-of-plane amplitudes are potentially overly large due to inaccuracies in the some of the chosen parameters, such as the cyclic pitch values. The in-plane amplitudes at the resonant rotor speed are also overly large due to the low damping ratio and assumed linearity. It can be seen that the model exhibits the expected behaviour of the blade in these operating conditions. The out-of-plane amplitudes are larger than the in-plane ones, by a factor of approximately ten, for the majority of the rotor speed range that has been examined. This difference is due to the value of C_l being larger than that of C_d which results in larger aerodynamic forces in the out-of-plane direction. Additionally, it can be seen that the out-of-plane amplitudes remained unaffected by the change in rotor speed. It is likely that, despite the changes in separation between natural and excitation frequencies caused by the change in rotor speed, the large amounts of aerodynamic damping present suppress any significant changes in amplitude. Conversely, the damping that is expected in the in-plane direction is significantly lower. Therefore, the changes in rotor speed result in a resonant interaction observed at 69.5 % of the nominal rotor speed. The magnitude of the in-plane oscillations at this rotor speed is approximately three times larger than that of the out-of-plane-plane oscillations; a significant increase from being approximately ten times smaller away from resonance.

Due to the variation in aerodynamic loads throughout the azimuth, it is not possible to calculate a single damping ratio for the motion of the blade in these conditions. However, an approximation of the instantaneous damping ratio at each azimuthal location can be made by isolating the aerodynamic terms that are linearly proportional to $\dot{\mathbf{Q}}$ (removing $\mathbf{D}_1$, $\mathbf{D}_3$ and $\mathbf{L}_1$ from Eq. (D.4)) and assuming the motion is harmonic. Whilst these assumptions will reduce the validity of the results they will still provide useful indications of the magnitudes of damping observed in the different modes and motions. As $\mathbf{C}_v$ and $\mathbf{C}_w$ are functions of azimuth, the damping

ratios varying harmonically, as seen in Fig. 3.18.

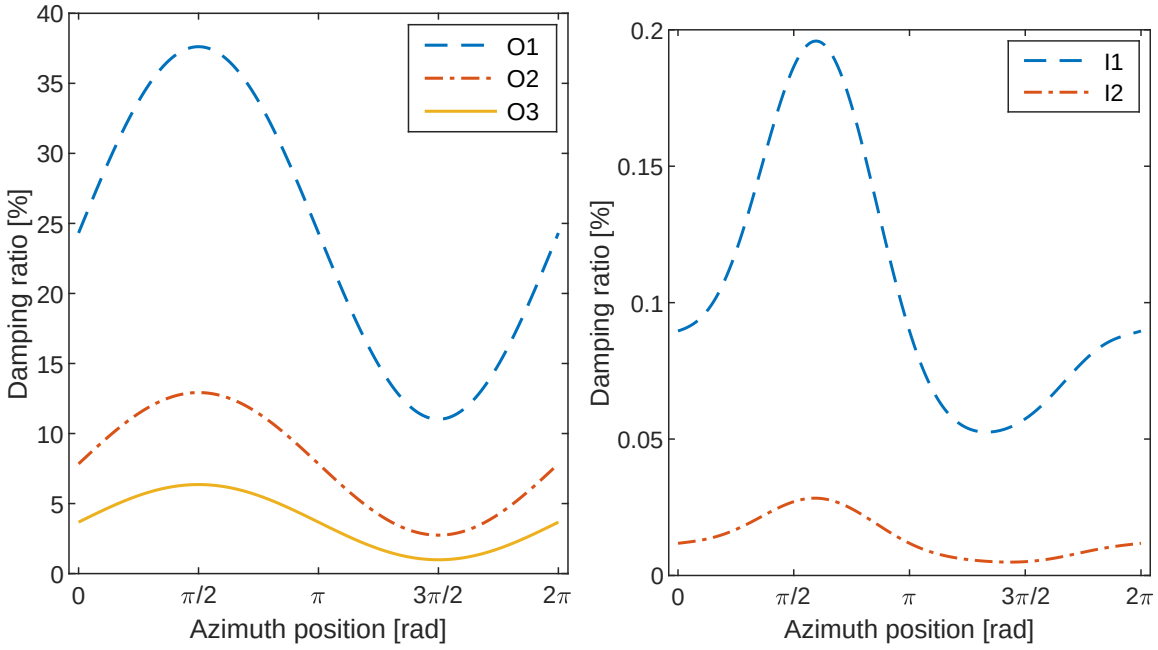

(a) Out-of-plane (b) In-plane

Figure 3.18: Harmonic variation of damping ratios for the first three out-of-plane modes and first two in-plane modes.

The most obvious observation is the difference in magnitude of the damping ratio between the different motions; the out-of-plane damping ratio is more than two orders of magnitude larger. The harmonic variation of the out-of-plane damping is due to the lack of non-zero terms in $\mathbf{L}_2$ beyond 1/rev. Conversely, $\mathbf{D}_2$ contains terms up to 3/rev which is the cause of its different shape. Additionally, it can be seen that in both orientations that damping ratio decreased in the higher-order modes. This trend is also observed in [63] and implies that while a lack of separation of the first out-of-plane mode may be considered acceptable, this is unlikely to be true of higher-order out-of-plane modes.

To assess the changes in vibratory loads at the resonant rotor speed, the steady-state responses of the blade under 0 %, 50 % and 100 % of the maximum compressive force were obtained. The moments and shear forces at the root of the blade are subsequently calculated using the following equations.

$$
\begin{aligned}
M_z &= EI_z v_*''(R_0) \\
F_y &= -EI_z v_*'''(R_0) + \Big(\frac{1}{2}\Omega^2 m\big(R^2 - x^2\big) - P\Big) v_*'(R_0) \\
M_y &= EI_y w_*''(R_0) \\
F_z &= -EI_y w_*'''(R_0) + \Big(\frac{1}{2}\Omega^2 m\big(R^2 - x^2\big) - P\Big) w_*'(R_0)
\end{aligned}
\tag{3.27}
$$

A Fourier analysis is then performed to calculate the magnitude of these loads across the rotor harmonics of interest. The reduction in the loads from the unloaded case due to the compressive load, at 50 % and 100 % of the maximum, is shown in Fig. 3.19.

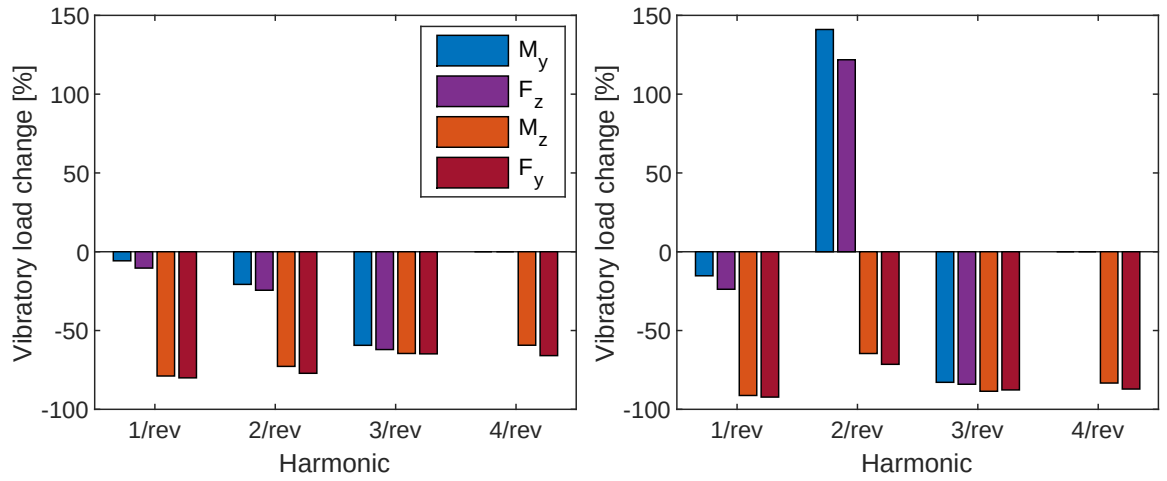

(a) P/P_m=50 % (b) P/P_m=100 %

Figure 3.19: Reduction in vibratory root loads at the resonant rotor speed, 69.5 %, at each harmonic due that is available through compressive loading.

It can be seen that with an applied load of 50 % of the maximum, there is a significant reduction in the out-of-plane and in-plane root loads across the full range of harmonics. As the in-plane motion experiences resonance in the unloaded case, which has been averted due to the compressive load induced change in natural frequency, the loads in this direction demonstrate the largest reduction in vibratory loads. It should be noted that significant reductions of the out-of-plane motion are also observed, particularly at the 3/rev harmonic. When the maximum load is applied, the magnitude of these reductions increases for the majority of the vibratory loads; however the out-of-plane loads at 2/rev increase. As the compressive load is increased the second out-of-plane mode is greatly reduced. This increases the separation between this mode and the 3/rev harmonic which in turn results in a reduction in vibratory loads at this frequency. However, the reduction in the natural frequency of the second in-plane mode reduces its separation with the 2/rev harmonic resulting in a subsequent increase in the loads at this frequency.

3.5 Chapter summary

This chapter demonstrated the core principles of the compressive loading based resonance avoidance concept.

Firstly, a boundary value problem model was created to represent a rotating cantilevered beam with an applied compressive load.

An experiment was subsequently created using a cantilevered beam with a tendon attached at the tip to transfer a compressively loaded force to the beam. The natural frequencies of the coupled beam-tendon system were obtained across a range of compressive load values. The results demonstrated that the modes of the beam were reduced by the application of the compressive load. The modes of the tendon were shown to increase significantly with tension, in line with that expected from analytical solutions of uncoupled tendons under tension. Some values of compressive loading resulted in significant interactions between modes dominated by the beam and the tendon in the form of veering.

The present beam model was adapted to represent the beam-tendon system of the experiment with coupling between the two entities occurring via the boundary conditions. The experiment and the model were compared in terms of the natural frequency values and mode shapes, via the MAC, to validate the model.

It was observed in the experimental results that there were two main influences of the compressively loaded tendon on the beam: the reduction in effective stiffness due to the compressive force and the interaction of the dynamic effects of the tendon itself. As the focus of this research is the former of these effects, an effort was made to develop an appropriate means with which to model the compressive force without the associated effects of the tendons dynamics. Therefore, a set of three modelling options for a point force located at the tip of the beam were hypothesised: one that was parallel to the plane of rotation and directed towards the centre of rotation, one orientated towards the root of the beam and one that was tangential to the tip of the beam.

These three models were subsequently compared to the aforementioned model with the dynamics of the tendon greatly reduced by lowering its mass. It was observed that with the force parallel to the plane of rotation, the change in natural frequencies was overpredicted. Conversely, the *tangent* model underpredicted the changes in natural frequencies and, in one instance, predicted changes in the wrong direction. However, the model with the force directed towards the root demonstrated an excellent correlation with the model of the coupled beam-tendon model and was therefore chosen as the method with which to model the compressive load for the remainder of the research.

The model of the beam, without tendon, and with the point force directed towards the root was used to assess the ability of compressive loading to alter the natural frequencies of rotor blades without exceeding 75 percent of the critical buckling load. For this assessment, the first six modes of the rotor blades of three different test aircraft were considered.

For all but the fundamental in-plane and out-of-plane modes, the desired change in natural frequency was achieved well within the prescribed maximum compressive value. Whilst the fundamental in-plane and out-of-plane modes were not always able to achieve the same change in natural frequencies, this is not necessarily a problem. The fundamental in-plane mode typically operates with a natural frequency much lower than that of the lowest harmonic and is therefore unlikely to encounter resonance even at greatly reduced rotor speeds. The fundamental out-of-plane mode typically experiences large amounts of damping and is also therefore unlikely to encounter significant vibratory loads.

The separation between natural and excitation frequencies has traditionally been used as the metric for the dynamic design of rotor blades. However, a simplified simulation for the vibratory loads experienced during forward flight was formulated to demonstrate the reduction in vibratory loads available through compressive loading. It was demonstrated that with the application of compressive loading, a reduction in vibratory loads was possible. However, it was also observed that if excessive compressive loads are applied, it is possible to create a resonant interaction that was not previously present.

The capability of compressive loading to alter the natural frequencies of a simplistic blade has been successfully demonstrated and it has been shown that this should lead to reduced vibratory loads during forward flight. Therefore, in the following chapter, a more refined model shall be developed and used to assess the range of operational rotor speeds available with the use of compressive loading.

CHAPTER 4

IN-VACUO RESONANCE AVOIDANCE OF ROTOR BLADES

In the previous chapter, Chapter 3, the effect of compressive loading on the in-plane and out-of-plane dynamic properties of a rotating untwisted blade with coincident mass and elastic axes was investigated and a relationship between altering these properties and reducing vibratory loads was established. In this chapter, the torsional motion is considered alongside the previously investigated in-plane and out-of-plane motion. Additionally, realistic coupling between these motions is introduced in the form of initial twist and an offset between the mass and elastic axes of a blade. Once these additional features have been incorporated into the model, a range of validation tests are performed to verify and validate the model. Subsequently, a case study is performed that incorporates the additional coupling and compressive load to determine the increase in rotor speed range that can be operated in, without encountering resonance, using the proposed compressive loading based resonance avoidance technique.

4.1 In-vacuo bending-bending-twist model

To investigate the additional effects of torsional motion, twist and non-coincident mass and elastic axes, a new sub-model is developed. This model is based on the Partial Differential Equations (PDEs) developed by *Houbolt and Brooks* [137]. These equations were developed specifically to be used in the modelling of rotor blades and have been widely used throughout industrial comprehensive rotor codes such as J134 [6] and S4 [163]. Similar to the model described in Section 3.1, they capture the effects of rigidity, blade inertia and internal tension but they also capture the torsional motion and remain valid for the blades with initial twist and non-coincident mass and elastic axes. The addition of these effects will introduce significant coupling between the in-plane, out-of-plane and torsional motions of the blade and more accurately reflect the

behaviour of real-world rotor blades.

4.1.1 Compressive load

As was concluded in Section 3.1.1, a point force applied on the elastic axis at the tip of the blade directed towards the root is the model of the compressive load to be used throughout this research. The force, as shown in Fig. 4.1, is again decomposed into components in the x, y and z directions.

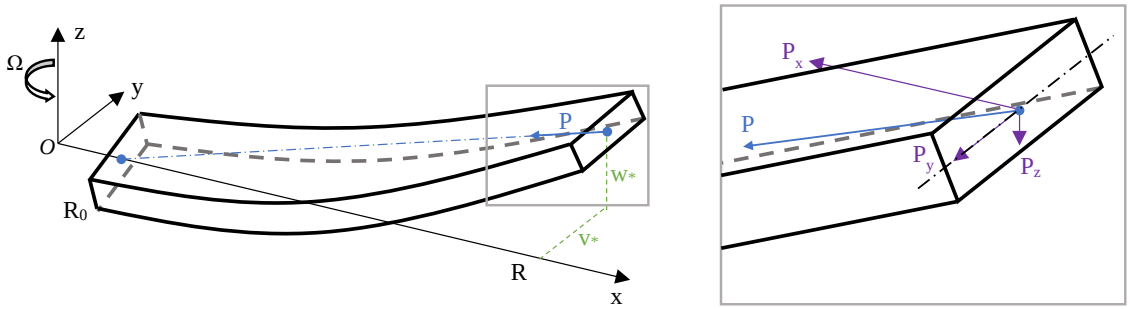

Figure 4.1: Schematic of compressive force decomposition

The geometry of the beam and its deformations can then be used to calculate the orientation of the unit vector between the tip and the root. Subsequently, the unit vector and the magnitude of the applied compressive load can be combined to calculate the component of the applied force in each direction as shown below in Eq. (4.1).

$$\begin{aligned} P_x &= P\frac{R-R_0}{\sqrt{(R-R_0)^2+v_*(R)^2+w_*(R)^2}} \\ P_y &= P\frac{v_*(R)}{\sqrt{(R-R_0)^2+v_*(R)^2+w_*(R)^2}} \\ P_z &= P\frac{w_*(R)}{\sqrt{(R-R_0)^2+v_*(R)^2+w_*(R)^2}} \end{aligned} \tag{4.1}$$

To allow these loads to be incorporated into the linear field equations and boundary conditions, it is necessary to linearise these loads. This is performed using a Taylor expansion about v_* and w_* equaling zero up to the second term, the results of which are shown in Eq. (4.2).

$$P_x = P \tag{4.2a}$$

$$P_y = P\frac{v_*(R)}{(R-R_0)} \tag{4.2b}$$

$$P_z = P\frac{w_*(R)}{(R-R_0)} \tag{4.2c}$$

As $(R-R_0) \gg v_*(R)$ and $(R-R_0) \gg w_*(R)$ the change in orientation of the load is minor, hence Eq. (4.2a) is expected. Furthermore, it can also be seen that Eqs. (4.2b) and (4.2c) take the mathematical form of linear springs of stiffness $\frac{P}{(R-R_0)}$ as was also observed in [114].

4.1.2 Field equation

The equations of motion that represent the motion of the blade within the domain are a set of three linear non-homogenous coupled PDEs; one for each of the three motions to be captured. Each of the three PDEs contains three states, v_*, w_*, and ϕ_*, and is a function of one spatial domain, x and one temporal domain, t. The terms pertaining to B_1, B_2, e_0, L_y, L_z and M_ϕ are removed as is commonplace with in-vacuo analyses based on these PDEs [1, 77, 164, 165, 166, 167]. The removal of these terms will simplify the equations which will reduce the computational cost, improve the ease with which the equations can be interpreted and ensure that only the desired physical phenomena are captured. The resulting equations are shown below

$$
\begin{aligned}
-(Tw_*')' + \Big[\underline{-Te_A\phi_*\cos(\theta)} + \underline{(EI_z - EI_y)\cos(\theta)\sin(\theta)v_*''} + [\underline{EI_z\sin^2(\theta)} + EI_y\underline{\underline{\cos^2(\theta)}}]w_*''\Big]'' \\
+ m\ddot{w}_* + \underline{me\ddot{\phi}_*\cos\theta} - \underline{(me\Omega^2 x\phi_*\cos(\theta))'} \\
= \underline{\big(Te_A\sin(\theta)\big)''} + \underline{\big(\Omega^2 mxe\sin(\theta)\big)'}
\end{aligned}
\tag{4.3a}
$$

$$
\begin{aligned}
-\big(Tv_*'\big)' + \Big[\underline{Te_A\phi_*\sin(\theta)} + [EI_z\underline{\underline{\cos^2(\theta)}} + \underline{EI_y\sin^2(\theta)}]v_*'' + \underline{(EI_z - EI_y)\cos(\theta)\sin(\theta)w_*''}\Big]'' \\
+ m\ddot{v}_* - \underline{me\ddot{\phi}_*\sin\theta} - m\Omega^2[v_* - \underline{e\phi_*\sin(\theta)}] + \underline{(me\Omega^2 x\phi_*\sin(\theta))'} \\
= \underline{\big(Te_A\cos(\theta)\big)''} + \underline{\big(\Omega^2 mxe\cos(\theta)\big)'} + \underline{\Omega^2 me\cos(\theta)}
\end{aligned}
\tag{4.3b}
$$

$$
\begin{aligned}
-\Big[Tk_A^2\phi_*'\Big]' - Te_A(w_*''\cos\theta - v_*''\sin\theta) - (GJ\phi_*')' + mk_m^2\ddot{\phi}_* + m\Omega^2\phi_*(k_{m2}^2 - k_{m1}^2)\cos 2\theta \\
+ me\Omega^2 x(w_*'\cos\theta - v_*'\sin\theta) - (\ddot{v}_* - \Omega^2 v_*)\sin\theta + \ddot{w}_*\cos\theta \\
= \big(Tk_A^2\theta'\big)' - m\Omega^2(k_{m2}^2 - k_{m1}^2)\sin(\theta)\cos(\theta)
\end{aligned}
\tag{4.3c}
$$

where internal tension is defined as it was presented in Section 3.1, shown below in Eq. (4.4).

$$
T = \frac{1}{2}\Omega^2 m\big(R^2 - x^2\big) - P \tag{4.4}
$$

The singly underlined terms in Eqs. (4.3a) and (4.3b) are the terms introduced by the inclusion of twist ($\theta \neq 0$) and non-coincident mass and elastic axes ($e \neq 0$, $e_A \neq 0$) that were not present in Section 3.1.2. The doubly underlined terms in Eqs. (4.3a) and (4.3b) are the modifications to terms that previously existed in Eqs. (3.3a) and (3.3b), respectively. If the singly underlined terms were removed and the doubly underlined terms were equal to one, it can be seen that Eqs. (4.3a) and (4.3b) would reduce to Eqs. (3.3a) and (3.3b). The additional equation, Eq. (4.3c), represents the torsional motion and was not present in Chapter 3.

As with the previous model, the principle of separation of variables and an assumed harmonic response is employed with the assumed solution taking the form shown in Eq. (4.5).

$$\begin{aligned} v_*(x,t) &= v(x)e^{st} \\ w_*(x,t) &= w(x)e^{st} \\ \phi_*(x,t) &= \phi(x)e^{st} \end{aligned} \tag{4.5}$$

Once the assumed solution was substituted into Eq. (4.3), the terms that are linearly proportional to e^{st} are gathered to form a set of Ordinary Differential Equations (ODEs) that represent the oscillatory shape of the blade. This process removes the temporal domain and ensures that the equations are suitably formatted for the numerical solver. The resulting set of equations are shown below in Eq. (4.6).

$$\begin{aligned} &-(Tw')' + \Big[-Te_A\phi\cos(\theta) + (EI_z - EI_y)\cos(\theta)\sin(\theta)v'' + [EI_z\sin^2(\theta) + EI_y\cos^2(\theta)]w'' \Big]'' \\ &\qquad + ms^2w + mes^2\phi\cos\theta - (me\Omega^2x\phi\cos(\theta))' = 0 \\ &-\big(Tv'\big)' + \Big[Te_A\phi\sin(\theta) + \big[EI_z\cos^2(\theta) + EI_y\sin^2(\theta)\big]v'' + (EI_z - EI_y)\cos(\theta)\sin(\theta)w'' \Big]'' \\ &\qquad + ms^2v - mes^2\phi\sin\theta - m\Omega^2[v - e\phi\sin(\theta)] + (me\Omega^2x\phi\sin(\theta))' = 0 \\ &-\Big[Tk_A^2\phi'\Big]' - Te_A(w''\cos\theta - v''\sin\theta) - (GJ\phi')' + mk_m^2s^2\phi + m\Omega^2\phi(k_{m2}^2 - k_{m1}^2)\cos 2\theta \\ &\qquad + me\Omega^2x(w'\cos\theta - v'\sin\theta) - (s^2v - \Omega^2v)\sin\theta + s^2w\cos\theta = 0 \end{aligned} \tag{4.6}$$

Finally, these equations were converted from this form, two fourth-order equations and one second-order ODEs, to a set of ten first-order equations to meet the format requirements of the numerical solver described in Section 2.3.1.

4.1.3 Boundary conditions

Similarly to the model and experiment in Chapter 3, cantilevered boundary conditions are enforced to replicate the hub configuration of a bearingless rotor. The field equations for the blade consist of one second-order and two fourth-order equations which necessitate ten boundary conditions to ensure the problem is properly posed. Half of these conditions will enforce a fixed root and the other half shall enforce a free tip, subject to the augmentation due to the applied compressive load.

The fixed boundary condition at the root consists of constraining the displacements and angles of the beam to zero, as seen in Eq. (4.7).

$$\begin{aligned} v_* &= 0 \\ w_* &= 0 \\ \phi_* &= 0 \\ v'_* &= 0 \\ w'_* &= 0 \end{aligned} \tag{4.7}$$

The free boundary conditions at the tip for a traditional cantilevered beam consists of constraining forces and moments at the elastic centre to zero. However, due to the application of the compressive load, the force and moment equilibria are enforced as a balance of internal loads within the blade and the externally applied compressive load as seen in Eq. (4.8)

$$\begin{aligned} M_x &= M_0 e^{st} \\ M_y &= M_0 e^{st} \\ M_z &= M_0 e^{st} \\ F_y &= -P_y \\ F_z &= -P_z \end{aligned} \tag{4.8}$$

Where the internal loads within the blade are defined as in [137].

$$\begin{aligned} M_x &= GJ\phi'_* + Tk_A^2\phi'_* \\ M_y &= \left[EI_y\cos(\theta)^2 + EI_z\sin(\theta)^2\right]w''_* + \left[EI_z - EI_y\right]\sin(\theta)\cos(\theta)v''_* - Te_A\phi_*\cos\theta \\ M_z &= \left[EI_y\sin(\theta)^2 + EI_z\cos(\theta)^2\right]v''_* + \left[EI_z - EI_y\right]\sin(\theta)\cos(\theta)w''_* + Te_A\phi_*\sin\theta \\ F_y &= Tv'_* - M'_z - \Omega^2 mex\sin(\theta)\phi_* \\ F_z &= Tw'_* - M'_y + \Omega^2 mex\cos(\theta)\phi_* \end{aligned} \tag{4.9}$$

The $M_0 e^{st}$ term is used to apply an excitation moment to the tip of the beam in each of the three directions. A moment load was chosen for the in-plane and out-of-plane orientations, as opposed to a transversal force, to provide consistency with the torsional motion.

Once the assumed motion of the blade, as stated in Eq. (4.5), and Eqs. (4.2) and (4.9) are substituted into Eqs. (4.7) and (4.8) the final boundary conditions are formed, as shown in Eq. (4.10).

$$
\begin{aligned}
v(R_0) &= 0 \\
w(R_0) &= 0 \\
\phi(R_0) &= 0 \\
v'(R_0) &= 0 \\
w'(R_0) &= 0 \\
GJ\phi'(R) + Tk_A^2\phi'(R) &= M_0 \\
\left[EI_y\cos(\theta)^2 + EI_z\sin(\theta)^2\right]w''(R) + \left[EI_z - EI_y\right]\sin(\theta)\cos(\theta)v''(R) - Te_A\phi(R)\cos\theta &= M_0 \\
\left[EI_y\sin(\theta)^2 + EI_z\cos(\theta)^2\right]v''(R) + \left[EI_z - EI_y\right]\sin(\theta)\cos(\theta)w''(R) + Te_A\phi(R)\sin\theta &= M_0 \\
Tv'(R) - M_z' - \Omega^2 mex\sin(\theta)\phi(R) + P\frac{v(R)}{(R-R_0)} &= 0 \\
Tw'(R) - M_y' + \Omega^2 mex\cos(\theta)\phi(R) + P\frac{w(R)}{(R-R_0)} &= 0
\end{aligned}
\tag{4.10}
$$

4.2 Model validation

Once the model for the coupled in-plane, out-of-plane and torsional motions of a twisted blade with non-coincident mass and elastic axes and an applied compressive load had been developed, it is verified and validated. After this, it is used to investigate the influence of compressive loading on the natural frequencies of rotor blades. The verification and validation shall be performed using existing results from other, independently developed, models and then by comparison with a Finite Element (FE) model.

4.2.1 Validation using existing results

The model shall be used to compare the results of two different models that are based on the same set of PDEs. The first comparison will be with a model of an untwisted non-rotating blade before proceeding to compare the present model to a model that incorporated twist and rotation.

4.2.1.1 Non-rotating model comparison

The first set of validation results to be used are those of *Murthy* [1] that were created using a model based on the same PDEs [137] but without the applied compressive load and solved using a transmission matrix method. The parameters of the beam used are described below in Table 4.1.

Table 4.1: Blade properties for non-rotating model comparison

Property	Value
Mass distribution, m [m]	0.863
Out-of-plane bending rigidity, EI_y [Nm^2]	71.77
In-plane bending rigidity, EI_z [Nm^2]	215.32
Torsional rigidity, GJ [Nm^2]	25.84
Radius, R [m]	1.016
Root cutout, R_0 [m]	0
Rotor speed, Ω_0 [rad s^{-1}]	0
Root pitch, $\theta(R_0)$ [rad]	0.785
Linear twist, δ [rad]	0
Mass radii of gyration about the major axis, k_{m1} [m]	0.0254
Mass radii of gyration about a perpendicular axis, k_{m2} [m]	0.0254
Polar radius of gyration, k_A [m]	0
Mass-elastic offset, e [m]	0.0359
Area-elastic offset, e_A [m]	0

It can be seen from the blade properties that these results will not capture the effect of twist and rotation. However, the inclusion of an offset between the mass and elastic axes ($e \neq 0$) will induce coupling between the different motions. A comparison of the natural frequencies calculated from the two models is shown below in Fig. 4.2.

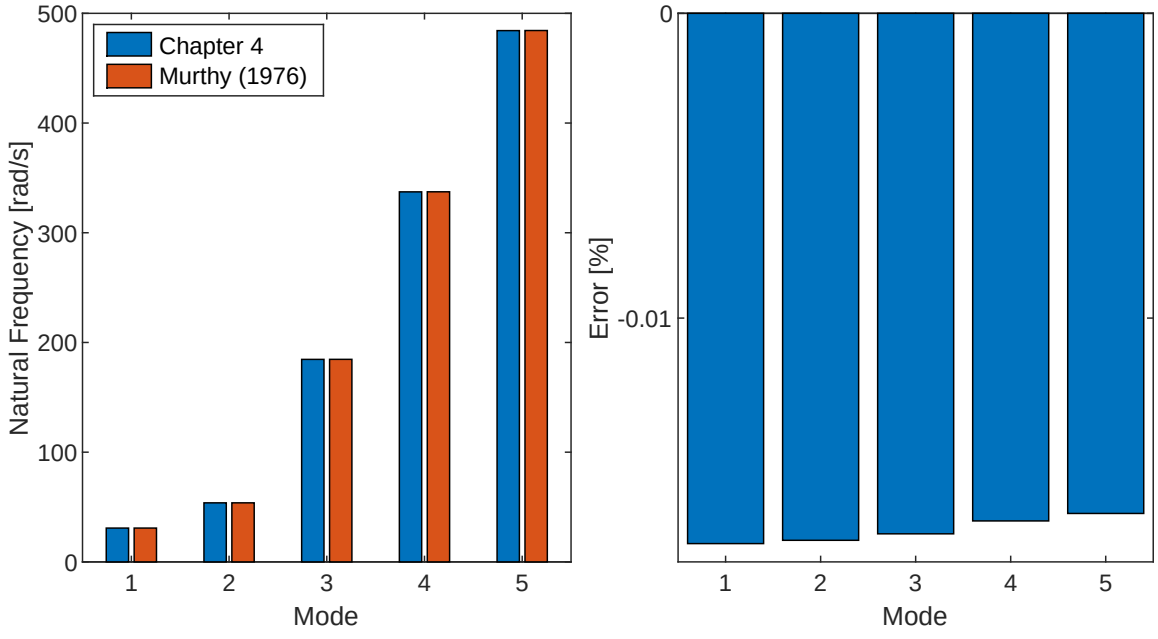

(a) Frequencies (b) Errors

Figure 4.2: Comparison of natural frequencies calculated from the present model and that of [1].

It can be seen that the natural frequencies calculated from the two models agree very well

which indicates that the present model was correctly implemented. In addition, the mode shapes that were provided are also compared, as seen in Fig. 4.3, and the correlation quantified using the Modal Assurance Criterion (MAC) [157].

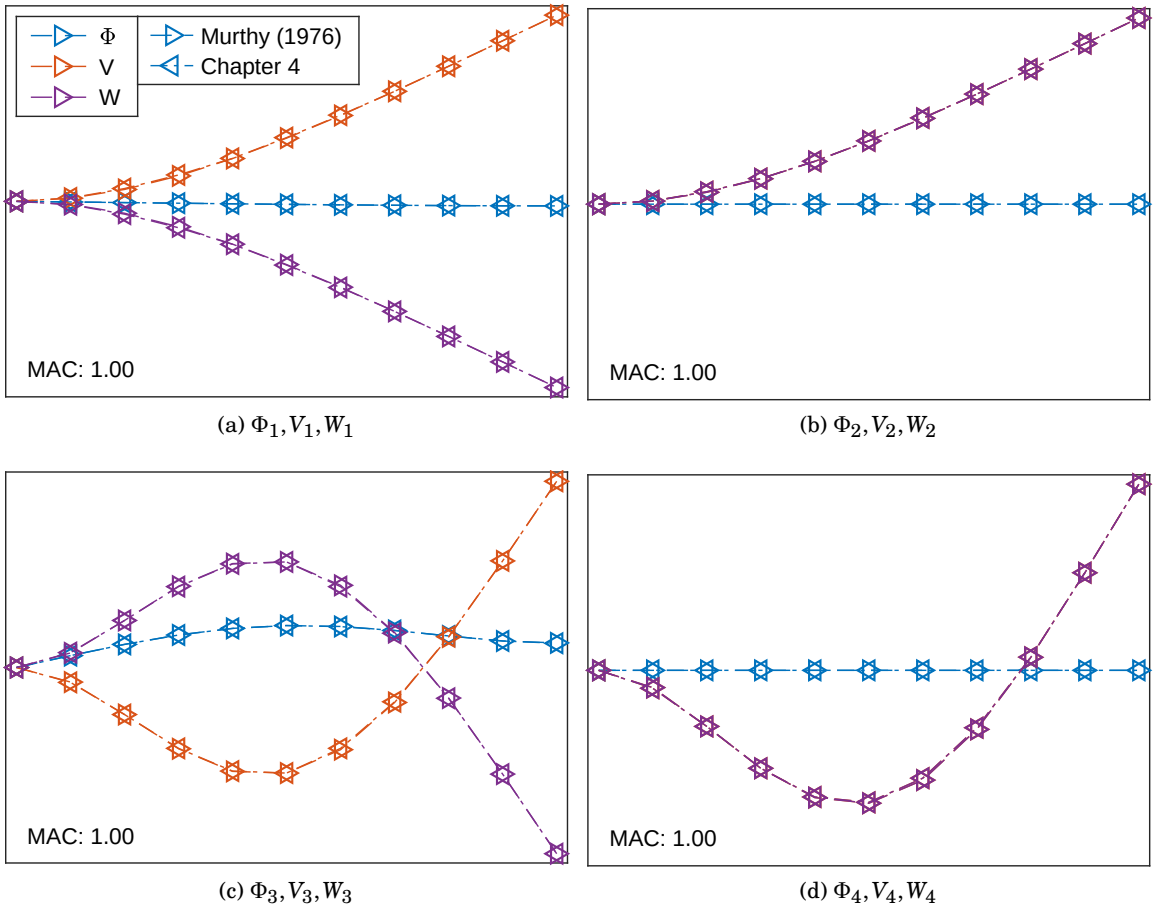

(a) Φ_1, V_1, W_1 (b) Φ_2, V_2, W_2

(c) Φ_3, V_3, W_3 (d) Φ_4, V_4, W_4

Figure 4.3: Comparison of the mode shapes calculated from the present model and that of [1].

As can be seen from the visual correlation between the mode shapes, and the corresponding MAC values, the agreement between the two models, both in terms of natural frequencies and mode shapes is excellent. This gives confidence that the model has been correctly implemented and is able to capture the effects of non-coincident mass and elastic axes.

4.2.1.2 Rotating model comparison

The second set of existing results to be compared are those of *Isakson and Eisley* [2] that were created using a model that was also based on the same PDEs [137] but solved using a Holzer-Myklestad type method. The parameters of the beam used are described below in Table 4.2.

Table 4.2: Blade properties for rotating model comparison

Property	Value
Mass distribution, m [m]	1.089
Out-of-plane bending rigidity, EI_y [Nm^2]	1.371×10^3
In-plane bending rigidity, EI_z [Nm^2]	1.371×10^4
Torsional rigidity, GJ [Nm^2]	1.581×10^3
Radius, R [m]	1.5
Root cutout, R_0 [m]	0
Rotor speed, Ω_0 [rad s^{-1}]	273.2
Root pitch, $\theta(R_0)$ [rad]	0.524
Linear twist, δ [rad]	-0.524
Mass radii of gyration about the major axis, k_{m1} [m]	0.00703
Mass radii of gyration about a perpendicular axis, k_{m2} [m]	0.115
Polar radius of gyration, k_A [m]	0.0233
Mass-elastic offset, e [m]	0.0164
Area-elastic offset, e_A [m]	0.0164

Additionally, it should be noted that unlike the present work, where B_1 and B_2 are set to zero and removed, this was not the case for the reference work. The blade parameters used in this model include the effects of centrifugal forces due to rotation and twist, which were not present in Section 4.2.1.1, in addition to an offset between the mass and elastic axes. The mode shapes were not provided in the reference data, therefore only the natural frequencies for the two configuration can be compared, as seen in Fig. 4.4.

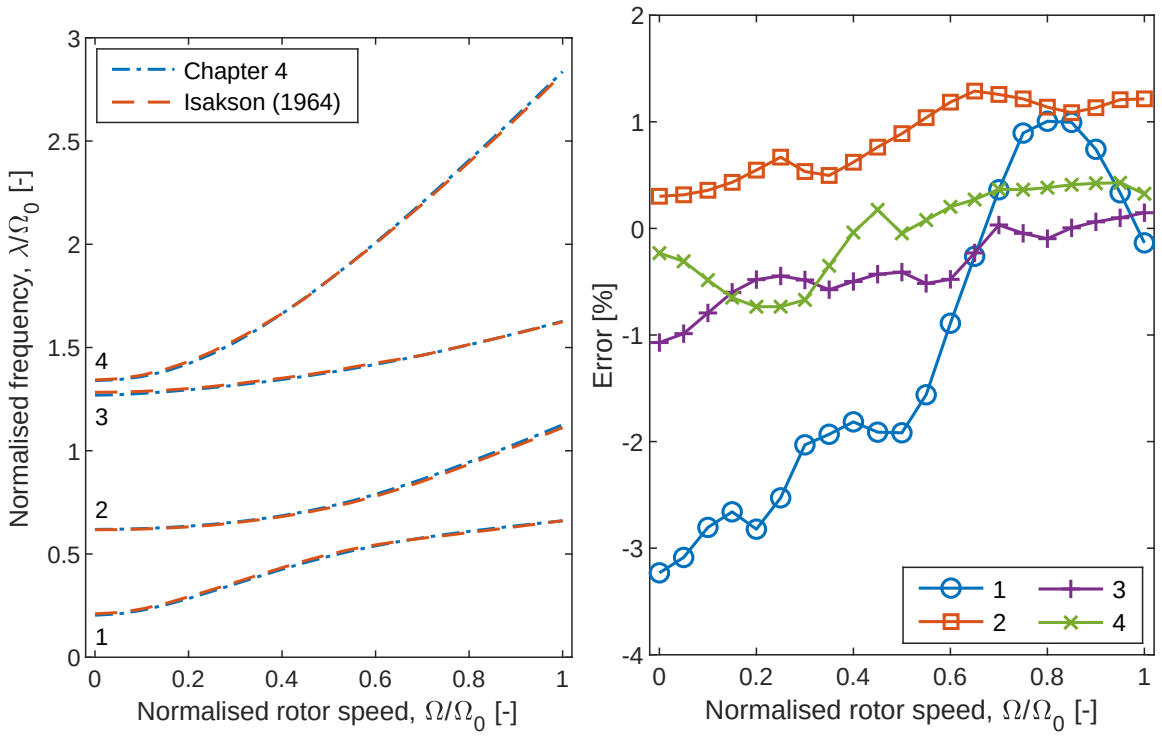

(a) Frequencies

(b) Errors

Figure 4.4: Comparison of the natural frequencies calculated from the present model and that of [2].

It can be seen that the introduction of the centrifugal loads associated with rotation and the effect of twist have induced significant veering interactions [43, 44] between the first and second mode. The effects have successfully been captured by the current model with almost all the errors being smaller than 3 % and the errors within the rotor speed of interest for variable speed rotors (0.6 to 1.0) being less than 2 %.

The correlation observed between the comparisons of the mode shapes and natural frequencies of the current model with two different models, as observed in Figs. 4.2 to 4.4, indicates that the present model has been correctly implemented and is capable of capturing the coupling effects of twist and non-coincident mass and elastic axes as well as the effects of centrifugal loading due to rotation.

4.2.2 Validation using finite elements

Whilst the comparisons performed in Section 4.2.1 verify the implementation of the underlying beam model, they did not include the compressive load. Therefore, an FE model that includes the compressive force shall be developed and used to verify the implementation of the compressive load in the present model. Firstly, the blade to be analysed and then the development of the FE

model shall be described before a comparison of the results provided by the two models is made.

4.2.2.1 Test blade description

The blade used for this validation study was designed to exhibit all of the effects that the model is capable of capturing, such as twist and non-coincident mass and elastic axes. The cross-section of this blade can be seen below in Fig. 4.5. The cross-sectional properties of the blade are calculated using a 2D FE solver, SaaS ShapeDesigner [168]. These properties and the operating conditions of the blade are summarised in Table 4.3.

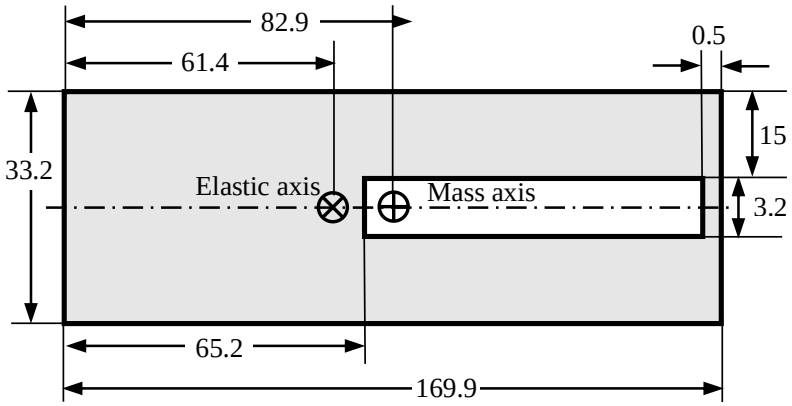

Figure 4.5: Cross-section geometry of FE test blade

Table 4.3: Blade properties for test blade. Additional properties are calculated as per the equivalences detailed in Appendix C

Property	Value
Mass distribution, m [m]	14.32
Out-of-plane bending rigidity, EI_y [Nm^2]	3.57×10^4
In-plane bending rigidity, EI_z [Nm^2]	8.90×10^5
Torsional rigidity, GJ [Nm^2]	3.90×10^4
Radius, R [m]	5.5
Root cutout, R_0 [m]	0.5
Mass-elastic offset, e [m]	-0.0215
Root pitch, $\theta(R_0)$ [rad]	0.28
Linear twist, δ [rad]	-0.14
Rotor speed, Ω_0 [rad s^{-1}]	50
Critical compressive force, P_c [N]	73.64×10^3
Maximum compressive force, P_m [N]	55.23×10^3

The cross-sectional shape is a hollow box section with a single line of symmetry along the major axis. This shape was chosen as it adheres to the singly symmetric assumption used in the PDEs that formulate the basis of the model and it induces an offset between the mass and

elastic axes whilst ensuring that the cross-section remains closed. A closed cross-section is what is typically observed in rotor blades and also ensures the offset between the mass and elastic axes is similar to that of a realistic blade. Remaining geometric dimensions were sized such that the blade exhibits similar structural properties to that of a realistic blade.

4.2.2.2 Finite element model

The full 3D FE model is developed using ABAQUS [169], a well-established FE package that has been extensively validated and used throughout industry.

The geometry, as defined in Section 4.2.2.1, is imported into the model and the material properties are defined as those stated in Appendix C. The cross-section is subsequently partitioned into a series of rectangles, as seen in Fig. 4.6, to improve meshing and ensure a node was present at the elastic axis of the beam.

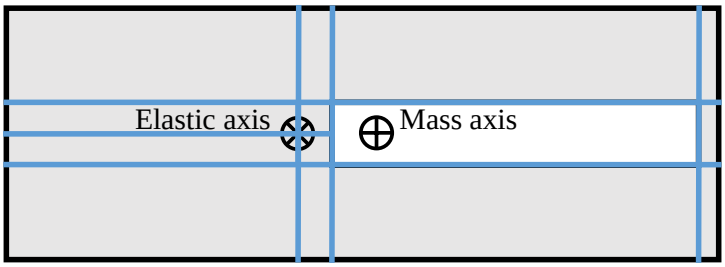

Figure 4.6: Partitioning of FE test blade cross-section

The geometry is subsequently meshed using the C3D8R element which is a general-purpose linear brick element, with reduced integration for improved computational efficiency. The mesh is generated using a top-down swept mesh technique which is possible due to the partitioning of the cross-section into simple quadrilaterals.

To capture the boundary conditions at the root, all rotations and displacement at the root are constrained to zero. To capture the boundary conditions at the tip, the applied force is applied in its decomposed form, as described in Section 4.1.1. P_x is applied as a constant concentrated force at the elastic axis at the tip. P_y and P_z are applied as springs of stiffness $\frac{P}{(R-R_0)}$ attached to the elastic axis also at the tip. Additionally, a rotational force is applied to the beam to capture the effects of the centrifugal forces associated with rotation. The aforementioned forces are applied during a general static solution step which is followed by a linear perturbation step to calculate the natural frequencies of the system.

To ensure the mesh is sufficiently fine that the results would be accurate, a mesh convergence study is performed. Initially, a coarse element size of 0.016 m, as seen in Fig. 4.8a, is used to calculate the first seven frequencies of the blade at its maximum rotor speed and compressive load value. The analysis is repeated using an element size that is half the size of the previous

iteration; approximately equivalent to an eight-fold increase in the number of elements. This process is repeated until all the modes in consecutive iterations are converged to within 1 %. The convergence history of these frequencies are shown below in Fig. 4.7.

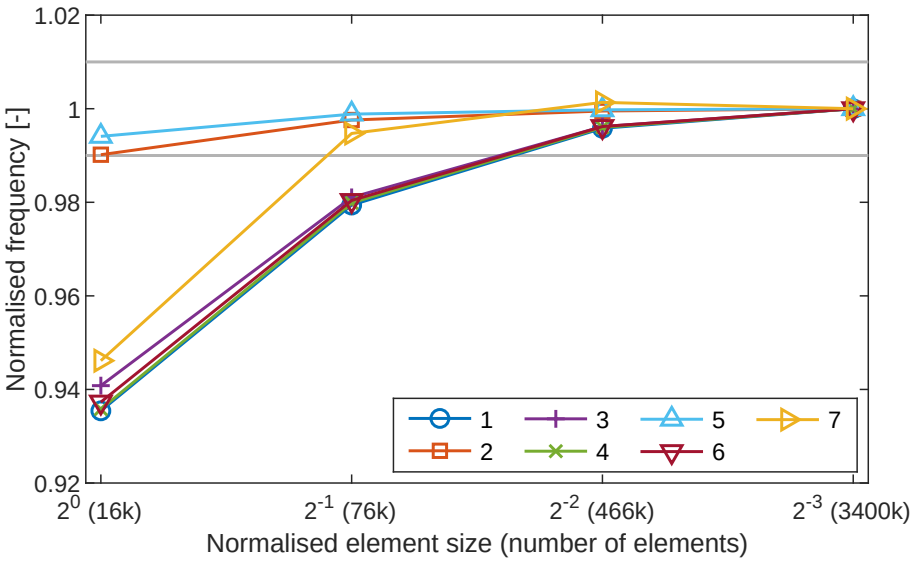

Figure 4.7: Mesh convergence of first seven modes in FE model.

It can be seen that two of the modes are sufficiently converged with the initial coarse mesh, however, a mesh of elements one-quarter of this size is required to ensure all of the modes are sufficiently converged. The final mesh used shall be using elements of size 0.04 m, as seen in Fig. 4.8b that result in a mesh containing 466 000 elements.

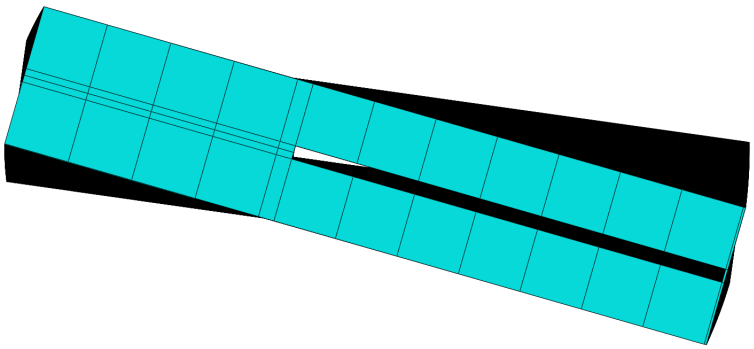

(a) Initial sectional mesh

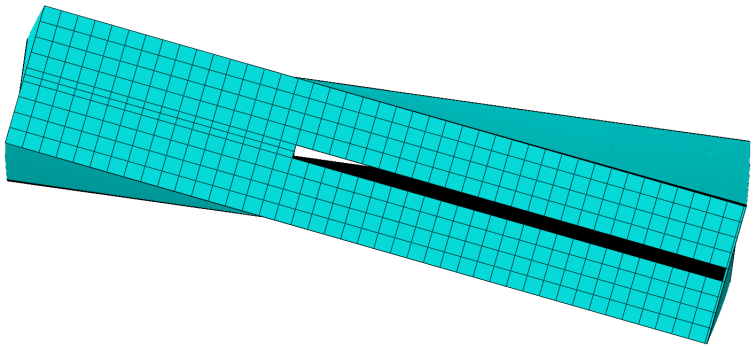

(b) Final sectional mesh

Figure 4.8: Test beam meshed with coarse and fine mesh.

Once the mesh is suitably converged the FE model can be used to calculate results to compare with that of the present model.

4.2.2.3 Results comparison

Once developed, the FE is used to calculate the natural frequencies and mode shapes of the test blade across a range of rotor speeds and compressive loadings. These results are compared with equivalent results calculated from the present model and used to validate it.

Firstly, the natural frequencies of the blade rotating at 60 % to 100 % of the nominal rotor speed with no compressive loading and with maximal compressive loading are compared in Fig. 4.9.

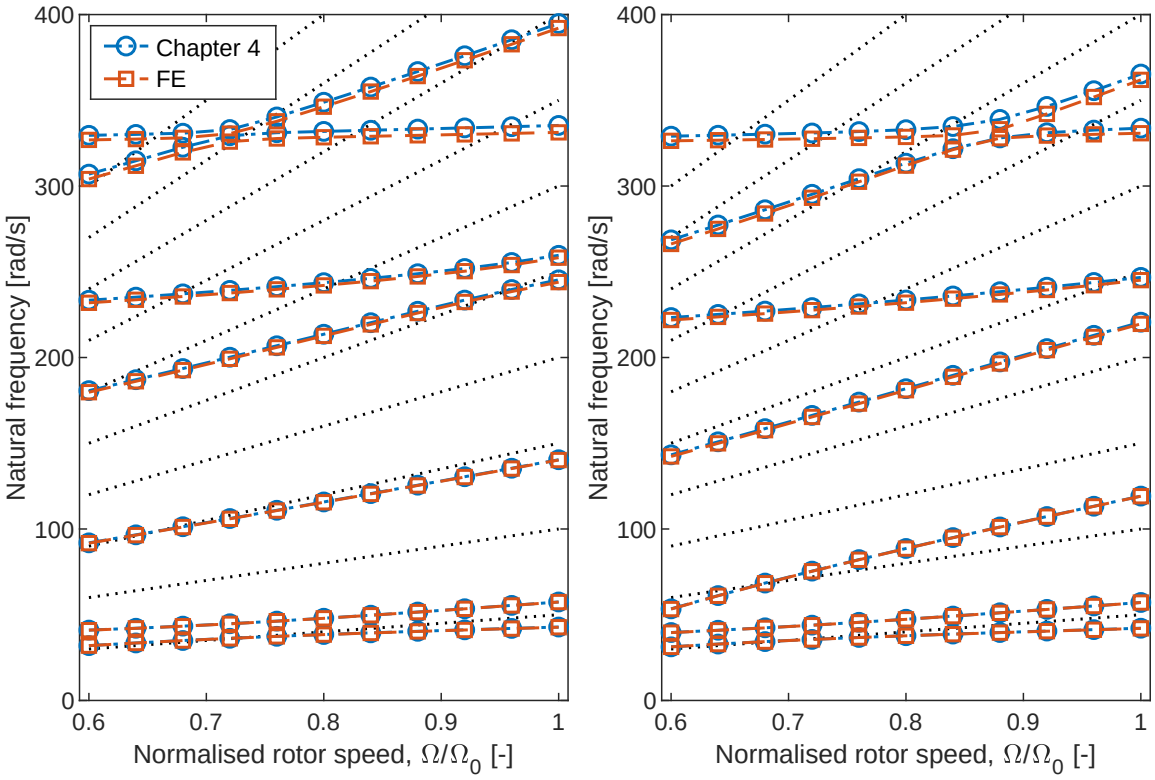

(a) Unloaded

(b) Loaded

Figure 4.9: Comparison of fan diagrams calculated using present and FE model.

It can be seen that the present model is able to capture the effects observed in the FE model well. The main difference to be observed is at higher frequencies where the present model slightly overpredicts the value of natural frequency. This overprediction is due to the omission of rotary inertia and transverse shear in the present model that is based on Euler-Bernoulli beam theory which is known to result in an overprediction of the natural frequencies of higher modes [136]. The errors in the natural frequency for each mode are shown below in Fig. 4.10.

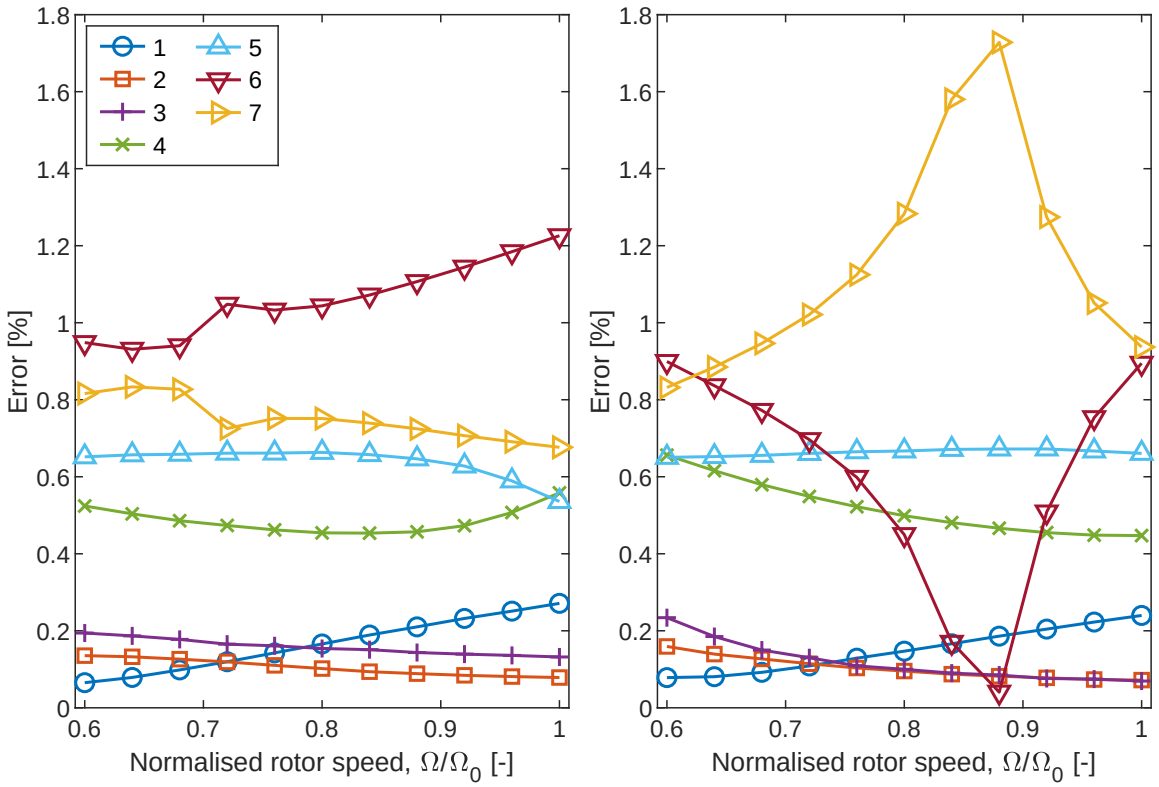

(a) Unloaded

(b) Loaded

Figure 4.10: Errors in natural frequencies calculated using present and FE model.

It can be seen that each of the modes calculated is overpredicted by the present model, however, these errors are low (<1.8 %) for all modes across the full range of rotor speeds and compressive loads. Additionally, the overprediction in the higher modes results in a slight shift of the rotor speed at which veering occurs which causes a symmetric reduction/increase of the errors of these modes.

In addition to comparing the natural frequencies, the mode shapes calculated by the two models are compared. These comparisons are performed at two conditions; the slowest rotor speed with no compressive loading and at the highest rotor speed with the maximum compressive loading.

To calculate the 1D mode shapes from the results of the 3D FE model, the displacement at the outermost corners of the cross-section are extracted for each radial station. The values at each radial station are then used to calculate the in-plane, out-of-plane and torsional deformation at the elastic axis that would correspond to the same displacements at the corners of the cross-section as those extracted from the 3D FE model.

The MAC comparison of these mode shapes, as seen in Fig. 4.11, demonstrates the ability of the model to calculate mode shapes.

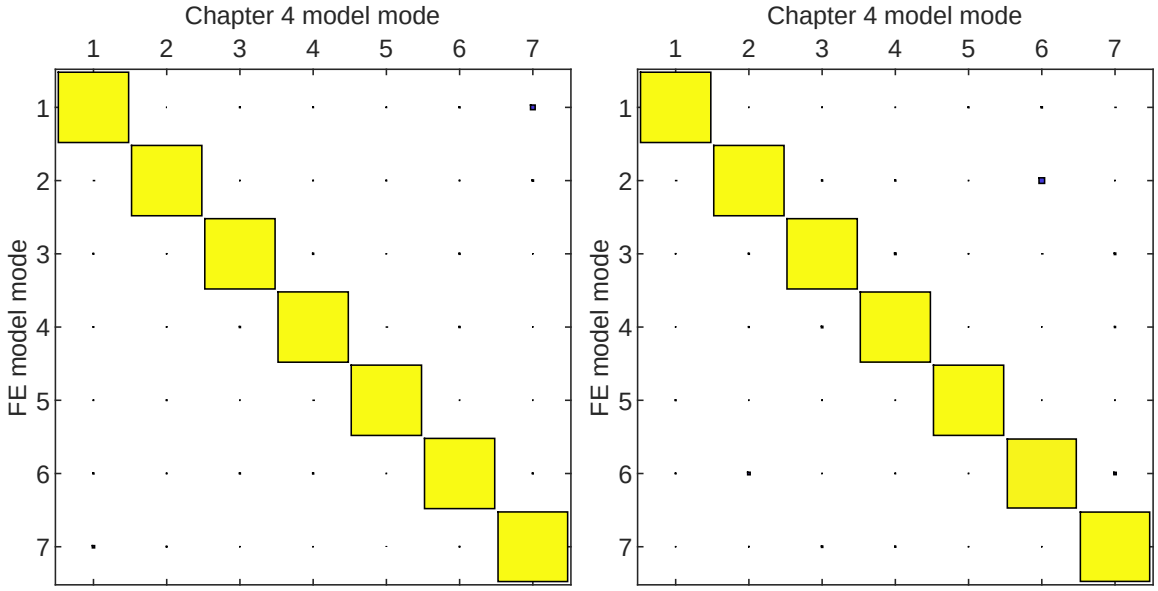

(a) Ω/Ω_0=60 %, P/P_m=0 % (b) Ω/Ω_0=100 %, P/P_m=100 %

Figure 4.11: MAC comparison of mode shapes calculated using present and FE model.

It has been shown that the present model is able to replicate natural frequencies and mode shapes calculated from a variety of external publications and that of a 3D FE model. These comparisons were performed across a wide range of rotor speeds and compressive loading values on blades that capture the effects of twist, non-coincident mass and elastic axes as well as torsional motion. The accuracy with which these results correlate gives confidence that the model has been developed and implemented correctly and is suitable for modelling the desired physical phenomena.

4.3 In-vacuo case study

With the development and validation of a model that includes twist, non-coincident mass and elastic axes as well as torsional motion, the main geometric features that influence the dynamic behaviour of a rotor blade are captured. Therefore, case studies to analyse the capability of compressive loading to avoid resonance in variable speed rotors for a range of aircraft are performed in this section.

Herein, the effects and significance of the additional capabilities of the model described in Section 4.1 to those of the model used in the previous chapter, Chapter 3, shall be assessed. Then, the resonances limiting the possible variable rotor speed operation for each of the three test aircraft described in Appendix C (MBB Bo105, Westland Lynx and Westland AW101) shall be identified. Subsequently, in-vacuo buckling analyses shall be performed to calculate the maximum allowable limit of the compressive loading for each aircraft. Finally, the optimal compres-

sive loading to reduce the identified resonances across a range of rotor speeds shall be calculated and the range of operational rotor speeds available will be compared with that of a rotor blade without compressive loading.

4.3.1 Implications of inter-directional coupling on the dynamic properties of a rotor blade

The model described in Section 4.1 includes the effects of twist, non-coincident mass and elastic axes as well as torsional motion, which were not captured by the model used in Chapter 3. The effects of these additional geometric features result in a model that is able to more accurately calculate the natural frequencies of a realistic rotor blade. Therefore, a brief study into the effects of the inclusion of torsional motion, twist and non-coincident mass and elastic axes shall be performed using the MBB Bo105 blade described in Appendix C.

Firstly, the present model is used, without the presence of twist or a non-coincident mass and elastic axes ($\theta(R_0) = 0$, $\delta = 0$, $e = 0$, $e_A = 0$), to calculate the natural frequencies of the blade over a range of rotor speeds. The model described in Section 4.1 is used to calculate the natural frequencies for the same range of rotor speeds, as seen in Fig. 4.12.

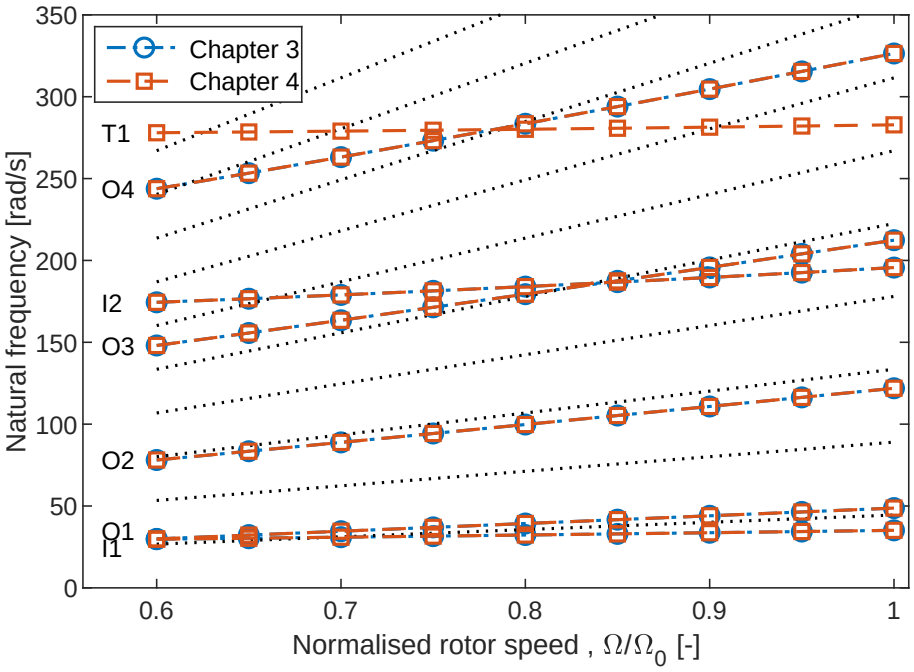

Figure 4.12: Comparison of fan diagrams for Bo 105 blade calculated using the present model and that of the previous chapter.

It can be seen that due to the exclusion of twist and a non-coincident mass and elastic axes, the two models provide identical results. The exception is that the inclusion of torsional motion

allows the present model to capture the first torsional mode (T1) as well as the original out-of-plane modes (O1-O4) and in-plane modes (I1-I2).

The present model is subsequently used to calculate the natural frequencies with the inclusion of collective pitch and twist. The collective pitch as defined as that of the maximum value the aircraft is capable of [122], $\theta(R_0) = 0.262$, to accentuate its influence and twist is defined as stated in Appendix C. The comparison of these natural frequencies for the untwisted and twisted cases are shown below in Fig. 4.13.

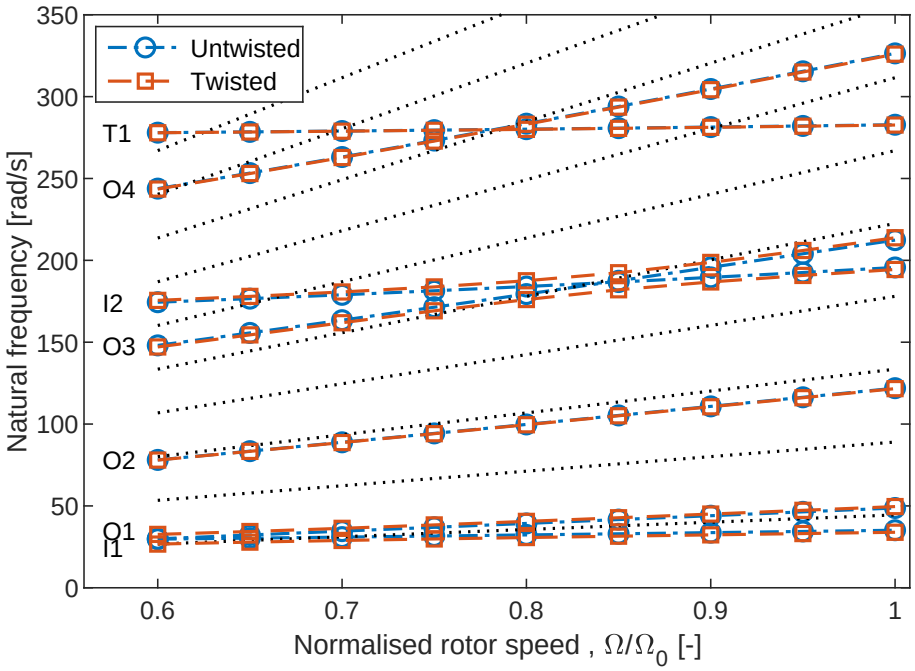

Figure 4.13: Comparison of fan diagrams for Bo 105 blade with and without twist.

It can be seen that the inclusion of twist results in some interaction between the in-plane and out-of-plane modes that were not observed previously. This is most noticeable in the interaction between the third out-of-plane mode and the second in-plane mode at rotor speeds between 0.7 and 1 but can also be seen in the interaction between the first in-plane mode and the first out-of-plane mode at rotor speeds between 0.6 and 0.8. In these regions, modes that previously crossed each other veer away from each other and continue along the trajectory of the other mode due to a phenomenon known as veering [43, 44]. For the second out-of-plane mode, which has no neighbouring in-plane modes, there is no change in behaviour. For the crossing of the fourth out-of-plane modes and the first torsional mode, there is no interaction in either the untwisted or twisted case. This behaviour would indicate that twist introduces coupling between in-plane and out-of-plane motion but has minimal impact on the coupling between torsional and out-of-plane motion.

Finally, the offset between the mass and elastic axes stated in Appendix C is introduced, as

seen in Fig. 4.14

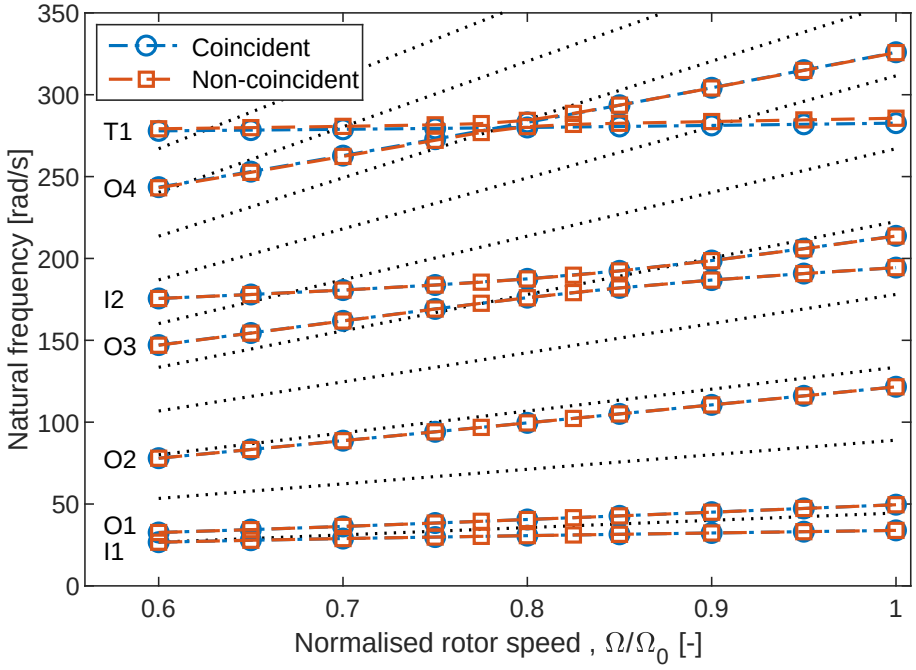

Figure 4.14: Comparison of fan diagrams for Bo 105 blade with coincident and non-coincident mass and elastic axes.

It can be seen that the introduction of a non-coincident mass and elastic axes influences the torsional motion of the blade but has minimal impact on the other motions. Due to the offset between the mass axes and the elastic axes (about which the torsional motion occurs), the rotational inertia is increased which causes the slight reduction in torsional natural frequency. Additionally, veering is observed between the fourth out-of-plane mode and first torsional mode. However, unlike the veering introduced by twist, this veering appears only with the torsional motion and the range of rotor speed that it effects is much smaller.

It can be seen from this brief investigation that the inclusion of twist and non-coincident mass and elastic axes introduces coupling between different motions. Twist introduces significant coupling between the in-plane and out-of-plane motions of the blade, the two most prominent transversal motions. A non-coincident mass and elastic axes introduces coupling between the out-of-plane and torsional motions, but over a much smaller range of rotor speeds.

4.3.2 In-vacuo resonant behaviour in a blade without compression

One of the main issues impeding the implementation of variable rotor speeds in rotorcraft is that of the resonance encountered at different rotor speeds, as discussed in detail in Section 1.2.2.2. Therefore, an assessment is made of the resonances encountered in each of the three aircraft described and defined in Appendix C: the MBB Bo 105, the Westland Lynx, and Westland AW101.

These aircraft exhibit a varying set of uses, sizes and performance characteristics which is reflected in their blade properties.

Firstly, the parameters of the case study shall be defined. The blade properties shall be defined using the required parameters from Appendix C and the collective pitch is again defined as that of the maximum value the Bo105 [122], $\theta(R_0) = 0.262$, to accentuate its influence. Whilst some studies looking at the performance benefits have found that reductions of 10 % to 20 % achieved significant performance improvements [16, 25, 11], the range of rotor speeds considered will be 60 % to 100 % of the nominal value to replicate the larger 40 % reduction of the Boeing A160T Hummingbird [28].

Firstly, the natural frequencies of the blades of the three test aircraft are calculated across the prescribed range of rotor speeds using the model described in Section 4.1. These frequencies are then used to identify the rotor speeds at which a resonant interaction between a mode and a rotor harmonic will occur, as shown in Fig. 4.15.

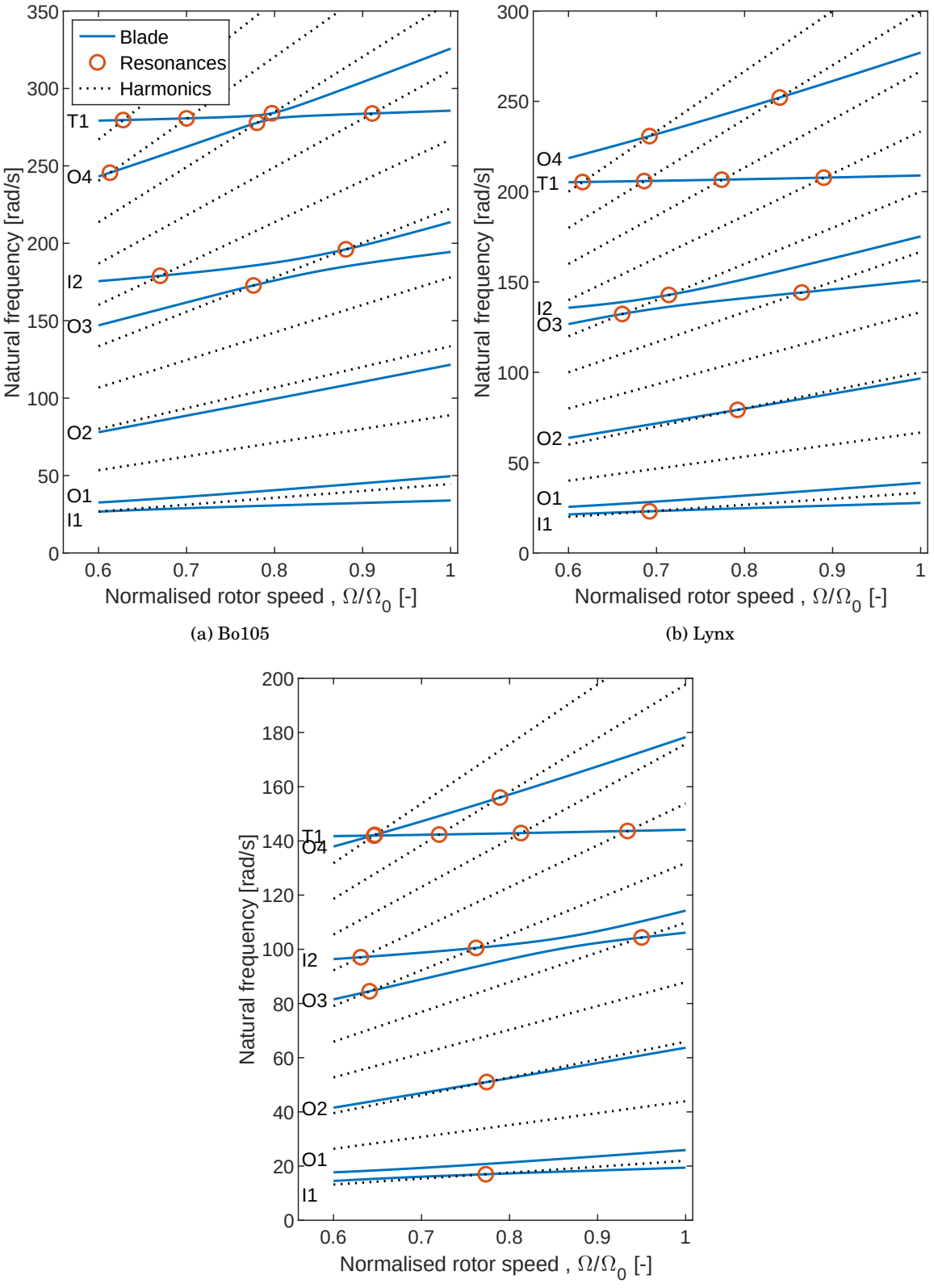

(a) Bo105

(b) Lynx

(c) AW101

Figure 4.15: Fan diagram for each test aircraft highlighting resonances.

It can be seen here that several resonant interactions are observed in each of the test aircraft. An observation that is common across each of the aircraft is that there are more resonances observed in the higher modes. This is because the natural frequencies of the lower modes of the blades track somewhat parallel to their nearest rotor harmonic. For example, Eq. (A.11) can be used to show that the asymptotes of the natural frequencies for the first in-plane and first two out of plane of a rotor blade, regardless of mass and stiffness, will be $\sim 0.5/rev$, $\sim 1.1/rev$ and $\sim 2.5/rev$ as the rotor speed increases. Therefore, as the natural frequencies for these modes start either side of the harmonic above their asymptotic value, they will typically cross one resonance as observed in Fig. 4.15. Conversely, the higher-order modes, such as the second in-plane mode have a natural frequency between the $6/rev$ and $8/rev$ harmonic at the lowest rotor speed but asymptotically tend towards $\sim 2.3/rev$ which means there are many more harmonics which may be crossed and therefore interacted with. This is evidenced in Fig. 4.15 with these higher modes exhibiting between one and four resonances. Additionally, the resonance of the first in-plane mode of the AW101 observed in Fig. 4.15c is likely unrealistic. Due to the fixed root boundary condition in the model, which differs from the articulated rotor observed in the AW101, the natural frequencies of the first in-plane mode is significantly higher than is realistic.

As the separation between natural and excitation frequencies is a commonly used design metric for avoiding resonance in rotor blades [68, 6], it shall also be used to evaluate resonance in the blades in more detail. This Modal Separation (MS) is quantified by calculating the separation between the natural frequency and the nearest harmonic, defined as follows.

$$\epsilon_i(\Omega) = \frac{\min(|\lambda_i(\Omega) - n\Omega|)}{\Omega} \tag{4.11}$$

The minimum of these values across each of the modes considered, herein referred to as Minimum Modal Separation (MMS), is the metric that determines the proximity of resonance.

The MS and MMS calculated from the natural frequencies and harmonics shown in Fig. 4.15 are shown in Fig. 4.16. Alongside the separation values, an acceptable level of separation, defined as 10 % of the rotor speed is shown [6]. This value can be used to determine which rotor speeds are sufficiently free from resonance to be used in operation.

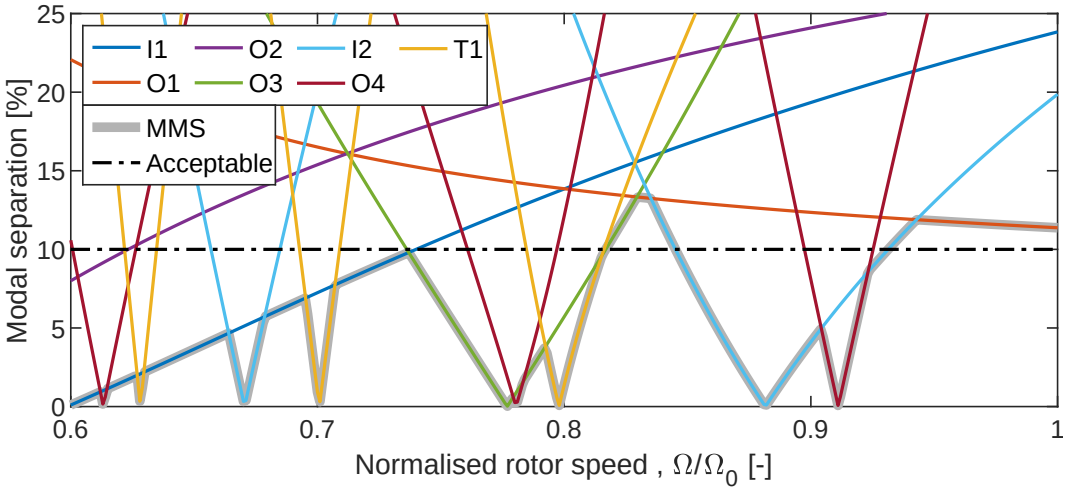

(a) Bo105

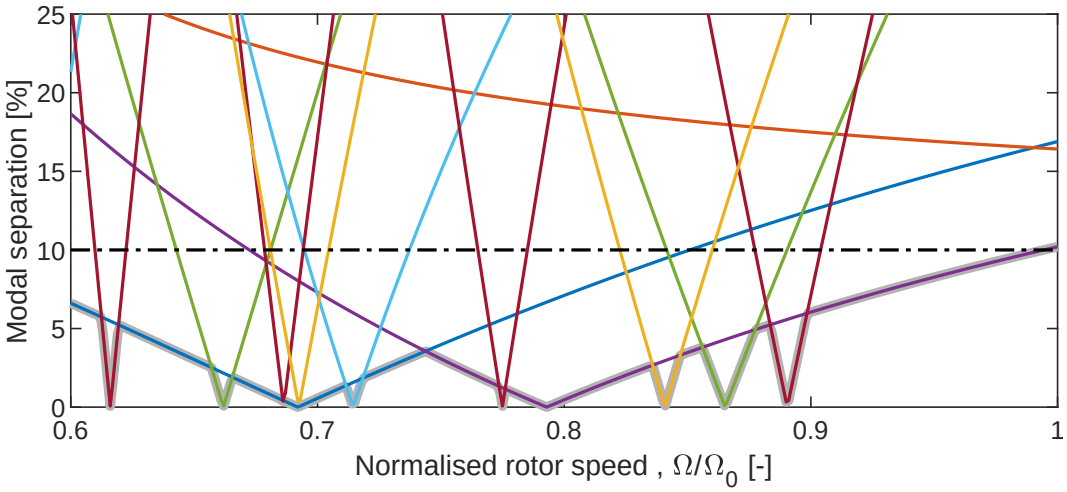

(b) Lynx

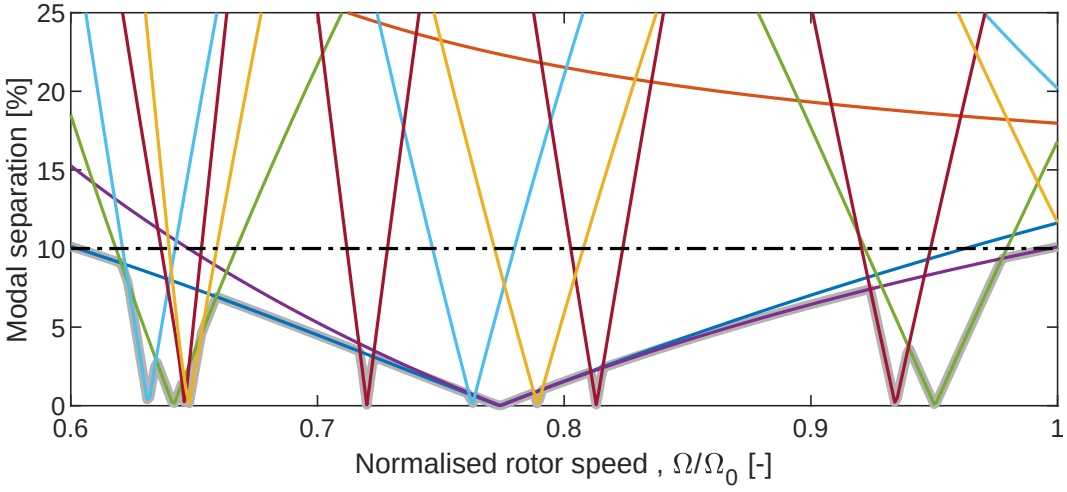

(c) AW101

Figure 4.16: Modal separation, normalised against rotor speed, for each mode across range of rotor speeds for each test aircraft.

It can be seen that the MMS is below the acceptable value for the overwhelming majority of the desired rotor speed range for the Lynx (between 60 % and 99.4 %) and AW101 (between 60.3 % and 99.6 %). The Bo105 has two rotor speed regions which have an acceptable value of MMS for operation; between 81.7 % and 84.5 % and between 93.2 % and 100.0 % of the nominal. This results in a total of 24.0 % of the desired rotor speed range being available and would require transitioning through a relatively large rotor speed range with unacceptable modal separation values if both regions are to be utilised. This lack of separation between natural and excitation frequencies across a range of rotor speeds is the source of the resonant interactions that inhibit the deployment of variable speed rotors. Therefore, the use of the applied compressive load shall be considered to increase the value of MMS across the desired range of rotor speeds.

It can be seen in Fig. 4.16 that the MMS value is dictated by different modes at different rotor speeds which signifies that the ability to alter the frequencies of multiple modes may be necessary to ensure a wide range of operational rotor speeds are available. Additionally, whilst the higher-order modes are responsible for more resonant interactions, as shown in Fig. 4.15, they cross the harmonic with which they are interacting more acutely which results in a small range of rotor speeds being affected by each resonant interaction. Conversely, the lower modes, whilst exhibiting fewer resonant interactions, preclude a larger range of rotor speeds than the higher modes. For example, in both the Lynx and AW101, the combination of the first in-plane mode and second out-of-plane mode alone would preclude the same range of rotor speeds as when the full set of modes is considered. Considering this, and the fact that lower harmonics contain more energy to excite these modes, as demonstrated in flight tests of a CH-53A [47], means that avoiding resonance in the lower order modes may be key to the success of this resonance avoidance system.

4.3.3 In-vacuo resonance avoidance using compressive loading

The results presented herein were presented in part in [153]

To avoid the resonant interactions observed across the desired range of rotor speeds that were demonstrated in Section 4.3.2, the ability of compressive loading to alter the natural frequencies shall be utilised to increase the range of rotor speeds that are safe to be operated in. Firstly, the maximum compressive load to be considered is calculated. Subsequently, a study to avoid the resonance of a single-mode, and then two modes concurrently, shall be performed to gain insight into the behaviour of the optimisation results. A detailed study of how the compressive loading performs as a means of resonance avoidance for the resonances that filter through to the fuselage and for the resonances that influence the blade shall be performed. To conclude, a comparison of the resonance avoidance performance for each different test aircraft shall be performed.

The upper limit of compressive loading considered in this case study is 75 % of the critical buckling loading, as specified in Section 4.3. Similarly, the buckling load of a beam can be defined

as the load at which the lowest natural frequency reaches zero [114, 111]. The variation of the natural frequencies of the lower modes with compressive load is shown below, in Fig. 4.17, alongside a summary of the critical buckling load and maximum applied load for each aircraft summarised in Table 4.4.

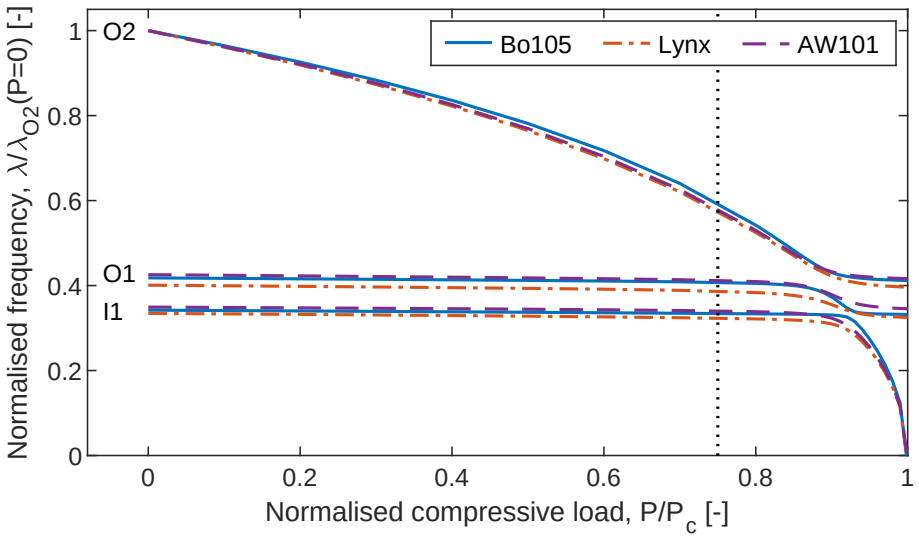

Figure 4.17: Natural frequencies of the lower under compressive loading up to the buckling load.

Table 4.4: Buckling and maximum allowable loads for each aircraft

Aircraft	MBB Bo105	Westland Lynx	Westland AW101
Critical compressive force, P_c [N]	21.15×10^3	24.27×10^3	34.46×10^3
Maximum compressive force, P_m [N]	15.86×10^3	18.20×10^3	25.85×10^3

Critical compressive force, P_c [N] Maximum compressive force, P_m [N]

Unlike Section 4.3, the first in-plane and first two out-of-plane modes are shown. For each test aircraft, it can be seen that the second out-of-plane is initially higher for the unloaded case. As the compressive loading increases, the second out-of-plane mode decreases more abruptly and veers with the first in-plane and out-of-plane modes. The veering is due to the coupling that is caused by the non-coincident mass and elastic axes and twist.

The cause of this behaviour is likely to be the orientation of the applied load. As observed in Section 4.3, the fundamental in-plane and out-of-plane modes exhibit very low levels of sensitivity to the compressive loading. Consequently, the buckling mode becomes the next lowest mode, the second out-of-plane mode. As the focus of this study was to identify the critical buckling load for the purposes of identifying an upper limit to the compressive loading, no further stability investigations shall be performed.

When compared to the values calculated in Chapter 3, as seen in Table 3.2, it can be seen that the values in Table 4.4 are lower by between 0.2 % to 1.3 %. This is expected, as beams

which exhibit coupled bending-torsion motions may buckle at lower loads than beams with pure flexural or torsional modes [111].

Once the upper limit for the buckling load is defined, the resonance avoidance capability of the compressive loading is assessed. Unlike the case study performed in Chapter 3, where the sensitivity of each mode of each test aircraft to the compressive loading was investigated, a more realistic study shall be employed that focuses on the problematic modes at each rotor speed. The inclusion of torsional motion and twist in the model allows for a more realistic representation of the blade and therefore a more accurate calculation of its natural frequencies. Due to this increased realism, the separation between natural and excitation frequencies becomes pertinent. Herein, the improvements in the MMS observed in the unloaded rotor blade, as described in Section 4.3.2, that are available due to compressive loading shall be demonstrated.

The natural frequencies of each blade across a range of rotor speeds, as seen in Fig. 4.15, are calculated for a range of compressive loads up to P_m. Consequently, the modal separation for each mode becomes a function of compressive loading as well as rotor speed and is defined as follows.

$$\epsilon_i(\Omega,P) = \frac{\min(|\lambda_i(\Omega,P) - n\Omega|)}{\Omega} \tag{4.12}$$

The MMS is again calculated at each rotor speed as the smallest separation from each of the modes considered as defined below.

$$\epsilon_m(\Omega,P) = \min_{\forall i}\left(\epsilon_i(\Omega,P)\right) \tag{4.13}$$

The optimum compressive load at each rotor speed is the compressive load at which the MMS is maximised.

Although mapping the full range of compressive loads and rotor speeds is a computationally intense method to determine this optimum, the use of local optimisation to calculate the optimum is not feasible. Due to the large number of natural frequencies and rotor harmonics, the optimisation would be highly multi-modal and therefore not possible to accurately solve using local optimisation.

The fan diagrams for the unloaded and maximally loaded cases for each rotorcraft are shown in Fig. 4.18.

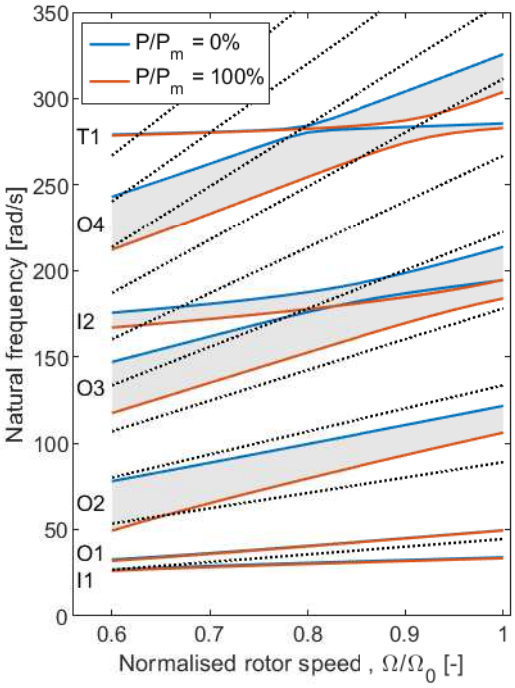

(a) Bo105

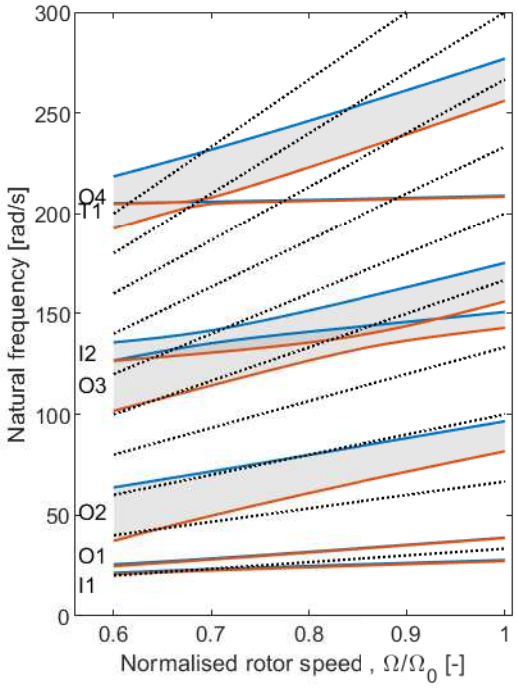

(b) Lynx

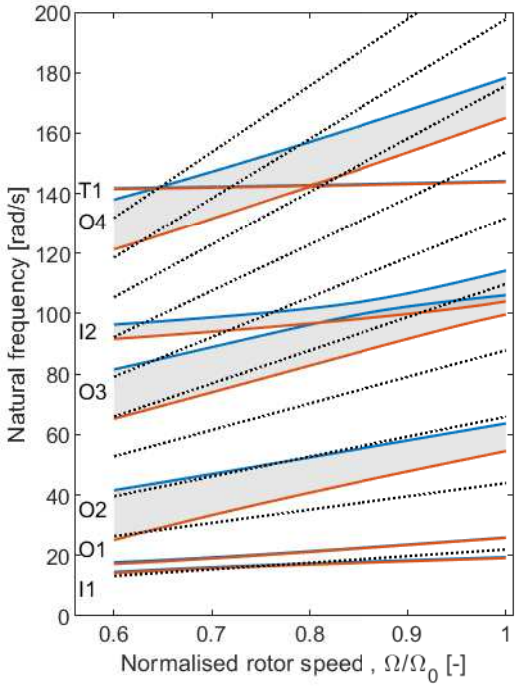

(c) AW101

Figure 4.18: Fan diagrams for test aircraft with different compressive loading profiles. Grey shaded regions denote the area between minimum and maximum loading.

It can be seen that compared to the unloaded case, as previously shown in Fig. 4.15, the maximally loaded case exhibits a lower value for the natural frequency of each mode at each rotor speed. Additionally, it can be seen that the magnitude of this reduction in frequency depends on the mode and rotor speed; trends that were previously observed in Chapter 3. When the blade is loaded, the values will vary between the upper limit (observed in the unloaded case) and the lower limit (observed in the maximally loaded case) as highlighted in Fig. 4.18.

To obtain the optimal compressive loading at each rotor speed, the MMS is used as an objective metric to be maximised. Firstly, we shall investigate how this methodology performs when optimising the resonance avoidance of a single mode, the third out-of-plane mode, of the Bo105 aircraft. This mode is ideal for demonstration due to its proximity and interaction with the second in-plane mode. The resulting optimal loading profile, natural frequencies and modal separation for the third out-of-plane mode (optimisation objective) and the second in-plane mode (not optimised) are shown below.

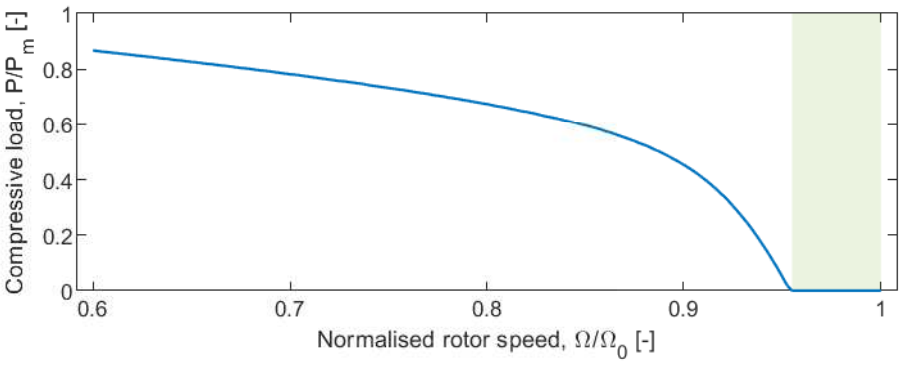

(a) Optimal loading profile

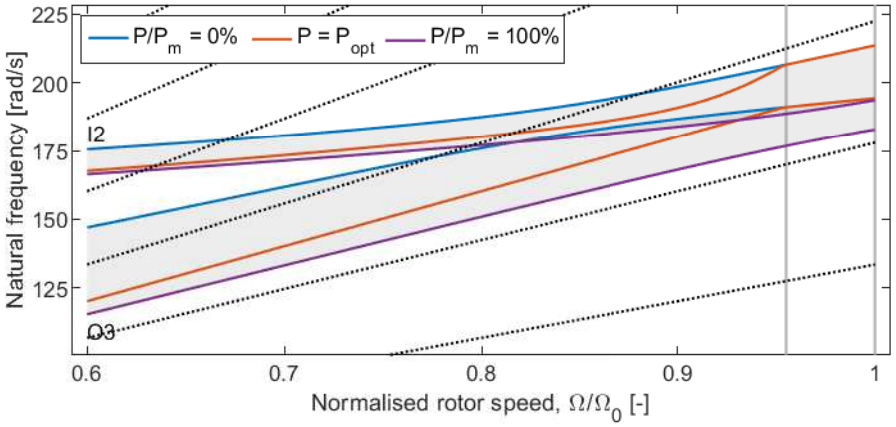

(b) Fan diagram

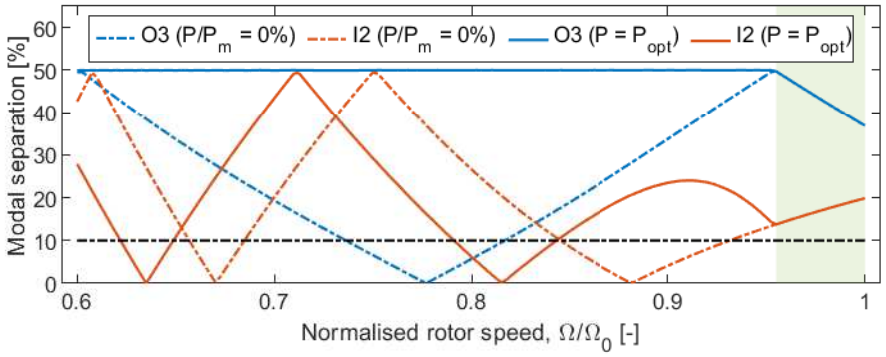

(c) Modal separation

Figure 4.19: Results of optimisation of single mode (O3). Grey shaded regions denote the area between minimum and maximum loading. Green shaded regions denote ranges where optimal compressive load is 0.

It can be seen in Fig. 4.19a that at the nominal rotor speed the optimum compressive load is 0 kN. This is because the natural frequency of the third out-of-plane mode (O3) is higher than its nearest harmonic and any applied compressive load would reduce the natural frequency

of this mode and its modal separation accordingly. This value for the optimum compressive load continues down to 95.5 % of the nominal rotor speed. During this region it can be seen in Fig. 4.19b that the natural frequency of the third out-of-plane mode moves away from its nearest harmonic which results in an increase in the modal separation, reaching a maximum of 50 %, as observed in Fig. 4.19c. Any further reductions in rotor speed would result in the natural frequency continuing to move further away from the harmonic below and towards the harmonic above. However, as the harmonic above is the closest, this would have a negative effect which can be observed as a reduction in the modal separation for the unloaded case. Therefore, the optimal loading below 95.5 % increases to ensure that the natural frequency sits equidistant between the two harmonics above and below as seen in Fig. 4.19b. Consequently, the modal separation for this mode can be in Fig. 4.19c to maintain a perfect 50 % separation.

Whilst this optimal loading profile can be seen to significantly improve the modal separation of the third out-of-plane mode, it has negative consequences for the second in-plane mode. As the compressive loading is applied, it reduces the natural frequency of the second in-plane mode as well as the third out-of-plane mode. The reduction in the natural frequency of the second in-plane mode causes a resonant interaction to occur at 81.5 % of the nominal rotor speed which was not present in the unloaded case, as can be seen in Fig. 4.19c.

To avoid the resonance caused by the second in-plane mode as well as the third out-of-plane, the procedure is repeated using the MMS of both modes as the objective function to be maximised. The resulting optimal loading profile, natural frequencies and modal separation are shown below.

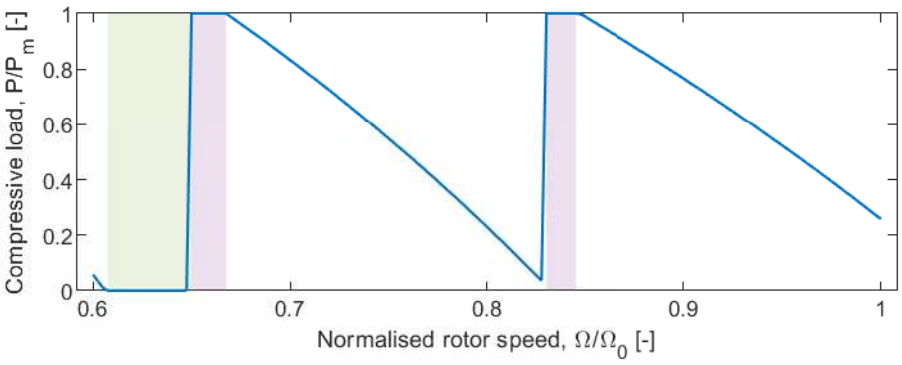

(a) Optimal loading profile

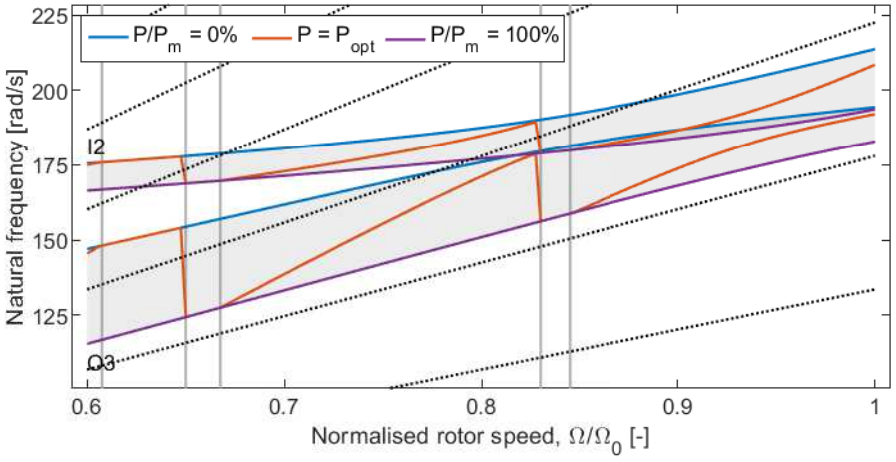

(b) Fan diagram

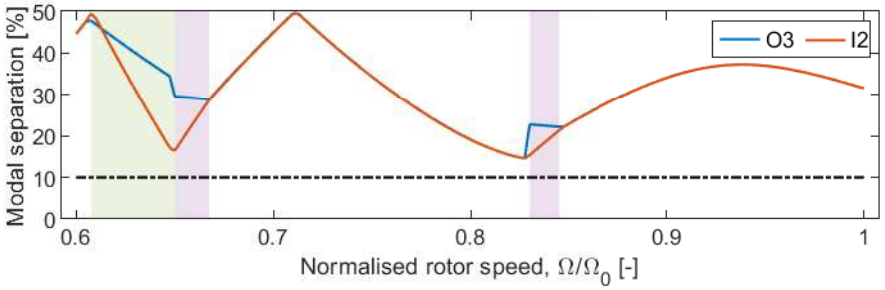

(c) Modal separation

Figure 4.20: Results of optimisation of two modes. Grey shaded regions denote the area between minimum and maximum loading. Green shaded regions denote ranges where optimal compressive load is 0. Purple shaded regions denote ranges where optimal compressive load is P_m.

It can be seen that using an objective function that accounts for both modes has a significant impact on the modal separation of the two modes. Instead of one mode achieving the maximum 50 % separation and the other exhibiting resonances, it has been possible to ensure that

both modes exceed the acceptable separation of 10 % for the entire rotor speed range as seen in Fig. 4.20c. As this occurs, there appear to be three different behaviours occurring throughout the rotor speed range observed. The first behaviour, herein referred to as *balanced modal separation*, can be observed from 100 % to 84.5 %, 83 % to 66.75 % and 60.75 % to 60 %. This behaviour is identified by an optimised compressive load neither at the minimum or maximum allowable limit and the separation of the two modes with the smallest separation is equal, as observed in Fig. 4.20c. This behaviour occurs because the separation of one mode is dictated by a harmonic above its natural frequency and the other is dictated by a harmonic below (as seen in Fig. 4.20b); any change in the compressive loading would improve the separation of one but worsen the other. The second behaviour, herein referred to as *compression limited*, can be observed from 84.5 % to 83 % and 66.75 % to 65 %. The behaviour is identified by the optimal compressive load equalling the maximum allowable compressive load. This behaviour occurs because the separation of the mode dominating the MMS (in this case the second in-plane mode) is below the harmonic dominating its separation but cannot be reduced any further; not because of the separation of another mode, but due to upper limit of the compressive load. The final behaviour, herein referred to as *baseline limited*, can be observed from 66.75 % to 65 %. This behaviour is identified by the optimal compressive load equalling 0 kN. This behaviour is the opposite of the *compression limited* and occurs because the separation of the mode dominating the MMS (in this case the second in-plane mode) is above the harmonic dominating its separation; i.e. any applied load would reduce its natural frequency and worsen its modal separation.

Unfortunately, there is little that can be done to alter the *baseline limited* behaviour as the compressive loading only has the ability to reduce, not increase, natural frequencies. It would be possible to reduce the presence of *compression limited* by increasing the maximum compressive load but this may induce structural stability issues. Furthermore, as the number of modes being considered increases, it is likely that there will be more of the *balanced modal separation* due to the increasing number of modes to be balanced.

Additionally, it should be noted that while some of the transitions between these behaviours, such as from the two large regions of *balanced modal separation* to their adjacent regions of *compression limited*, are smooth this is not always the case. The changes in behaviour at 65 % and 83 % are very abrupt which may be infeasible or practically unachievable and therefore may have to be implemented more gradually.

Once the MMS improvements achievable using compressive loading have been investigated for one and two modes, the procedure can be applied to a full set of modes to assess the capability of compressive loading to avoid resonance. Herein the resonances that filter through to the fuselage are considered. This consists of using the first four out-of-plane modes (O1-O4), first two in-plane modes (I1-I2) and the first torsional mode (T1) interacting with the $N_b, N_b \pm 1, 2N_b, 2N_b \pm 1$ harmonics. The resulting optimal loading profile, natural frequencies, modal separation and mode(s) dominating the MMS value at each rotor speed are shown below.

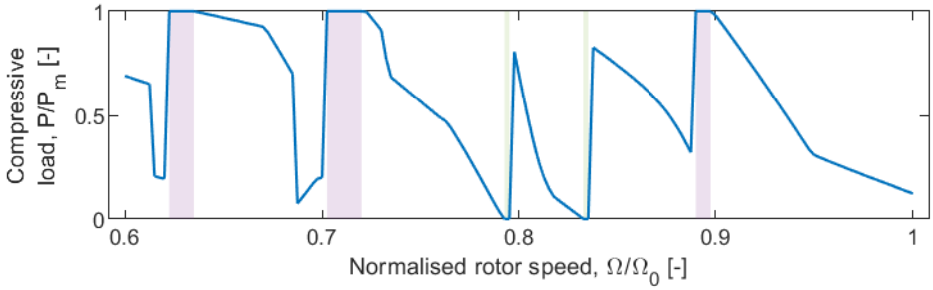

(a) Optimal loading profile

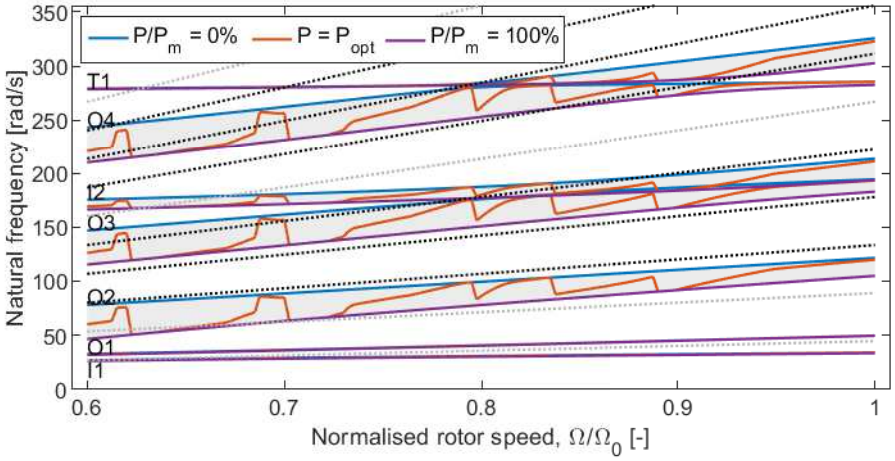

(b) Fan diagram

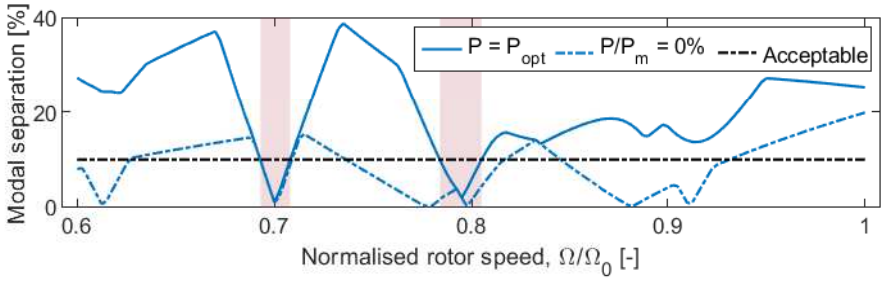

(c) Modal separation

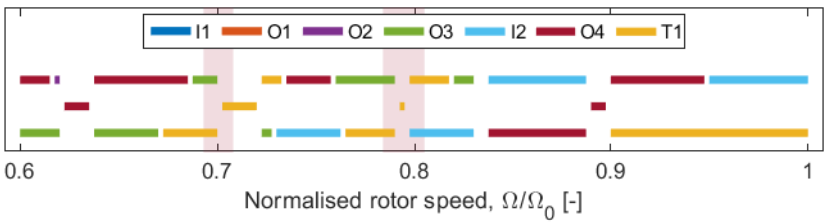

(d) Mode(s) which dictate the value of MMS

Figure 4.21: Results of optimisation of fuselage filtered modes. Grey shaded regions denote the area between minimum and maximum loading. Purple shaded regions denote ranges where optimal compressive load is P_m. Red shaded regions denote ranges where the MMS is below an acceptable level.

It can be seen from Fig. 4.21a that the *balanced modal separation* remains the dominant behaviour across the range of rotor speeds investigated. However, due to the increase in the number of modes included in the optimisation, there are significantly more abrupt changes in the optimal compressive loading profile.

Fig. 4.21c shows that the compressive loading has been able to provide significant improvements to the modal separation. In rotor speed ranges where the separation was already acceptable, it has been further increased which would likely result in reduced vibration levels in the fuselage, benefiting passenger comfort and the performance of sensitive equipment. In other rotor speed ranges, the modal separation has increased from an unacceptable level to an acceptable level which would permit the aircraft a larger range of operational rotor speeds.

Unfortunately, there are still two rotor speed regions which remain lower than the acceptable limit, as highlighted in Figs. 4.21c and 4.21d. Fig. 4.21d shows which mode (for *baselime limited* or *compression limited* regions), or modes (for *balanced modal separation* regions), are dominating the MMS. It can be seen that the first torsional mode is one of, if not the only, mode dominating the MMS and preclude an acceptable level of modal separation. The cause of this is likely to be due to the lack of sensitivity of the first torsional mode to the compressive loading, as observed in Fig. 4.21b, making it almost impossible to avoid this mode interacting with the 8/rev and 9/rev harmonic. However, these rotor speed regions are relatively narrow which may mean that a rotor can traverse this region sufficiently quickly to avoid the accumulation of large vibratory loads and operate in one of the other rotor speed ranges with an acceptable MMS.

The results presented in Fig. 4.21 only capture resonances of the first four out-of-plane modes (O1-O4), first two in-plane modes (I1-I2) and the first torsional mode (T1) interacting with the $N_b, N_b \pm 1, 2N_b, 2N_b \pm 1$ harmonics as it is resonances at these harmonics which filter from the rotor blade to the fuselage and influence the vibratory loads experienced by the people and equipment onboard. However, it is important to investigate all interactions in the rotating frame as they may include additional resonances which, although they may not affect the people or equipment in the fuselage, will influence the vibratory loads in the blade which may cause structural damage to the blade itself. Therefore, the optimisation presented in Fig. 4.21 is repeated considering the first ten rotor harmonics. The results of this optimisation procedure are shown below.

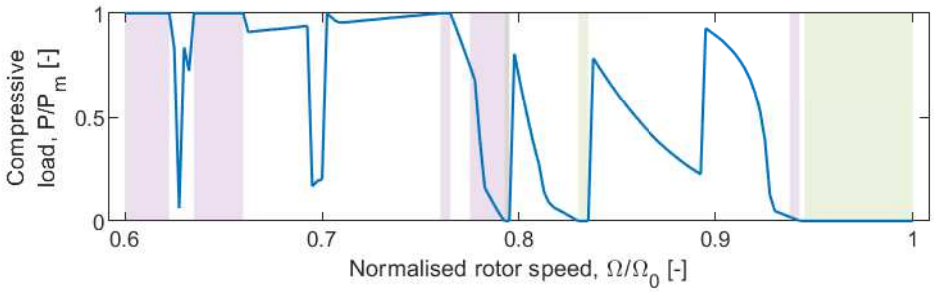

(a) Optimal loading profile

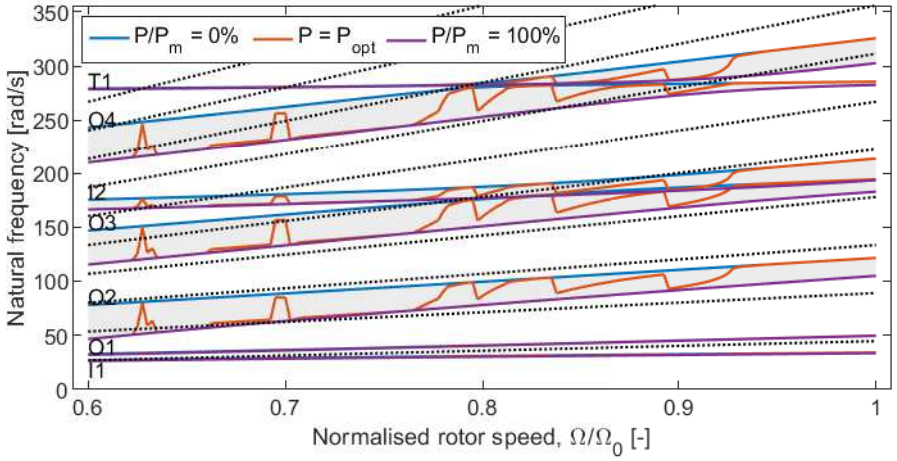

(b) Fan diagram

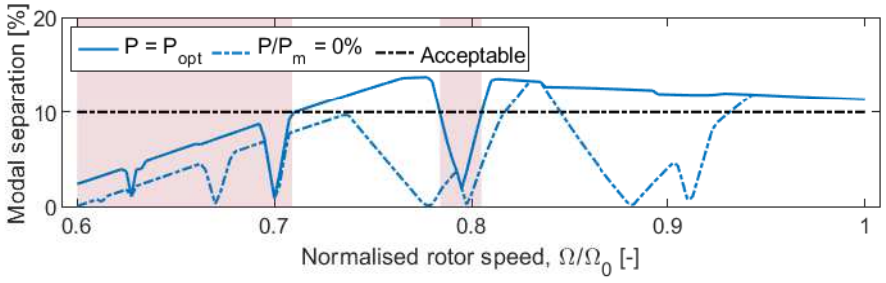

(c) Modal separation

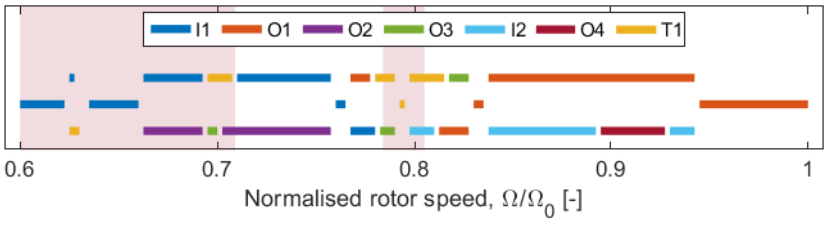

(d) Mode(s) which dictate the value of MMS

Figure 4.22: Results of optimisation of all modes of the MBB blade. Grey shaded regions denote the area between minimum and maximum loading. Green shaded regions denote ranges where optimal compressive load is 0. Purple shaded regions denote ranges where optimal compressive load is P_m. Red shaded regions denote ranges where the MMS is below an acceptable level.

The inclusion of the additional harmonics introduces extra resonances which instigates changes to the optimum loading profile and subsequently natural frequencies as seen when comparing Figs. 4.22a and 4.22b to Figs. 4.21a and 4.21b.

These resonances significantly reduce the MMS values across the range of rotor speeds. This reduction results in significant regions of the rotor speed above 70.9 % of the nominal rotor speed changing from unacceptable to acceptable. Whilst the rotor speed region below 70.9 % exhibits an improvement, it is not enough to change the MMS value to an acceptable value.

It can be seen in Fig. 4.22d that the first in-plane mode is, partly or solely, dictating the MMS. Therefore, the two modes which cause the unacceptable MMS values are the first in-plane and first torsion modes; modes which can be seen in Fig. 4.22b to be insensitive to the compressive loading. This indicates that modes which exhibit limited sensitivity to the compressive loading may be the limiting factor for this resonance avoidance technique.

This optimisation is repeated for the other two test aircraft defined in Appendix C to assess how compressive loading performs as a resonance avoidance technique for different aircraft. The results of the optimisation for the Lynx are shown below.

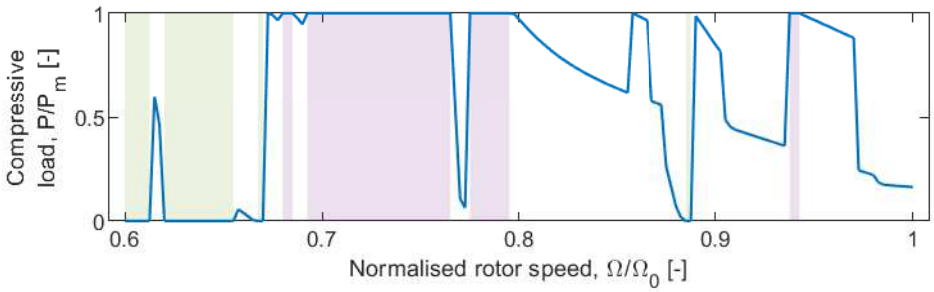

(a) Optimal loading profile

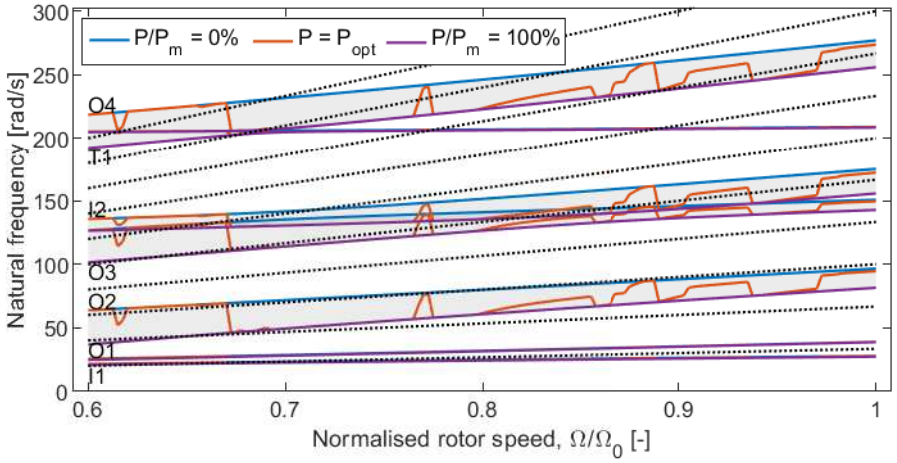

(b) Fan diagram

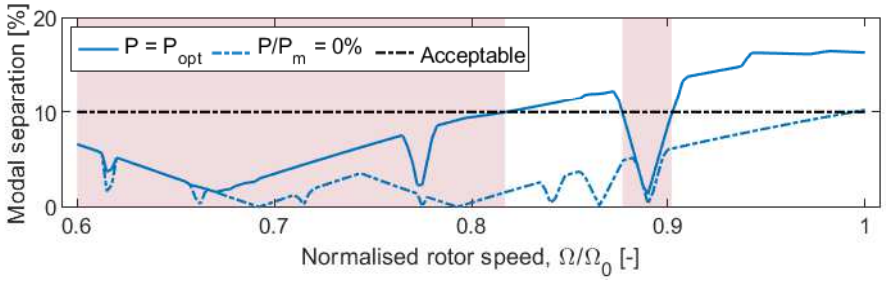

(c) Modal separation

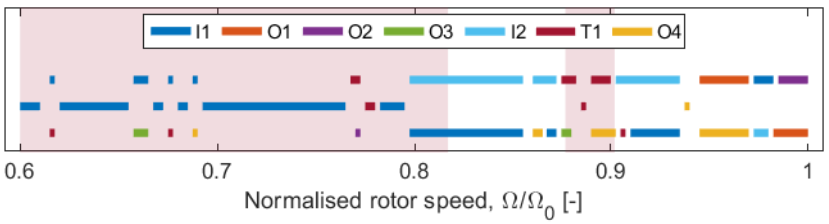

(d) Mode(s) which dictate the value of MMS

Figure 4.23: Results of optimisation of all modes of Lynx blade. Grey shaded regions denote the area between minimum and maximum loading. Green shaded regions denote ranges where optimal compressive load is 0. Purple shaded regions denote ranges where optimal compressive load is P_m. Red shaded regions denote ranges where the MMS is below an acceptable level.

Similarly to the optimisation of the MBB, the optimal loading profile shown in Fig. 4.23a largely exhibits *balanced modal separation* with a significant number of abrupt changes.

The MMS also exhibits significant improvements across a wide range of rotor speeds. Although the compressive loading is unable to allow as large a proportion of the desired rotor speed range as the MBB, it offers a significant improvement of the available rotor speed range from the unloaded case.

Fig. 4.23d shows that, similar to the MBB, the rotor speed ranges that exhibit an unacceptable MMS value are dominated by either the first torsional mode or the first in-plane mode. These modes can be seen in Fig. 4.23b to exhibit a similar insensitivity to compressive loading which is the likely cause of the low value of MMS.

The results of the optimisation for the AW101 are shown below.

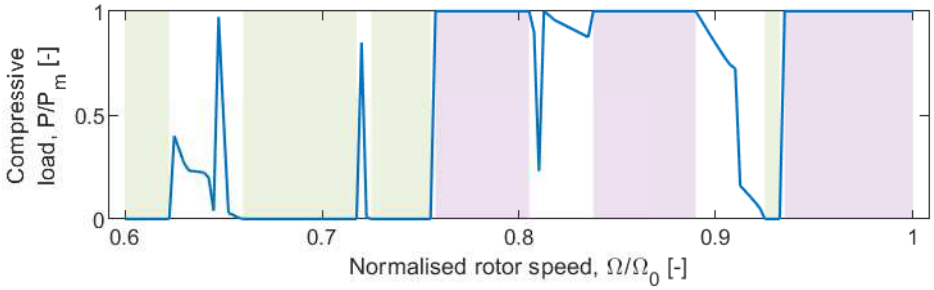

(a) Optimal loading profile

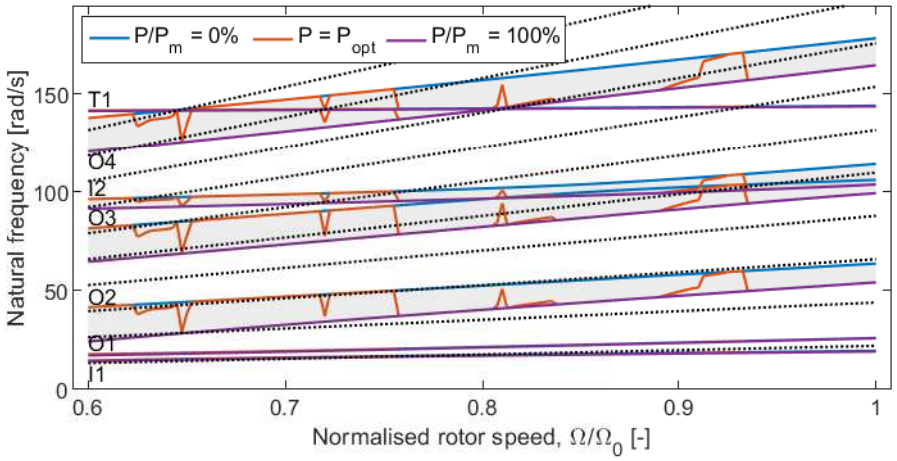

(b) Fan diagram

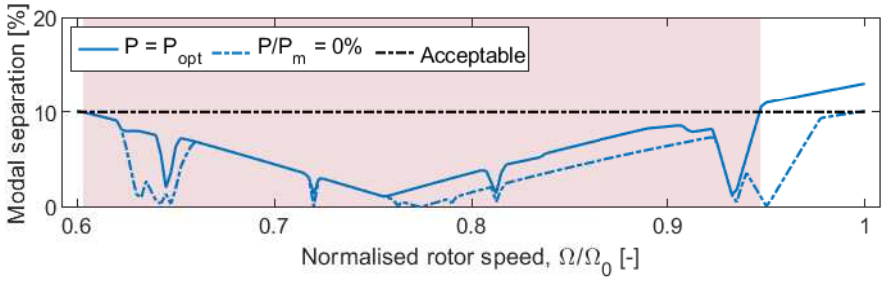

(c) Modal separation

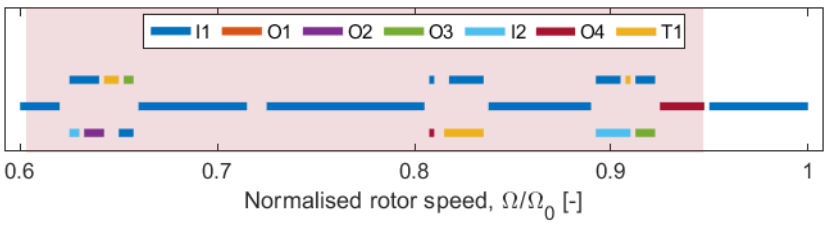

(d) Mode(s) which dictate the value of MMS

Figure 4.24: Results of optimisation of all modes of AW101 blade. Grey shaded regions denote the area between minimum and maximum loading. Green shaded regions denote ranges where optimal compressive load is 0. Purple shaded regions denote ranges where optimal compressive load is P_m. Red shaded regions denote ranges where the MMS is below an acceptable level.

Similarly to the optimisation of the MBB, the optimal loading profile shown in Fig. 4.24a exhibits significant amounts *balanced modal separation* and abrupt changes in compressive load.

The MMS also exhibits improvements across a range of rotor speeds. Although the compressive loading is unable to allow as large an amount of the desired rotor speed range as the MBB or Lynx, it offers a significant improvement of the available rotor speed range from the unloaded case.

Fig. 4.24d shows that, similar to the MBB and Lynx, the rotor speed ranges that exhibit an unacceptable MMS value are dominated by either the first torsional mode or the first in-plane mode. These modes can be seen in Fig. 4.24b to exhibit a similar insensitivity to compressive loading which is the likely cause of the low value of MMS.

A comparison of the fraction of the desired rotor speed range that is available for the unloaded and optimally loaded cases are shown below for each aircraft.

Table 4.5: Summary of rotor speed range improvements due to optimal compressive loading

Aircraft	MBB Bo105		Westland Lynx		Westland AW101	
	Unloaded	Optimal	Unloaded	Optimal	Unloaded	Optimal
Operable range [% of desired]	24.3	67.5	1.5	39.5	1.5	14.0
Largest resonant range [% of desired]	54.3	27.3	98.5	54.3	98.5	86.0
Lowest operable speed [% of nominal]	81.7	70.9	99.4	81.7	60	60

It can be seen in Table 4.5 that although none of the aircraft tested are able to achieve the full range of desired rotor speed, the amount of the rotor speed can be used has increased significantly for each of the test aircraft. Furthermore, it can be seen that the largest resonant range and the lowest operable rotor speed has improved, where possible, for each aircraft. Therefore, if any of the above aircraft were to utilise a variable rotor speed, the range of rotor speeds that can be utilised and the difference between the lowest and highest speed would be improved. Additionally, if the rotor were to have to cross a resonant region to operate in a different region with an acceptable MMS then crossing this resonant region quickly such that there is minimal time for damaging vibratory loads to accumulate is imperative. In this case, the significant reduction of the size of the largest resonant rotor speed range will improve the speed with which this region can be crossed.

Finally, whilst the desired rotor speed range was a 40 % reduction, it should be noted that other studies looking at the performance benefits have found that reductions of 10 % to 20 % achieved significant performance improvements [16, 25, 11]. Therefore, even if some regions of the 40 % are not available, it is likely that significant performance improvements would still be

made.

If the use of compressive loading to avoid resonance is to be improved to yield results even greater than that already demonstrated, then the avoidance of the resonances involving the modes that exhibit a low sensitivity to the compressive loading should be targeted as these modes are the modes limiting further improvements of the MMS for each aircraft tested. There are several potential options to consider:

1. The first in-plane and out-of-plane modes only interacts with $1/rev$ harmonic. Therefore, if it were possible to alter the stiffness or mass stiffness distributions of the blade to reduce this frequency there would be an increase in separation from the first in-plane mode across a wide range of rotor speeds. This would not be possible for the first torsional mode as it interacts with multiple harmonics both above and below it.

2. As seen in Figs. 4.22c, 4.23c and 4.24c, none of the aircraft are able to utilise much, if any, of the rotor speed range between 60 % and 70 % of the nominal. Therefore, it may be beneficial to target only a 30 % reduction in rotor speed as this would increase the critical buckling load and allow for a larger maximum compressive load to be employed.

3. It can be seen in Figs. 4.22b, 4.23b and 4.24b that these modes exhibit minimal sensitivity to changes in rotor speed. Therefore, it may be feasible to deploy more traditional passive resonance avoidance techniques as described in Section 1.3.1. For most rotorcraft, it is already commonplace to have an in-plane damper installed to avoid ground resonance for the first in-plane mode. It may be possible to deploy a torsional pendulum absorber to avoid resonances associated with the first torsional mode that would be effective across a range of rotor speeds [78]. The nature of this mode to be insensitive to centrifugal forces and therefore compressive loading makes it well suited for suppression using passive absorbers.

It has successfully been shown that the range of rotor speeds that exhibit an unacceptable amount of separation from their nearest rotor harmonic can be improved significantly with the use of an applied compressive load. Without exceeding 75 % of the most conservative buckling load, the fraction of the desirable rotor speed range that could be utilised increased by 43.3 %, 38.0 % and 12.5 % for the Bo105, Lynx and AW101, respectively. The most significant limitation of the method is the insensitivity of the first in-plane mode and first torsional mode to compressive loading.

4.4 Chapter Summary

This chapter expanded on the core concept of compressive loading based resonance avoidance as introduced in Chapter 3. An assessment of the in-vacuo resonant interactions present in rotors

and the potential for these to be avoided using compressive loading was then made.

To more accurately reflect the behaviours exhibited by rotor blades, the model was expanded to account for the additional phenomena of twist and non-coincident mass and elastic axes as well as torsional motion. The Boundary Value Problem (BVP) model is based upon a set of coupled PDEs with an associated set of coupled boundary conditions.

To demonstrate that the additional features have been correctly captured, a series of verification and validation studies were performed. Firstly, the natural frequencies and mode shapes calculated by the model were compared with those from a set of independently performed studies using the same PDEs that also captured the effects of twist, non-coincident mass and elastic axes and torsional motion. These studies showed good correlation which gives confidence in the implementation of the underlying beam model. Secondly, a FE model of a beam with twist and non-coincident mass and elastic axes and an applied compressive load was developed. The natural frequencies and mode shapes calculated by the FE model across a range of rotor speeds and compressive loading values were subsequently compared to those calculated using the present BVP model. The agreement between these sets of results was also good which further suggested that the underlying beam model, and its ability to capture the effects of compressive loading, were correctly implemented.

A study of these additional phenomena was performed to identify their effects on rotor blade dynamics. It was revealed that the inclusion of twist introduces significant coupling between the in-plane and out-of-plane motions across a wide range of rotor speeds. Conversely, the inclusion of non-coincident mass and elastic axes introduced coupling between the out-of-plane and torsional motions but these effects are only observed over a much smaller range of rotor speeds.

Once the effects of the additional phenomena were investigated, the resonant behaviour of rotor blades without a compressive loading based resonance avoidance technique was assessed. The natural frequencies of the first seven modes across a range of rotor speeds were calculated without any applied compressive loads. The separation of these modes from their nearest harmonic was calculated with the minimum of these values dictating the presence of resonance. It was observed that as the higher modes start further from this asymptotic limit, they will cross motor rotor harmonic which will result in more resonant interactions. Conversely, the lower modes will encounter fewer interactions but each interaction will influence a wider range of rotor speeds that a resonant interaction of the higher modes.

Once the baseline resonances had been assessed, the capability of compressive loading to alter the natural frequencies of the blade and avoid resonance was assessed. The maximum compressive load considered was 75 % of the critical buckling load, as used in Chapter 3. It was shown that for each of the aircraft significant improvements in the separation between natural frequencies and rotor harmonics was achieved. This increased the range of rotor speeds that was safe to operate in for each aircraft. The acceptable fraction of the desired rotor speed range for the Bo105 increased from 24.3 % to 67.5 %. The acceptable fraction of the desired rotor speed

range for the Lynx increased from 1.5 % to 39.5 %. The acceptable fraction of the desired rotor speed range for the AW101 increased from 1.5 % to 14.0 %.

Further to the demonstration of the ability of compressive loading to alter the natural frequencies of rotor blades in Chapter 3, it has successfully been shown that the resonances observed in realistic rotor blades can be avoided using compressive loading. In the following chapter, the implications of aerodynamic loading shall be considered and their impact on the proposed resonance avoidance technique shall be assessed.

CHAPTER 5

RESONANCE AVOIDANCE OF ROTOR BLADES IN HOVER

In the previous chapter, Chapter 4, the effect of compressive loading on the in-plane, out-of-plane and torsional dynamic properties of a rotating twisted blade with non-coincident mass and elastic axis was investigated. This chapter shall incorporate axial deformation, hovering aerodynamics and geometric nonlinearities to further improve the realism of the model and enhance its ability to investigate the effectiveness of the compressive loading concept. Once these additional features have been incorporated into the model, a range of validation tests are performed to verify the implementation of the model and validate its ability to accurately capture the new features. Subsequently, a case study is used to determine the increase in rotor speed range that can be operated in without encountering resonance, using a compressive loading based resonance avoidance technique.

5.1 Aeroelastic bending-bending-twist model

To investigate the additional effects of geometric nonlinearities and aerodynamic loading in hover, a new sub-model is developed. This model is based on the Partial Differential Equations (PDEs) developed by *Hodges and Dowell* [138]. These equations are an extension of those used in the previous chapter and capture geometric nonlinearities ensuring their validity up to moderate deflections. Additionally, they allow the incorporation of an aerodynamic model. The aerodynamic model chosen for the present work is that of *Greenberg* [139] which is an extension of the work completed by *Theodorsen* [170], resulting in an unsteady aerodynamic model of an oscillating rotor blade in hover. The inclusion of aerodynamic loading and geometric nonlinearities will increase the realism with which model represents a real-world rotor blade.

5.1.1 Linearisation procedure

To solve the upcoming nonlinear PDEs, a linearisation procedure is required. The chosen procedure uses small perturbation theory and is identical to that used in [171, 131] to linearise similar equations for the purpose of aeroelastic analysis of high aspect ratio wings and rotor blades. This process has been seen to correlate well with nonlinear models when investigating rotorcraft vibratory loads [172]. This process is performed by using an assumed solution that takes the form of a static time-invariant deformation combined with a small harmonic oscillation. Thus the assumed solution is written as follows.

$$\begin{aligned} u_*(x,t) &= u_0(x) + u(x)e^{st} \\ v_*(x,t) &= v_0(x) + v(x)e^{st} \\ w_*(x,t) &= w_0(x) + w(x)e^{st} \\ \phi_*(x,t) &= \phi_0(x) + \phi(x)e^{st} \end{aligned} \tag{5.1}$$

This form allows the problem to be separated into two distinct Boundary Value Problem (BVP)s; one for the static deformation of the blade and one for the small oscillations about that deformation. However, it is acknowledged that due to the assumption of an identical period for the harmonic motion across each of the deformations, it would not be possible to capture nonlinearities of different periods. A linearisation of the upcoming field equations and boundary conditions is performed to provide the separate field equations and boundary conditions for each BVP. Terms which are constant with respect to time are gathered to form a set of ordinary differential equations and boundary conditions which represent the static deformation of the blade.

Terms which are linear with respect to the time-dependent part of the assumed solution are gathered to form a set of partial differential equations that represent the small harmonic motion of the blade about the static deformation. The principle of separation of variables is employed to split the spatial and temporal components of the solution. The e^{st} terms are dropped, resulting in a BVP defined solely on the spatial domain.

5.1.2 Field equations

Unlike the field equations used in Chapters 3 and 4, the present field equations contain two components: the structural equations of motion and the aerodynamic loading model. The two components are combined to create a single set of tightly coupled field equations which avoid the use of an iterative procedure to ensure a coherent structural and aerodynamic response. This will avoid the computational expense and inaccuracies that are often associated with loosely coupled aero-structural models solved using an iterative procedure.

5.1.2.1 Structural model

The equations of motion that represent the motion of the blade within the domain are a set of four nonlinear non-homogenous coupled PDEs; one for each of the four motions to be captured. Each of the four PDEs contains four states, u_*, v_*, w_*, and ϕ_*, and is a function of one spatial domain, x and one temporal domain, t. It was shown in Section 4.3.1 that the effect of the non-coincident mass and elastic axes on the natural frequencies and their sensitivity to rotor speeds and compressive loading was relatively minor, particularly in comparison to that of twist. Therefore, in addition to the terms removed in Section 4.1.2, terms pertaining to e, e_A are also removed to improve the ease with which the implications of the aerodynamic loads and geometric nonlinearities are identified and understood. The resulting equations are shown below in Eq. (5.2).

$$\begin{aligned} &-(Tw_*')' + \Big[(EI_z - EI_y)\underline{\cos(\theta+\phi_*)\sin(\theta+\phi_*)}v_*'' \\ &+ [EI_z\underline{\sin^2(\theta+\phi_*)} + EI_y\underline{\cos^2(\theta+\phi_*)}]w_*''\Big]'' + m\ddot{w}_* = L_z \end{aligned} \tag{5.2a}$$

$$\begin{aligned} &-(Tv_*')' + \Big[[EI_z\underline{\cos^2(\theta+\phi_*)} + EI_y\underline{\sin^2(\theta+\phi_*)}]v_*'' \\ &+ (EI_z - EI_y)\underline{\cos(\theta+\phi_*)\sin(\theta+\phi_*)}w_*''\Big]'' + 2m\Omega\dot{u}_* + m\ddot{v}_* - m\Omega^2 v_* = L_y \end{aligned} \tag{5.2b}$$

$$-T' - m(\Omega^2 x + 2\Omega\dot{v}_*) = L_x \tag{5.2c}$$

$$\begin{aligned} &-\Big[EAk_A{}^2\underline{(\theta+\phi_*)'\Big(u_*' + \frac{v_*'^2}{2} + \frac{w_*'^2}{2}\Big)}\Big]' - (GJ\phi_*')' \\ &+ (EI_z - EI_y)\Big[\underline{(w_*''^2 - v_*''^2)}\cos\theta\sin\theta + \underline{v_*''w_*''}\cos 2\theta\Big] + mk_m^2\ddot{\phi}_* \\ &+ m\Omega^2\phi_*(k_{m2}{}^2 - k_{m1}{}^2)\cos 2\theta = M_\phi - m\Omega^2(k_{m2}{}^2 - k_{m1}{}^2)\cos\theta\sin\theta \end{aligned} \tag{5.2d}$$

Where

$$T = EA\Big(u_*' + \underline{\frac{v_*'^2}{2}} + \underline{\frac{w_*'^2}{2}} + k_A{}^2\theta'\phi_*'\Big) \tag{5.3}$$

There are several underlined terms present in these equations. A number of these have been underlined to highlight their presence but it should be noted that any term where multiple states are multiplied together will contribute to the nonlinear nature of these equations. It is due to the presence of these terms that the linearisation procedure described in Section 5.1.1 is required. An example of how this procedure works is shown below.

$$v''_* w''_* = v''_0 w''_0 + \underline{v''_0 w'' e^{st}} + \underline{v'' e^{st} w''_0} + \underline{\underline{v'' w'' e^{2st}}} \tag{5.4}$$

It can be seen that, due to the assumed solution form shown in Eq. (5.1), the nonlinear term can be separated into four different terms. The first term is a nonlinear term containing only states pertaining to the static deformation. These terms are gathered to form the statics BVP which retains the nonlinear characteristic of the original equation. The next two terms (singly underlined) are linearly dependent on the oscillatory term e^{st} and the static state. These terms are gathered to form the linear dynamics BVP. The presence of the static states in these terms represents the influence that the static deformation will impart on the dynamic behaviour. The remaining term (doubly underlined) is a product of two of the oscillatory perturbations. The other oscillatory terms are assumed to be small with respect to the static terms, so their product is considered negligible and is therefore omitted from the model.

There is no requirement to modify these equations to account for the compressive load. As this load is applied at the tip, it is therefore incorporated via the boundary conditions. As the structural equations of motion account for axial loads and deformations, they are capable of capturing the propagation of the compressive load in their original form.

In the original derivation, L_x, L_y, L_z, M_ϕ are generalised non-conservative forces and moments but for the purpose of this model they are to be used to incorporate the aerodynamic loading into the field equations [3].

5.1.2.2 Aerodynamic model

Aerodynamic loads are the dominating source of rotor blade forcing and therefore an important component of any models of the structural behaviour of a rotor blade. Due to this, a wealth of different strip theories and inflow models have been created for rotor blade aeroelastic analysis of rotor blades [173, 174].

Reduced frequency is a dimensionless value for frequency which is used to evaluate aerodynamic unsteadiness. At low reduced frequencies it is applicable to use a quasi-steady assumption: the aerodynamic characteristics and the flow velocity vector of an aerofoil whose motion consists of variable linear and angular motions, are assumed equal to that of an aerofoil with constant motions [175]. However, for motions in an unsteady flow with higher reduced frequencies (above 0.05 [176]), the quasi-steady assumption cannot be used as *apparent mass* forces, not associated with the creation of vorticity, become significant [175].

As a quasi-steady model would not be suitable for the present work, an unsteady model is chosen instead. *Greenberg* [139] extended the method of *Theodorsen* [170] using a nonstationary incompressible potential flow based theory to investigate the effects of sinusoidal in-plane, out-of-plane and torsional motion of an aerofoil in a pulsating airflow. This research was directly intended for the use in the aeroelastic analysis of rotors to help mitigate the effects of inaccuracies caused by the complex flowfield that rotors create which has ensured its relevance in research to the present day [177, 178]. This makes it an ideal basis for the required aerodynamic model. This two-dimensional unsteady blade element model is used to calculate a set of distributed forces in- and out-of- the plane of rotation and a distributed torsional moment about the elastic axis of the blade. The unsteady circulatory and non-circulatory forces and moments for an oscillating aerofoil are calculated as follows.

$$L_{NC} = \frac{1}{2} C_{l,\alpha} \rho_\infty \frac{c^2}{4} \Big(-\ddot{w}_* + (\Omega x + \dot{v}_*)\dot{\phi}_* + \ddot{v}_*(\theta + \phi_*) + \frac{c}{4}\ddot{\phi}_* \Big)$$

$$\begin{aligned} L_C = C_{l,\alpha} \rho_\infty (\Omega x + \dot{v}_*) \frac{c}{2} \Big(& \Omega x(\theta + \phi_0) + \dot{v}_*(\theta + \phi_0) C(k) \\ & + \big(\frac{c}{2}\dot{\phi}_* + \Omega x(\phi_* - \phi_0) \big) C(k) - \dot{w}_* C(k) \underline{-v_{in}} + \dot{v}_*(\phi_* - \phi_0) C(2k) \Big) \end{aligned} \tag{5.5}$$

$$\begin{aligned} M_{NC} = -\frac{1}{2} C_{l,\alpha} \rho_\infty \frac{c^2}{4} \Big(& -(\Omega x + \dot{v}_*)^2 (\theta + \phi_*) + \frac{c}{4}\ddot{v}_*(\theta + \phi_*) \\ & - (\Omega x + \dot{v}_*)(-\dot{w}_* \underline{-v_{in}}) + \frac{c^2}{4}\frac{3}{8}\ddot{\phi}_* - \frac{c}{4}\ddot{w}_* \Big) \end{aligned}$$

$$M_C = -\frac{1}{2} C_{l,\alpha} \rho_\infty (\Omega x + \dot{v}_*) \frac{c^2}{4} \Big(-\dot{w}_* \underline{-v_{in}} + (\Omega x + \dot{v}_*)(\theta + \phi_*) + \frac{c}{2}\dot{\phi}_* \Big)$$

It is not possible to obtain an analytical solution for the Wagner function. However, an accurate numerical approximation was developed by Jones [179].

$$C(k) \approx 1 - \frac{0.165}{1 - (0.0455/k)i} - \frac{0.335}{(1 - (0.3/k)i} \tag{5.6}$$

$$k = \frac{\mathrm{Im}(s)c}{2\Omega R}$$

The original equations [139] do not account for an inflow velocity. Therefore, the original equations have been extended (similarly to [3]) to include an inflow velocity by substituting the terms

$\dot{w}_* C(k)$ and $\dot{w}_*$ with the terms $\dot{w}_* C(k) + v_{in}$ and $\dot{w}_* + v_{in}$, respectively, see underlined terms in Eq. (5.5). The inflow velocity is assumed to be steady, constant along the span and equal to the value calculated using Blade Element Momentum Theory at 75 % of the span [180] and is defined as follows.

$$v_{in} = \text{sign}\Big((\theta + \phi_0)|_{x=0.75R}\Big)\Omega\frac{N_b c}{8}\left(\sqrt{1 + \frac{12R}{N_b c}\Big|(\theta + \phi_0)|_{x=0.75R}\Big|} - 1\right) \tag{5.7}$$

These circulatory and non-circulatory forces and moments are derived for an inviscid flow which neglects profile drag. Therefore, an additional force to account for this, D, is to be included.

$$D = \frac{1}{2}\rho_\infty\Big((v_{in} + \dot{w}_*)^2 + (\Omega x + \dot{v}_*)^2\Big)cC_{d0} \tag{5.8}$$

The non-circulatory aerodynamic force is calculated as the integral of the pressure perpendicular to the chordline of the aerofoil, which is inclined to the plane of rotation by the local twist and torsional deformation. Therefore, this force needs to be decomposed into components in the undeformed coordinate axes, x,y,z. Similarly, the circulatory aerodynamic force and drag force are perpendicular to the local freestream flow, which is inclined to the plane of rotation due to the out-of-plane motion of the blade and the inflow velocity. Therefore, these forces also needs to be decomposed into components in the undeformed coordinate axes. These decompositions are performed according to Fig. 5.1 by the following geometric transformation which is similar to that used in [3].

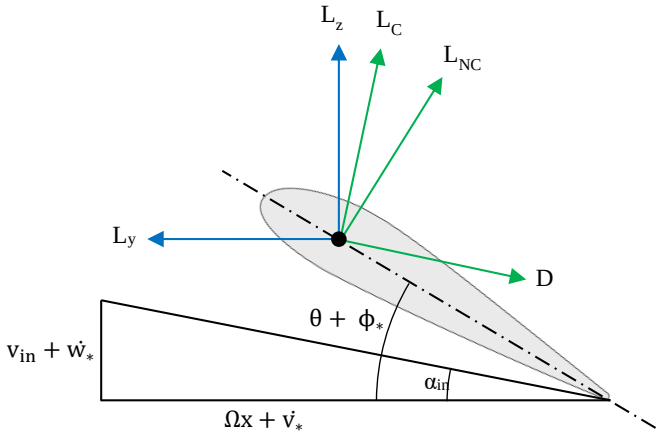

Figure 5.1: Decomposition of aerodynamic loads into undeformed axes.

$$
\begin{aligned}
L_x &= 0 \\
L_y &= -L_{NC}\sin(\theta+\phi_*) - L_C\sin(\alpha_{in}) - D\cos(\alpha_{in}) \\
L_z &= L_{NC}\cos(\theta+\phi_*) + L_C\cos(\alpha_{in}) - D\sin(\alpha_{in}) \\
M_\phi &= M_{NC} + M_C
\end{aligned}
\tag{5.9}
$$

with

$$
\begin{aligned}
\sin(\alpha_{in}) &= \frac{(v_{in}+\dot{w_*})}{\sqrt{(v_{in}+\dot{w_*})^2+(\Omega x+\dot{v_*})^2}} \\
\cos(\alpha_{in}) &= \frac{(\Omega x+\dot{v_*})}{\sqrt{(v_{in}+\dot{w_*})^2+(\Omega x+\dot{v_*})^2}}
\end{aligned}
\tag{5.10}
$$

Eq. (5.10) are accommodated in the linearisation procedure using a Taylor series expansion representation up to the second term; higher-order terms are neglected as they would not be retained in either BVP.

Defining the aerodynamic loading in this form allows Eq. (5.9) to be substituted directly in to Eq. (5.2) forming a single set of coupled aeroelastic field equations.

5.1.3 Compressive load

As was concluded in Section 3.1.1 and used in Chapter 4, a point force applied on the elastic axis at the tip of the blade directed towards the root is the model of the compressive load to be used throughout this research. The force, as shown in Fig. 5.2, is again decomposed into components in the x,y,z directions.

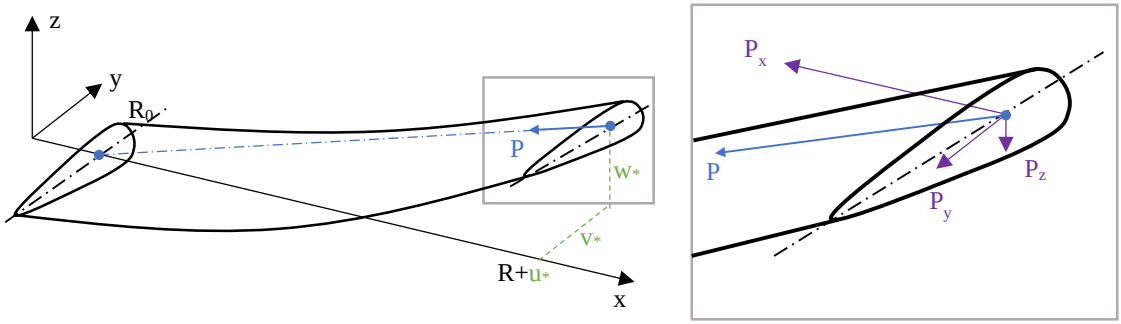

Figure 5.2: Schematic of compressive force decomposition

The geometry of the beam is again used to calculate the component of the applied force in each direction, including the newly incorporated axial deformation, as shown below in Eq. (5.11).

$$\begin{aligned} P_x &= P\frac{R+u_*(R)-R_0}{\sqrt{(R+u_*(R)-R_0)^2+v_*(R)^2+w_*(R)^2}} \\ P_y &= P\frac{v_*(R)}{\sqrt{(R+u_*(R)-R_0)^2+v_*(R)^2+w_*(R)^2}} \\ P_z &= P\frac{w_*(R)}{\sqrt{(R+u_*(R)-R_0)^2+v_*(R)^2+w_*(R)^2}} \end{aligned} \tag{5.11}$$

To allow these loads to be incorporated into the field equations and boundary conditions, it is necessary to linearise these loads. This is performed using a Taylor series expansion about u_0, v_0 and w_0 up to the second term. The results of which are shown in Eq. (5.12).

$$\begin{aligned} P_x = &\frac{P(R-R_0+u_0)}{\left((R-R_0+u_0)^2+v_0^2+w_0^2\right)^{\frac{1}{2}}}+\frac{Pue^{st}}{\left((R-R_0+u_0)^2+v_0^2+w_0^2\right)^{\frac{1}{2}}} \\ &-\frac{P(R-R_0+u_0)^2ue^{st} \;+\; P(R-R_0+u_0)v_0ve^{st} \;+\; P(R-R_0+u_0)w_0we^{st}}{\left((R-R_0+u_0)^2+v_0^2+w_0^2\right)^{\frac{3}{2}}} \end{aligned} \tag{5.12a}$$

$$\begin{aligned} P_y = &\frac{Pv_0}{\left((R-R_0+u_0)^2+v_0^2+w_0^2\right)^{\frac{1}{2}}}+\frac{Pve^{st}}{\left((R-R_0+u_0)^2+v_0^2+w_0^2\right)^{\frac{1}{2}}} \\ &-\frac{Pv_0^2ve^{st} \;+\; Pv_0w_0we^{st} \;+\; P(R-R_0+u_0)v_0ue^{st}}{\left((R-R_0+u_0)^2+v_0^2+w_0^2\right)^{\frac{3}{2}}} \end{aligned} \tag{5.12b}$$

$$\begin{aligned} P_z = &\frac{Pw_0}{\left((R-R_0+u_0)^2+v_0^2+w_0^2\right)^{\frac{1}{2}}}+\frac{Pwe^{st}}{\left((R-R_0+u_0)^2+v_0^2+w_0^2\right)^{\frac{1}{2}}} \\ &-\frac{Pw_0^2we^{st} \;+\; Pv_0w_0ve^{st} \;+\; P(R-R_0+u_0)w_0ue^{st}}{\left((R-R_0+u_0)^2+v_0^2+w_0^2\right)^{\frac{3}{2}}} \end{aligned} \tag{5.12c}$$

The resulting terms define the applied loads in the x,y,z axes. It can be seen that the first term in each is time-variant and will therefore reside in the BVP for the static deformation. The remaining terms are linearly proportional to e^{st} and will therefore appear in the BVP pertaining to the oscillatory perturbations about the statically deformed shape. It can be seen that these terms are functions of the statically deformed shape which indicates that the coupling between

the static deformation and oscillatory motion will be coupled by the compressive load in addition to the aerodynamic loading.

5.1.4 Boundary conditions

Similarly to the model and experiment in Chapters 3 and 4, cantilevered boundary conditions are enforced to replicate the hub configuration of a bearingless rotor. The field equations for the beam consist of two second-order and two fourth-order equations which necessitate twelve boundary conditions to ensure the problem is properly posed. Half of these conditions will enforce a fixed root and the other half shall enforce a free tip, subject to the augmentation due to the applied compressive load.

The fixed boundary condition at the root consists of constraining the displacements and angles of the beam to zero, as seen in Eq. (5.13).

$$\begin{aligned} u_* &= 0 \\ v_* &= 0 \\ w_* &= 0 \\ \phi_* &= 0 \\ v'_* &= 0 \\ w'_* &= 0 \end{aligned} \tag{5.13}$$

The free boundary conditions at the tip for a traditional cantilevered beam consists of constraining forces and moments at the elastic centre to zero. However, due to the application of the applied compressive load at the elastic centre of the tip, the force and moment equilibria are enforced as a balance of internal loads within the beam and the externally applied compressive load as seen in Eq. (5.14)

$$\begin{aligned} M_{x'} &= M_0 e^{st} \\ M_{y'} &= M_0 e^{st} \\ M_{z'} &= M_0 e^{st} \\ F_x &= -P_x \\ F_y &= -P_y \\ F_z &= -P_z \end{aligned} \tag{5.14}$$

It can be seen that the force equilibria are in the undeformed x,y,z axes that remain unchanged by deformation of the blade. Conversely the moment equilibria are in the deformed x,y,z axes (denoted as x',y',z') that follow the deformation of the blade. As the three force equilibria and the three moment equilibria are independent of one another, it is possible to evaluate them about different coordinate frames as long as each coordinate frame is consistently orthogonal. These different coordinate frames were chosen to remain consistent with the boundary conditions stated in [138]. As the applied compressive load is also located at the elastic centre, there is no moment created. The calculation of the internal loads are adopted directly from [138] and are defined as follows.

$$\begin{aligned}
M_{x'} &= GJ\phi'_* + EAk_A^2(\theta+\phi)'\left(u' + \frac{v'^2}{2} + \frac{w'^2}{2}\right) \\
M_{y'} &= EI_y\left[v''_* \sin(\theta+\phi_*) - w''_* \cos(\theta+\phi_*)\right] \\
M_{z'} &= EI_z\left[v''_* \cos(\theta+\phi_*) + w''_* \sin(\theta+\phi_*)\right] \\
F_x &= EA\left(u'_* + \frac{v'^2_*}{2} + \frac{w'^2_*}{2} + k_A^2\theta'\phi'\right) \\
F_y &= -M'_{y'}\sin(\theta+\phi) - M'_{z'}\cos(\theta+\phi) + F_x v'_* \\
F_z &= M'_{y'}\cos(\theta+\phi) - M'_{z'}\sin(\theta+\phi) + F_x w'_*
\end{aligned} \tag{5.15}$$

These equations are subject to the same assumed motion as defined in Section 5.1.1 and are linearised using the same procedure exemplified in Eq. (5.4).

5.1.5 Reduced statics

To allow for comparison with the model utilised in Chapter 4 and to be able to isolate the separate effects of the static deformation and aerodynamic loading, a separate simplified version of the present model, herein referred to as the *reduced statics* model, is created. The simplification consists of enforcing zero in-plane, out-of-plane and torsional static deformation and an analytically derived prescribed value for axial deformation that captures the effects of centrifugal loading and the applied compressive load as follows.

$$\begin{aligned}
v_0(x) = w_0(x) = \phi_0(x) &= 0 \\
u_0(x) &= \frac{1}{EA}\left(\frac{1}{2}\Omega^2 m\left(R^2\left(x-R_0\right) - \frac{1}{3}\left(x^3 - R_0^3\right)\right) - P\left(x-R_0\right)\right)
\end{aligned} \tag{5.16}$$

The analytical calculation of axial static deformation is derived by using the static form of Eq. (5.2c) to calculate the internal tension of the blade due to centrifugal loading, augment-

ing this with the applied compressive load and formulating the result in terms of static axial deformation according to Eq. (5.3).

5.2 Model validation

To ensure that the model has been developed and implemented correctly, a set of complementary verification studies are performed. Firstly, a model comparison study is performed to demonstrate the capability of the model to correctly capture the effects of rotation, compressive loading, and inter-motion coupling. Secondly, results from an existing aeroelastic study of rotor blades are replicated to demonstrate the model's ability to capture coupled aero-structural effects.

5.2.1 In-vacuo verification

The in-vacuo model of a pretwisted rotor blade with an applied compressive load, based on the linear equations of motion derived by *Houbolt and Brooks* [137], was successfully verified and validated using a combination of experimental data and finite element simulations in Chapter 4. This model will be used as an in-vacuo reference model herein.

Results from the model described in Section 5.1 are compared to results from the in-vacuo reference to verify the ability of the current model to capture the effects of rotation, compressive loading, and the coupling of the in-plane, out-of-plane and torsional motions due to twist.

To facilitate this comparison, the ability of the present model to capture aerodynamic loads and static deformations is removed to bring the present model in line with the in-vacuo reference model with which it is to be compared. This is accomplished by using the *reduced statics* version of the model and enforcing zero aerodynamic loading.

$$L_x = L_y = L_z = M_\phi = 0 \tag{5.17}$$

The rotor blade considered for this comparison is a bearingless blade with properties and operating conditions similar to that of the Bo105 defined in Appendix C. A lower limit of 60 % of the nominal rotor speed is again used to replicate the 40 % reduction observed in the A160T Hummingbird [28]. To ensure that a buckling instability is not induced by the compressive loading, the compressive loading shall not exceed the maximum allowable load calculated in Section 4.3.3.

The present model and the in-vacuo reference model are used to calculate the natural frequencies of the first torsion, first two in-plane modes and first four out-of-plane modes across a range of rotor speeds. This calculation is performed for an unloaded case and a maximally loaded case. For each of these cases, the natural frequencies calculated by both models are compared and the errors between the two models are calculated, as seen in Fig. 5.3.

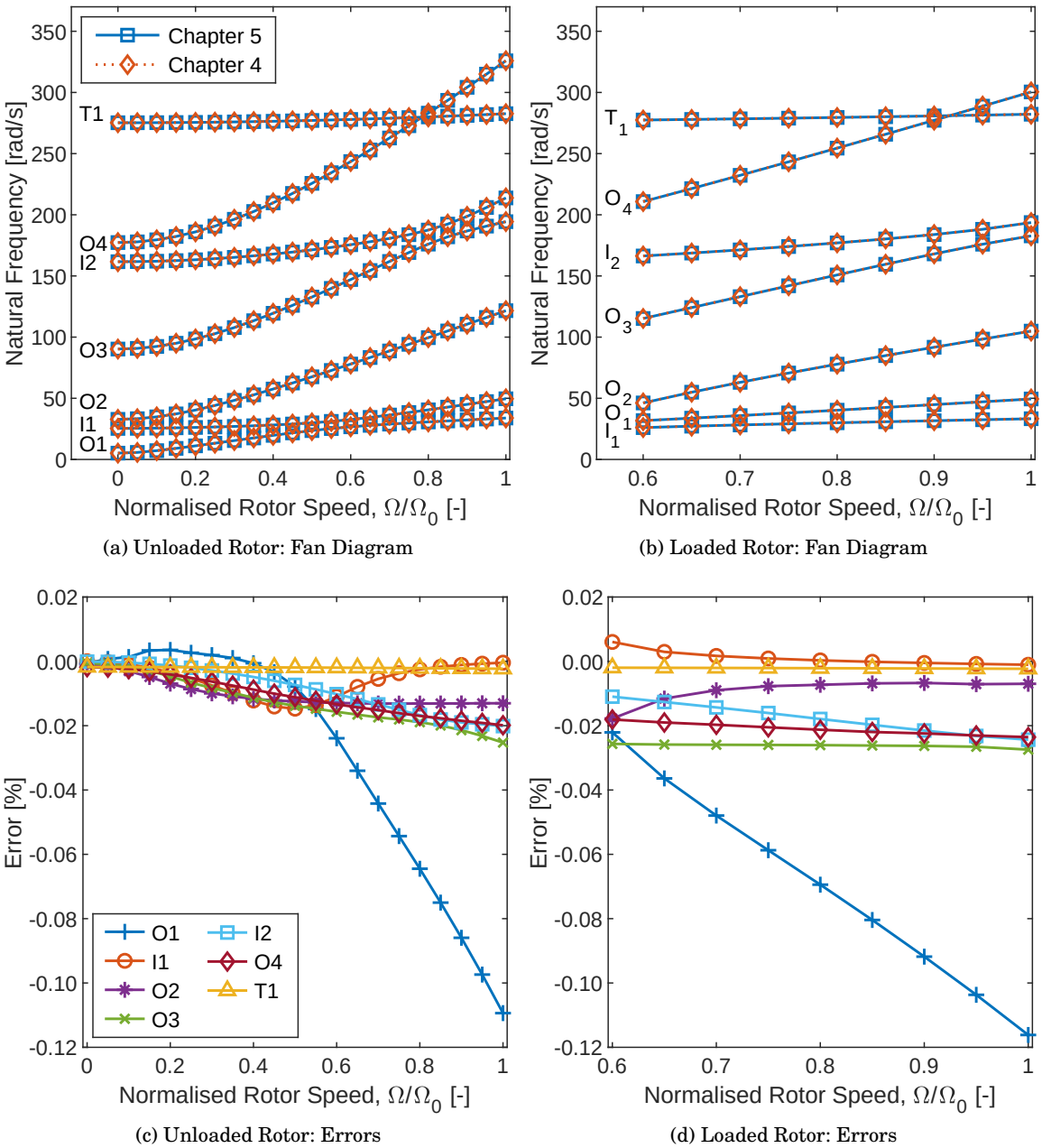

(a) Unloaded Rotor: Fan Diagram

(b) Loaded Rotor: Fan Diagram

(c) Unloaded Rotor: Errors

(d) Loaded Rotor: Errors

Figure 5.3: Comparison of in-vacuo fan diagrams for a rotor blade with, and without compressive loading, calculated using the present model with the in-vacuo reference

It can be seen in Fig. 5.3 that the agreement between the two models is very good. This level of agreement is maintained even near regions where coupling between the modes significantly influences the frequencies, namely O1 with I1 and O3 with I2. The errors for both the loaded and unloaded cases are all smaller than 0.12 % with the majority smaller than 0.03 %. Despite the use of the *reduced statics* model, there are still some differences between the models which are likely the cause of the small discrepancies observed: the present model captures the effects

of oscillatory axial extension and Coriolis forces which are not present in the in-vacuo reference model. The correlation between the two models demonstrates the capability of the present model to capture the effects of rotation, compressive loading and inter-motion coupling.

5.2.2 Aeroelastic verification

To ensure that aeroelastic elements of the model have been correctly implemented, the present model is compared with the model developed by *Hodges and Ormiston* [3]. The properties of the untwisted blade used for this comparison study correspond to those used in the reference work and are presented in Table 5.1. Two cases are used for this verification: one using a torsionally soft blade ($\lambda_{T1}/\Omega = 5$); and one using a torsionally stiff blade ($\lambda_{T1}/\Omega = 8$).

Table 5.1: Blade properties and operating conditions for verification case

Property	Value		Property	Value		Property	Value
$(k_A/k_m)^2$	1.5		N_b	4		λ_{T1}/Ω	5 , 8
k_m/R	0.025		$C(k)$	1		λ_{I1}/Ω	0.7
k_{m1}/kk_{m2}	0		$C_{l,\alpha}$	2π		λ_{O1}/Ω	1.15
$3\rho_\infty C_{l,\alpha} cR/m$	5		C_{d0}	0.01			
$\frac{c}{R}$	$\frac{\pi}{40}$		δ	0			

Firstly, torsional, in-plane and out-of-plane static deformations at the blade tip are calculated for a range of blade pitch angles to assess the static aeroelastic capabilities of the present model. The results of these analyses are presented in Fig. 5.4 for the torsionally soft case for which equivalent analyses were presented in [3].

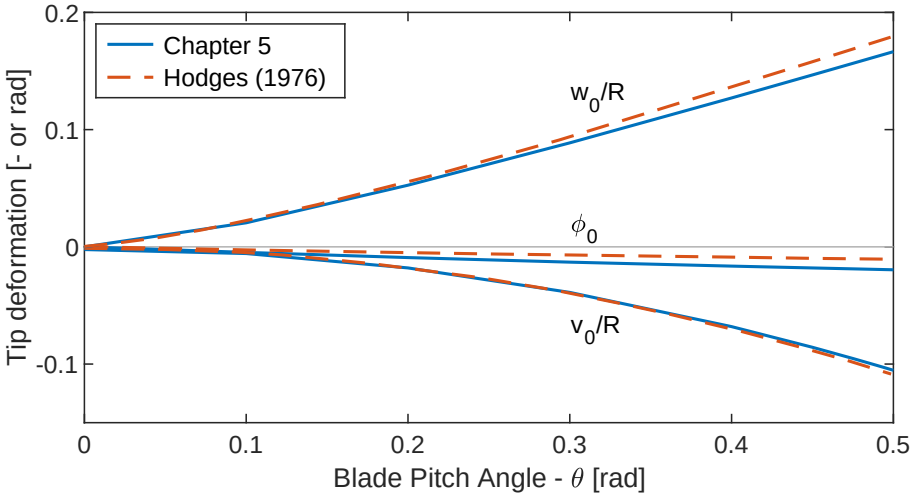

Figure 5.4: Comparison of static deformation of the blade tip calculated using the present model with the aeroelastic reference [3].

It can be seen that there is good agreement between the two sets of results. The most im-

portant difference is likely to be the discrepancy in the torsional deformation. The results from the present model feature increased negative (nose down) blade twist at the tip when compared with the results of the aeroelastic reference model. This discrepancy results in a reduction of the aerodynamic loads, most notably lift. The reduction of these loads is a likely cause of the under-predicted in-plane and out-of-plane deflections. Similar under-prediction of in-plane and out-of-plane deflections was also observed in [131] during a similar validation study using a different modelling approach.

Once the static deformations had been calculated, the natural frequencies for the modes presented in [3] - first torsional (T_1), out-of-plane (O_1) and in-plane (I_1) - are calculated for a range of blade pitch angles to assess the dynamic aeroelastic performance of the present model. The results of these analyses are presented in Fig. 5.5 for both the torsionally soft and torsionally stiff cases presented in [3].

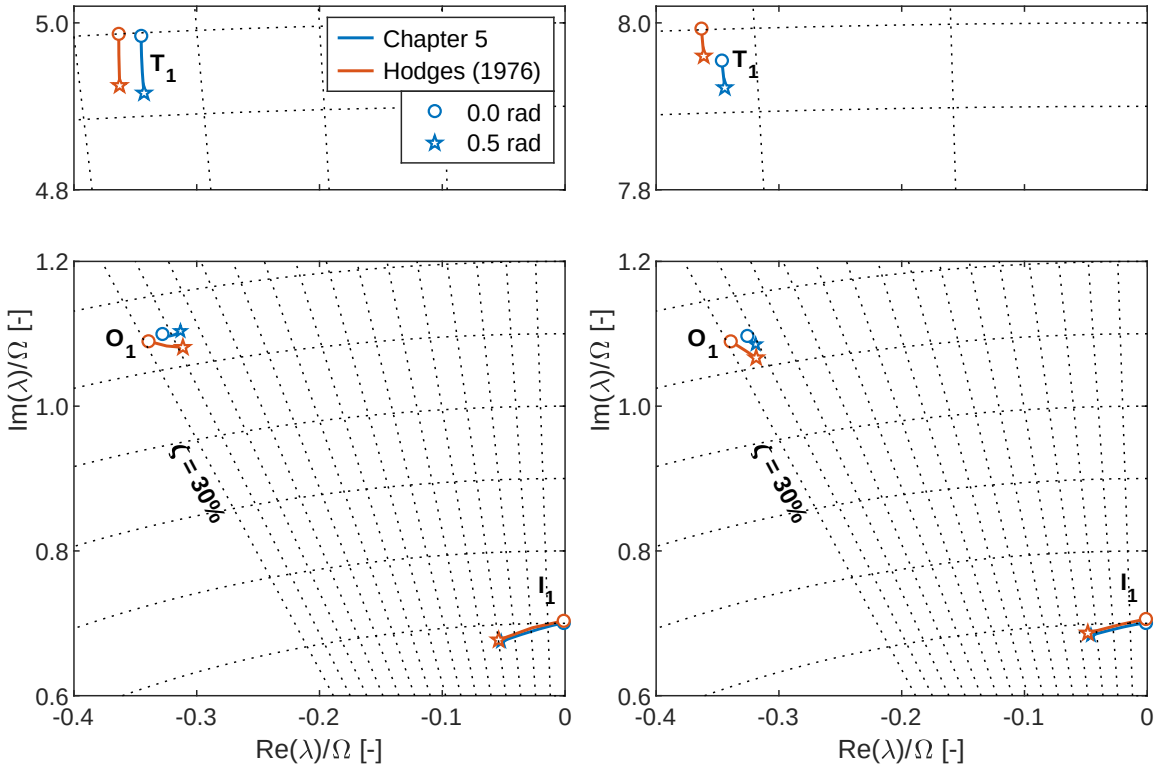

(a) Torsionally Soft

(b) Torsionally Stiff

Figure 5.5: Comparison of eigenvalues from the present model with the aeroelastic reference [3]. Radial lines denote constant damping ratio increments of 2 %. Circular lines denote constant undamped natural frequency.

Again, it can be seen that the agreement between the two sets of results is acceptable. The modal loci exhibit similar magnitudes and trends between the two different models. To quantify the errors, the undamped natural frequencies and damping ratios are calculated for blade pitch

angles of 0.0 rad and 0.5 rad and the errors between these values are shown in Fig. 5.6.

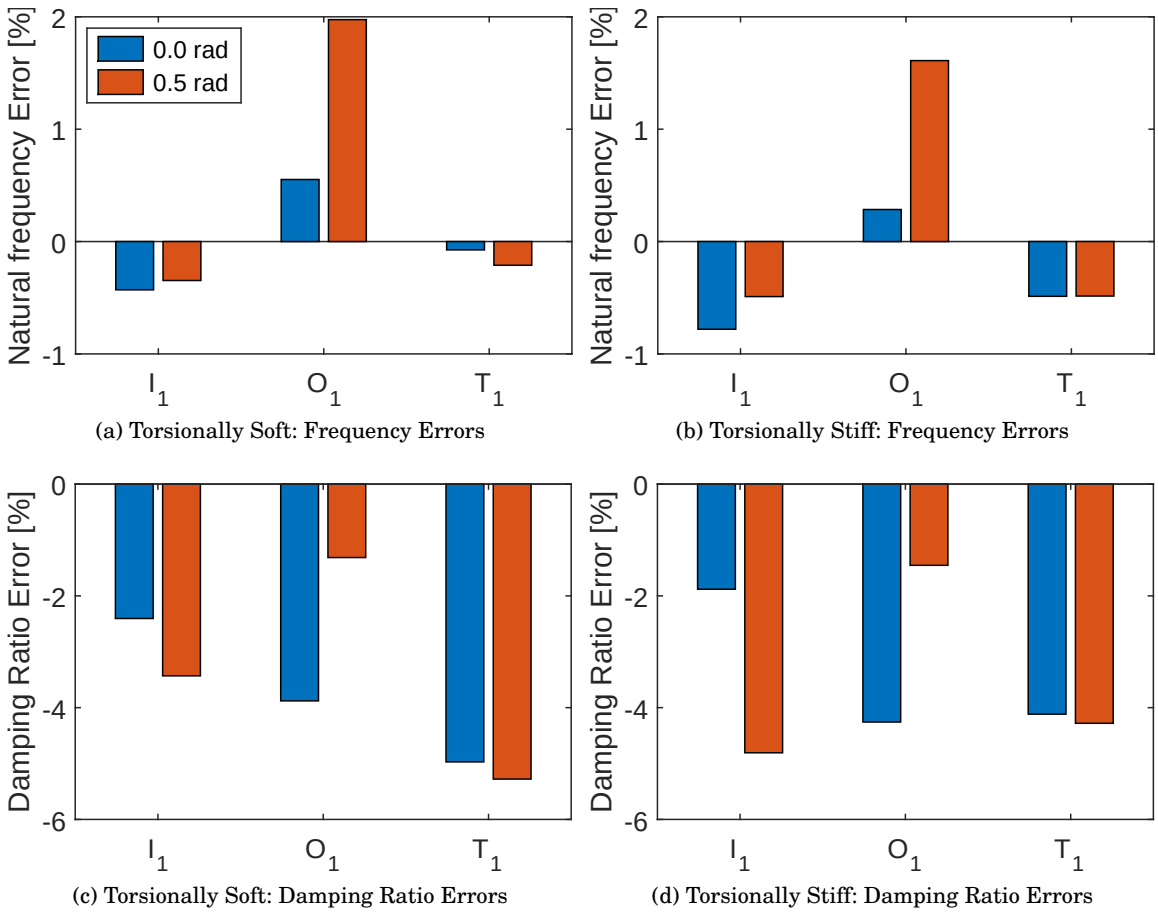

(a) Torsionally Soft: Frequency Errors

(b) Torsionally Stiff: Frequency Errors

(c) Torsionally Soft: Damping Ratio Errors

(d) Torsionally Stiff: Damping Ratio Errors

Figure 5.6: Natural frequency and damping ratio errors at minimum and maximum blade pitch angle

It can be seen that the errors in frequency shown in Figs. 5.6a and 5.6b are all smaller than 2 % which confirms the correlation between the models. Additionally, it can be seen that the sign and magnitude of these errors are reasonably consistent between different blade pitch angles and torsional stiffnesses. The error in the damping ratio values shown in Figs. 5.6c and 5.6d are also low, all near to or smaller than 5 %. It can also be seen that a similar observation can be made about the consistency of the sign and magnitude of the errors.

There are several differences between the models which are the likely sources of the discrepancies observed.

The trigonometric terms in the aerodynamic model are treated differently in each of the models. In the present work the denominator of Eq. (5.10) is the total aerodynamic velocity whereas in [3] this is assumed to be approximately equal to the horizontal component, $(\Omega x + v_*)$. This results in several extra terms occurring in the present model which, while comparatively small,

will alter the observed aerodynamic loading.

In the aeroelastic reference model [3], the solutions are obtained using a two-stage Galerkin method. Initially, a subset of six uncoupled, non-rotating mode shapes are used to calculate the static equilibrium and perform an in-vacuo free-vibration analysis to calculate the coupled, rotating mode shapes. The coupled-rotating mode shapes are then used to calculate the frequencies of the dynamic perturbations about the static deformations. In contrast, the present model uses a collocation method which uses local cubic polynomials between collocation points to define candidate solutions. The mesh of collocation points and the polynomials are refined until specified convergence criteria within the solution domain are met.

Additionally, the aforementioned differences may compound errors in the natural frequency comparisons. Any errors in the static deformation caused by these differences will propagate into the dynamic analyses via the geometric nonlinearities and by altering the aerodynamic loads.

Overall, the agreement in the in-vacuo and aeroelastic validation is more than sufficient. It gives confidence that the model has been developed and implemented correctly and is able to capture the effects of compressive and aerodynamic loading on the natural frequencies of pretwisted rotor blades.

5.3 Aeroelastic case study

With the development and validation of a model that includes geometric nonlinearities and aerodynamic loading in hover, the fidelity of the model has been extended beyond that presented in Chapter 4. Herein, the effects and significance of the additional capabilities of the model described in Section 5.1 to those of the model used in the previous chapter, Chapter 4, shall be assessed. A subsequent case study shall be performed to assess the resonance avoidance capability of compressive loading for a set of test aircraft described in Appendix C.

5.3.1 Implications of aerodynamic loading in hover on the dynamic properties of a rotor blade

The results presented herein were presented, in part, in [181] and are in preparation to be submitted as a peer-reviewed journal publication.

It is expected that there will be two main impacts of geometric nonlinearities and aerodynamic loading introduced into the model. Firstly, is the direct impact that the time-dependent aerodynamic loads will have on the rotor blade's dynamic properties. Secondly, is the impact that the static time-invariant deformations, that are caused by the time-invariant aerodynamic loads, will have on the dynamic properties of the blade. It has already been observed that the dynamic properties of fixed wings with a high aspect ratio may undergo significant change with

wing deformation [182] and it is expected that this behaviour will also be influential in rotor blades.

To investigate these behaviours, a case study using three different test configurations is performed. The first configuration, referred to as *untwisted*, uses the *reduced statics* version of the model, as detailed in Section 5.1.5, and a version of the blade with twist removed. These modifications remove the structural coupling and ensure that the only interaction between different modes is via the aerodynamic loading. The second configuration, referred to as *twisted*, uses the *reduced statics* version of the model but reintroduces twist and therefore structural coupling. The final configuration, referred to as *full*, uses the full version of the model and retains the twist from the previous configuration. This configuration will introduce the effects of the static deformation into the model. The collective pitch for the *twisted* and *full* configurations, is again defined as the maximum value the aircraft is capable of [122], to accentuate its influence and retain equivalence to the studies performed in Section 4.3. A summary of these configurations can be found in Table 5.2.

Table 5.2: Case Study configurations

Configuration	Untwisted	Twisted	Full
Root pitch, $\theta(R_0)$ [rad]	0.140	0.262	0.262
Linear twist, δ [rad]	0	-0.140	-0.140
Model fidelity	Reduced Statics	Reduced Statics	Full

The aerodynamic parameters defined below are common across each of the aforementioned configurations. The air density is set to the value observed at an altitude of 3000 m [122]; an altitude which will represent a more realistic operating condition and is below the service ceiling for this aircraft.

Table 5.3: Aerodynamic properties for each configuration.

Property	Value
Lift coefficient slope, $C_{l,\alpha}$ [rad^{-1}]	2π
Parasitic drag coefficient, C_{d0} []	0.01
Air density, ρ_∞ [kg/m^3]	0.895

The rotor blade considered is again the MBB, as defined in Appendix C, and a lower limit of 60 % of the nominal rotor speed is again used to replicate the reduction of the A160T Hummingbird [28]. Firstly, the critical buckling load is calculated for each model configuration and subsequently used to determine the allowable upper limit of the compressive load. Secondly, the natural frequencies and damping ratios of the blade are investigated across a range of operating conditions to understand the influences of rotor speed and compressive loading across the range of modes assessed.

The maximum compressive load to be applied is again calculated as 75 % of the critical buckling load as calculated in-vacuo at the lowest rotor speed, 60 % of the nominal. The progression of the first three modes as the critical load is approached is shown below in Fig. 5.7.

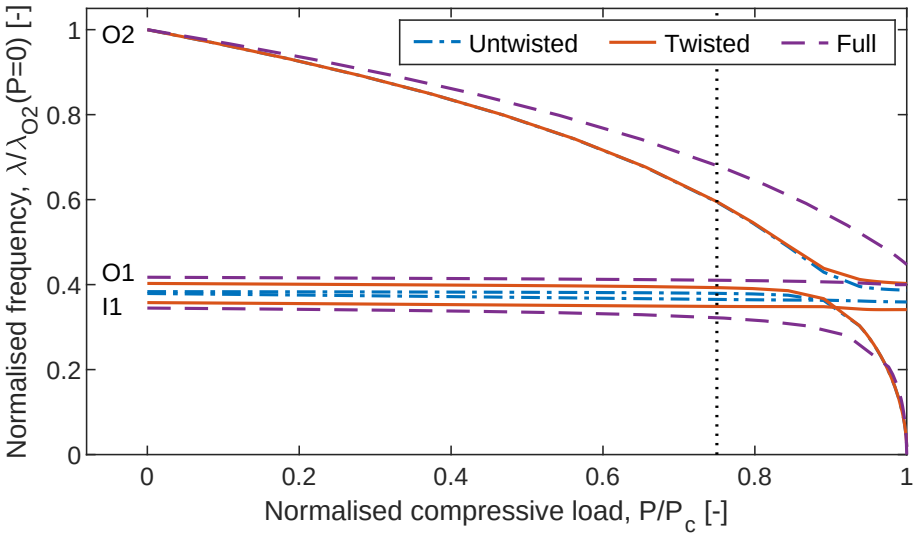

Figure 5.7: Natural frequencies of the lower three modes under compressive loading up to the buckling load.

For the *untwisted* and *twisted* configurations, the mode which leads to buckling is initially the second out-of-plane mode. However, as the compressive loading is applied, the natural frequency of this mode reduces and veers with the other two modes. The cause of this behaviour is likely to be the orientation of the applied load. The first in-plane and out-of-plane modes exhibit very low levels of sensitivity to the compressive loading. Consequently, the buckling mode becomes the next lowest mode, the second out-of-plane mode. The most notable difference between these two configurations is the proximity of the lower two frequencies in the *untwisted* configuration which is not present in the *twisted* one, due to the coupling introduced by the twist. Conversely, the *full* configuration behaves very differently. The inclusion of the static deformations caused by the aerodynamic forces changes the orientation of the applied load; resulting in the buckling mode no longer being the second out-of-plane mode but the first out-of-plane mode. The final buckling loads, and corresponding maximum allowable loads, are summarised below where it can be seen that the different buckling mode of the *full* configuration results in a lower critical and maximum load.

Table 5.4: Compressive loading limits

Configuration	Untwisted	Twisted	Full
Critical compressive force, P_c [N]	21.33×10^3	21.33×10^3	18.44×10^3
Maximum compressive force, P_m [N]	16.00×10^3	16.00×10^3	13.83×10^3

Once the upper limit for the applied compressive load had been established, the undamped natural frequencies and damping ratios for the first torsion (T1), first two in-plane (I1-I2) and first four out-of-plane (O1-O4) modes across a range of rotor speeds and compressive loads.

$$\lambda_0 = |\lambda| \tag{5.18a}$$

$$\zeta = \frac{-Re(\lambda)}{\lambda_0} \tag{5.18b}$$

These values for the *untwisted* configuration are shown in Fig. 5.8.

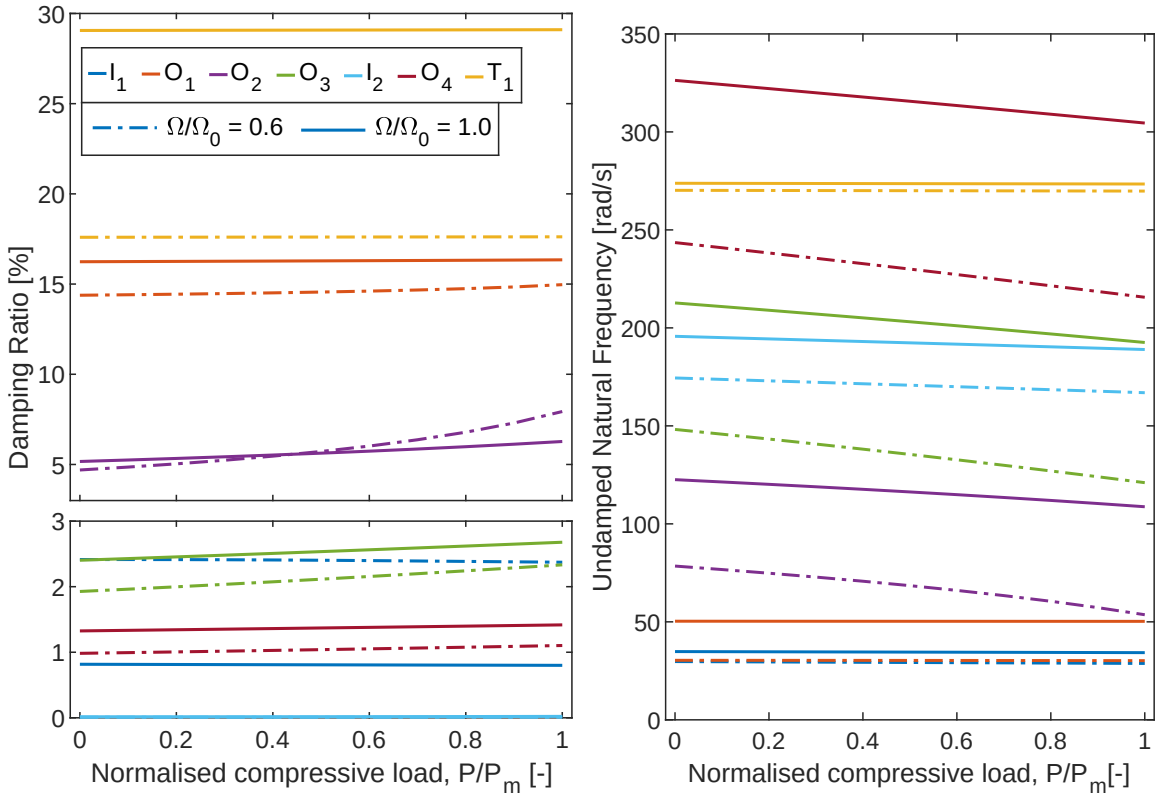

Figure 5.8: Aeroelastic properties across range of rotor speed and compressive loading for *untwisted* configuration

The trends in the undamped natural frequencies are similar to those observed in [153] and Chapter 4. The torsional mode is insensitive to centrifugal and compressive loading. The fundamental in-plane and out-of-plane modes are also insensitive to compressive loading. The higher-order out-of-plane modes are sensitive to the compressive loading, especially at the lower rotor speed. The higher-order in-plane mode is more sensitive than the fundamental in-plane mode but less sensitive than the higher-order out-of-plane modes. The similarity of these trends with those observed in previous in-vacuo research [153] and Chapter 4 indicates that the inclusion of aerodynamic loading does not fundamentally change the effects previously investigated.

The inclusion of aerodynamic loading introduces aerodynamic damping which has previously not been investigated in this work. Similarly to the trend of its natural frequency, the damping ratio of the torsional mode (T1) is unaffected by compressive loading, however, it is increased considerably by an increase in rotor speed. The lack of sensitivity of the natural frequency of this mode to compressive loading may indicate that resonance involving the torsional mode may be difficult to mitigate using compressive loading. However, the high damping ratio may result in a low amplitude of response during resonance. On the contrary, the damping ratios of the in-plane and out-of-plane modes exhibit considerable sensitivity. It can be seen that the damping ratios of lower-order out-of-plane modes are significantly larger than higher-order modes which is consistent with the previously observed values in [63]. A similar trend is observed in the in-plane modes, however, their damping ratios are notably lower due to the relative differences in the magnitude of the loads created in each direction by the oscillatory motion of the blade. In the out-of-plane direction, the blade motion forms a relatively large component of the effective angle of attack, as seen in Eq. (5.5), and therefore the out-of-plane aerodynamic force. In the in-plane direction, the blade velocity due to oscillatory deformations is significantly smaller than that due to the rotation of the blade which results in the in-plane aerodynamic force being dominated by the blade rotation. It can be seen that as the compressive loading is applied, the damping ratio increases. The application of the compressive load opposes the centrifugal load and reduces the effective stiffness which in turn reduces the critical damping value and therefore increases the damping ratio. This effect is more pronounced at the lower rotor speed as the reduction in effective stiffness is more sensitive to the compressive load. For the unloaded case, it can be observed that the damping ratios are higher at the higher rotor speed. This is due to the increase in velocity which increases the magnitude of the loads that dictate aerodynamic damping. However, as the compressive load is applied, the aforementioned higher sensitivity to compressive loading at lower rotor speeds may result in a higher damping ratio, despite a slower rotor speed, as seen in the second out-of-plane mode beyond 50 % of the maximum compressive load.

Increasing damping ratio, in addition to increasing the separation between natural and excitation frequencies, may be an additional means with which to reduce vibratory loads [68]. The ability of compressive loading to effectively alter both of these properties increases its effectiveness as a means for resonance avoidance.

Following the evaluation of the behaviour of the blade in the *untwisted* configuration, the *twisted* configuration was analysed to assess the influence of including structural coupling via twist. The aeroelastic properties of the blade in this configuration are shown in Fig. 5.9.

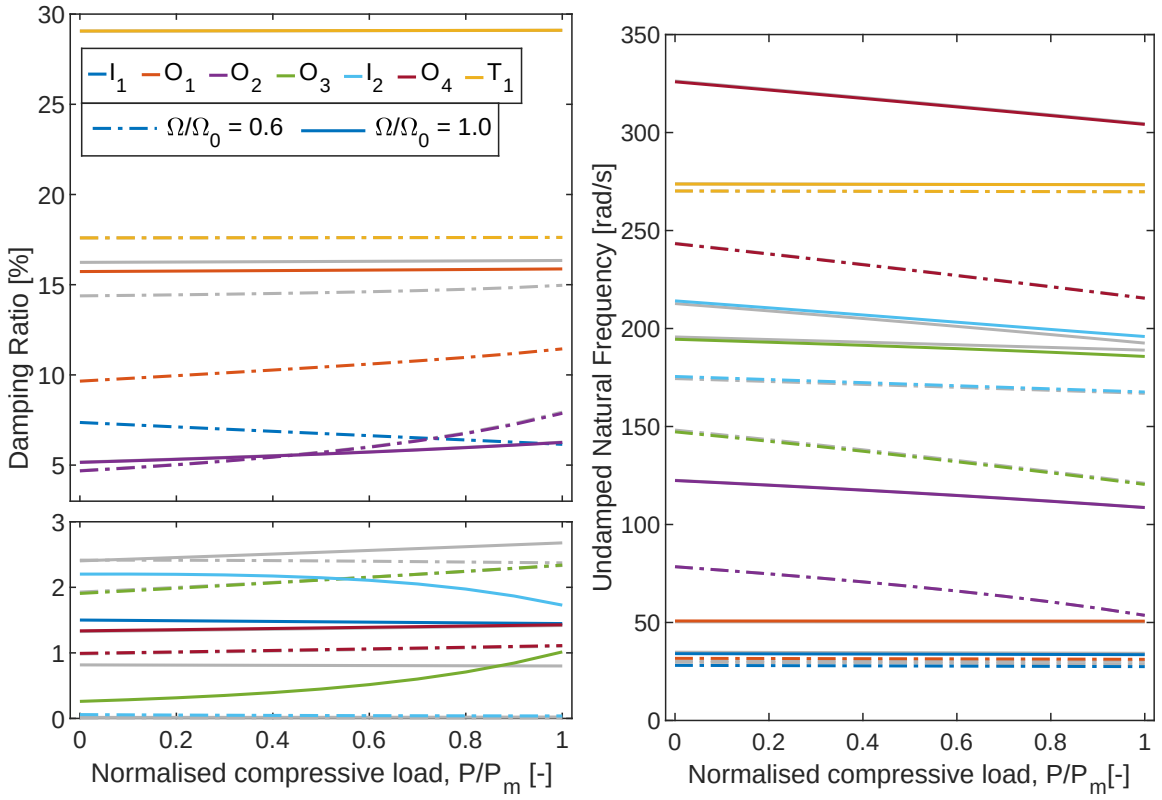

Figure 5.9: Aeroelastic properties across range of rotor speed and compressive loading for *twisted* configuration. Values for the *untwisted* configuration are shown in grey.

When comparing the behaviour of the aeroelastic properties of the blade in the *untwisted* and the *twisted* configurations, it can be seen that the amount of change observed differs greatly between modes. The second and fourth out-of-plane modes as well as the first torsional mode exhibit no discernible difference from the *untwisted* configuration. This is because none of these modes interact with any other mode for either the loaded or unloaded case, even with the inclusion of twist, as observed in Fig. 5.3. The first in-plane and out-of-plane modes exhibit a minimal change in natural frequency but, when compared to the *untwisted* configuration, the damping ratio of the first out-of-plane mode has reduced and the first in-plane mode has increased which is likely due to the coupling between these modes. The aeroelastic properties of the third out-of-plane mode and second in-plane mode are unchanged at the lower rotor speed where no coupling is observed. However, at higher rotor speeds there is considerable coupling between these modes, as observed in Fig. 5.3. The veering in the region results in a switching of the natural frequencies and damping ratios. As the compressive load is increased the natural frequency of the third out-of-plane mode will reduce, moving towards the second in-plane mode. The increased proximity of these modes to each other increases the coupling further and the damping ratios of the two modes can be observed to converge. The inclusion of twist in this configuration demonstrates that the presence of structural coupling influences both the natural

frequencies and damping ratios of the modes that exhibit coupling.

Once the blade's aeroelastic properties in the *twisted* configuration had been analysed, the *full* configuration was investigated to assess the impacts of including the static deformations of the blade. The calculated static deformation of the blade in the *full* configuration is compared to the prescribed values used in the *twisted* configuration in Fig. 5.10.

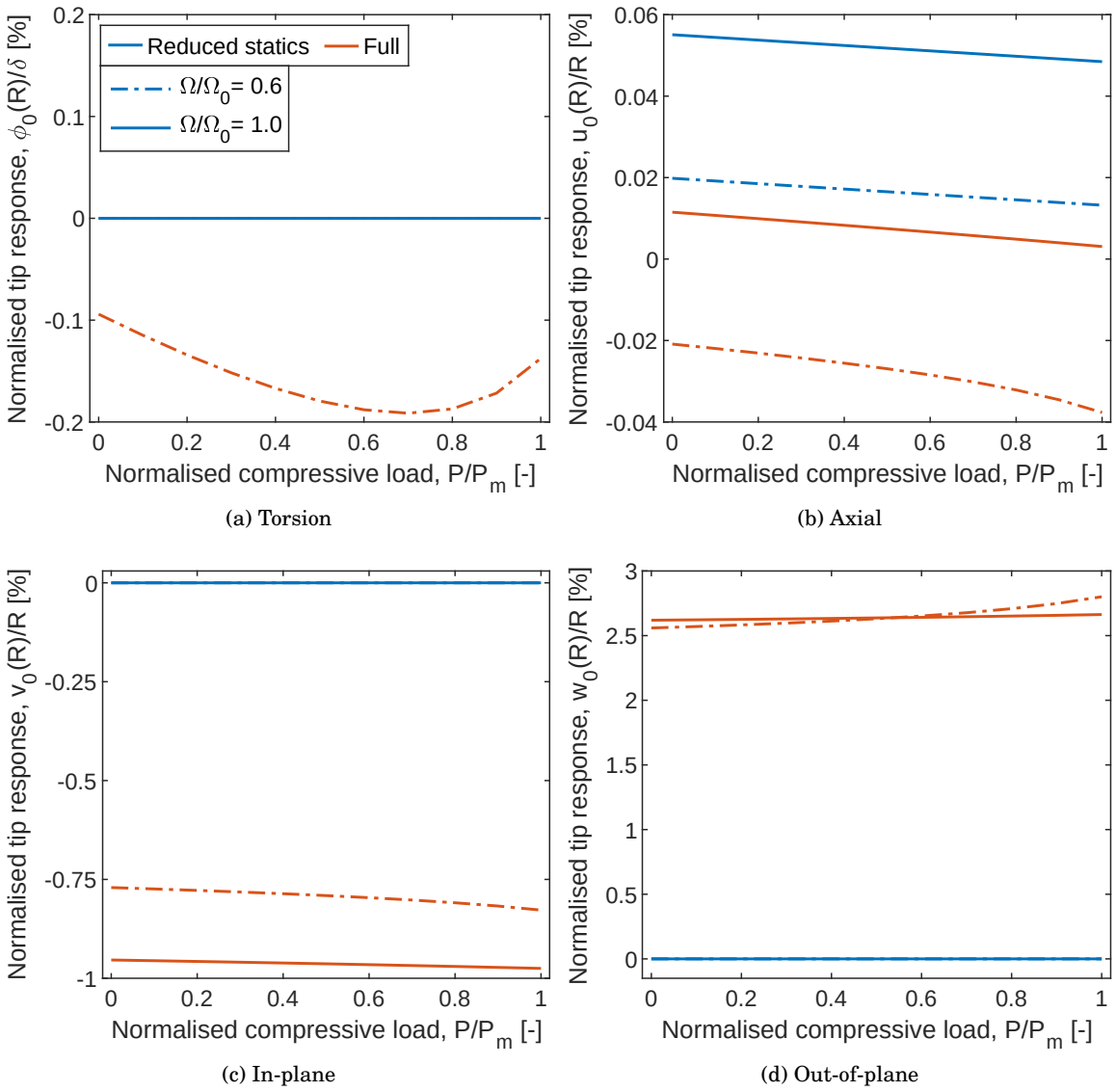

(a) Torsion

(b) Axial

(c) In-plane

(d) Out-of-plane

Figure 5.10: Steady state deformations of the blade tip with different statics models.

It can be seen that the drag and lift loads cause negative and positive steady-state deformations in the in-plane and out-of-plane directions, respectively. The application of a compressive load reduces the effective stiffness of the blade which increases the magnitude of these deflections. Similarly to the analyses of the dynamic properties shown previously, the sensitivity of

the steady-state deformations to the applied loading is larger at the slower rotor speed due to the lower centrifugal loading.

For the torsional deformation, the centrifugal loading induces two effects: the trapeze effect [42] and the tennis racket effect [138]. The trapeze effect untwists the blade, giving a positive twist deformation, whereas the tennis racket effect induces a negative twist deformation. As an applied compressive load is introduced, this opposes the centrifugal load causing an increase in twist via the trapeze effect. Despite the influence of these effects, the deformations are very small, contributing less than 0.4 % of the overall geometric angle of attack of the blade at the tip.

Unlike the other motions, the axial direction has a non-zero prescribed value for the *twisted* configuration. Due to the centrifugal loading, there is a positive axial extension at the tip which is larger at the higher rotor speed. As a compressive load is applied this value reduces as the blade is compressed. However, the reduction due to the compressive loading is significantly smaller than the extension due to centrifugal forces which indicates that the centrifugal load remains the dominant loading component in this direction. When considering the *full* configuration, it should be noted that, in addition to the axial deformation due to centrifugal and applied compressive loads, the phenomenon of geometric shortening at the tip of the blade due to in-plane and out-of-plane deformation is captured. This effect results in an effective shortening of the blade due to out of plane transversal deformation as exemplified below.

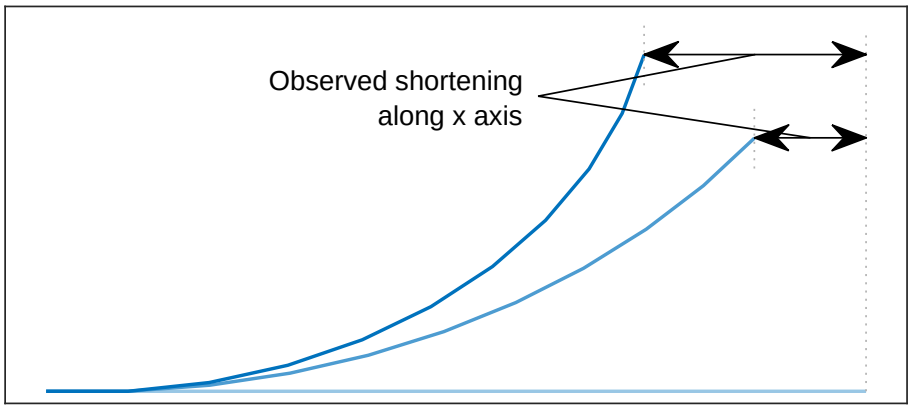

Figure 5.11: Example of geometric shortening.

Geometric shortening results in an axial deformation of the blade which offsets the axial deformation from those values calculated analytically. For the lower rotor speed at high levels of loading, it can be observed that the offset between the two configurations is not constant. This is due to the increase in in-plane and out-of-plane deformation exacerbating the shortening effect. At the higher rotor speeds, the deformations are changed much less and therefore have a smaller impact on the shortening.

To evaluate the influence of the static deformations on the blade's dynamics, the aeroelastic

properties for the final study are calculated, as shown in Fig. 5.12. In the final configuration considered for this study, the changes in the aeroelastic properties shall be contrasted with those discussed for the *twisted* configuration to isolate and identify additional behaviour caused by the static deformations.

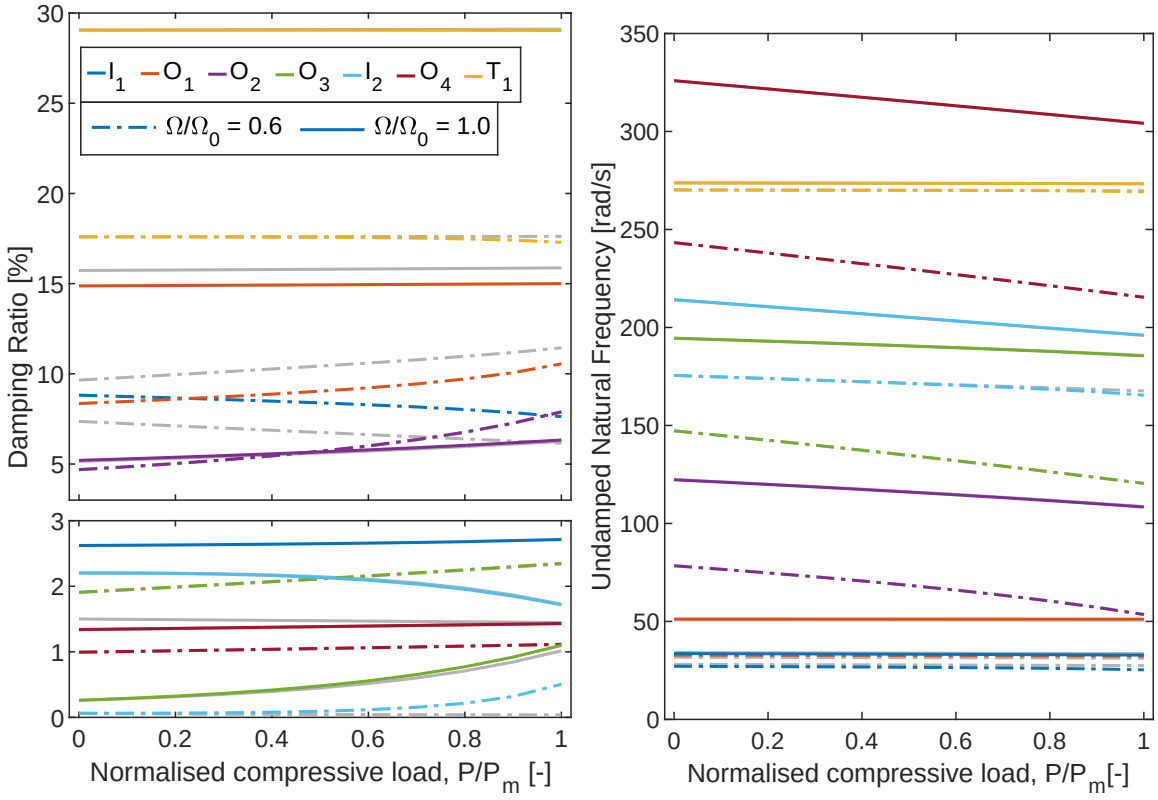

Figure 5.12: Aeroelastic properties across range of rotor speed and compressive loading for *full* configuration. Values for the *twisted* configuration are shown in grey.

When considering the undamped natural frequencies in Fig. 5.12, it can be seen that there is almost no discernible difference in the trends from the *twisted* configuration.

When considering the damping ratios, the trends are largely similar to the *twisted* configuration. The inclusion of static deformation appears to have a negligible effect on the damping ratios of the second, third and fourth out-of-plane modes, second in-plane mode and the first torsional mode. Similarly to the inclusion of twist in the *twisted* configuration, the inclusion of static deformation in the *full* configuration increases the damping ratio of the first in-plane mode and reduces that of the first out-of-plane mode. This is likely to be due to the static deformation further increasing the coupling between these modes which increases the convergence of their damping ratios towards one another.

It can be concluded from this case study that the inclusion of aerodynamic loading alone does not fundamentally change the behaviour of the undamped natural frequencies from that ob-

served in Chapters 3 and 4. However, the inclusion of geometric nonlinearities and aerodynamically induced static deformations does exacerbate the previously observed responses to applied compressive loading.

Conversely, the aerodynamic damping has no parallel in Chapters 3 and 4 to be compared to. Each of the modes observed exhibited a significant increase in damping ratio with an increase in rotor speed due to the corresponding increase in local air velocity and subsequently aerodynamic loads. Out-of-plane modes exhibit larger damping values than in-plane modes but both orientations saw higher values in their lower modes than in their higher modes. As structural coupling was introduced, the modes were observed to share damping values, as well as natural frequencies, across regions of veering. The application of a compressive load tended to increase the damping ratios. This is expected to be due to the reduction of the undamped natural frequency, which lowers the critical damping value. As the natural frequencies of the out-of-plane modes are most sensitive to compressive loading, they exhibited the most change. On the contrary, the torsional mode, whose natural frequency is almost unaffected by compressive loading demonstrated a similarly negligible change in damping ratio with the application of a compressive load.

5.3.2 In-air resonant behaviour in a blade without compression

As was demonstrated in Section 4.3.3, it is possible to use compressive loading to increase the range of rotor speeds that exhibit an acceptable level of separation between the natural frequencies of the rotor blade and its rotor harmonics significantly beyond the range observed for a rotor blade without compressive loading. However, the use of separation between natural frequencies and rotor harmonics does not account for the influence of damping. Herein the inclusion of aerodynamic loading will introduce aerodynamic damping into the behaviour of the blade. Therefore, a new metric, which accounts for the changes in damping ratio as well as natural frequency that were observed in Section 5.3.1, is developed. The metric is then used to assess the resonant interactions of a rotor blade without compressive loading and evaluate the improvement available through the use of an applied compressive load.

The proposed metric consists of integrating the area under the Frequency Response Function (FRF) of the rotor blade to calculate a cumulative response to the prescribed range of frequencies. This metric is similar to Power Spectral Density (PSD) which has been used historically to compare and improve the dynamic performance of vibrating entities [183, 184, 185]. An example of this metric, herein referred to as Cumulative Aeroelastic Response (CAR), is shown below to demonstrate how it captures resonance and the ability to capture the avoidance of resonance due to changing natural frequencies and damping ratios.

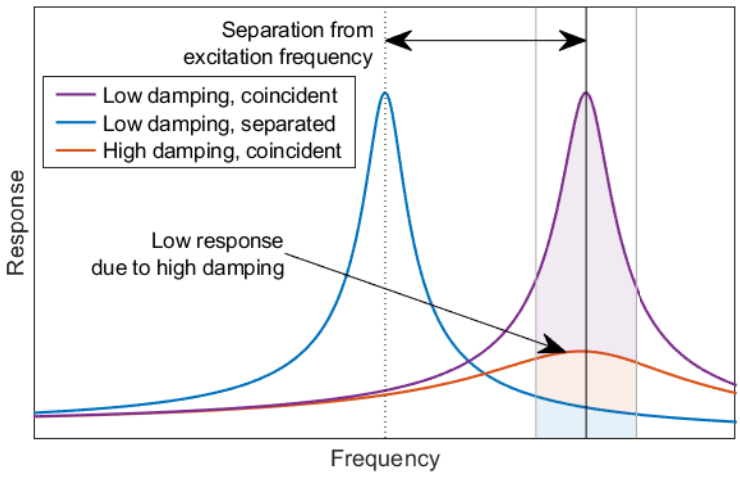

Figure 5.13: Example of CAR for one region of interest.

As seen in Fig. 5.13, the case with low damping and a natural frequency that coincides with the frequency region of interest has a large amount of area, indicating a large response to excitation in this frequency region. However, if the natural frequency is reduced or the damping ratio is increased, as seen in the other two configurations, this lowers the FRF value in the prescribed region and subsequently lowers the area under the FRF.

For rotorcraft, the frequency regions that are of interest are those surrounding each of the rotor harmonics to be evaluated. In the case where there are multiple regions to be evaluated, these values shall be summed to give the cumulative area under the FRF for the specified regions. An example of CAR being evaluated around the first three rotor harmonics is shown below.

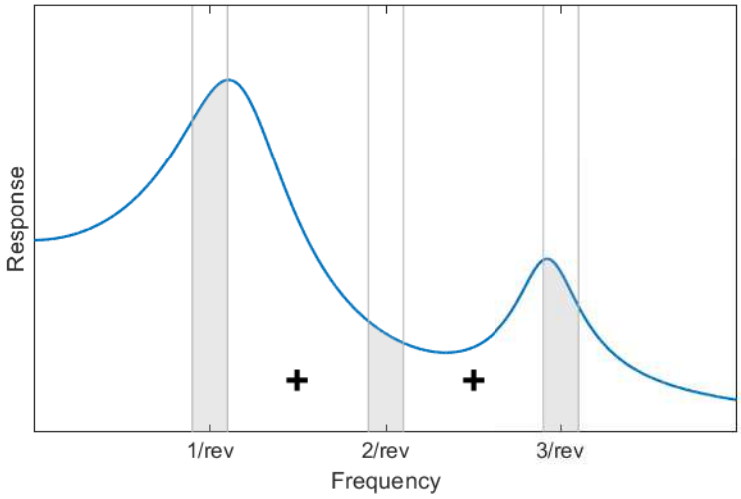

Figure 5.14: Example of CAR for multiple regions of interest.

This type of metric has successfully been used on high aspect ratio fixed-wing aircraft to optimise their aeroelastic response to a gust [186].

To enable to calculation of this metric, a few of alterations were made to the model and the algorithmic procedure. Instead of using an *eigenvalue* solution to calculate the natural frequency, a *harmonic* solution is obtained to evaluate the response shape of the blade to excitation across the range of frequencies that are of interest. The excitation is provided by means of a constant unit load (total load on the blade equalling 1 N or 1 N m for transversal and torsional load respectively). The choice of a constantly distributed force will avoid emphasising different sections of the blade and ensure that all modes are sufficiently excited. These loads are implemented by replacing Eq. (5.9) with the following.

$$\begin{aligned} L_x &= 0 \\ L_y &= -L_{NC}\sin(\theta+\phi_*) - L_C\sin(\alpha_{in}) - D\cos(\alpha_{in}) + \underline{L_{y0}e^{st}} \\ L_z &= L_{NC}\cos(\theta+\phi_*) + L_C\cos(\alpha_{in}) - D\sin(\alpha_{in}) + \underline{L_{z0}e^{st}} \\ M_\phi &= M_{NC} + M_C + \underline{M_{\phi 0}e^{st}} \end{aligned} \tag{5.19}$$

where

$$L_{y0} = L_{z0} = M_{\phi 0} = \frac{1}{R-R_0} \tag{5.20}$$

The underlined term indicates the additional harmonic excitation load.

Once the response shape had been calculated, the combined response of the blade at its tip, incorporating the in-plane and out-of-plane translation and torsional deformation, is used to calculate the FRF as follows.

$$H = \frac{\sqrt{u(R)^2 + v(R)^2 + w(R)^2 + \left(\mu\phi(R)\right)^2}}{\int_{R_0}^{R} \frac{1}{R-R_0} dx} = \sqrt{u(R)^2 + v(R)^2 + w(R)^2 + \left(\mu\phi(R)\right)^2} \tag{5.21}$$

Subsequently, the FRF is used to calculate the CAR.

$$\eta(\Omega, P) = \sum_{\forall n} \int_{n\Omega-\Delta s}^{n\Omega+\Delta s} H(s,\Omega,P) ds \tag{5.22}$$

As the exact numerical value of CAR lacks direct physical meaning, it shall be presented as a deviation from the value at the nominal rotor speed without compressive loading, $\eta(\Omega,P)/\eta(\Omega_0,0)$. As it can be assumed that the nominal operating conditions are safe to operate in, this value shall be used as the upper acceptable limit of response.

The algorithmic procedure remains similar to that detailed in Section 2.3.2.2, but with the replacement of the eigenvalue analyses inside the nested loops, as seen below.

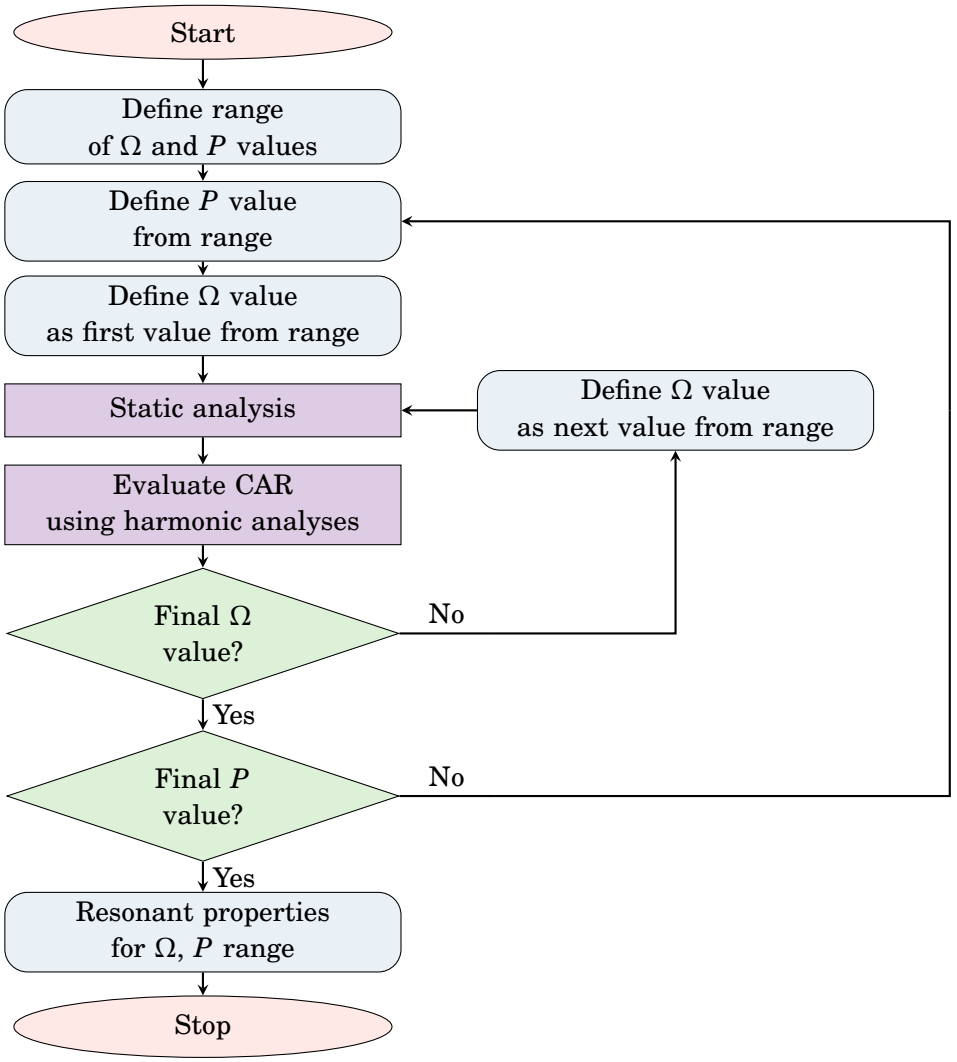

Figure 5.15: Process to calculate the response of the rotor blade for each value of rotor speed and compressive load.

A nested loop of rotor speeds and compressive loads is used to ensure the full range of operating conditions is investigated. Within these loops, a static analysis is used to calculate the statically deformed shape of the blade at each operating condition. A harmonic analysis is then performed across the prescribed range of frequencies ($n\Omega - \Delta s$ to $n\Omega + \Delta s$) which are used to evaluate Eq. (5.22).

This newly defined metric and algorithmic procedure shall be in a two-stage case study: firstly to evaluate the baseline response of the aircraft, without any applied compressive loading, to a variable rotor speed and secondly to investigate the improvements to the baseline response that

is available through the use of an applied compressive load.

To evaluate the response of the aircraft without any applied compressive loading to a variable rotor speed, the previously described analysis is performed to identify the resonances that will be encountered. This analysis is performed for two of the three test aircraft defined in Appendix C: the Bo105 and the Lynx. The AW101 is excluded from the upcoming investigation as it was observed in Chapter 4 that it exhibited an overly high fundamental in-plane natural frequency. The rotor speed range remains between 60 % and 100 % of the nominal to replicate the reduction observed in the A160T Hummingbird [28] and the studies previously performed in Chapters 3 and 4. For these analyses, the aerodynamic properties remain identical to those used in Section 5.3.1.

The resulting cumulative aeroelastic response, as defined by Eq. (5.22), for the first ten harmonics of the Bo105 using $\Delta s = 0.25$, is shown below alongside the damped natural frequencies and damping ratios for the first seven modes.

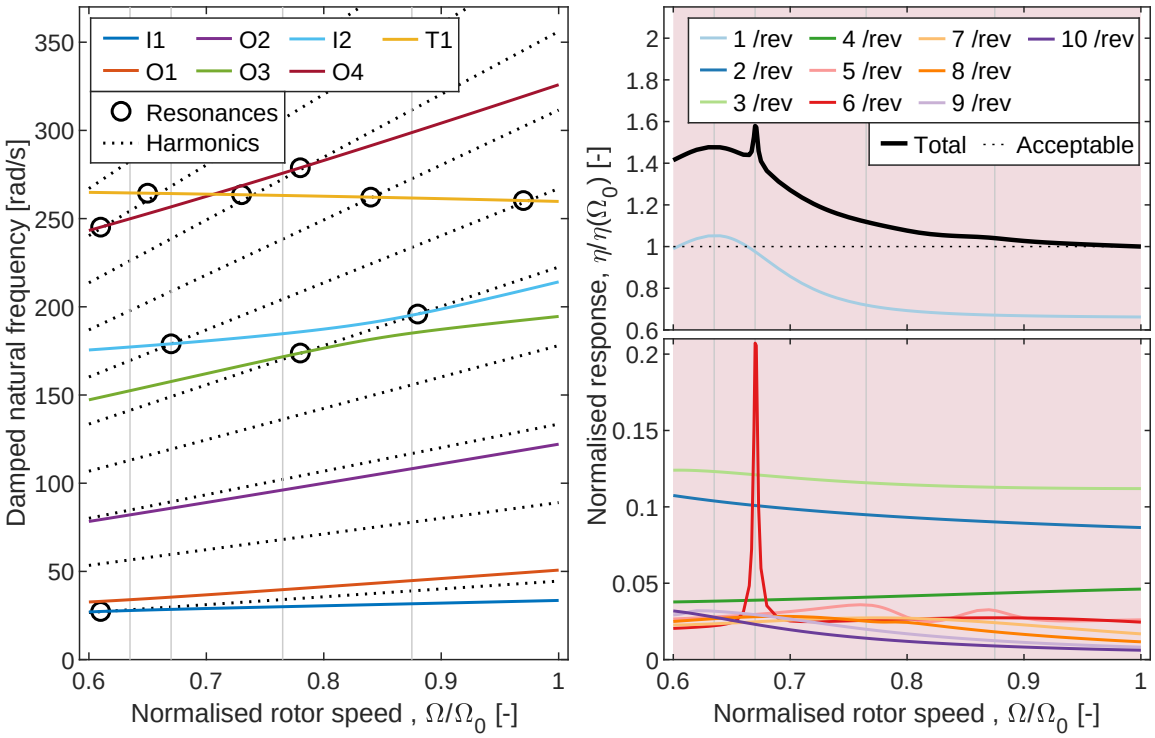

(a) Fan diagram

(b) Cumulative aeroelastic response

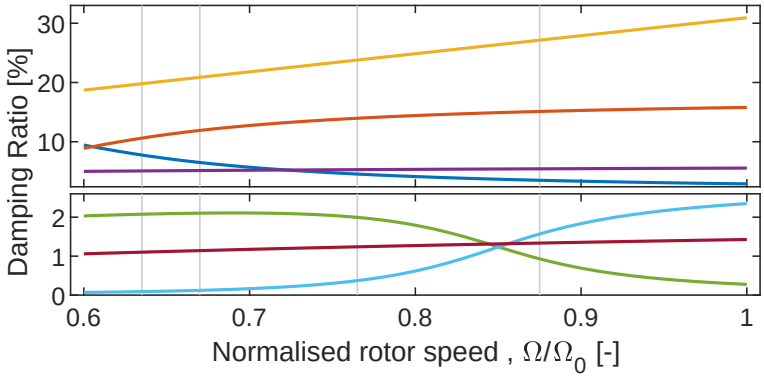

(c) Damping ratios

Figure 5.16: Aeroelastic response of Bo105 without compressive loading across a range of rotor speeds.

It can be seen in Fig. 5.16b that at the nominal rotor speed, the total response (the sum of contributions from each harmonic) is inherently exhibiting the limiting acceptable response. As the rotor speed reduces, the total response increases beyond an acceptable level which would inhibit the safe use of these rotor speeds in operation. There is a trend for the lower harmonics to contribute a larger component of the overall total and it can be observed that the lowest three harmonics, which are the most significant contributors to the total value, all exhibit an increase in response as the rotor speed reduces.

When considering the features of the total response, it can be seen that there are two peaks: one broad peak that spans the majority of the rotor speed range and one narrow peak at 67 % of the nominal rotor speed. When we consider the constituent harmonics that contribute to the overall total, which are also shown in Fig. 5.16b, we can see that the broad peak corresponds to the 1/rev harmonic and the narrow peak corresponds to the 6/rev harmonic. It can be seen in Fig. 5.16a that the broad resonant peak is due to the interaction of the first in-plane mode with the 1/rev harmonic that occurs at the slower rotor speeds. As the rotor speed increases there is increased separation between the first in-plane mode and the 1/rev harmonic which reduces the contribution of this harmonic to the overall total. The narrow peak at 67 % of the nominal rotor speed is due to the interaction of the second in-plane mode and the 6/rev harmonic. Despite the generally lower contribution of this harmonic to the overall total, it can be seen that due to the very low damping ratio observed in Fig. 5.16c, the increase in the response is large. While not obviously contributing to the overall total, it should be noted that there are two small additional responses observed in the 5/rev harmonic at 76 % and 87 % of the nominal rotor speed. Despite interacting with a similar harmonic to that of the narrow band, their damping ratios are not as low which is the cause of the smaller magnitudes of their increase. The remaining six interactions highlighted in Fig. 5.16a occur due to interaction of the fourth out-of-plane mode and the first torsional mode. The fourth out-of-plane mode is interacting with all but the highest harmonics and the first torsional mode has a very high damping ratio, hence these interactions are not observed in Fig. 5.16b.

This analysis was also performed for the Lynx, as shown below.

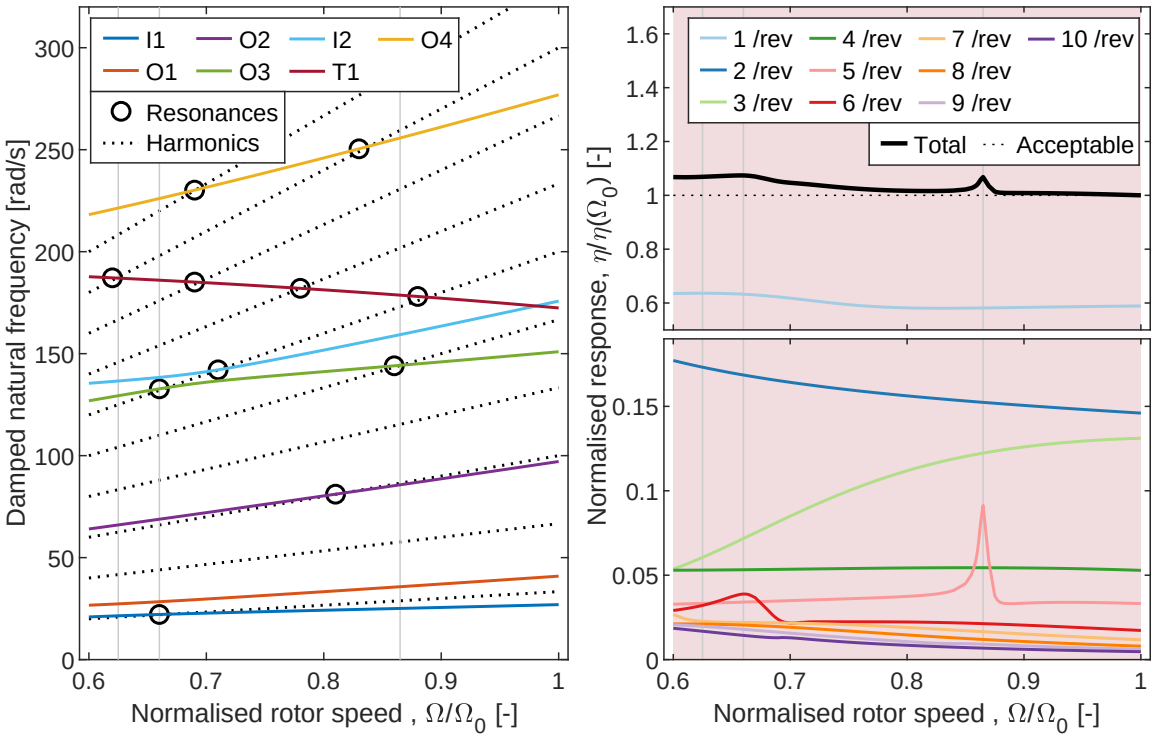

(a) Fan diagram

(b) Cumulative aeroelastic response

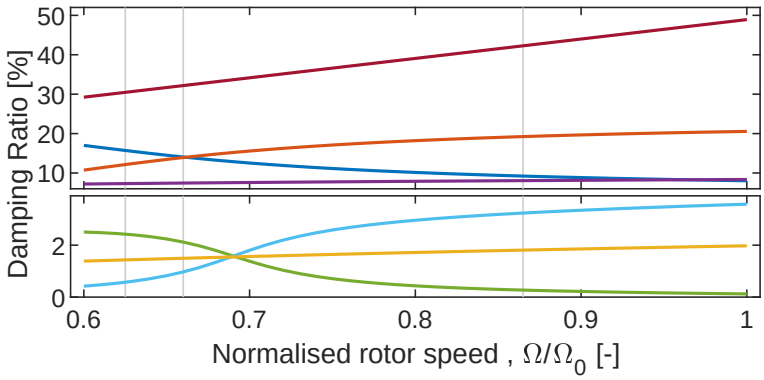

(c) Damping ratios

Figure 5.17: Aeroelastic response of Lynx without compressive loading across a range of rotor speeds.

The behaviour observed in the Lynx is greatly similar to that observed in the Bo105 discussed previously. The increase in the contributions of the 1/rev and 2/rev harmonic result in a total response that is higher than the acceptable level for the entire rotor speed range. There is a peak due to the interaction between the first in-plane mode and the 1/rev harmonic. However, due to the damping ratio being higher than that observed in the Bo105, this peak is significantly smaller. There is a peak in the 5/rev harmonic due to an interaction with the second in-plane mode (labelled as the third in-plane mode but after veering, it will be the second in-plane) which

is narrow due to the very low damping ratio. There is a small peak in the 6/rev harmonic due to interactions with the second in-plane mode and third out-of-plane mode which occurs at a rotor speed where these two modes are exhibiting veering which causes them both to have reasonably low damping ratios. The interaction between the second out-of-plane mode and the 3/rev harmonic observed in Fig. 5.17a is not present in Fig. 5.17b due to the high damping ratio that it exhibits.

5.3.2.1 In-air resonant behaviour in a blade with compression

Before the compressive load can be used to improve the response of the blade, an upper limit for the compressive load must be established. This is calculated as 75 % of the critical buckling load which is defined as the load at which the lowest natural frequency reaches zero as is used in Chapters 3 and 4 and Section 5.3.1. The critical buckling load is calculated at the lowest rotor speed considered for this analysis to ensure the limit load is conservative. The evolution of the lowest natural frequency with compressive load is shown below in Fig. 5.18 and the summary of the compressive and limit loads are shown in Table 5.5 alongside the values from Chapter 4 for reference.

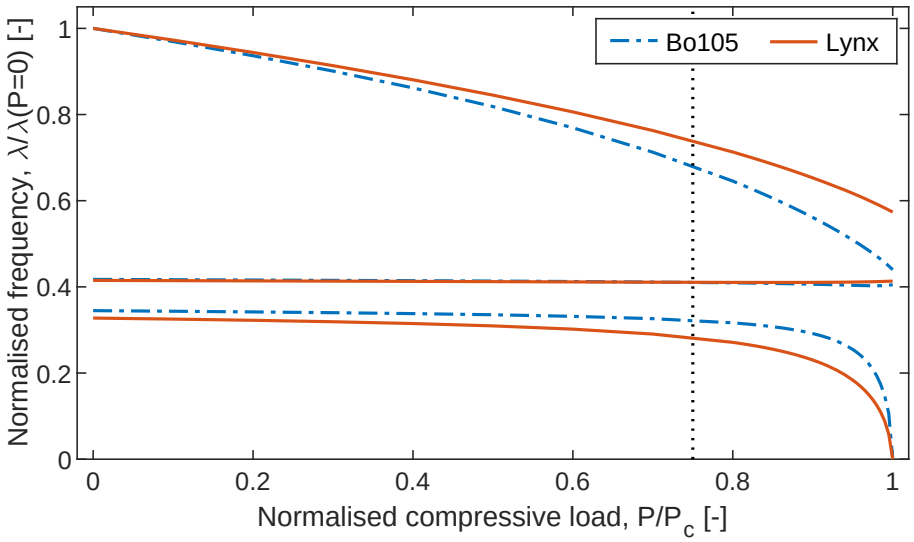

Figure 5.18: Natural frequencies of the lower three modes under compressive loading up to the buckling load.

Table 5.5: Buckling and maximum allowable loads for each aircraft

Aircraft	MBB Bo105	Westland Lynx
Critical compressive force from Chapter 4, P_c [N]	21.15×10^3	24.27×10^3
Critical compressive force, P_c [N]	18.44×10^3	17.04×10^3
Maximum compressive force, P_m [N]	13.83×10^3	12.78×10^3

It can be seen for each aircraft, that the critical buckling load is lower than that observed in the previous chapter and that the mode which drives the buckling is no longer the third mode, but the first. This change in behaviour is due to the inclusion of the static deformation due to aerodynamic loading. As observed in Section 5.3.1, the inclusion of static deformation increases the sensitivity of the lowest modes in each direction to compressive loading which causes them to dictate the buckling load which is lower than that of the third mode. The reduction in limit load may prove beneficial as it will reduce the power, size and mass requirements of a potential actuation method used to implement a compressive loading based resonance avoidance technique.

Once the maximum compressive load has been established, the CAR can be calculated across the full range of rotor speeds from 60 % to 100 % of the nominal and up to the maximum compressive load allowable. From this set of results, the compressive load which results in the minimum CAR is obtained as the optimal compressive loading profile. The resulting aeroelastic response for each aircraft is shown below alongside the reference unloaded case.

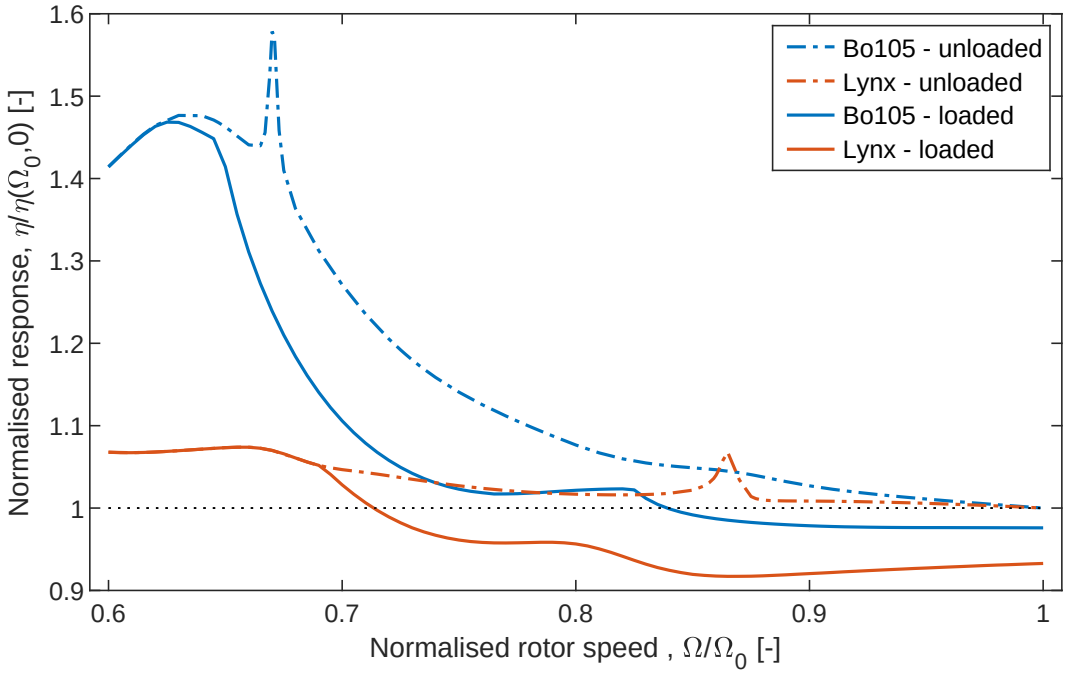

Figure 5.19: Baseline and optimised aeroelastic response of each aircraft across a range of rotor speeds, akin to Total value in Fig. 5.17.

It can be seen in Fig. 5.19 that the unloaded cases for both aircraft perform poorly. The CAR are above the acceptable limit for the entire range of rotor speeds investigated and a narrow peak is observed at 67 % and 87 % for the Bo105 and Lynx, respectively. However, with the inclusion of the compressive loading these peaks have been eradicated and the overall response has been reduced over the majority of the rotor speed range evaluated. The reductions are most

significant at the higher rotor speed where they have been reduced to an acceptable level which would permit the rotor speeds for the Bo105 and Lynx to be reduced by 16 % and 28.5 %, respectively. To better understand the cause of these improvements the contributions to the total response from each harmonic, the optimal compressive loading profile and the natural frequency and damping ratio of each mode shall be examined. These results are shown below for the Bo105 in Figs. 5.20 and 5.21.

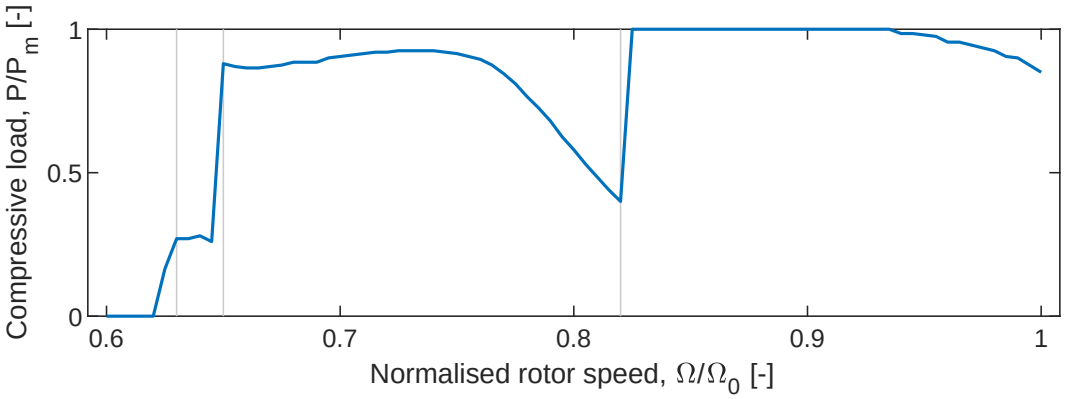

(a) Optimal loading profile

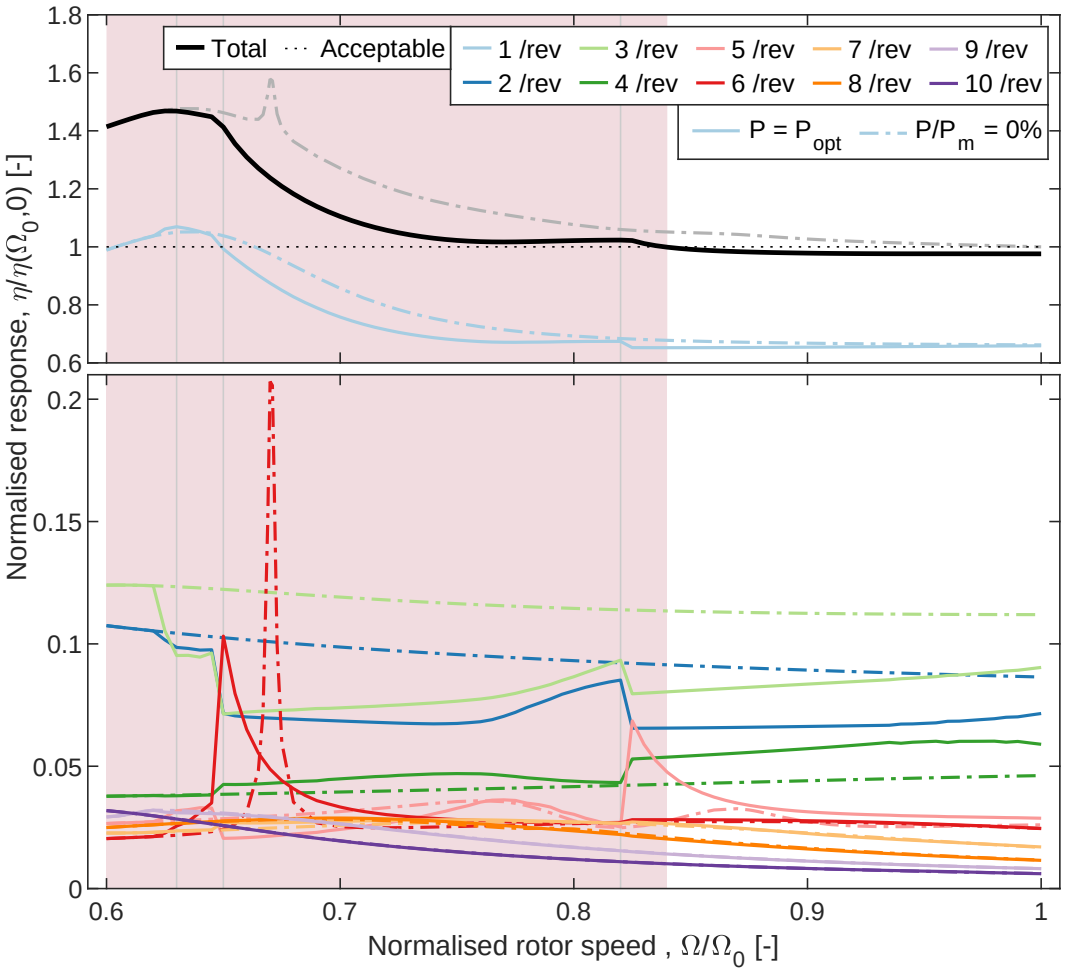

(b) Cumulative aeroelastic response

Figure 5.20: Optimised aeroelastic response of Bo105 with compressive loading across a range of rotor speeds.

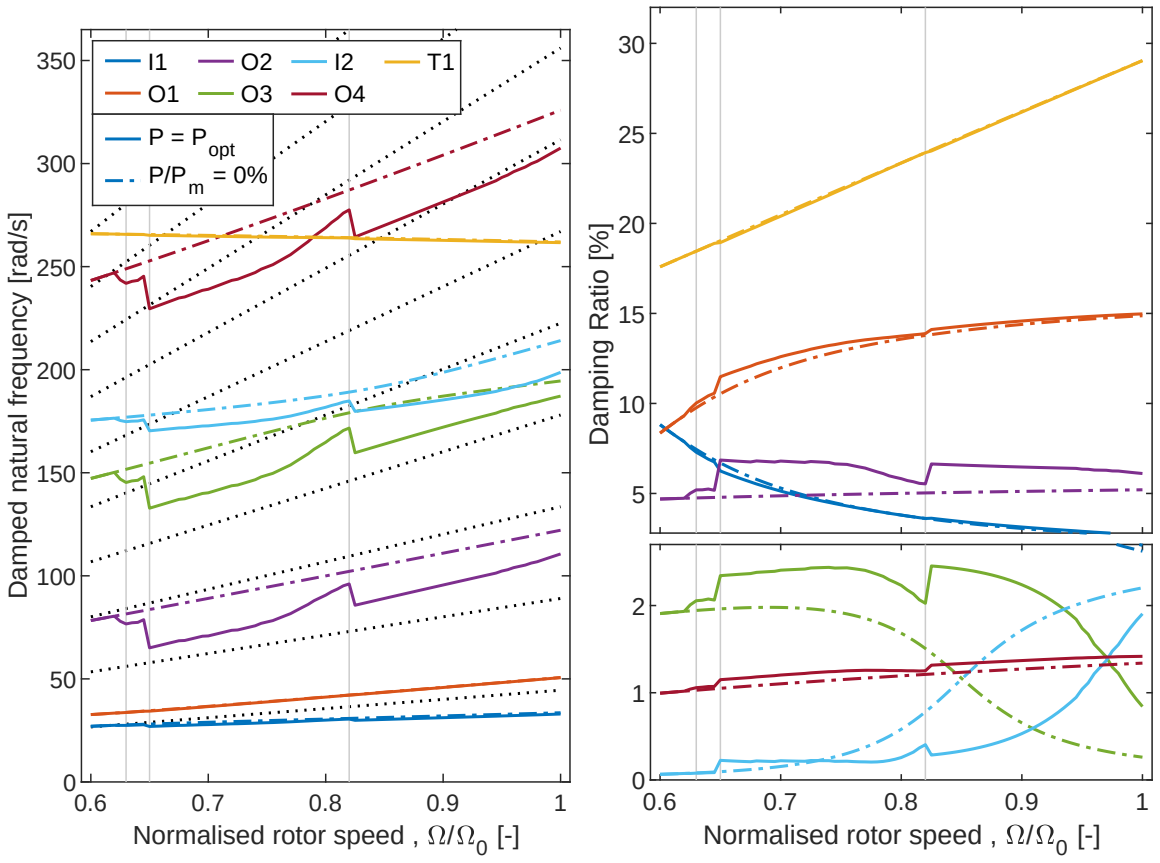

(a) Fan diagram

(b) Damping ratios

Figure 5.21: Aeroelastic properties of Bo105 corresponding to optimised aeroelastic response.

When considering the breakdown of the contribution of each harmonic, it is possible to determine the origin of the reduction in CAR. It can be seen in Fig. 5.20 that the compressive load causes a small reduction in response from the first harmonic as well as a reduction in the response of the second and third harmonic. The fourth harmonic exhibits an increase in response but the other harmonics remain largely unchanged. It can be seen in the aeroelastic properties shown in Fig. 5.21 that there is minimal change in the natural frequency and damping ratio of the first in-plane and first out-of-plane mode which is the likely cause of the small amount of change in the response from the first harmonic. The main source of improvement is due to the change in natural frequency and damping ratio of the second in-plane mode. Compared to the unloaded case, the natural frequency is exhibiting increased separation from its nearest harmonic and an increased damping ratio which drives the reduction in response from the second and third harmonics. The increase in the fourth harmonic is due to the reduction of the natural frequency of the third out-of-plane mode which reduces its separation from the fourth harmonic considerably.

As the rotor speed reduces from 100 % to 92 %, the compressive load is high but not at the

maximum allowable load, which indicates that there is a minimum in CAR value; any increase or decrease in compressive load would increase the overall response. From 92 % to 82.5 % of the nominal rotor speed, the behaviour is largely the same. However, the compressive load is at its limit which indicates that further improvements could be yielded if a larger compressive load were possible. From 82.5 % to 82 % there is an abrupt reduction in compressive load due to the second in-plane mode. This mode exhibits a very low damping ratio which means that it can safely exist in proximity to its nearest harmonic that would not be possible for modes with higher damping ratios. However, the low damping ratio also means that when the separation between natural frequency and rotor harmonic is too low, the impact on the overall response, as seen in Fig. 5.20b is significant, and will necessitate a targeted remediation; hence the abrupt change in compressive load to regain a suitable level of separation. Below 82 % of the nominal rotor speed, the behaviour returns to that observed in 92 % to 82.5 % of the nominal until it reaches 65 %. At this point, the aforementioned second in-plane mode interacts with the sixth harmonic causing an increase in the overall response which is again mitigated using an abrupt change in compressive load. Below 64.5 % of the nominal rotor speed, the first in-plane mode is in close proximity to the first harmonic and the contribution of this harmonic increases such that it dominates the total response. As this mode is relatively insensitive to the compressive loading there are minimal improvements to the response at this rotor speed.

The aforementioned analysis is also performed for the Lynx. The optimal compressive loading profile, CAR and aeroelastic properties of the blade are shown below in Figs. 5.22 and 5.23.

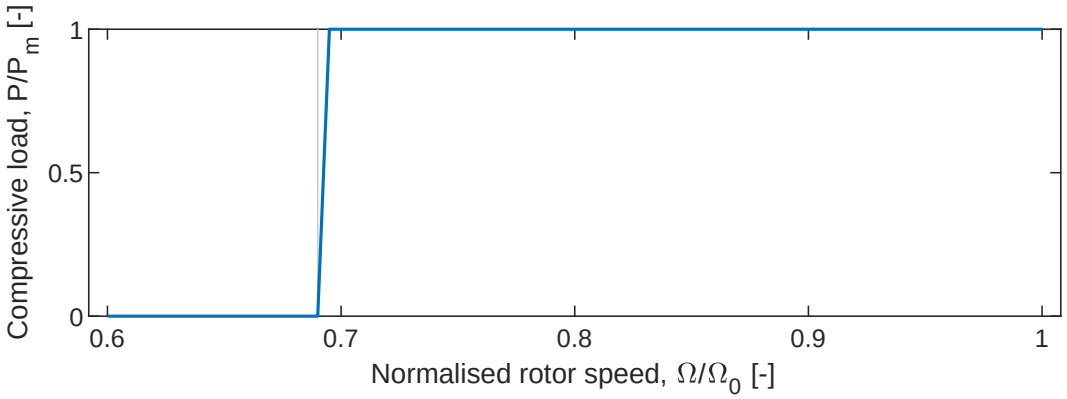

(a) Optimal loading profile

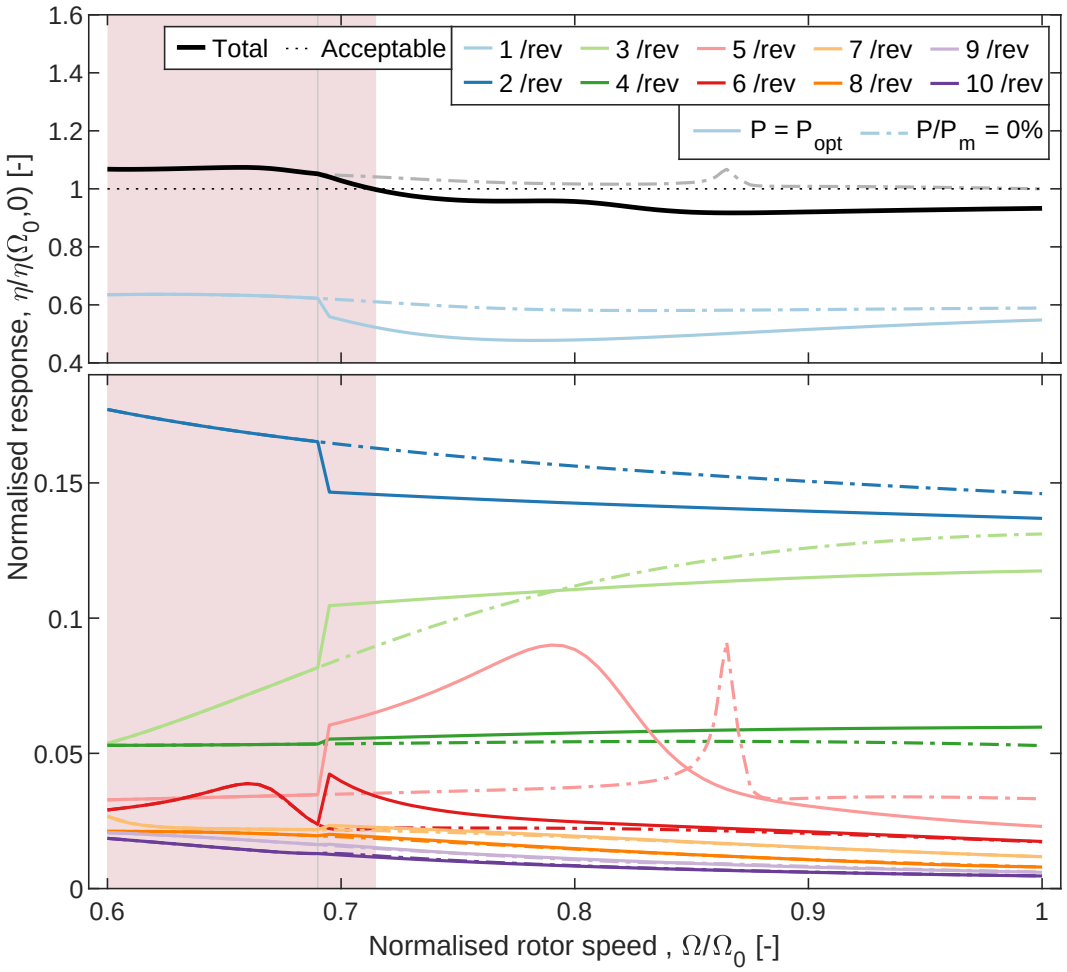

(b) Cumulative aeroelastic response

Figure 5.22: Optimised aeroelastic response of Lynx with compressive loading across a range of rotor speeds.

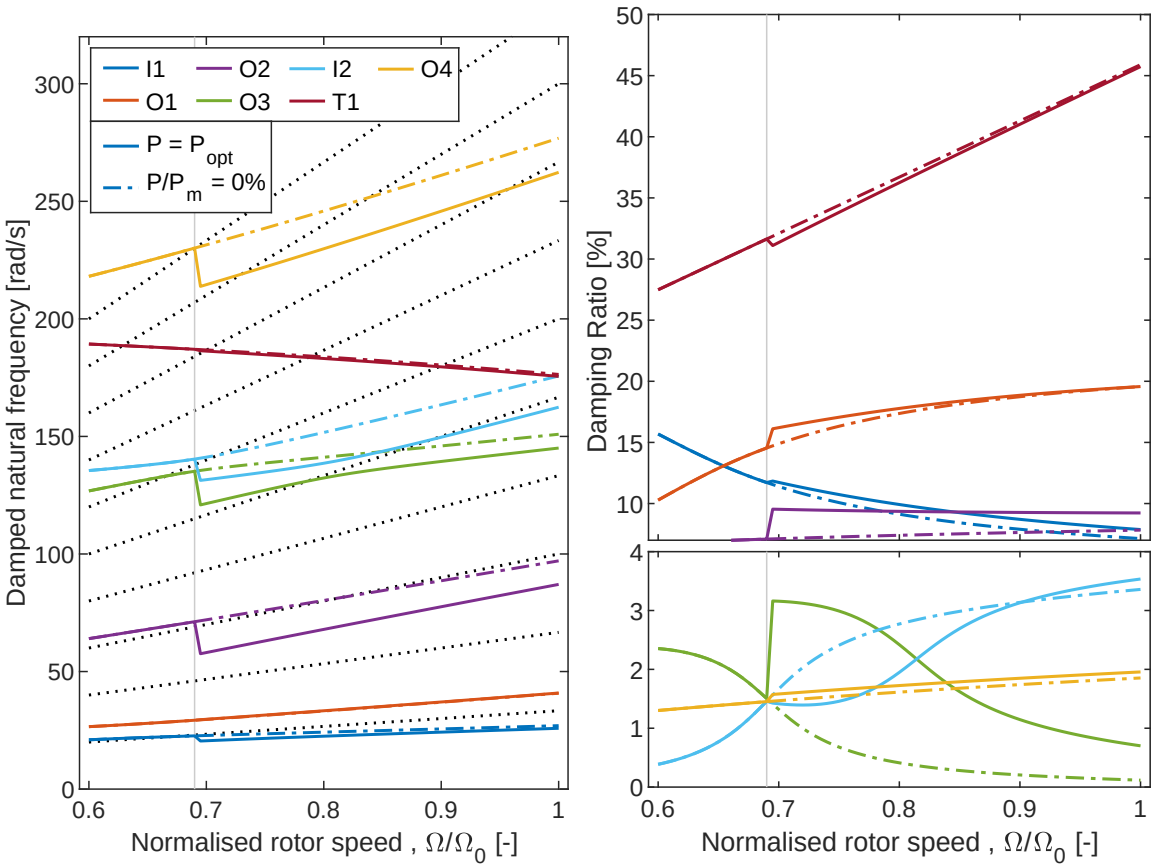

(a) Fan diagram

(b) Damping ratios

Figure 5.23: Aeroelastic properties of Lynx corresponding to optimised aeroelastic response.

It can be seen in Fig. 5.22a that the optimal compressive loading profile differs greatly from that of the Bo105; existing in only its minimum and maximum load. Despite the simplistic loading profile, the compressive load can yield significant reduction in the contributions from the first and second harmonics which are the cause of the reduced total response. The fifth harmonic exhibits a shifting and warping of the resonant peak observed while the remaining harmonics are relatively unchanged.

The aeroelastic properties shown in Fig. 5.23 can provide insight into the aforementioned changes in the contributions of each harmonic to the total CAR. The reduction in the response of the first harmonic is due to the increased separation of the first in-plane mode and the increased damping ratio of the first in-plane and out-of-plane mode. The reduction in the second harmonic is likely due to the increase in the damping ratios of the first and second out-of-plane mode. The improvements in the third harmonic are due to the increased separation and damping ratio of the second out-of-plane mode. With regards to the fifth harmonic, the peak in the unloaded case has been avoided due to the increase in separation and damping ratio. However, the reduction in the natural frequency shifts the aforementioned resonance to a lower rotor speed, albeit a

much less narrow peak due to the increase in damping ratio.

It can be seen that the inclusion of aerodynamic damping and the subsequent change in resonance metric have had a marked change on the optimum loading profile and the corresponding resonant condition when compared to Chapter 4. There is a trend for the modes with higher damping ratios to target a large separation whereas the modes with low damping ratios can operate with much lower separation. However, when the modes with low damping ratios exhibit very low separation their response dominates the overall response of the blade. The influence of an increased damping ratio is also able to improve the response to the excitation of a particular harmonic, even if the separation reduces. This indicates that the ability to change damping ratio may be as influential in the approach to avoiding resonance as the ability to increase the separation between natural and excitation frequencies.

5.4 Chapter Summary

This chapter expanded on the in-vacuo resonance avoidance work detailed in the previous chapter, Chapter 4, to include the influence of aerodynamic loading in hover. Therefore, an investigation into the effects of these aerodynamic loads was made; followed by an assessment of the in-air resonant interactions present in rotors and the potential for these to be avoided using compressive loading.

The model was expanded to incorporate a set of nonlinear PDEs and a 2D unsteady aerodynamic model for hover to incorporate the effects of moderate geometric nonlinearities and aerodynamic loading in hover. The inclusion of these phenomena increased the accuracy with which the model represented a realistic blade and provided additional insight into the behaviour of a hovering rotor blade with an applied compressive load. To solve the nonlinear PDEs, the BVP was separated in to two: one BVP representing the static, time-invariant, deformation of the blade and one BVP to represent the oscillations about this deformed shape.

To demonstrate that the additional phenomena had been correctly captured, a pair of complementary verification and validation studies were performed. Firstly, an in-vacuo code comparison study was performed. The natural frequencies of a test blade were calculated using the present model and compared to the equivalent results calculated from the model developed in Chapter 4. The agreement between the two sets of results was good; indicating the ability of the model to capture the effects of rotation and compressive loading. Secondly, an aeroelastic comparison was performed using [3]. The statically deformed shape, natural frequencies and damping ratios of a test blade are calculated for a range of blade pitch values and compared with the equivalent values from [3]. The agreement observed demonstrated the ability of the model to capture the effects of geometric nonlinearities and aerodynamic loading on the static and dynamic response of the blade.

A study of these additional phenomena was performed to identify their effects on the dynam-

ics of a rotor blade. It was observed that the inclusion of aerodynamic loading and static deformation reduced the blade buckling load by 14 %. Additionally, it was seen that the undamped natural frequencies exhibited similar trends to that observed in Chapter 4. However, the inclusion of the aerodynamic loading introduced aerodynamic damping and it was noted that as rotor speed increased, the damping ratios also increased due to the higher local airspeed. It was also discovered that as compressive loading is applied, there is a reduction in natural frequency, and therefore critical damping, which results in an increase in damping ratio. As coupling was introduced via twist, aerodynamic loading and geometric nonlinearities, it was observed that when modes veered, their damping ratios switched as well as their natural frequencies as was previously observed.

Once the effects of the additional phenomena were investigated, a study was performed to identify the baseline behaviour of a rotor with a variable rotor speed and no compressive loading to assess the improvements available through the application of a compressive load. To perform this study a new metric had to be developed. The metric used in Chapter 4 was based on the separation of the natural frequencies of the rotor blade and their nearest rotor harmonic but this would not capture the effects of damping which had been introduced by the aerodynamic forces. Therefore, a new metric which calculates the area under the FRF of the rotor blade around each harmonic was created. The value at the nominal rotor speed with no compressive loading was defined as the upper limit of acceptability. A subsequent study of the rotor blades of the Bo105 and Lynx attempting a reduction in rotor speed of 40 % with no applied compressive loading revealed a number of trends. Lower harmonics contributed more to the total response than the higher harmonics. In-plane modes, which tend to exhibit low damping ratios, are highly impactful across a narrow range of rotor speeds whereas the out-of-plane modes, which tend to exhibit high damping ratios, impart a smaller impact but across a much broader range of rotor speeds. Due to the changes in response levels of each harmonic, the CAR exceeded the acceptable limit for all but the nominal rotor speed for each aircraft. With the application of compressive loading, it was possible to reduce the CAR across the majority of the rotor speed range investigated. The magnitude of these improvements was sufficiently large that the value dropped to within the acceptable limit for some rotor speeds below the nominal value; permitting the rotor speed for the Bo105 and Lynx to be reduced by 16 % and 28.5 %, respectively. The improvements were observed mainly in the lower rotor harmonics as these are the largest contributors to the overall response. Typically, the optimised profile consisted of targeting maximum separation of the lower order out-of-plane modes; even at the expense of low separation of the lower order in-plane modes. However, when the separation of the lower order in-plane modes was too low, it would significantly impact the overall response and the alleviation of these loads would dominate the optimal compressive loading value. As well as managing the separation of different modes to reduce the CAR, akin to the approach used in Chapter 4, significant benefits were available through the increase in damping ratio that is available through applied compressive loading.

CHAPTER 6

CONCLUSION AND FUTURE WORK

This research has covered a broad range of investigations to understand the influence that compressive loading has on the dynamic properties of rotor blades with a variable rotor speed and the potential for these influences to be utilised in a compressive loading based resonance avoidance system. The aforementioned investigations suggest that compressive loading would be able to mitigate against the excessive vibratory loads associated with a variable rotor speed which in turn would help enable the performance benefits of variable speed rotors to be realised on a wider scale than is currently possible.

A summary of the conclusions obtained from the aforementioned chapters and the recommended future work that would most purposefully advance the proposed resonance avoidance technique are provided in Sections 6.1 and 6.2, respectively.

6.1 Conclusions

Detailed discussions and summaries for each chapter are available in Sections 3.5, 4.4 and 5.4. The most significant conclusions from the research presented are summarised herein.

1. It has been observed for the first time that the application of a load located at the tip of a rotating rotor blade, that is directed towards its root, is able to reduce its natural frequencies. It was shown on three full-scale rotors that a reduction of 20 % of the rotor frequency was possible at both the nominal rotor speed and when operating at a rotor speed reduced by 40 % for almost all modes without the applied load exceeding a limit which was set to avoid buckling. The exceptions to this were the first in-plane mode and the first out-of-plane modes. Due to the orientation of the applied load, these modes exhibited significantly lower sensitivities than the higher-order modes. It was observed for

the given conditions that torsional modes are less sensitive to compressive loading than in-plane modes which in turn are less sensitive than out-of-plane modes. Additionally, the sensitivity of natural frequencies to compressive loading is greater at low rotor speeds due to the lower amount of centrifugal loading.

2. Using a time domain model of an untwisted rotor blade in forward flight, the novel behaviour of reducing vibratory loads at the hub using an applied compressive load was demonstrated. At the arbitrarily chosen load value of 50 % of the maximum, the in-plane forces and moments across the first four rotor harmonics were all shown to reduce by over 50 %. For the out-of-plane forces and moments, the reductions of these values varied from 0 % to 60 % for the different harmonics. Additionally, it was shown that excessively large compressive loads may increase the root loads. This is expected to be due to the reduction of the natural frequencies being sufficiently enough that they begin to interact with harmonics which they previously wouldn't have.

3. Using a variable compressive load, that was conservatively limited to avoid buckling, the separation between the natural frequencies of the blades of a range of aircraft and their rotor harmonics could be increased across a wide range of rotor speeds. The increase in separation due to the newly proposed compressive load based resonance avoidance technique increased the fraction of the desired rotor speed range that was deemed operable by a factor of at least three for each rotor evaluated.

4. The addition of unsteady aerodynamic loads has a minimal impact on the influence of compressive loading or a variable rotor speed on the undamped natural frequencies of the rotor blade. Conversely, the introduction of aerodynamic loads introduces aerodynamic damping with ratios which were observed to increase significantly with rotor speed. The largest change observed was an increase in the damping ratio of the torsion of 65 % as the rotor speed increased from 60 % to 100 % of the nominal speed. It was also observed that as compressive loading is applied, damping ratios reduce due to the reduction in natural frequency lowering the critical damping value.

5. In-plane modes tended to exhibit low damping ratios which result in their contribution to the overall response only being observed during very narrow bands of rotor speeds. However, due to the low damping ratios, the magnitude of the influence that these modes imparted was large. Conversely, the out-of-plane modes exhibited a much higher damping ratio which results in an influence that has smaller magnitude but is observed over a wider range of rotor speeds. These contrasting behaviours resulted in the optimum compressive loading profile primarily targeting a reduction in the response of the out-of-plane modes. However, during rotor speed ranges where the in-plane response was large, these dictated the optimum compressive loading profile.

6. The inclusion of the compressive loading improved or maintained the aeroelastic vibratory response of the blade across the full range of desired rotor speeds. The observed improvement permitted an expansion of the rotor speed ranges that were safe to operate in by over 15 % of the nominal speed for each aircraft evaluated.

7. A theoretical sizing of hydraulic actuators required to achieve the prescribed limit load was performed for each rotor based on the industry standard hydraulic pressure of 20.7 MPa (3000PSI). It was estimated that the bore of the actuator would be approximately 10 % of the blade chord and would require up to 0.1 % of the installed power during actuation.

6.2 Future work

The previously detailed work has demonstrated the ability of an applied compressive load to alter the dynamic properties of a rotor blade across a range of rotor speeds and utilise this to avoid resonance in rotors which operate with a wide range of rotor speeds. However, there are several studies outside of the scope of this research that should be prioritised to progress the concept towards real world deployment. These studies are summarised below:

1. In the presented work, the rotor blade considered has either operated in-vacuo or with aerodynamic effects limited to hovering conditions. As helicopters often operate in forward flight, and it is in these operating conditions that the airflow asymmetry in the rotor and cyclic trim conditions cause the largest excitation loads, it is imperative that the effectiveness of the concept be evaluated on a rotor blade that includes the aerodynamic loading associated with forward flight. This evaluation should span the range of forward speeds and rotor speeds that are likely to be required of a rotorcraft with a variable rotor speed. One possible method to create this model is to utilise the same concept used in Section 3.4.1 but updating the equations of motion and mode shapes to match those used and calculated in Section 5.1. This model would benefit from the increased realism of incorporating the excitation loads, which would originate from the asymmetry in the flowfield and trim conditions, as well as evaluating the performance of the concept directly, using vibratory loads or stresses at the blade root, as opposed to using a proxy for vibratory loads, such as frequency separation or Cumulative Aeroelastic Response (CAR). Additionally, it would be possible to calculate the power requirements of the rotor which would allow the performance of the rotor and the associated vibratory loads to be evaluated in conjunction with one another.

2. In the present work, an upper limit for the compressive load of 75 % of the static buckling load was used to ensure that a buckling instability was not induced. The static buckling load was used as the limiting load but aeroelastic instabilities such as flutter were not accounted for. As shown in Section 5.3.1, the application of a compressive load can lower

the damping ratio of a mode. Although this did not lead to a dynamic instability in the present work, where the compressive load was limited to 75 % of the static buckling load, it is possible that a dynamic instability would be encountered at a compressive load lower than that of the static buckling load. Therefore, a model, such as the one described in Section 5.1, should be used to investigate the static and dynamic instabilities of a compressively loaded rotor. This would provide a more accurate critical compressive load and understanding of the behaviour of the blade as an instability is approached. This would, in turn, allow for a less conservative proportion of this load to be employed which may increase the allowable maximum load and subsequently improve the resonance avoidance capability.

3. As the presented work indicates that a compressive load would be able to reduce the effects of resonance observed in variable speed rotors, it becomes increasingly pertinent to investigate potential means with which the compressive load could be applied. Several potential solutions for transmitting the load from the root to the tip have been suggested: a flexible tendon made from wire or rope; a scissor-like lattice; or a flexible beam with a varying cross section to tailor its dynamic behaviour. The method for creating the load, such as a hydraulic actuator or an electric servo-gearbox combination, should also be considered. A thorough investigation of these options is required to ensure the chosen method can impart the required loads without incurring excessive negative impacts such as large weight or power requirements.

4. The present work considered a compressive force located on the elastic axis of the beam at the tip of the beam. However, it is expected that changing the spanwise location of the load or its location in the cross section may alter the response the different modes to compressive loading. An optimisation study should be performed to identify the ideal location for the applied load. It is possible that by changing the location of the applied load, it may be possible to increase the sensitivity of problematic modes.

5. An experimental free vibration analysis of a compressively loaded non-rotating beam with a symmetric cross section was performed in the presented work. However, experimental works involving asymmetric cross sections, that mimic that of a rotor blade, as well as rotation and the associated aerodynamic loads be completed. These studies would improve the validation of the presented work, provide additional insight and may be a means to explore effects such as changing the location of the applied compressive load.

The completion of the above works would build on the research presented thus far and aid in the progression of the concept from its current state towards deployment in full scale rotorcraft which would in turn unlock the benefits of variable speed rotors as stated previously.

APPENDIX A

SIMPLIFIED ANALYTICAL CALCULATIONS

The PDEs of Houbolt and Brooks [137] are used to represent the behaviour of the rotating beam. To isolate the dynamic behaviour of the beam, the static terms (terms independent of the state of the beam) are not considered. It is assumed that the motion of the beam is harmonic, using Eq. (A.1).

$$\begin{aligned} v_*(x,t) &= v(x)e^{st} \\ w_*(x,t) &= w(x)e^{st} \\ \phi_*(x,t) &= \phi(x)e^{st} \end{aligned} \tag{A.1}$$

Furthermore, it is assumed that: the cross section is uniform and doubly symmetric, the beam has no twist and the material has a constant density which results in the simplifications stated in Eq. (A.2).

$$B_1 = B_2 = e_0 = e = e_A = \theta = (k_{m2}^2 - k_{m1}^2) = 0 \tag{A.2}$$

These assumptions remove all coupling between the motions, resulting in the set of uncoupled equations of motion, Eq. (A.3).

$$\begin{aligned} GJ\phi'' + \frac{J}{A}\left(T\phi'\right)' - k_m^2 ms^2\phi = 0 \\ EI_z v^{iv} - (Tv')' + ms^2 v - \Omega^2 mv = 0 \\ EI_y w^{iv} - (Tw')' + ms^2 w = 0 \end{aligned} \tag{A.3}$$

Where

$$T = \frac{1}{2} m\Omega^2 (R^2 - x^2) - P \tag{A.4}$$

The modal form of Eq. (A.3) are calculated by evaluating Eq. (A.5).

$$\begin{aligned} \int_{R_0}^{R} \left[GJ\phi'' + \frac{J}{A}\left(T\phi'\right)' - k_m^2 ms^2\phi \right] \phi dx = 0 \\ \int_{R_0}^{R} \left[EI_z v^{iv} - (Tv')' + ms^2 v - \Omega^2 mv \right] v dx = 0 \\ \int_{R_0}^{R} \left[EI_y w^{iv} - (Tw')' + ms^2 w \right] w dx = 0 \end{aligned} \tag{A.5}$$

The boundary conditions for a cantilevered beam, see Eq. (A.6), are applied and the substitution of $\bar{\phi}$, $\bar{v}$, $\bar{w}$ and $\bar{x}$ is used to normalise the resulting equations with respect to radius.

$$\begin{aligned} v = w = \phi = v' = w' \Big|_{x=R_0} = 0 \\ M_x = M_y = M_z = F_y = F_z \Big|_{x=R} = 0 \end{aligned} \tag{A.6}$$

Where

$$\begin{aligned} M_x &= (GJ + Tk_A^2)\phi' \\ M_y &= EI_y w'' \\ M_z &= EI_z v'' \\ F_y &= Tv' - M_z' \\ F_z &= Tw' - M_y' \end{aligned} \tag{A.7}$$

The result is a set of Southwell styled equations [121] , Eq. (A.8), that can be used to calculate the natural frequencies of a rotating beam with an applied compressive load.

$$
\begin{aligned}
-\lambda_{\phi i}^2 &= \frac{GJ}{mk_m^2(R-R_0)^2}\frac{K_{G\phi,i}}{M_{\phi,i}} + \Omega^2\frac{K_{R1\phi,i}\left(1^2-(\frac{R_0}{R})^2\right)+K_{R2\phi,i}\frac{(R-R_0)R_0}{R^2}+K_{R3\phi,i}\frac{(R-R_0)^2}{R^2}}{M_{\phi,i}} - \frac{P}{m(R-R_0)^2}\frac{K_{G\phi,i}}{M_{\phi,i}} \\
-\lambda_{vi}^2 &= \frac{EI_z}{m(R-R_0)^4}\frac{K_{Gv,i}}{M_{v,i}} + \Omega^2\left(\frac{K_{R1v,i}\left(1^2-(\frac{R_0}{R})^2\right)+K_{R2v,i}\frac{(R-R_0)R_0}{R^2}+K_{R3v,i}\frac{(R-R_0)^2}{R^2}}{M_{v,i}} - 1\right) - \frac{P}{m(R-R_0)^2}\frac{K_{Cv,i}}{M_{v,i}} \\
-\lambda_{wi}^2 &= \frac{EI_y}{m(R-R_0)^4}\frac{K_{Gw,i}}{M_{w,i}} + \Omega^2\frac{K_{R1w,i}\left(1^2-(\frac{R_0}{R})^2\right)+K_{R2w,i}\frac{(R-R_0)R_0}{R^2}+K_{R3w,i}\frac{(R-R_0)^2}{R^2}}{M_{w,i}} - \frac{P}{m(R-R_0)^2}\frac{K_{Cw,i}}{M_{w,i}}
\end{aligned}
\tag{A.8}
$$

Where

$$
\begin{array}{lll}
K_{G\phi,i} = \int_0^1 \bar{\phi}_i'^2 d\bar{x} & K_{Gv,i} = \int_0^1 \bar{v}_i''^2 d\bar{x} & K_{Gw,i} = \int_0^1 \bar{w}_i''^2 d\bar{x} \\
K_{R1\phi,i} = \frac{1}{2}\int_0^1 \bar{\phi}_i'^2 d\bar{x} & K_{R1v,i} = \frac{1}{2}\int_0^1 \bar{v}_i'^2 d\bar{x} & K_{R1w,i} = \frac{1}{2}\int_0^1 \bar{w}_i'^2 d\bar{x} \\
K_{R2\phi,i} = -\int_0^1 \bar{x}\bar{\phi}_i'^2 d\bar{x} & K_{R2v,i} = -\int_0^1 \bar{x}\bar{v}_i'^2 d\bar{x} & K_{R2w,i} = -\int_0^1 \bar{x}\bar{w}_i'^2 d\bar{x} \\
K_{R3\phi,i} = -\frac{1}{2}\int_0^1 \bar{x}^2\bar{\phi}_i'^2 d\bar{x} & K_{R3v,i} = -\frac{1}{2}\int_0^1 \bar{x}^2\bar{v}_i'^2 d\bar{x} & K_{R3w,i} = -\frac{1}{2}\int_0^1 \bar{x}^2\bar{w}_i'^2 d\bar{x} \\
 & K_{Cv,i} = \int_0^1 \bar{v}_i'^2 d\bar{x} & K_{Cw,i} = \int_0^1 \bar{w}_i'^2 d\bar{x} \\
M_{\phi,i} = \int_0^1 \bar{\phi}_i^2 d\bar{x} & M_{v,i} = \int_0^1 \bar{v}_i^2 d\bar{x} & M_{w,i} = \int_0^1 \bar{w}_i^2 d\bar{x}
\end{array}
\tag{A.9}
$$

The analytical solutions for the modeshapes of a non-rotating cantilevered beam [187], Eq. (A.10), can be used to evaluate the integrals in Eq. (A.9), as summarised in Table A.1. As the change in modeshapes with loading and rotation are likely to be small [111], the integrals are assumed to be approximately constant with rotor speed.

$$
\begin{aligned}
\Phi_i &= \sin\left(\frac{(2i-1)\pi\bar{x}}{2}\right) \\
V_i, W_i &= \cos\left(\frac{(2i-1)\pi\bar{x}}{2}\right) - \cosh\left(\frac{(2i-1)\pi\bar{x}}{2}\right) - \\
&\frac{\cos\left(\frac{(2i-1)\pi}{2}\right)+\cosh\left(\frac{(2i-1)\pi}{2}\right)}{\sin\left(\frac{(2i-1)\pi}{2}\right)+\sinh\left(\frac{(2i-1)\pi}{2}\right)}\left(\sin\left(\frac{(2i-1)\pi\bar{x}}{2}\right) - \sinh\left(\frac{(2i-1)\pi\bar{x}}{2}\right)\right)
\end{aligned}
\tag{A.10}
$$

Table A.1: Evaluation of integrals for non-rotating cantilevered beam

Mode, i	1^{st}	2^{nd}	3^{rd}	4^{th}
$K_{G\phi,i}$	1.234	11.10	30.84	60.45
$K_{R1\phi,i}$	0.6169	5.552	15.42	30.23
$K_{R2\phi,i}$	-0.3669	-5.302	-15.17	-29.98
$K_{R3\phi,i}$	-0.08062	-1.726	-5.015	-9.95
$M_{\phi,i}$	0.5000	0.5000	0.5000	0.5000
$K_{Gv,i}$, $K_{Gw,i}$	6.980	491.2	3805	14617
$K_{R1v,i}$, $K_{R1w,i}$	1.364	16.45	38.63	71.45
$K_{R2v,i}$, $K_{R2w,i}$	-1.843	-24.12	-52.32	-91.44
$K_{R3v,i}$, $K_{R3w,i}$	-0.6862	-9.869	-20.78	-35.4
$K_{Cv,i}$, $K_{Cw,i}$	2.728	32.90	77.27	142.9
$M_{v,i}$, $M_{w,i}$	0.5603	1.012	0.9997	1.000

These values can be substituted into Eq. (A.8) to create equations for the natural frequencies of each mode as they varying with compressive load and rotor speed. A set of examples for these equations for the first torsional, first two in-plane and first three out-of-plane modes of a blade with $R_0 = 0$ are shown in Eq. (A.11).

$$
\begin{aligned}
-\lambda_{\phi1}^2 &= 2.468\frac{GJ}{mk_m^2R^2} + 1.072\Omega^2 - 2.468\frac{P}{mR^2} \\
-\lambda_{v1}^2 &= 12.46\frac{EI_z}{mR^4} + 0.2099\Omega^2 - 4.869\frac{P}{mR^2} \\
-\lambda_{v2}^2 &= 485.4\frac{EI_z}{mR^4} + 5.501\Omega^2 - 32.51\frac{P}{mR^2} \\
-\lambda_{w1}^2 &= 12.46\frac{EI_y}{mR^4} + 1.201\Omega^2 - 0.4869\frac{P}{mR^2} \\
-\lambda_{w2}^2 &= 485.4\frac{EI_y}{mR^4} + 6.501\Omega^2 - 32.51\frac{P}{mR^2} \\
-\lambda_{w3}^2 &= 3806\frac{EI_y}{mR^4} + 17.86\Omega^2 - 77.29\frac{P}{mR^2}
\end{aligned}
\tag{A.11}
$$

APPENDIX B

BEAM-TENDON ORTHOGONALITY

Due to the presence of the tendon, Eq. (2.10) is no longer an applicable orthogonality condition as it is only valid for beam systems. As modal identification of beam-tendon systems has not previously been performed using this method, an existing orthogonality condition for this system is not available. Therefore, the orthogonality condition for a cantilevered beam-tendon system, coupled via its root and tip attachments, is derived herein. The process follows that of [1] whereby the equations of motion are written in terms of the first modeshape and the i^{th} modeshape; each of the equations of motion are then multiplied by the i^{th} modeshape and the first modeshape, respectively, subtracted from each other and integrated along the span of the beam; the results of this for each equation of motion are then summed together; finally the equations are simplified using integration by parts and the appropriate boundary conditions.

Firstly, the equations of motion for the system, Eq. (3.14),are written in terms of the first and i^{th} modes, respectively, as seen in Eq. (B.1).

$$\begin{aligned} -\left(-PW_1'\right)' + EI_y W_1^{iv} &= -ms_1^2 W_1 \\ -\left(PW_{t1}'\right)' &= -m_t s_1^2 W_{t1} \\ -\left(-PV_1'\right)' + EI_z V_1^{iv} &= -ms_1^2 V_1 \\ -\left(PV_{t1}'\right)' &= -m_t s_1^2 V_{t1} \end{aligned} \tag{B.1a}$$

$$\begin{aligned} -\left(-PW_i'\right)' + EI_y W_i^{iv} &= -ms_i^2 W_i \\ -\left(PW_{ti}'\right)' &= -m_t s_i^2 W_{ti} \\ -\left(-PV_i'\right)' + EI_z V_i^{iv} &= -ms_i^2 V_i \\ -\left(PV_{ti}'\right)' &= -m_t s_i^2 V_{ti} \end{aligned} \tag{B.1b}$$

Eqs. (B.1a) and (B.1b) are the multiplied by the i^{th} and first modeshapes, respectively. Then each Ordinary Differential Equation (ODE) in Eq. (B.1b) is subtracted from the corresponding ODE in Eq. (B.1a). The resulting set of ODEs are then integrated along the span to produce the following.

$$\int_{R_0}^{R}\left[\left(\left(PW_1'\right)'W_i+EI_yW_1^{iv}W_i\right)-\left(\left(PW_i'\right)'W_1+EI_yW_i^{iv}W_1\right)\right]dx$$
$$=\int_{R_0}^{R}\left[\left(-ms_1^2W_1W_i\right)-\left(-ms_i^2W_iW_1\right)\right]dx$$

$$\int_{R_0}^{R}\left[\left(-\left(PW_{t1}'\right)'W_{ti}\right)-\left(-\left(PW_{ti}'\right)'W_{t1}\right)\right]dx$$
$$=\int_{R_0}^{R}\left[\left(-m_ts_1^2W_{t1}W_{ti}\right)-\left(-m_ts_i^2W_{ti}W_{t1}\right)\right]dx$$

(B.2)

$$\int_{R_0}^{R}\left[\left(\left(PV_1'\right)'V_i+EI_zV_1^{iv}V_i\right)-\left(\left(PV_i'\right)'V_1+EI_zV_i^{iv}V_1\right)\right]dx$$
$$=\int_{R_0}^{R}\left[\left(-ms_1^2V_1V_i\right)-\left(-ms_i^2V_iV_1\right)\right]dx$$

$$\int_{R_0}^{R}\left[\left(-\left(PV_{t1}'\right)'V_{ti}\right)-\left(-\left(PV_{ti}'\right)'V_{t1}\right)\right]dx$$
$$=\int_{R_0}^{R}\left[\left(-m_ts_1^2V_{t1}V_{ti}\right)-\left(-m_ts_i^2V_{ti}V_{t1}\right)\right]dx$$

When each of the equations in Eq. (B.3) are summed together, the form one single equation which can be simplified using integration by parts.

$$
\begin{aligned}
&P\left[W_1'W_i\right]_{R_0}^{R}+P\left[W_i'W_1\right]_{R_0}^{R}+EI_y\left[W_1'''W_i-W_1''W_i'\right]_{R_0}^{R}+EI_y\left[W_i'''W_1-W_i''W_1'\right]_{R_0}^{R}\\
&\quad+\int_{R_0}^{R}\left[\left(\cancel{-PW_1'W_i'}+\cancel{EI_yW_1''W_i''}\right)-\left(\cancel{-PW_i'W_1'}+\cancel{EI_yW_i''W_1''}\right)\right]dx\\
&\quad-P\left[W_{t1}'W_{ti}\right]_{R_0}^{R}-P\left[W_{ti}'W_{t1}\right]_{R_0}^{R}\\
&\quad+\int_{R_0}^{R}\left[\left(\cancel{PW_{t1}'W_{ti}'}\right)-\left(\cancel{PW_{ti}'W_{t1}'}\right)\right]dx\\
&+P\left[W_1'W_i\right]_{R_0}^{R}+P\left[W_i'W_1\right]_{R_0}^{R}+EI_y\left[W_1'''W_i-W_1''W_i'\right]_{R_0}^{R}+EI_y\left[W_i'''W_1-W_i''W_1'\right]_{R_0}^{R}\\
&\quad+\int_{R_0}^{R}\left[\left(\cancel{-PW_1'W_i'}+\cancel{EI_yW_1''W_i''}\right)-\left(\cancel{-PW_i'W_1'}+\cancel{EI_yW_i''W_1''}\right)\right]dx\\
&\quad-P\left[W_{t1}'W_{ti}\right]_{R_0}^{R}-P\left[W_{ti}'W_{t1}\right]_{R_0}^{R}\\
&\quad+\int_{R_0}^{R}\left[\left(\cancel{PW_{t1}'W_{ti}'}\right)-\left(\cancel{PW_{ti}'W_{t1}'}\right)\right]dx\\
&=m\left(s_i^2-s_1^2\right)\int_{R_0}^{R}\left[W_1W_i+V_1V_i\right]dx+m_t\left(s_i^2-s_1^2\right)\int_{R_0}^{R}\left[W_{t1}W_{ti}+V_{t1}V_{ti}\right]dx
\end{aligned}
\tag{B.3}
$$

Subsequently, the boundary conditions can be used to further reduce these equations. From the boundary conditions at the root, the moment equilibria at the tip (for an unforced beam, $M_0 = 0$) and the tendon specific boundary conditions, as seen in Eqs. (3.15) and (3.16), the following terms can be substituted to reduce Eq. (B.3).

$$
\begin{aligned}
v(R_0)=w(R_0)=v'(R_0)=w'(R_0)=w_t(R_0)=v_t(R_0)=0\\
w''(R)=v''(R)=0\\
w_t(R)=w(R)\\
v_t(R)=v(R)
\end{aligned}
\tag{B.4}
$$

$$
\begin{aligned}
&\Big(PW_1'(R)+EI_yW_1'''(R)-PW_{t1}'(R)\Big)W_i(R)\\
&+\Big(PW_i'(R)+EI_yW_i'''(R)-PW_{ti}'(R)\Big)W_1(R)\\
&+\Big(PV_1'(R)+EI_zV_1'''(R)-PV_{t1}'(R)\Big)V_i(R)\\
&+\Big(PV_i'(R)+EI_zV_i'''(R)-PV_{ti}'(R)\Big)V_1(R)\\
=m\Big(s_i^2-s_1^2\Big)&\int_{R_0}^{R}\Big[W_1W_i+V_1V_i\Big]dx+m_t\Big(s_i^2-s_1^2\Big)\int_{R_0}^{R}\Big[W_{t1}W_{ti}+V_{t1}V_{ti}\Big]dx
\end{aligned}
\tag{B.5}
$$

When considering the remaining boundary condition,the force equilibria, the following terms can be substituted to reduce Eq. (B.5) further.

$$
\begin{aligned}
PW'(R)+EI_yW'''(R)-PW_t'(R)&=M_ts^2W(R)\\
PV'(R)+EI_yV'''(R)-PV_t'(R)&=M_ts^2V(R)
\end{aligned}
\tag{B.6}
$$

The resulting equation is as follow.

$$
\begin{aligned}
&2M_ts^2\Big(W_1(R)W_i(R)+V_1(R)V_i(R)\Big)\\
=m\Big(s_i^2-s_1^2\Big)&\int_{R_0}^{R}\Big[W_1W_i+V_1V_i\Big]dx+m_t\Big(s_i^2-s_1^2\Big)\int_{R_0}^{R}\Big[W_{t1}W_{ti}+V_{t1}V_{ti}\Big]dx
\end{aligned}
\tag{B.7}
$$

Finally, as the mass of the beam is significantly greater than that of the tip insert ($\int m dx \gg M_t$), Eq. (B.7) can be further reduced to.

$$
m\Big(s_i^2-s_1^2\Big)\int_{R_0}^{R}\Big[W_1W_i+V_1V_i\Big]dx+m_t\Big(s_i^2-s_1^2\Big)\int_{R_0}^{R}\Big[W_{t1}W_{ti}+V_{t1}V_{ti}\Big]dx=0 \tag{B.8}
$$

Ignoring the case when the condition is satisfied because the frequencies are identical, the integral term will equate to zero if a modeshape is being compared to the known shape of the first mode. Alternatively, this term can be altered to compare a response shape to the known first modeshape, as seen below.

$$\Gamma = m \int_{R_0}^{R} \left[W_1 W_i + V_1 V_i \right] dx + m_t \int_{R_0}^{R} \left[W_{t1} W_{ti} + V_{t1} V_{ti} \right] dx \tag{B.9}$$

APPENDIX C

AIRCRAFT PARAMETERS

For case studies performed within this research, three test aircraft are available: The MBB Bo 105, the Westland Lynx, and the Westland AW101. These aircraft are very different in terms of their design and usage, as seen from the specifications shown in Table C.1. The difference in their specification and design will allow any differences in the performance of compressive loading based resonance avoidance due to the aircraft to be evaluated.

Table C.1: Comparison of aircraft specifications

Aircraft	MBB Bo105 [188, 189]	Westland Lynx [190, 191]	Westland AW101 [192, 193]
Gross mass, M_g	2069	2578	10500
Occupants	4	8	30
Mach at cruise, M_v	0.1652	0.2251	0.2397
Installed power, P_i	626×10^3	1670×10^3	4698×10^3

As the various models developed to analyse the effects of compressive loading are based on constant blade parameters, it is required that distributed parameters be appropriately represented using a single, lumped value. The parameters in questions are: the torsional and bending cross-sectional stiffnesses of the blade; the mass distribution of the blade; and the offset between the elastic axis and the mass axis of the blade. The lumped equivalent of the mass distribution of the blade and the offset between the elastic axis and the mass axis of the blade is the mean value calculated from the distributed values between R_C and R. An exception is made for the Westland AW101, which is evaluated from R_C to the start of the tip, as it has a very non-uniform planform. The values of all of the required parameters, with the exception of cross-sectional stiffnesses are summarised in Table C.2. A comparison of the distributed and

lumped parameters are shown in Fig. C.1. The use of a lumped value for these parameters may introduce discrepancies between the calculated natural frequencies and those that would be observed in reality. However, the purpose of using these different parameter sets is to assess how the proposed resonance avoidance concept would perform in different types and sizes of aircraft. Therefore, the exact replication of the blade is not essential.

Table C.2: Blade properties for each test aircraft.

Aircraft	MBB Bo105 [188, 189]	Westland Lynx [190, 191]	Westland AW101 [192, 193]
Mass distribution, m	7.55	7.64	12.93
Radius, R	4.91	6.40	9.30
Aerodynamic blade root, R_C	1.03	1.81	3.11
Root cutout, R_0	0.38	0.80	1.30
Chord, c	0.275	0.327	0.420
Mass-elastic offset, e	-0.0195	-0.0047	-0.0022
Linear twist, δ	-0.140	-0.110	-0.096
Rotor speed, Ω_0	44.5	33.3	22.0
Number of blades, N_b	4	4	5

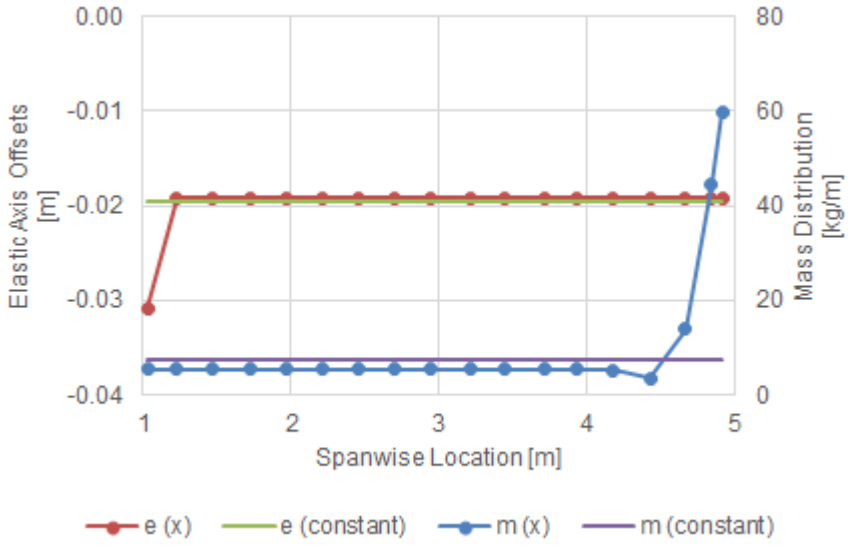

(a) MBB Bo 105

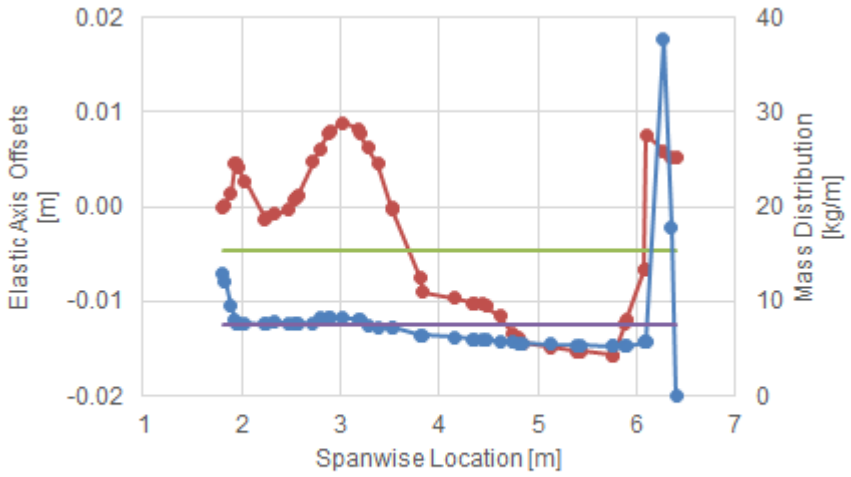

(b) Westland Lynx

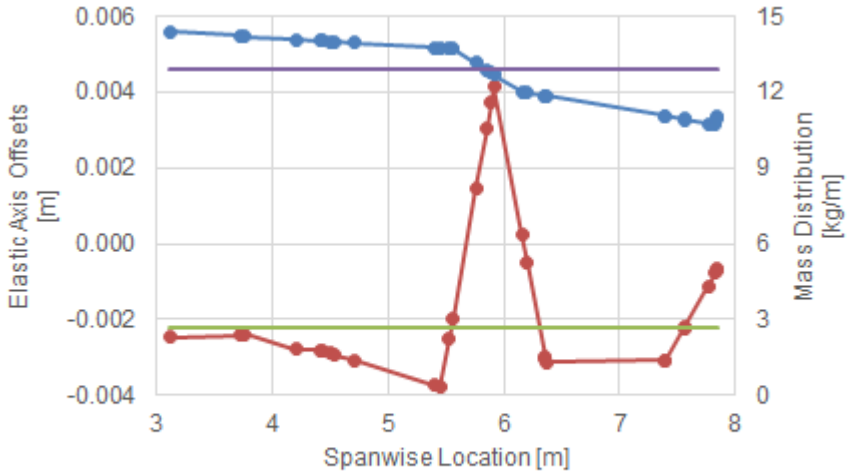

(c) Westland AW101

Figure C.1: Comparison of distributed and lumped values of elastic axis offset and mass distribution for each aircraft.

For the MBB Bo 105, a similar process can be used to calculate the equivalent lumped stiffness values shown in Table C.3. A comparison of the distributed and lumped parameters are shown in Fig. C.2.

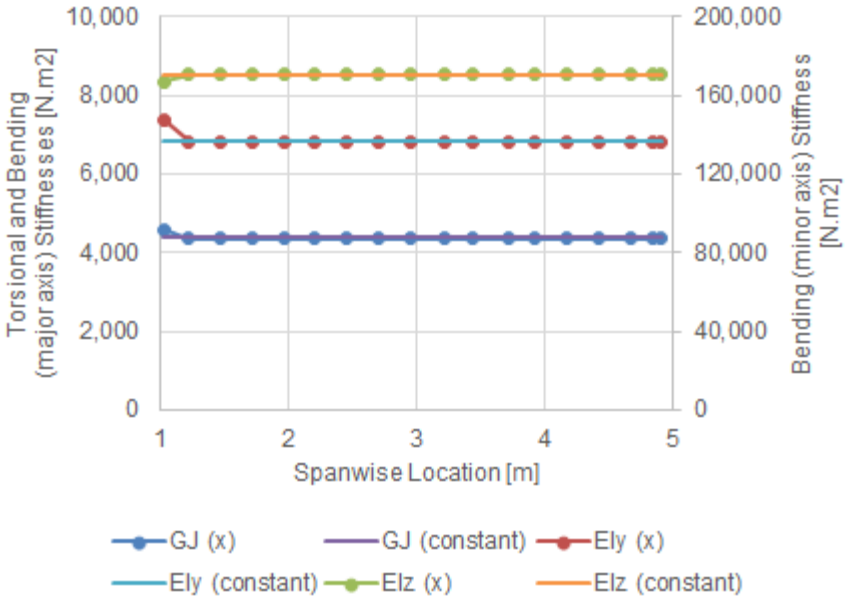

Figure C.2: Comparison of distributed and lumped values of stiffness for MBB Bo 105.

Unfortunately, due to the large variation in the stiffness parameters of the Westland Lynx and the Westland AW101, the same process cannot be applied to these aircraft. Instead, the stiffness values for these aircraft are calculated such that the natural frequencies of the the blade, as calculated using the equations in Appendix A, at the operational rotor speed correspond with target values. For the Westland Lynx, these values are extracted from a fan diagram calculated using Westland's J134 analysis code [190]. For the Westland AW101, these values are set to be the same as the normalised values of the MBB Bo 105, i.e. a value of 6.4/*rev* for T1 observed from the MBB Bo 105 is the target for the Westland AW101. The subsequent stiffness parameters are summarised in Table C.3.

Table C.3: Blade stiffness properties for each test aircraft.

Aircraft	MBB Bo105	Westland Lynx	Westland AW101
Out-of-plane bending rigidity, EI_y	6.85×10^3	1.58×10^4	4.16×10^4
In-plane bending rigidity, EI_z	1.70×10^5	2.38×10^5	8.74×10^5
Torsional rigidity, GJ	4.37×10^3	5.20×10^3	1.83×10^4

From these lumped value properties, it can be seen that the different requirements of the aircraft results in significantly different blade properties. It can be seen that the AW101 is significantly heavier than the Bo105 and Lynx, which results in a much larger blade radius, chord, mass and stiffnesses as well as the number of blades. Despite the vehicle mass of Lynx

being 25 % greater than that of the Bo105, it has significantly more installed power (+167 %), rotor disc area (+167 %) and a much higher out-of-plane stiffness (+167 %). The disproportionate increases in these properties are indicative of the different operational requirements of these two aircraft. The Bo105 is a utility helicopter with deployment roles in military reconnaissance, police services and coastal search and rescue across the world. Conversely, the Lynx is a multi-purpose military helicopter with a record breaking top speed [194] in excess of $400\,\mathrm{km\,h^{-1}}$ and the ability to perform aerobatic manoeuvres such as rolls and loops [195]. Unlike the other major parameters, the rotor speed decreases from the Bo105 to the Lynx and then the AW101. Due to compressibility effects on the advancing side of a rotor, there is an upper limit on the allowable tip speed of a rotor blade, which necessitates a reduction in rotor speed with the increasing rotor radius.

Due to the assumptions made during this calculation procedure, the calculated parameter values and subsequent modal properties are unlikely to be an exact match of their real world counterparts. However, the purpose of using multiple of aircraft is not to exactly replicate their characteristics, but to use the variation to assess how the performance of the proposed concept changes with different rotor blades.

Furthermore, additional property values that are required can be calculated from the parameters previously detailed. The properties for the Westland Lynx were specifically for the metal blade and due to the era of the data (1976) it can be assumed that the same is true of the MBB Bo 105 blade. The values for these properties are summarised in Table C.4.

Table C.4: Material properties of aircraft blades

Material property	Value
Density, ρ	2700
Youngs modulus, E	69.0×10^9
Shear modulus, G	26.5×10^9

These values, in conjunction with the values in Table C.2, can be used to calculate values for J, I_y, I_z and A. Using the equations for elastic and mass cross section properties, Eqn (35) and Eqn (56) from [138], and the assumption that the cross section has a constant material density equivalences can be made to calculate the remaining parameters.

$$Ae_A \equiv \iint_A \eta \, d\eta \, d\zeta \, , \quad me \equiv \iint_A \rho\eta \, d\eta \, d\zeta \quad \rightsquigarrow \quad e_A = e$$

$$I_y \equiv \iint_A \zeta^2 \, d\eta \, d\zeta \, , \quad mk_{m1}^2 \equiv \iint_A \rho\zeta^2 \, d\eta \, d\zeta \quad \rightsquigarrow \quad k_{m1} = \sqrt{\frac{I_y}{A}}$$

$$I_z \equiv \iint_A \eta^2 \, d\eta \, d\zeta \, , \quad mk_{m2}^2 \equiv \iint_A \rho\eta^2 \, d\eta \, d\zeta \quad \rightsquigarrow \quad k_{m2} = \sqrt{\frac{I_z}{A}} \tag{C.1}$$

$$k_{m1}^2 + k_{m2}^2 = k_m^2 \quad \rightsquigarrow \quad k_m = \sqrt{k_{m1}^2 + k_{m2}^2}$$

$$Ak_A^2 \equiv \iint_A (\eta^2 + \zeta^2) \, d\eta \, d\zeta \, , \quad mk_{m1}^2 \equiv \iint_A \rho\zeta^2 \, d\eta \, d\zeta \, ,$$
$$mk_{m2}^2 \equiv \iint_A \rho\eta^2 \, d\eta \, d\zeta \, , \quad k_{m1}^2 + k_{m2}^2 = k_m^2 \quad \rightsquigarrow \quad k_A = k_m$$

APPENDIX D

FORWARD FLIGHT MODEL

Due to the asymmetric aerodynamic flowfield experienced by a rotor during forward flight, as well as the accompanying cyclic trim, there is a large amount of variation in the aerodynamic loads that are imposed upon a blade in this flight regime. This variation is periodic but not harmonic which invalidates the assumed solution form introduced in Eq. (3.13).

Therefore, a different form of model, without this assumption, is developed. There are multiple methods for creating models in the time domain. *Gennaretti and Bernardini* [196] and *Thomas et al* [197] assumed that the response of the blade could be represented using a linear weighted combination of shape functions and used a harmonic balance procedure to calculate the steady-state aeroelastic response helicopter rotors. *Tanabe and Saito* [127] and *Tang and Dowell* [198] used modal decomposition, a process which also uses a linear weighted combination of shape functions but using modeshapes for the shape functions, to perform a time marching simulation of the aeroelastic response of a rotor blade. Alternatively, a two-dimensional solver could be used to solve equations of motion in the space and time domain simultaneously. *Khater et al* [199] developed a Chebyshev spectral collocation method for solving Burgers' type equations which was capable of solving sets of coupled two-dimensional nonlinear partial differential equations.

The model developed herein uses the principle of modal decomposition to calculates a time-marching solution for the aeroelastic response of a rotor blade. The model is based on the same equations used for the main model in Chapter 3, Eqs. (3.3a) and (3.3b), but without the harmonic motion assumption which removes the temporal domain and with the inclusion distributed aerodynamic lift and drag. These equations are shown below in Eq. (D.1).

$$\begin{aligned} -\left[\left(\frac{1}{2}\Omega^2 m\left(R^2-x^2\right)-P\right)v_*'\right]' + EI_z v_*^{iv} + m\ddot{v_*} - m\Omega^2 v_* &= L_y \\ -\left[\left(\frac{1}{2}\Omega^2 m\left(R^2-x^2\right)-P\right)w_*'\right]' + EI_y w_*^{iv} + m\ddot{w_*} &= L_z \end{aligned} \tag{D.1}$$

The aerodynamic forcing is calculated using quasi-steady lift and drag equations. The lift coefficient is calculated using a flat plate theory and an angle of attack calculated from cyclic pitch angles and the out-of-plane velocity. The drag coefficient is calculated from the induced drag, calculated from the lift coefficient without an out-of-plane velocity, and a parasitic drag value. The equations for these are shown below in Eq. (D.2).

$$\begin{aligned} L_y &= -\frac{1}{2}\rho_\infty\left(\Omega x + \dot{v_*} + v_f \sin\psi\right)^2 c C_d \\ L_z &= \frac{1}{2}\rho_\infty\left(\Omega x + v_f \sin\psi\right)^2 c C_l \\ C_d = \frac{C_l^2}{\pi\frac{R}{c}} + C_{d0} &= \frac{\left(2\pi\left(a_s \sin\psi + a_c\cos\psi\right)\right)^2}{\pi\frac{R}{c}} + C_{d0} \\ C_l &= 2\pi\left(a_s\sin\psi + a_c\cos\psi - \frac{\dot{w_*}}{\Omega x + v_f\sin\psi}\right) \end{aligned} \tag{D.2}$$

The deformation of the blade can be represented as a linear sum of spanwise shape functions and contribution factors as defined in Eq. (D.3). For this analysis, the shape functions used are the modeshapes calculated using the in-vacuo model described in Section 3.1. The benefits of this are that the modeshapes are orthogonal which ensures that a diverse range of combined deformation shapes can be formed.

$$\begin{aligned} w_*(x,t) &= \sum_{\forall i} q_{w\,i}(t) W_i(x) \\ v_*(x,t) &= \sum_{\forall i} q_{v\,i}(t) V_i(x) \end{aligned} \tag{D.3}$$

Eq. (D.3) and Eq. (D.2) can be substituted in to Eq. (D.1), multiplied by W_j and V_j and integrated along the length of the blade to form a set of equations in terms of modal mass, stiffness and forcing matrices as seen in Eq. (D.4).

$$\begin{aligned} \mathbf{M}_v\ddot{\mathbf{Q}} + \mathbf{K}_v\mathbf{Q} &= \mathbf{D}(\psi) \\ \mathbf{M}_w\ddot{\mathbf{Q}} + \mathbf{K}_w\mathbf{Q} &= \mathbf{L}(\psi) \end{aligned} \tag{D.4}$$

As the mass and stiffness matrices are constant with respect to azimuth they can be calculated as constants using Eq. (D.5).

$$
\begin{aligned}
\mathbf{M}_v(i,j) &= \int_{R_0}^{R} V_j(x) m V_i(x) dx \\
\mathbf{M}_w(i,j) &= \int_{R_0}^{R} W_j(x) m W_i(x) dx \\
\mathbf{K}_v(i,j) &= \int_{R_0}^{R} V_j(x) \Big(- \Big[\Big(\frac{1}{2} \Omega^2 m \big(R^2 - x^2 \big) - P \Big) V_i'(x) \Big]' + E I_z V_i^{iv}(x) - m \Omega^2 V_i(x) \Big) dx \\
\mathbf{K}_w(i,j) &= \int_{R_0}^{R} W_j(x) \Big(- \Big[\Big(\frac{1}{2} \Omega^2 m \big(R^2 - x^2 \big) - P \Big) W_i'(x) \Big]' + E I_z W_i^{iv}(x) \Big) dx
\end{aligned}
\tag{D.5}
$$

As the forcing terms are functions of azimuth they cannot be treated the same way. These terms are factorised into constant integral terms and azimuthally varying factors as seen in Eq. (D.6).

$$
\begin{aligned}
\mathbf{D}(i) &= \Big(\mathbf{D}_1 + \mathbf{D}_2 \dot{\mathbf{Q}} + \mathbf{D}_3 \dot{\mathbf{Q}}^2 \Big) \mathbf{C}_v(\psi) \\
\mathbf{L}(i) &= \Big(\mathbf{L}_1 + \mathbf{L}_2 \dot{\mathbf{Q}} \Big) \mathbf{C}_w(\psi)
\end{aligned}
\tag{D.6}
$$

where

$$\mathbf{C}_v = \begin{bmatrix} 1 \\ \sin\psi \\ \cos\psi \\ \sin 2\psi \\ \cos 2\psi \\ \sin 3\psi \\ \cos 3\psi \\ \sin 4\psi \\ \cos 4\psi \end{bmatrix} \tag{D.7}$$

$$\mathbf{C}_w = \begin{bmatrix} 1 \\ \sin\psi \\ \cos\psi \\ \sin 2\psi \\ \cos 2\psi \\ \sin 3\psi \\ \cos 3\psi \end{bmatrix}$$

$$\mathbf{D}_1(i,:) = \int_{R_0}^{R} \begin{bmatrix} -(C_{d0}V_i(x)v_f^2 c\rho_\infty)/4 - (C_{d0}\Omega^2 V_i(x)c\rho_\infty x^2)/2 - (\pi V_i(x)v_f^2 a_c^2 c^2\rho_\infty)/(4R) \\ -(3\pi V_i(x)v_f^2 a_s^2 c^2\rho_\infty)/(4R) - (\pi\Omega^2 V_i(x)a_c^2 c^2\rho_\infty x^2)/R \\ -(\pi\Omega^2 V_i(x)a_s^2 c^2\rho_\infty x^2)/R \\ \\ -C_{d0}\Omega V_i(x)v_f c\rho_\infty x - (\pi\Omega V_i(x)v_f a_c^2 c^2\rho_\infty x)/R \\ -(3\pi\Omega V_i(x)v_f a_s^2 c^2\rho_\infty x)/R \\ \\ -(2\pi\Omega V_i(x)v_f a_c a_s c^2\rho_\infty x)/R \\ \\ -(\pi V_i(x)v_f^2 a_c a_s c^2\rho_\infty)/R - (2\pi\Omega^2 V_i(x)a_c a_s c^2\rho_\infty x^2)/R \\ \\ (V_i(x)\rho_\infty\pi\Omega^2 a_s^2 c^2 x^2)/R - (V_i(x)a_c^2\rho_\infty\pi\Omega^2 c^2 x^2)/R \\ +(V_i(x)\rho_\infty\pi v_f^2 a_s^2 c^2)/R + (C_{d0}V_i(x)\rho_\infty v_f^2 c)/4 \\ \\ (\Omega V_i(x)v_f\rho_\infty x\pi a_s^2 c^2)/R - (\Omega V_i(x)v_f a_c^2\rho_\infty x\pi c^2)/R \\ \\ (2\pi\Omega V_i(x)v_f a_c a_s c^2\rho_\infty x)/R \\ \\ (\pi V_i(x)v_f^2 a_c a_s c^2\rho_\infty)/(2R) \\ \\ (V_i(x)\rho_\infty\pi v_f^2 a_c^2 c^2)/(4R) - (V_i(x)a_s^2\rho_\infty\pi v_f^2 c^2)/(4R) \end{bmatrix}^T dx \tag{D.8}$$

$$\mathbf{D}_2(i,j,:) = \int_{R_0}^{R} \begin{bmatrix} -V_j(x)((2\Omega V_i(x)\rho_\infty x\pi a_c^2 c^2)/R + (2\Omega V_i(x)\rho_\infty x\pi a_s^2 c^2)/R \\ +C_{d0}\Omega V_i(x)\rho_\infty xc) \\ -V_j(x)((V_i(x)v_f\rho_\infty \pi a_c^2 c^2)/R + (3V_i(x)v_f\rho_\infty \pi a_s^2 c^2)/R + C_{d0}V_i(x)v_f\rho_\infty c) \\ -(2\pi V_i(x)V_j(x)v_f a_c a_s c^2\rho_\infty)/R \\ -(4\pi\Omega V_i(x)V_j(x)a_c a_s c^2\rho_\infty x)/R \\ -V_j(x)((2\Omega V_i(x)\rho_\infty x\pi a_c^2 c^2)/R - (2\Omega V_i(x)a_s^2\rho_\infty x\pi c^2)/R) \\ -V_j(x)((V_i(x)v_f\rho_\infty \pi a_c^2 c^2)/R - (V_i(x)v_f a_s^2\rho_\infty \pi c^2)/R) \\ (2\pi V_i(x)V_j(x)v_f a_c a_s c^2\rho_\infty)/R \\ 0 \\ 0 \end{bmatrix}^T dx \tag{D.9}$$

$$\mathbf{D}_3(i,j,k,:) = \int_{R_0}^{R} \begin{bmatrix} -V_j(x)V_k(x)((V_i(x)\rho_\infty \pi a_c^2 c^2)/R + (V_i(x)\rho_\infty \pi a_s^2 c^2)/R + (C_{d0}V_i(x)\rho_\infty c)/2) \\ 0 \\ 0 \\ -(2\pi V_i(x)V_j(x)V_k(x)a_c a_s c^2 \rho_\infty)/R \\ -V_j(x)V_k(x)((V_i(x)\rho_\infty \pi a_c^2 c^2)/R - (V_i(x)a_s^2 \rho_\infty \pi c^2)/R) \\ 0 \\ 0 \\ 0 \\ 0 \end{bmatrix}^T dx \tag{D.10}$$

$$\mathbf{L}_1(i,:) = \int_{R_0}^{R} \begin{bmatrix} \pi\Omega W_i(x)v_f a_s c\rho_\infty x \\ W_i(x)a_s c\rho_\infty \pi\Omega^2 x^2 + (3W_i(x)a_s c\rho_\infty \pi v_f^2)/4 \\ W_i(x)a_c c\rho_\infty \pi\Omega^2 x^2 + (W_i(x)a_c c\rho_\infty \pi v_f^2)/4 \\ \pi\Omega W_i(x)v_f a_c c\rho_\infty x \\ -\pi\Omega W_i(x)v_f a_s c\rho_\infty x \\ -(\pi W_i(x)v_f^2 a_s c\rho_\infty)/4 \\ -(\pi W_i(x)v_f^2 a_c c\rho_\infty)/4 \end{bmatrix}^T dx \tag{D.11}$$

$$\mathbf{L}_2(i,j,:) = \int_{R_0}^{R} \begin{bmatrix} -\pi\Omega W_i(x) W_j(x) c\rho_\infty x \\ -\pi W_i(x) W_j(x) v_f c\rho_\infty \\ 0 \\ 0 \\ 0 \\ 0 \\ 0 \end{bmatrix}^T dx \tag{D.12}$$

It can be seen from the presence of $\sin 3\psi$ and $\cos 3\psi$ in $\mathbf{L}_1$ and $\sin 4\psi$ and $\cos 4\psi$ in $\mathbf{D}_1$ in Eq. (D.6) that the model will be able to excite frequencies up to 3/rev in the out-of-plane direction and 4/rev in the in-plane direction. Eq. (D.4) can be reformulated in to state space format in terms of modal participation factors and solved using ode45, an initial conditions Ordinary Differential Equation (ODE) solver. The solution process continues until two consecutive rotations of the blade exhibit deformations, and their respective derivatives, along the entire length of the blade that correlate to within 0.1 % of the amplitude of an oscillation. Once the deformations and derivatives have suitably converged, the final modal participation factors of the rotation can be processed to calculate the blade deformations using Eq. (D.3) and subsequent vibratory loads using Eq. (D.13).

$$\begin{aligned} M_z &= EI_z v_*'' \\ F_y &= -EI_z v_*''' + \left(\frac{1}{2}\Omega^2 m\left(R^2 - x^2\right) - P\right) v_*' \\ M_y &= EI_y w_*'' \\ F_z &= -EI_y w_*''' + \left(\frac{1}{2}\Omega^2 m\left(R^2 - x^2\right) - P\right) w_*' \end{aligned} \tag{D.13}$$

References

[1] V. R. Murthy, "Dynamic characteristics of rotor blades," *Journal of Sound and Vibration*, vol. 49, no. 4, pp. 483–500, 1976.

[2] G. Isakson and J. G. Eisley, "Natural frequencies in coupled bending and torsion of twisted rotating and nonrotating blades," tech. rep., 1964.

[3] D. H. Hodges and R. A. Ormiston, "Stability of elastic bending and torsion of uniform cantilever rotor blades in hover with variable structural coupling," tech. rep., 1976.

[4] I. Goulos, V. Pachidis, R. D'Ippolito, J. Stevens, and C. Smith, "An Integrated Approach for the Multidisciplinary Design of Optimum Rotorcraft Operations," *Journal of Engineering for Gas Turbines and Power*, vol. 134, no. 9, p. 091701, 2012.

[5] R. B. Taylor, "Helicopter rotor blade design for minimum vibration," tech. rep., NASA CR-3825, 1984.

[6] S. Moffatt and N. Griffiths, "Structural Optimisation and Aeroelastic Tailoring of the BERP IV Demonstrator Blade," in *American Helicopter Society 65th Annual Forum*, 2009.

[7] P. P. Friedmann, "Helicopter vibration reduction using structural optimization with aeroelastic/multidisciplinary constraints - A survey," *Journal of Aircraft*, vol. 28, no. 1, pp. 8–21, 1991.

[8] P. Konstanzer, B. Enenkl, P. Aubourg, and P. Cranga, "Recent Advances in Eurocopter's Passive and Active Vibration Control," in *American Helicopter Society 64th Annual Forum*, 2008.

[9] D. Han, V. Pastrikakis, and G. N. Barakos, "Helicopter performance improvement by variable rotor speed and variable blade twist," *Aerospace Science and Technology*, vol. 54, pp. 164–173, 2016.

[10] M. Allongue, H. J. Marze, and F. Potdevin, "The Quiet Helicopter 'from research to reality'," in *55th Annual AHS Forum Proceedings*, pp. 87–103, 1999.

[11] R. Rammer, A. Kus, J. B. Maurice, O. Dieterich, and P. Konstanzer, "Bluecopter demonstrator: Mastering dynamics challenges," *42nd European Rotorcraft Forum 2016*, vol. 2, pp. 822–834, 2016.

[12] A. E. Karem, "Optimum speed rotor," 1999.

[13] A. Datta, H. Yeo, and T. R. Norman, "Experimental Investigation and Fundamental Understanding of a Full-Scale Slowed Rotor at High Advance Ratios," in *American Helicopter Society 66th Annual Forum*, pp. 1–26, 2011.

[14] F. B. Gustafson and A. Gessow, "Effect of rotor-tip speed on helicopter hovering performance and maximum forward speed," tech. rep., 1946.

[15] G. A. Misté and E. Benini, "Variable-Speed Rotor Helicopters: Performance Comparison Between Continuously Variable and Fixed-Ratio Transmissions," *Journal of Aircraft*, vol. 53, no. 5, pp. 1189–1200, 2016.

[16] J. H. Steiner, *An Investigation Of Performance Benefits And Trim Requirements Of A Variable Speed Helicopter Rotor*.
PhD thesis, 2008.

[17] D. Han, C. Dong, and G. N. Barakos, "Performance Improvement of Variable Speed Rotors by Gurney Flaps," in *43rd European Rotorcraft Forum*, 2017.

[18] W. Johnson, G. K. Yamauchi, and M. E. Watts, "NASA Heavy Lift Rotorcraft Systems Investigation," Tech. Rep. December, 2005.

[19] G. Couluris, C. Hange, D. Wardwell, D. Signor, and J. Phillips, "A potential impact analysis of estol aircraft on newark airport operations," in *AIAA Modeling and Simulation Technologies Conference and Exhibit*, p. 6700, 2007.

[20] H. Yeo and W. Johnson, "Aeromechanics analysis of a heavy lift slowed-rotor compound helicopter," *Journal of Aircraft*, vol. 44, no. 2, pp. 501–508, 2007.

[21] C. Russell and W. Johnson, "Conceptual design and performance analysis for a large civil compound helicopter," in *AHS Future Vertical Lift Aircraft Design Conference*, (San Francisco), pp. 1–16, 2012.

[22] M. W. Floros and W. Johnson, "Performance Analysis of the Slowed-Rotor Compound Helicopter Configuration," *Journal of the American Helicopter Society*, vol. 54, no. 2, 2009.

[23] W. Johnson, "Rotorcraft aeromechanics applications of a comprehensive analysis," in *AHS International Meeting on Advanced Rotorcraft Technology and Disaster Relief*, Citeseer, 1998.

[24] H. Kang, H. Saberi, and F. Gandhi, "Dynamic Blade Shape for Improved Helicopter Rotor Performance," *Journal of the American Helicopter Society*, vol. 55, no. 3, 2010.

[25] G. M. Bowen-Davies, *Performance and Loads of Variable Tip Speed Rotorcraft at High Advance Ratios*.
PhD thesis, 2015.

[26] E. Ward, I. Chopra, and A. Datta, *Aeromechanical Behavior Of Twist-Morphing, High-Speed, Slowed RPM Rotors*.
PhD thesis, 2018.

[27] D. Han and E. C. Smith, "Lagwise dynamic analysis of a variable speed rotor," *Aerospace Science and Technology*, vol. 29, no. 1, pp. 277–286, 2013.

[28] D. Han, J. Wang, E. C. Smith, and G. A. Lesieutre, "Transient Loads Control of a Variable Speed Rotor During Lagwise Resonance Crossing," *AIAA Journal*, vol. 51, no. 1, pp. 20–29, 2013.

[29] P. P. Walsh and P. Fletcher, *Gas turbine performance*.
John Wiley and Sons, 2004.

[30] J. S. Litt, J. M. Edwards, and J. A. DeCastro, "A Sequential Shifting Algorithm for Variable Rotor Speed Control," tech. rep., ARL-TR-4086, 2007.

[31] G. A. Misté and E. Benini, "Performance of a Turboshaft Engine for Helicopter Applications," in *Proceedings of the ASME 2012 Gas Turbine India Conference*, (Mumbai, India), pp. 1–15, 2012.

[32] M. D'Angelo, "Wide Speed Range Turboshaft Study," tech. rep., Contractor Report 198380, 1995.

[33] G. E. Welch, "Assessment of Aerodynamic Challenges of a Variable-Speed Power Turbine for Large Civil Tilt-Rotor Application," tech. rep., TM-2010-216758, 2010.

[34] G. E. Welch, "Computational Assessment of the Aerodynamic Performance of a Variable-Speed Power Turbine for Large Civil Tilt-Rotor Application," tech. rep., TM-2011-217124, 2011.

[35] P. X. Palcic, T. Garcia, and Y. Gmirya, "Variable speed transmission for a rotary wing aircraft," 2007.

[36] M. A. Stevens, R. F. Handschuh, and D. G. Lewicki, "Concepts for Variable/Multi-Speed Rotorcraft Drive System," tech. rep., ARLâĂŞTRâĂŞ4564, 2008.

[37] D. G. Lewicki, H. Desmidt, E. C. Smith, and S. W. Bauman, "Two-Speed Gearbox Dynamic Simulation Predictions and Test Validation," tech. rep., TM-2010-216363, 2010.

[38] H. Desmidt, K.-w. Wang, A. Arbor, and E. C. Smith, "Variable-Speed Simulation of a Dual-Clutch Gearbox Tiltrotor Driveline," tech. rep., TM-2012-217212, 2012.

[39] Z. B. Saribay, *Analytical Investigation of the Pericyclic Variable-Speed Transmission System for Helicopter Main-Gearbox*.
PhD thesis, 2009.

[40] S. Newman, *Foundations of helicopter flight*.
Elsevier, 1994.

[41] D. H. Hodges, *Nonlinear composite beam theory*.
American Institute of Aeronautics and Astronautics, 2006.

[42] F. Jiang, W. Yu, and D. H. Hodges, "Analytical Modeling of Trapeze and Poynting Effects of Initially Twisted Beams," *Journal of Applied Mechanics*, vol. 82, no. 6, 2015.

[43] H. Yoo and S. Shin, "Vibration analysis of rotating cantilever beams," *Journal of Sound and Vibration*, vol. 212, no. 5, pp. 807–828, 1998.

[44] J. L. du Bois, S. Adhikari, and N. A. J. Lieven, "Eigenvalue curve veering in stressed structures: An experimental study," *Journal of Sound and Vibration*, vol. 322, pp. 1117–1124, 2009.

[45] E. Balmes, "High modal density, curve veering, localization: a different perspective on the structural response," 1993.

[46] B. Glaz, P. P. Friedmann, and L. Liu, "Vibration Reduction and Performance Enhancement of Helicopter Rotors Using an Active/Passive Approach," *Proceedings of the 49th AIAA/ASME/ASCE/AHS/ASC Structures, Structural Dynamics, and Materials Conference*, no. April, pp. 1–18, 2008.

[47] E. Beno, "Ch-53a main rotor and stabilizer vibratory airloads and forces," tech. rep., Department of the Navy SER-65593, 1970.

[48] J. Pearson, R. Goodall, and I. Lyndon, "Active control of helicopter vibration," *Computing & Control Engineering Journal*, pp. 277–284, 1994.

[49] A. I. Phuriwat and F. Gandhi, *Semi-Active Control of Helicopter Vibration Using Controllable Stiffness and Damping Devices*.
PhD thesis, 2002.

[50] B. Berry and I. Chopra, "Wind tunnel testing for performance and vibratory loads of a variable-speed mach-scale rotor," in *Proceedings of the American Helicopter Society 67th Annual Forum*, 2011.

[51] W. Johnson, *Helicopter theory*.
Courier Corporation, 2012.

[52] J. M. Giraud, "The dolphin n4 design," in *54th AHS Forum*, 1998.

[53] G. Putrich, "FARNBOROUGH: Cutaway & technical description: Defying convention - Boeing A160 Hummingbird," *Flightglobal*, 2010.

[54] J. DiOttavio and D. Friedmann, "Operational benefits of an optimal, widely variable speed rotor," in *Proceedings of AHS 66th Annual Forum, Phoenix*, vol. 1, pp. 1865–1871, 2010.

[55] F. A. Internationale, "Record id 15059," 2008.
http://archive.li/u8aZT.

[56] Unicopter, "X2 data."

[57] R. Blackwell and T. Millott, "Dynamics Design Characteristics of the Sikorsky X2 Technology Demonstrator Aircraft," in *64th Annual Forum Proceedings-American Helicopter Society*, vol. 1, pp. 886–898, 2008.

[58] D. Walsh, S. Weiner, K. Arifian, T. Lawrence, S. Wilson, T. Millott, and R. Blackwell, "High Airspeed Testing of the Sikorsky X2 TechnologyTM Demonstrator," *67th Annual Forum of the American Helicopter Society*, pp. 1–12, 2011.

[59] A. Bagai, "Aerodynamic Design of the X2 Technology Demonstrator Main Rotor Blade," in *64th Annual Forum of the AHS*, pp. 29–44, 2008.

[60] Rotor and W. International, "Eurocopter x3 tops 2010 sikorsky x2 unofficial speed record."

[61] M. D. Maisel, D. J. Giulianetti, and D. C. Dugan, "The History of The XV-15 Tilt Rotor Research Aircraft: From Concept to Flight," *NASA Special Publication 4517*, p. 194, 2000.

[62] NAVAIR, "V-22 osprey 2010 guidebook," tech. rep., Tech. Rep. NAVAIR PMA-275 Control Num- ber 10-28, 2010.

[63] S. P. King, "The minimisation of helicopter vibration through blade design and active control," *Aeronautical Journal*, vol. 92, no. 917, pp. 247–263, 1988.

[64] J. E. Mottershead and Y. M. Ram, "Inverse eigenvalue problems in vibration absorption: Passive modification and active control," *Mechanical Systems and Signal Processing*, vol. 20, no. 1, pp. 5–44, 2006.

[65] G. Reichert, "Helicopter Vibration Control - A Survey," in *Sixth European Rotorcraft and Powered LIft Aircraft Forum*, (Bristol, UK), 1980.

[66] R. G. Loewy, "Helicopter vibrations- a technological perspective," *American Helicopter Society, Journal*, vol. 29, pp. 4–30, 1984.

[67] H. Strehlow, R. Mehlhose, P. Znika, and D. Roth, "Review of mbb's passive and active vibration control activities," *The Royal Aeronautical Society in London*, 1990.

[68] R. H. Blackwell, "Blade Design for Reduced Helicopter Vibration," *Journal of the American Helicopter Society*, vol. 28, no. 3, pp. 33–41, 1983.

[69] J. I. Pritchard and H. M. Adelman, "Optimal placement of tuning masses for vibration reduction in helicopter rotor blades," *AIAA Journal*, vol. 28, no. 2, pp. 309–315, 2008.

[70] R. H. Markievicz, *A study of the aeroolastic behaviour of helicopter rotor blades featuring swept tips*.
PhD thesis, 1990.

[71] C. W. Ellis and R. Jones, "Application of an Absorber to Reduce Helicopter Vibration Levels," *Journal of the American Helicopter Society*, vol. 8, no. 3, pp. 30–39, 1963.

[72] J. Q. Sun, M. R. Jolly, and M. A. Norris, "Passive, adaptive and active tuned vibration absorbersâĂŤa survey," *Journal of mechanical design*, vol. 117, no. B, pp. 234–242, 1995.

[73] L. Kela and P. VÃďhÃďoja, "Recent studies of adaptive tuned vibration absorbers/neutralizers," *Applied Mechanics Reviews*, vol. 62, no. 6, 2009.

[74] W. F. Paul and K. C. Mard, "Vibration damped helicopter rotor," 1970.

[75] D. Han and E. C. Smith, "Lagwise loads analysis of a rotor blade with an embedded chordwise absorber," *Journal of Aircraft*, vol. 46, no. 4, pp. 1280–1290, 2009.

[76] C. Hebert and G. A. Lesieutre, "Rotorcraft blade lag damping using highly distributed tuned vibration absorbers," *39th AIAA/ASME/ASCE/AHS/ASC Structures, Structural Dynamics, and Materials Conference and Exhibit*, pp. 2452–2457, 1998.

[77] M.-N. H. Hamouda and G. A. Pierce, "Helicopter Vibration Suppression Using Simple Pendulum Absorbers on the Rotor Blade," *Journal of the American Helicopter Society*, vol. 29, no. 3, pp. 19–29, 2009.

[78] E. Abouobaia, R. Bhat, and R. Sedaghati, "Hybrid Torsional Vibration Damper Incorporating Conventional Centrifugal Pendulum Vibration Absorber and Magnetorheological Damper," in *ASME Conference on Smart Materials, Adaptive Structures and Intelligent Systems*, (Newport, Rhode Island, USA), 2014.

[79] P. R. Payne, "Higher harmonic rotor control: the possibilities of third and higher harmonic feathering for delaying the stall limit in helicopters," *Aircraft Engineering and Aerospace Technology*, vol. 30, no. 8, pp. 222–226, 1958.

[80] P. J. Arcidiacono, "Theoretical Performance of Helicopters Having Second and Higher Harmonic Feathering Control," *Journal of the American Helicopter Society*, vol. 6, no. 2, pp. 8–19, 1961.

[81] R. P. Cheng, C. R. Theodore, and R. Celi, "Effects of Two/rev Higher Harmonic Control on Rotor Performance," *Journal of the American Helicopter Society*, vol. 48, no. 1, pp. 18–27, 2003.

[82] R. P. Cheng and R. Celi, "Optimum Two-Per-Revolution Inputs for Improved Rotor Performance," *Journal of Aircraft*, vol. 42, no. 6, pp. 1409–1417, 2005.

[83] D. A. Wachspress, T. R. Quackenbush, and C. L. Solomon, "On minimum induced power of the helicopter rotor," in *American Helicopter Society 61st Annual Forum Proceedings*, (Grapevine, TX), 2005.

[84] K. Nguyen, *Higher Harmonic Control Analysis for Vibration Reduction of Helicopter Rotor Systems*.
PhD thesis, University of California, Los Angeles, 1989.

[85] J. Shaw, N. Albion, E. J. Hanker, and R. S. Teal, "Higher Harmonic Control: Wind Tunnel Demonstration of Fully Effective Vibratory Hub Force Suppression," *Journal of the American Helicopter Society*, vol. 34, no. 1, pp. 14–25, 1989.

[86] D. M. Walsh, "Flight tests of an open loop higher harmonic control system of an s- 76a helicopter," in *Proceedings of the 42nd Annual Forum of the American Helicopter Society*, (Alexandria, VA), 1986.

[87] N. D. Ham, "Helicopter individual-blade-control research at MIT," *Vertica*, vol. 11, no. 1, 1987.

[88] D. Feszty, F. Nitzsche, D. Waechter, E. Bianchi, M. Gennaretti, and G. L. Ghiringhelli, "The SHARCS Project: Smart Hybrid Active Rotor Control System For Noise And Vibration Attenuation Of Helicopter Rotor Blades," in *31st European Rotorcraft Forum*, (Florence, Italy), 2005.

[89] R. Kube and B. G. Van Der Wall, "Ibc effects on bvi noise and vibrations - a combined numerical and experimental investigation," in *Proceedings of the 55th International Annual Forum of the American Helicopter Society*, (Montreal, Canada), 1999.

[90] K. F. Guinn, "Individual blade control independent of a swashplate," *Journal of the American Helicopter Society*, vol. 27, no. 3, pp. 25–31, 1982.

[91] S. John, N. M. Wereley, and J. Sirohi, "Development of a piezohydraulic active pitch link for a swashplateless helicopter rotor," *Journal of Aircraft*, vol. 46, no. 1, pp. 328–331, 2009.

[92] T. A. Millott, *Vibration reduction in helicopter rotors using an actively controlled partial span trailing edge flap located on the blade*.
PhD thesis, California, Los Angeles, 1993.

[93] J. H. Milgram, *A Comprehensive Aeroelastic Analysis of Helicopter Main Rotors with Trailing Edge Flaps for Vibration Reduction*.
PhD thesis, University of Maryland, 1 1997.

[94] S. Dawson, "Wind tunnel test of an active flap rotor - bvi noise and vibration reduction," in *51st Annual Forum of the American Helicopter Society*, (Fort worth, TX), 1995.

[95] T. Chiu and P. P. Friedmann, "Vibration suppression in helicopter rotor/flexible fuselage system using the acsr approach with disturbance rejection," in *Proceedings of the 52nd Forum of the American Helicopter Society*, (Washington, DC), 1996.

[96] W. A. Welsh, P. C. Von Hardenberg, P. W. Von Hardenberg, and A. E. Staple, "Test and evaluation of fuselage vibration utilizing active control of structural response (acsr) optimized to ads-27," in *Proceedings of the 46th Annual Forum of the American Helicopter society*, (Washington, DC), 1990.

[97] A. E. Staple, "An evaluation of active control of structural response as a means of reducing helicopter vibration," in *Proceedings of the 46th Annual Forum of the American Helicopter society*, (Washington, DC), 1990.

[98] W. Welsh, C. Fredrickson, C. Rauch, and I. Lyndon, "Flight test of an active vibration control system on the uh-60 black hawk helicopter," in *51st Annual Forum of the American Helicopter Society*, (Fort worth, TX), 1995.

[99] N. Hackett, "Eh101 active control of structural response development, productionisation and certification," in *Proceedings of the EH101 Avionics, Civil and Military Conference*, (London, United Kingdom), 1995.

[100] R. K. Goodman and T. A. Millott, "Design, development, and flight testing of the active vibration control system for the sikorsky s-92," in *Proceedings of the 56th Annual Forum of the American Helicopter society*, (Virginia Beach, Virginia), 2000.

[101] R. Rajamani and J. K. Hedrick, "Semi-Active suspensions - a comparison between theory and experiments," *Vehicle System Dynamics*, vol. 20, no. 1, pp. 504–518, 1992.

[102] J. Onoda, T. Endot, H. Tamaoki, and N. Watanabe, "Vibration Suppression by Variable-Stiffness Members," *AIAA Journal*, vol. 29, no. 6, pp. 977–983, 1991.

[103] F. Nitzsche, "Tailoring the dynamic response of helicopter rotors using smart materials," in *Proceedings of the AIAA/ASME Adaptive Structures Forum*, 1995.

[104] F. Nitzsche, "Smart spring-type actuation for helicopter individual blade control," in *Sixth International Conference on Adaptive Structures*, (Key West, Florida), 1996.

[105] G. Bir, I. Chopra, K. Kim, J. Wang, E. Smith, S. Vellaichamy, R. Ganguli, M. Nixon, and S. Torok, "University of maryland advanced rotorcraft code (umarc) theory manual," tech. rep., UM-AERO Report 92-02, 1992.

[106] J. L. du Bois, N. A. J. Lieven, and S. Adhikari, "A tensioned cable as an adaptive tuned vibration absorber for response suppression in rotorcraft," in *25th International Conference on Noise and Vibration engineering, ISMA2012 in conjunction with the 4th International Conference on Uncertainty in Structural Dynamics, USD 2012*, pp. 237–250, 2012.

[107] M. A. Acar and C. Yilmaz, "Design of an adaptive-passive dynamic vibration absorber composed of a string-mass system equipped with negative stiffness tension adjusting mechanism," *Journal of Sound and Vibration*, vol. 332, no. 2, pp. 231–245, 2013.

[108] J.-D. Yau, "Train-induced vibration control of simple beams using string-type tuned mass dampers," *Journal of Mechanics*, vol. 23, no. 4, pp. 329–340, 2007.

[109] T. Turkstra and S. Semercigil, "Elimination of Resonance with a Switching Tensile Support," *Journal of Sound and Vibration*, vol. 163, no. 2, pp. 359–362, 1993.

[110] L. N. Virgin and R. H. Plaut, "Effect of axial load on forced vibration of beams," *Journal of Sound and Vibration*, vol. 168, no. 3, pp. 395–405, 1993.

[111] L. N. Virgin, *Vibration of Axially-Loaded Structures*. Cambridge University Press, 2007.

[112] J. L. du Bois, N. A. J. Lieven, and S. Adhikari, "Adaptive Passive Control of Dynamic Response Through Structural Loading," in *48th AIAA/ASME/ASCE/AHS/ASC Structures, Structural Dynamics, and Materials Conference*, pp. 1–14, 2007.

[113] Y. Q. Zhang, Y. Lu, S. L. Wang, and X. Liu, "Vibration and buckling of a double-beam system under compressive axial loading," *Journal of Sound and Vibration*, vol. 318, pp. 341–352, 2008.

[114] S. Nudehi, R. Mukherjee, and S. W. Shaw, "Active Vibration Control of a Flexible Beam Using a Buckling-Type End Force," *Journal of Dynamic Systems, Measurement, and Control*, vol. 128, no. 2, pp. 278–286, 2006.

[115] Z. Tian, B. Mokrani, D. Alaluf, and L. J. Jiang, "Active tendon control of suspension bridge with two different configurations," in *International Conference on Noise and Vibration Engineering*, pp. 1–16, 2016.

[116] A. Preumont, Y. Achkire, and F. Bossens, "Active Tendon Control of Large Trusses," *AIAA Journal*, vol. 38, no. 3, pp. 493–498, 2000.

[117] J. Issa, R. Mukherjee, and S. W. Shaw, "Vibration Suppression in Structures Using Cable Actuators," *Journal of Vibration and Acoustics*, vol. 132, no. 3, p. 031006, 2010.

[118] Y. Suzuki and Y. Kagawa, "Active vibration control of a flexible cantilever beam using shape memory alloy actuators," *Smart Materials and Structures*, vol. 19, no. 8, pp. 1–9, 2010.

[119] M. N. Svendsen, S. Krenk, and J. Høgsberg, "Resonant vibration control of rotating beams," *Journal of Sound and Vibration*, vol. 330, no. 9, pp. 1877–1890, 2011.

[120] M. Krishnan, M. I. Albakri, M. Maza, and P. A. Tarazaga, "Adaptive Flutter Induction Using Active Compressive Loads," in *International Modal Analysis Conference*, (Orlando, Florida), pp. 399–404, 2019.

[121] R. V. Southwell and B. S. Gough, *On the Free Transverse Vibrations of Airscrew Blades*. H.M. Stationery Office, 1922.

[122] R. W. Prouty, *Helicopter performance, stability, and control*. Kreiger Publishing Company, 2003.

[123] K.-V. Truong, H. Yeo, and R. A. Ormiston, "Structural dynamics modeling of rectangular rotor blades," *Aerospace Science and Technology*, vol. 30, pp. 293–305, 2013.

[124] D. Kunz, "Comprehensive Rotorcraft Analysis: Past, Present, and Future," in *46th AIAA/ASME/ASCE/AHS/ASC Structures, Structural Dynamics and Materials Conference*, no. April, (Austin, Texas), pp. 1–11, 2005.

[125] W. Johnson, "A History of Rotorcraft Comprehensive Analyses," in *AHS 69th Annual Forum*, (Phoenix, Arizona), 2013.

[126] J. S. Park and Y. J. Kee, "Code-to-code comparison study on rotor aeromechanics in descending flight," *Journal of Mechanical Science and Technology*, vol. 29, no. 8, pp. 3153–3163, 2015.

[127] Y. Tanabe and S. Saito, "A Simplified CFD / CSD Loose Coupling Approach For Rotor Blade Deformation," tech. rep., 2009.

[128] F. D. Gakhov, *Boundary value problems*.
Elsevier, 2014.

[129] M. Gennaretti, G. Bernardini, J. Serafini, and M. M. Colella, "Helicopter Vibratory Loads Alleviation Through Combined Action of Trailing-Edge Flap and Variable-Stiffness Devices," *International Journal of Aerospace Engineering*, vol. 2015, pp. 1–13, 2015.

[130] H.-Y. Ryu and S.-J. Shin, "Prediction of the aeromechanics for HART II rotor in descending flight using mixed variational geometrically exact beam analysis," *Journal of Mechanical Science and Technology*, vol. 29, no. 1, pp. 141–150, 2015.

[131] M. R. Amoozgar, H. Shahverdi, and A. S. Nobari, "Aeroelastic Stability of Hingeless Rotor Blades in Hover Using Fully Intrinsic Equations," *AIAA Journal*, vol. 55, no. 7, pp. 2450–2460, 2017.

[132] C. E. Cesnik and D. H. Hodges, "Vabs: a new concept for composite rotor blade cross-sectional modeling," *Journal of the American helicopter society*, vol. 42, no. 1, pp. 27–38, 1997.

[133] D. H. Hodges, "Geometrically exact, intrinsic theory for dynamics of curved and twisted anisotropic beams," *AIAA journal*, vol. 41, no. 6, pp. 1131–1137, 2003.

[134] L. Shang, P. H. Xia, and D. H. Hodges, "Aeroelastic Response Analysis of Composite Blades Based on Geometrically Exact Beam Theory," *Journal of the American Helicopter Society*, vol. 64, no. 2, pp. 1–14, 2019.

[135] S. P. Timoshenko, *Vibration problems in engineering*.
Van Nostrand, Princeton, 3 ed., 1955.

[136] M. Rafiee, F. Nitzsche, and M. Labrosse, "Dynamics, vibration and control of rotating composite beams and blades: A critical review," *Thin-Walled Structures*, vol. 119, no. January, pp. 795–819, 2017.

[137] J. C. Houbolt and G. W. Brooks, "Differential equations of motion for combined flapwise bending, chordwise bending, and torsion of twisted nonuniform rotor blades," tech. rep., Technical Note 3905, 1957.

[138] D. H. Hodges and E. H. Dowell, "Nonlinear equations of motion for the elastic bending and torsion of twisted nonuniform rotor blades," tech. rep., NASA Technical Note D-7818, 1974.

[139] J. M. Greenberg, "Airfoil in sinusoidal motion in a pulsating stream," *National Advisory Committee For Aeronautics Technical Note 1326*, no. 1326, 1947.

[140] J. Rauleder, V. Ondra, and D. Komp, "Aerodynamic Performance of Morphing Blades and Rotor Systems," in *AHS International 74th Annual Forum & Technology Display*, no. May, 2018.

[141] V. Ondra, R. P. Dibble, and B. Titurus, "Towards an application of an active tendon in rotorcraft : A numerical and experimental study of coupled bending- torsion vibration of a beam-tendon system," in *International Seminar on Modal analysis*, (Leuven, Belgium), 2018.

[142] V. Ondra, R. P. Dibble, B. Titurus, and B. K. S. Woods, "An active tendon concept in rotorcraft with variable speed rotors : free vibration perspective," in *AIAA SciTech*, (San Diego, California), pp. 1–14, 2019.

[143] V. Ondra and B. Titurus, "Theoretical and experimental modal analysis of beam-tendon system," *Mechanical Systems and Signal Processing*, vol. 132, pp. 55–71, 2019.

[144] V. Ondra and B. Titurus, "Free vibration analysis of a rotating pre-twisted beam subjected to tendon-induced axial loading," *Journal of Sound and Vibration*, p. 114912, 2019.

[145] P. Thomson, G. J. Balas, and P. H. Leo, "The use of shape memory alloys for passive structural damping," *Smart Materials and Structures*, vol. 4, no. 1, pp. 36–41, 1995.

[146] D. Schillinger, J. A. Evans, A. Reali, M. A. Scott, and T. J. Hughes, "Isogeometric collocation: Cost comparison with Galerkin methods and extension to adaptive hierarchical NURBS discretizations," *Computer Methods in Applied Mechanics and Engineering*, vol. 267, pp. 170–232, 2013.

[147] P. K. Masjedi and H. R. Ovesy, "Chebyshev collocation method for static intrinsic equations of geometrically exact beams," *International Journal of Solids and Structures*, vol. 54, pp. 183–191, 2015.

[148] P. K. Masjedi and A. Maheri, "Chebyshev collocation method for the free vibration analysis of geometrically exact beams with fully intrinsic formulation," *European Journal of Mechanics*, vol. 66, pp. 329–340, 2017.

[149] L. F. Shampine, J. A. Kierzenka, and M. W. Reichelt, "Solving boundary value problems for ordinary differential equations in MATLAB with bvp4c," tech. rep., Tutorisl notes 75275, 2000.

[150] J. A. Kierzenka and L. F. Shampine, "A BVP Solver Based on Residual Control and the MATLAB PSE," *ACM Transactions on Mathematical Software*, vol. 27, no. 3, pp. 299–316, 2001.

[151] G. Mogenier, T. Baranger, G. Ferraris, R. Dufour, and L. Durantay, "A criterion for mode shape tracking: application to Campbell diagrams," *Journal of Vibration and Control*, vol. 20, no. 2, pp. 179–190, 2012.

[152] R. P. Dibble and B. Titurus, "Helicopter rotor blade modal tuning using internal preloads," in *International Seminar on Modal Analysis*, (Leuven, Belgium), 2016.

[153] R. P. Dibble, V. Ondra, and B. Titurus, "Resonance avoidance for variable speed rotor blades using an applied compressive load," *Aerospace Science and Technology*, vol. 88, pp. 222–232, 2019.

[154] J. S. Bendat and A. G. Piersol, *Random data: analysis and measurement procedures*, vol. 729.
John Wiley and Sons, 2011.

[155] B. Peeters, H. Van der Auweraer, P. Guillaume, and J. Leuridan, "The polymax frequency-domain method: A new standard for modal parameter estimation?," *Shock and Vibration*, vol. 11, no. 3-4, pp. 395–409, 2004.

[156] L. Meirovitch, *Analytical Methods in Vibrations*.
The Macmillan Company, NY, 1967.

[157] R. J. Allemang, "The Modal Assurance Criterion - Twenty Years of Use and Abuse," *Journal of Sound and Vibration*, no. August, pp. 14–21, 2003.

[158] R. P. Dibble, B. K. S. Woods, and B. Titurus, "Static Aeroelastic Response of a Rotor Blade Under Internal Axial Loading," in *European Rotorcraft Forum*, (Milan, Italy), 2017.

[159] R. Schindler and E. Pfisterer, "Impacts of rotor hub design criteria of the operational capabilities of rotorcraft systems," 1986.

[160] J. Falls, *Design and Performance Prediction of Swashplateless Helicopter Rotor With Trailing Edge Flaps and Tabs*.
PhD thesis, 2010.

[161] F. Gandhi, "Centrifugal Force Actuated Variable Span Helicopter Rotor," vol. 2, no. 12, 2012.

[162] R. Timings, *Mechanical Engineer's Pocket Book*.
Newnes, 3 ed., 2005.

[163] B. G. van der Wall and J. Yin, "DLR's S4 Rotor Code Validation With HART II Data: The Baseline Case," *Proceedings of the 1st International Forum on Rotorcraft Multidisciplinary Technology*, pp. 0–5, 2007.

[164] G. Surace, V. Anghel, and C. Mares, "Coupled BendingâĂŞBendingâĂŞTorsion Vibration Analysis of Rotating Pretwisted Blades: an Integral Formulation and Numerical Examples," *Journal of Sound and Vibration*, vol. 206, no. 4, pp. 473–486, 1997.

[165] V. R. Murthy and C. E. Hammond, "Vibration Analysis of Rotor Blades with Pendulum Absorbers," *Journal of Aircraft*, vol. 18, no. 1, pp. 23–29, 2008.

[166] N. T. Sivaneri and I. Chopra, "Dynamic Stability of a Rotor Blade Using Finite Element Analysis," *AIAA Journal*, vol. 20, no. 5, pp. 716–723, 1982.

[167] P. J. Magari, L. A. Shultz, and V. R. Murthy, "Dynamics of Helicopter Rotor Blades," *Computers and Structures*, vol. 29, no. 5, pp. 763–776, 1988.

[168] SaaS, "User guide & techniques," 2010.

[169] Simulia, "Abaqus analysis user guide," 2016.

[170] T. Theodorsen, "General Theory of Aerodynamic Instability and the Mechanism of Flutter," tech. rep., 1949.

[171] D. M. Tang and E. H. Dowell, "Experimental and Theoretical Study on Aeroelastic Response of High-Aspect-Ratio Wings," *AIAA Journal*, vol. 39, no. 8, pp. 1430–1441, 2001.

[172] U. Saetti and J. F. Horn, "Use of Harmonic Decomposition Models in Rotorcraft Flight Control Design with Alleviation of Vibratory Loads," in *43rd European Rotorcraft Forum*, 2017.

[173] P. P. Friedmann and C. Yuan, "Effect of modified aerodynamic strip theories on rotor blade aeroelastic stability," *American Institute of Aeronautics and Astronautics Journal*, vol. 15, no. 7, pp. 932–940, 1977.

[174] R. T. N. Chen, "A survey of nonuniform inflow models for rotorcraft flight dynamics and control applications," 1989.

[175] Y. C. Fung, *An introduction to the theory of Aeroelasticity*.
Courier Dover Publications, 1993.

[176] G. J. Leishman, *Principles of Helicopter Aerodynamics*.
Cambridge University Press, 2000.

[177] M. Amoozgar and H. Shahverdi, "Aeroelastic stability analysis of hingeless rotor blades in hover using fully intrinsic equations and dynamic wake model," *Aircraft Engineering and Aerospace Technology*, 2019.

[178] J. C. Ho and H. Yeo, "Rotorcraft comprehensive analysis calculations of a coaxial rotor with lift offset," *International Journal of Aeronautical and Space Sciences*, 2019.

[179] R. T. Jones, "Operational treatment of the nonuniform lift theory in airplane dynamics," tech. rep., NACA Technical Note 667, Oct. 1938.

[180] A. Gessow and G. C. Myers, *Aerodynamics of the Helicopter*. Frederick Ungar, 1952.

[181] R. P. Dibble, V. Ondra, B. K. S. Woods, and B. Titurus, "Aeroelastic eigenvalue analysis of a variable speed rotor blade with an applied compressive load," in *AIAA SciTech*, (San Diego, California), 2019.

[182] M. J. Patil and D. H. Hodges, "On the importance of aerodynamic and structural geometrical nonlinearities in aeroelastic behavior of high-aspect-ratio wings," *Journal of Fluids and Structures*, vol. 19, no. 7, pp. 905–915, 2004.

[183] D. Younesian, E. Esmailzadeh, and R. Sedaghati, "Passive vibration control of beams subjected to random excitations with peaked psd," *Journal of Vibration and Control*, vol. 12, no. 9, pp. 941–953, 2006.

[184] Z. Mohamed, A. K. Chee, A. W. I. M. Hashim, M. O. Tokhi, S. H. M. Amin, and R. Mamat, "Techniques for vibration control of a flexible robot manipulator," *Robotica*, vol. 24, no. 4, p. 499âĂŞ511, 2006.

[185] H. Li, M. Le, Z. Gong, and W. Lin, "Motion profile design to reduce residual vibration of high-speed positioning stages," *IEEE/ASME Transactions On Mechatronics*, vol. 14, no. 2, pp. 264–269, 2009.

[186] C. P. Szczyglowski, S. A. Neild, B. Titurus, J. Z. Jiang, and E. Coetzee, "Passive gust load alleviation in a truss-braced wing using an inerter-based device," *Journal of Aircraft*, 2019.

[187] S. S. Rao, *Vibration of Continuous Systems*. 2007.

[188] J. A. Staley, "Validation of Rotorcraft Flight Simulation Program through Correlation with Flight Data for Soft-in-Plane Hingeless Rotors," tech. rep., AMRDL-TR-75-50, 1976.

[189] J. W. R. Taylor, *Jane's All the World's Aircraft, 1988-89*. Jane's Defence Data, 1988.

[190] B. H. Lau, A. W. Louie, N. Griffiths, and C. P. Sotiriou, "Performance and rotor loads measurements of the Lynx XZ170 helicopter with rectangular blades," 1993.

[191] M. J. Taylor, "Flight international world aircraft & systems directory," 2002.

[192] W. Chan, *A Coupled Rotor-Fuselage Aeroelastic Analysis Using Complex Rotor Modes*. PhD thesis, City University, London, 1996.

[193] J. W. R. Taylor, *Jane's All the World's Aircraft, 2003-04*. Jane's Defence Data, 2003.

[194] F. A. Internationale, “Record id 11659,” 1986.
https://www.fai.org/fai-record-file/?recordId=11659.

[195] L. Jeram-Croft, *Royal Navy Lynx*.
Pen and Sword, 2017.

[196] M. Gennaretti and G. Bernardini, “Aeroelastic response of helicopter rotors using a 3D unsteady aerodynamic solver,” *Aeronautical Journal*, vol. 110, no. 1114, pp. 793–801, 2006.

[197] J. P. Thomas, E. H. Dowell, and K. C. Hall, “Nonlinear inviscid aerodynamic effects on transonic divergence, flutter, and limit-cycle oscillations,” *AIAA Journal*, vol. 40, no. 4, pp. 638–646, 2002.

[198] D. Tang and E. H. Dowell, “Damping prediction for hingeless rotor aeroelastic stability with experimental correlation,” *Journal of Aircraft*, vol. 33, no. 6, 1996.

[199] A. H. Khater, R. S. Temsah, and M. M. Hassan, “A Chebyshev spectral collocation method for solving Burgers ’-type equations,” *Journal of Computational and Applied Mathematics*, vol. 222, no. 2, pp. 333–350, 2008.